Lappeenrannan teknillinen yliopisto

Lappeenranta University of Technology

Asko Parviainen

DESIGN OF AXIAL-FLUX PERMANENT-MAGNET LOW-SPEED MACHINES AND PERFORMANCE COMPARISON BETWEEN RADIAL-FLUX AND AXIAL-FLUX MACHINES

Thesis for the degree of Doctor of Science (Technology) to be presented with due permission for public examination and criticism in the auditorium 1382 at Lappeenranta University of Technology, Lappeenranta, Finland on the 19th of April, 2005, at noon.

Acta Universitatis

Lappeenrantaensis

208

ISBN 952-214-029-5
ISBN 952-214-030-9 (PDF)
ISSN 1456-4491

Lappeenrannan teknillinen yliopisto
Digipaino 2005

ABSTRACT

Asko Parviainen

DESIGN OF AXIAL-FLUX PERMANENT-MAGNET LOW-SPEED MACHINES AND PERFORMANCE COMPARISON BETWEEN RADIAL-FLUX AND AXIAL-FLUX MACHINES

Lappeenranta 2005

153 p.
Acta Universitatis Lappeenrantaensis 208
Diss. Lappeenranta University of Technology
ISBN 952-214-029-5, ISBN 952-214-030-9 (PDF), ISSN 1456-4491

This thesis presents an alternative approach to the analytical design of surface-mounted axial-flux permanent-magnet machines. Emphasis has been placed on the design of axial-flux machines with a one-rotor-two-stators configuration. The design model developed in this study incorporates facilities to include both the electromagnetic design and thermal design of the machine as well as to take into consideration the complexity of the permanent-magnet shapes, which is a typical requirement for the design of high-performance permanent-magnet motors.

A prototype machine with rated 5 kW output power at 300 min^{-1} rotation speed has been designed and constructed for the purposes of ascertaining the results obtained from the analytical design model.

A comparative study of low-speed axial-flux and low-speed radial-flux permanent-magnet machines is presented. The comparative study concentrates on 55 kW machines with rotation speeds 150 min^{-1}, 300 min^{-1} and 600 min^{-1} and is based on calculated designs. A novel comparison method is introduced. The method takes into account the mechanical constraints of the machine and enables comparison of the designed machines, with respect to the volume, efficiency and cost aspects of each machine. It is shown that an axial-flux permanent-magnet machine with one-rotor-two-stators configuration has generally a weaker efficiency than a radial-flux permanent-magnet machine if for all designs the same electric loading, air-gap flux density and current density have been applied. On the other hand, axial-flux machines are usually smaller in volume, especially when compared to radial-flux machines for which the length ratio (axial length of stator stack vs. air-gap diameter) is below 0.5. The comparison results show also that radial-flux machines with a low number of pole pairs, $p < 4$, outperform the corresponding axial-flux machines.

Keywords: Permanent-magnet synchronous motor, axial-flux PMSM, radial-flux PMSM

UDC 621.313.8 : 621.313.323

Acknowledgements

I wish to express my gratitude to my supervisor Prof. Juha Pyrhönen for his valuable comments and guidance throughout the work as well as for giving me the opportunity to participate in several other interesting projects in the process of and related to my Ph.D. work.

I wish to thank the pre-examiners Prof. Essam Hamdi and Prof. Valeria Hrabovcova for their valuable comments and corrections.

I wish to thank D.Sc. Markku Niemelä for his comments and suggestions related to this work and for his encouraging guidance during the laboratory work.

I am also grateful to D.Sc. Jouni Ikäheimo, M.Sc. Jari Pekola and Mr. Juhani Mantere from ABB for their valuable advice, discussions and support during the work. The project was partly financed by Carelian Drives and Motor Centre, CDMC, which is the research centre of ABB companies and Lappeenranta University of Technology, and the Academy of Finland.

I am indebted to the laboratory personnel, Mr. Harri Loisa, Mr. Jouni Ryhänen and Mr. Martti Lindh, for the professional assistance during the construction of the laboratory prototypes as well as for the practical arrangements in the laboratory. I also wish to thank all my friends; their support has been very important to me.

Special thanks are due to D.Sc. Patrick Lombard and D.Sc. Marc Vilcot from CEDRAT, who, in the beginning of the project, offered me the opportunity to work at CEDRAT. The experience I gained on the various aspects of finite element analysis during that working period proved to be very useful later on.

Special thanks are due to FM Julia Vauterin for valuable work to perform the language proof of this thesis.

Financial support provided by Tekniikan Edistämissäätiö, Jenny ja Antti Wihurin rahasto, Lahja ja Lauri Hotisen rahasto, Lappeenrannan teknillisen yliopiston tukisäätiö and Walter Ahlströmin säätiö is highly acknowledged.

For D.Sc. Pia Salminen, I wish to express my special thanks for her encouragement and understanding during the last, busy years.

Finally, I'm deeply indebted to my parents, Kaisa and Veikko, as well as to my brother Jaakko for their untiring support throughout all the years.

Contents

Nomenclature

Roman letters

A	Electric loading, linear current density [A/m]
a	Number of parallel coil branches
B	Magnetic flux density [Vs/m^2]
C	Output coefficient
D	Diameter [m]
d	Thickness of lamination [m]
e, E	Induced voltage: instantaneous value, RMS value [V]
F	Force [N], magneto motive force [A]
f	Frequency [1/s]
f_n	Natural frequency [1/s]
G	Mass [kg]
g	Physical length of air-gap [m]
h	Heat transfer coefficient [W/m^{2}K]
H	Magnetic field strength [A/m]
i, I	Current: instantaneous value, RMS value [A]
J	Current density [A/m^2]
j	Index term
k	Coefficient
K	Crystallographic constant
k_e	Coefficient for the induced voltage
k_i	Current waveform factor
k_P	Electric power waveform factor
L	Inductance [Vs/A]
l	Length [m]
M	Mutual inductance [Vs/A]
m	Number of phases
N	Number of computation planes
n	Number of harmonics
n_s	Rotation speed [min^{-1}]
N_s	Number of winding turns in series per stator winding
Nu	Nusselt number
P	Active power [W]
p	Number of pole pairs
Pr	Prandtl Number
Q	Number of slots
q	Number of slots per pole and phase
r	Radius [m]
R	Resistance [V/A]
Re	Reynolds number
S	Surface area [m^2]
T	Temperature [K], Torque [Nm], Period [s]
t	Time [s]
Ta	Taylor number
U	Voltage [V]
v	Speed [m/s]
V	Volume [m^3]
W	Energy [J]
w	Width [m]
w_c	Coil span
y	Length [m]

Matrix/vectors

$\mathbf{\Phi}$	Magnetic flux
$\mathfrak{R}$	Reluctance
μ_m	Magnetic dipole moment
B	Magnetic flux density
F	Magneto motive force
G	Thermal conductivity
H	Magnetic field strength
J	Polarisation
M	Magnetisation
P	Power loss
T	Temperature

Greek letters

μ_r	Relative permeability
μ_0	Permeability of free space [Vs/Am]
ε	Emissivity
α	Relative magnet width
σ	Electrical conductivity [S/m]
ρ	Density of material [kg/m^3]
Ω	Angular frequency [1/s]
ω	Angular frequency [1/s]
ξ	Winding factor
τ_p	Pole pitch [m]
ν	Cinematic viscosity [m^2/s]
υ	Poisson's ratio
λ	Thermal conductivity [W/mK]
$\tilde{\lambda}$	Relative permeance
η	Efficiency
χ	Skin depth [m]
$\mathfrak{R}$	Reluctance [A/Vs]
$\wp$	Cost [€]
ζ	Stefan-Boltzman constant [W/m^{2}K^4]
Θ	Magnetic voltage [A]
Γ	Modulus of elasticity [N/m^2]

Subscripts

σ	Leakage
σPM	Permanent magnet leakage
a	Armature
act	Active
AF	Axial-flux
agap	Air-gap
ave	Average
ax	Axial
b	Bearing
C	Carter's
c	Coersivity
cen	Centrifugal
ci	Intrinsic coersivity

cog	Cogging torque
con	Convection
cond	Conduction
cross	Cross sectional
Cu	Copper
D	Diameter
d	Direct axis
def	Deflection
dif	Differential
ex	Excess loss
eff	Effective
em	Electromagnetic
end	End-winding
ext	External
f	Friction
Fe	Iron
h	Hydraulic
hys	Hysteresis loss
i	Index term
in	Internal
input	Input
l	Length
m	Mean
M	Motor
max	Maximum
md	Direct axis magnetizing
mq	Quadrature axis magnetizing
n	Natural
opt	Optimal
out	Outer
output	Output
p	Pole
ph	Phase
PM	Permanent Magnet
q	Quadrature axis
r	Remanence
rad	Radiation
rel	Relative
RF	Radial-flux
rms	Root mean square
rotor	Rotor
s	Stator
sat	Saturation
slot	Slot
str	Stray load loss
sup	Support
sur	Surface
t	Tooth
T	Torque
th	Thermal
tot	Total
trap	Trapezoidal
tt	Tooth tip
w	Wire

wet	Wetted
y	Yoke
zz	Zigzag

Acronyms

2D	Two-dimensional
3D	Three-dimensional
ABB	Asea Brown Boveri
AF	Axial-flux
AFIPM	Axial-Flux Interior rotor Permanent Magnet
AFPM	Axial-Flux Permanent Magnet
AlNiCo	Aluminium-Nickel-Cobalt
B	Boron
BBC	Brown Boveri Company
CDMC	Carelian Drives and Motor Centre,
Co	Cobalt
DC	Direct Current
DTC	Direct Torque Control
EMF	Electro Motive Force
Fe	Iron
FEA	Finite Element Analysis
FEM	Finite Element Method
IM	Induction Motor
Nd	Neodymium
Ni	Nickel
PM	Permanent Magnet
PMSM	Permanent-magnet Synchronous Motor
RF	Radial-flux
RFPM	Radial-flux Permanent Magnet
RMS	Root Mean Square
Si	Silicon
Sm	Samarium
SMC	Soft Magnetic Composite
V	Vanadium

1. Introduction

This study concentrates on axial-flux machines with one rotor – two stators configuration. This particular axial-flux machine configuration proves to be the most adequate structure for the considered low-speed high-torque industrial applications. The reason for that is that, firstly, fixing of the stators may be arranged reasonably easily. Secondly, an electrical machine equipped with two stators is capable of operating (with some precautions) even though one of its stators is electrically disconnected and finally, an axial loading of bearings is small due to the internal rotor configuration.

Electrical machines have been designed, constructed and improved by several engineer generations. Yet, electrical machines have been under constant development and improvement. The primary reason for such an interest is the fact that the power electronics have been developed and new, better suitable construction materials have been found. The possibility to feed the motor via a frequency converter opens new perspectives in the machine designing since the line frequency (50 Hz or 60 Hz) is no more a limiting factor for the selection of the machine pole pair number. Using new materials, such as soft magnetic composites and high performance permanent magnets, renders possible the improvement of the machine construction and thus the improvement of the machine performance characteristics. Secondly, the trend of development is to build integrated systems in which the electrical machine is not necessarily a stand-alone machine typically connected via a shaft and gearbox to the controlled unit, Fig. 1.1 (a); preferably, it is an integrated part of the overall system according to Fig. 1.1 (b). Consequently, in direct drive applications the torque quality aspects are becoming an increasingly important subject of design since the power transmission chain does not absorb torque fluctuations in a similar manner as it does if gearboxes are used between the electrical machine and the controlled unit. Thus, the designer will meet the demanding task to minimize the cogging torque as well as the pulsations in the electromagnetic torque of the machine without loosing too much in the other performance of the machine.

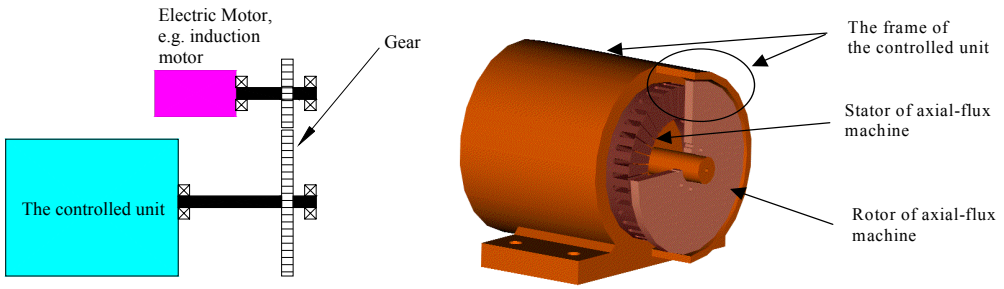

(a) (b)

Fig. 1.1. (a) Conventional electric drive system: The controlled unit is driven by the induction motor via a gear. (b) Integrated system in which the axial-flux machine may be fixed directly inside the frame structures of the controlled unit. The rotor of the electric machine is located on the same shaft as the controlled unit.

The development of the permanent-magnet synchronous machine has been fast since the invention of the high-performance Neodymium-Iron-Boron (Nd-Fe-B) permanent magnet material in 1983. Especially low-speed and variable speed industrial applications are recognized to be a potential application area for such permanent-magnet machines. In several industrial applications induction machines with step-down gearboxes are used in order to obtain the desired rotational speed for the driven machinery. Connecting the electrical motor to the device

without a gearbox reduces the maintenance costs as well as the space requirements and improves the reliability of the system. The desired high-performance low-speed direct drive can be achieved by using permanent-magnet machines and new control methods such as the direct torque control (DTC) or other high performance vector control methods. Permanent-magnet machines are well suitable for low-speed applications since their performance, e.g. efficiency and power factor, does not depend on the rotation speed to the same extent as it is the case for induction machines, Fig. 1.2.

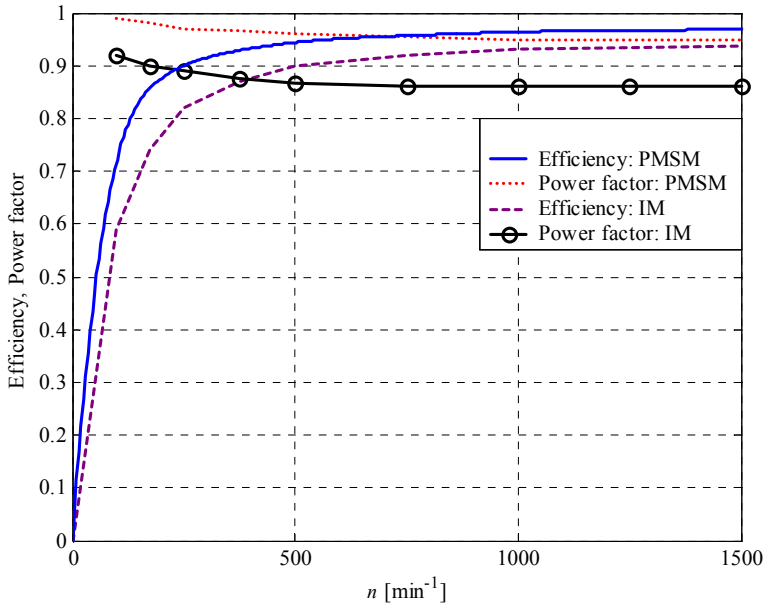

Fig. 1.2. Comparison of efficiencies and power factors of 55 kW, 1500 min^{-1} induction and surface-mounted permanent-magnet motor as a function of rotation speed. Curves calculated based on constant torque and flux approach. The IM rotor absolute slip producing the nominal torque is about 20 min^{-1}.

In integrated systems, an important demand is to select the most suitable electrical machine for a particular application. Traditionally, it has been used almost exclusively machines of the radial-flux type. Due to the development of the permanent magnet materials, for some particular applications, using radial-flux machines seem to be no more the most adequate solution. If the machine axial length is limited by the application demands or if it appears to be possible to integrate the rotor directly into the driven machinery, the electrical machine based on the axial-flux topology may be a competitive or even a better choice. Compared to radial-flux machines, axial-flux machines have been manufactured and also less used. Therefore, it is obvious that the process of designing and manufacturing axial-flux machines is still developing. For radial-flux machines, the process of manufacturing is well established since it could be optimised through the enormous amount of induction machines that has been manufactured during the latest century. The radial-flux permanent-magnet motor can be manufactured based on the same process of manufacturing the induction machine since the required machines parts for both machine types are basically the same. The manufacturing of axial-flux machines requires a different type of production equipment, which demands expensive investments as a result of which the unit price remains high if only a small amount of machines is manufactured. Thus, it must be sought for driving forces that provide the motivation and encouragement that increases the use and construction of axial-flux machines. Such driving forces may arise from the difference of the machine performance or material costs, or directly from the geometrical restrictions set by the particular application requirements.

1.1. Motivation and target of the work

It is the industry's interest to build reliable, high-performance electrical machines at the lowest cost possible. Constraints restricting the business are the efficiency, cooling and mechanical properties of the machines. If industry is offered an opportunity to choose between two alternative electrical machines, which have the same performance, e.g. efficiency, but of which one can be built at a lower manufacturing cost, it is obvious that the latter, cheaper design will be preferred. An important tool needed for decision-making is then a performance comparison between the considered electrical machines. A theoretical comparison between similar machines types can be done reasonably but comparison between the different machine topologies is a cumbersome task since there exist many variables and it is difficult to decide which variables should be kept as constants and which may vary. In order to establish a reliable comparison, a sufficient amount of different machine designs has to be considered. In this thesis, a comparison between axial-flux and radial-flux permanent-magnet machines is given.

The research work was encouraged to start by the ABB companies. The motivation for the research work is to attain two, basically independent purposes:

1. The first objective of the work is to develop a suitable analytical design method and a corresponding design tool for the preliminary design of surface-mounted axial-flux permanent-magnet machines. The motivation for this work is supported by the fact that the 3D finite element analysis is very time consuming to perform and is not very practical to be applied in the preliminary machine design phase. Furthermore, investigations of the literature on the subject reveal that the analytical design of surface-mounted axial-flux permanent-magnet machines is not yet well established. In textbooks or in relevant papers the design of axial-flux machines is usually carried out on the average radius of the stator, which may lead to significant inaccuracy in performing the design if the magnet shape is complex or the flux density variation in the iron parts varies strongly with respect to the radius. In this thesis, an analytical method to perform the design of axial-flux machines, even for complex magnet structures, is introduced.
2. The second objective of the work is to complete a performance and constructional comparison between the low-speed radial-flux and axial-flux permanent-magnet machines. Comparison was done based on the existent ABB permanent-magnet machine family (ABB, 2004). ABB motors are designed for industrial applications in the speed range of 120 – 600 min^{-1} and covering a power range of 17 kW up to 2500 kW.

The work for the developing of an analytical design tool was carried out in an early stage of this study and the tool was improved in the course of the thesis project. The latest, significant improvement was the addition of a thermal model, which was included to be part of iterative procedure of designing axial-flux permanent-magnet machines. The proposed design tool is kept relatively simple and it is not developed to replace the finite element analysis (FEA) in machine designing. Thereby, some simplifications are accepted and included in the computation model, e.g. the reluctance networks used are kept simple on purpose. Furthermore, the optimisation of different designs is not considered in the analytical design procedure.

The thesis includes two main parts, treating respectively the two above-mentioned objectives of the research work. The first part includes a review of the discussed permanent-magnet machines and used materials, as well as design considerations related to the analytical modelling of axial-flux surface-mounted permanent-magnet machines. The constructed prototype machine and the measurement results obtained from the prototype machine are also introduced in this part. In the second part of the work a relevant theory needed for drawing the comparison is provided and the results of the comparison are reported. The comparison part is further divided into two parts including structural aspects and a performance comparison. The mechanical studies provide some necessary practical design limitations, which are used as mechanical design constraints in the performance comparison.

1.2. Scientific contribution of the work and relevant publications

The scientific contributions are:

1. An analytical design procedure is developed for the purpose of designing axial-flux surface-mounted permanent-magnet machines. The developed computation method employs quasi-3D computation and is combined with the thermal model.
2. A structural comparative study on radial-flux and axial-flux permanent-magnet machine topologies is done. The two-stator-one-rotor axial-flux construction is considered.
3. Results of an extended performance analysis between low-speed radial-flux and axial-flux permanent-magnet machines are presented. The performance comparison part is extended in this work to cover the practical mechanical constraints.

Furthermore, in the discussion on the constructed prototype machine and measurement results some aspects are treated, which may be considered to offer new and useful scientific information on the performance characteristics of the studied axial-flux permanent-magnet machine structure.

The most relevant publications related to the thesis are:

1. A. Parviainen, M. Niemelä, J. Pyrhönen. "Modeling Axial-flux Permanent-Magnet Machines". *IEEE Transaction on Industry Applications*. Vol. 40, No. 5, 2004, pp. 1333-1340.
2. A. Parviainen, M. Niemelä, J. Pyrhönen. "Design of Axial-flux Permanent Magnet Machines: Thermal Analysis". In *Proceedings of International Conference on Electrical Machines*, ICEM'04, Cracow, Poland, 5-8 September 2004, on CD-ROM.
3. Parviainen, M. Niemelä, J. Pyrhönen "Analytical, 2D FEM and 3D FEM modelling of PM axial-flux machines", In *Proceedings of 10th European Conference on Power Electronics and Applications*, EPE'03, Toulouse, France, 1-4 September 2003, on CD-ROM.
4. A. Parviainen, M. Niemelä, J. Pyrhönen, "A Novel Axial-flux Permanent Magnet Machine to Laboratory Use", In *Proceedings of 11th International Symposium on Electromagnetic Fields in Electrical Engineering*, Maribor, Slovenia, 18-20 September 2003, pp. 277-280. (Accepted to be published in Kluwer monograph: Computer Modeling in Electromagnetics)
5. A. Parviainen, J. Pyrhönen, M. Niemelä, "Axial-flux Interior Permanent Magnet Synchronous Motor with Sinusoidally Shaped Magnets", *Studies in Applied Electromagnetics and Mechanics*, Vol 22. ISSN: 1383-7281. IOS Press, Amsterdam, 2002, pp. 271-276.
6. A. Parviainen, M. Niemelä, J. Pyrhönen, "Reduction of Torque Pulsations in Axial-flux Interior PM Synchronous Machines", *Proceedings of Nordic Workshop on Power and Industrial Electronics*, Stockholm, Sweden, 12-14 August 2002, on CD-ROM.

1.3. Axial-flux permanent-magnet machines

The history of electrical machines shows that the first machines were – more or less – realised in a form of the axial-flux machine. The first one was invented by Faraday in 1821 and was practically a primitive permanent-magnet DC machine (Atherton, 1984). Radial-flux machines

were invented later and were patented firstly by Davenport in 1837 (Chan, 1987). Since then radial-flux machines have dominated excessively the markets of the electrical machines. The first attempts to enter the industrial motor market with radial-flux PMSMs in the 1980's was made by the former BBC, which produced line-start motors with SmCo-magnets. The main idea in the early stage of the PMSMs was to increase the efficiency of the traditional electric motors by permanent magnet excitation. However, the efficiency increase was not enough for the customers and the attempts to enter the market failed. Despite of this setback, several manufacturers introduced permanent-magnet machines successfully during the latest decade. Regardless of the success of radial-flux permanent-magnet machines, axial-flux permanent-magnet machines have also been under research interest particularly due to special-application-limited geometrical considerations. A possibility to obtain a very neat axial length for the machine makes axial-flux machines very attractive into applications in which the axial length of the machine is a limiting design parameter. Such applications are, for example, electrical vehicles wheel motors (Profumo et al., 1997) and elevator motors (Hakala et. al., 2000). Axial-flux machines have usually been used in integrated high-torque applications.

Several axial-flux machine configurations can be found regarding the stator(s) position with respect to the rotor(s) positions and the winding arrangements giving freedoms to select the most suitable machine structure into the considered application. Possible configurations are:

- Structure with one rotor and one stator, Fig. 1.3 (a).
- Structure, in which the stator is located between the rotors, Fig. 1.3 (b).
- Structure, in which the rotor is located between the stators, Fig. 1.3 (c).
- Multistage structure including several rotors and stators Fig. 1.3 (d).

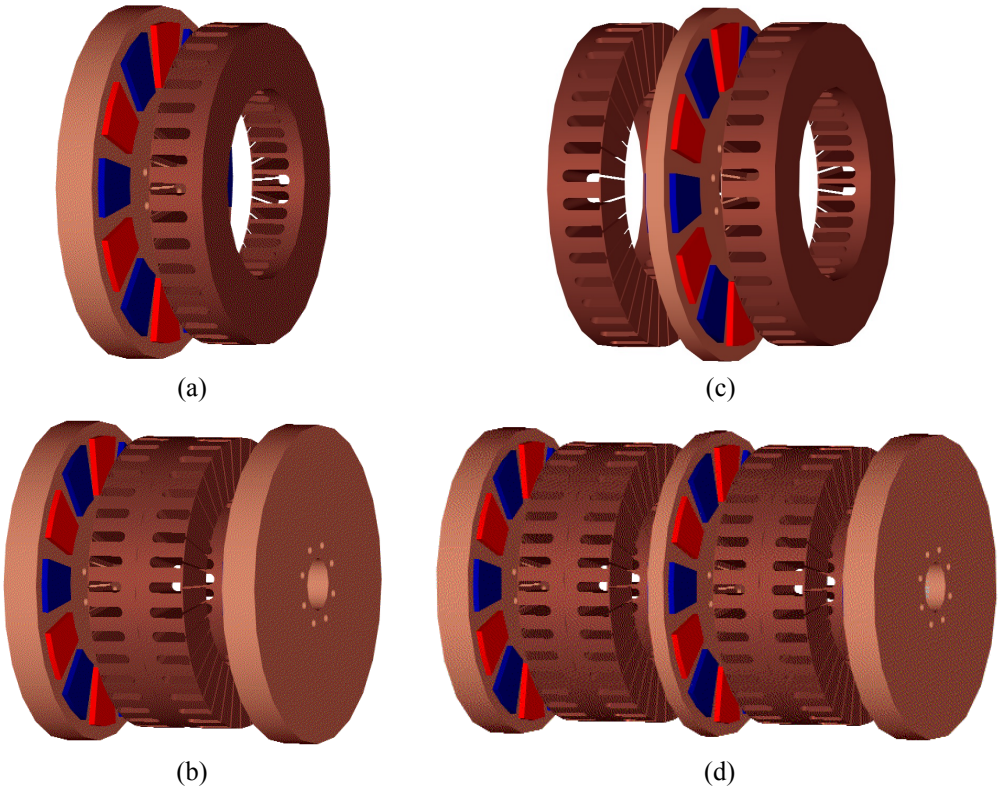

Fig. 1.3. Axial-flux machine configurations. (a) Single-rotor – single-stator structure. (b) Two-rotors – single-stator structure. (c) Single-rotor – two-stators structure, called hereafter also as AFIPM machine (Axial-Flux Interior rotor Permanent-Magnet machine). (d) Multistage structure including two stator blocks and three rotor blocks.

The single-rotor – single-stator structure, shown in Fig. 1.3 (a), is the simplest axial-flux permanent-magnet machine configuration (Campbell, 1974; Kurronen, 2003). This structure suffers, however, from an unbalanced axial force between the rotor and the stator as a consequence of which more complex bearing arrangements and a thicker rotor disk are needed, this compared to structures in which the axial forces are balanced.

The one stator – two rotors structure, illustrated in Fig. 1.3 (b), is a "TORUS" type axial-flux machine that has its phase coils wound around the slotted stator (Huang et al., 2001; Aydin et al., 2001) or non-slotted stator. The first "TORUS" type permanent-magnet machine, with non-slotted stator, was introduced in the late 1980's (Spooner and Chalmers, 1988). The toroidally wound phase winding has short end-windings, which improves the machine efficiency and power density. As a drawback, the fixing of the stator to the frame is more complex, and compared to the opposite structure in which the rotor is located between the stators (hereafter referred to as Axial-flux Interior rotor Permanent-magnet machine, AFIPM), less space is left for the winding (Profumo et al., 1998; Parviainen et al., 2002a; Sahin et al., 2001).

More complex arrangements can be found by assembling several machines lined up on the same shaft and by forming a multistage axial-flux machine according to Fig. 1.3 (d). Such machines may be considered for ship propulsion drive use (Carrichi et al., 1995), pump (Carrichi et al., 1998) and high-speed permanent-magnet generator applications (El-Hasan et al., 2000) and research purposes (Braid et al., 2003).

It may also be found variations related to the magnet arrangement in rotor. The arrangement of the magnets has an effect on the main flux path in the machine rotor or stator as well as possible winding configurations. In the case of the "TORUS" topology the main flux may flow axially through the stator or it may flow circumferentially in the stator yoke. Possible flux paths for this configuration (b) are illustrated in Fig. 1.4 in 2D plane.

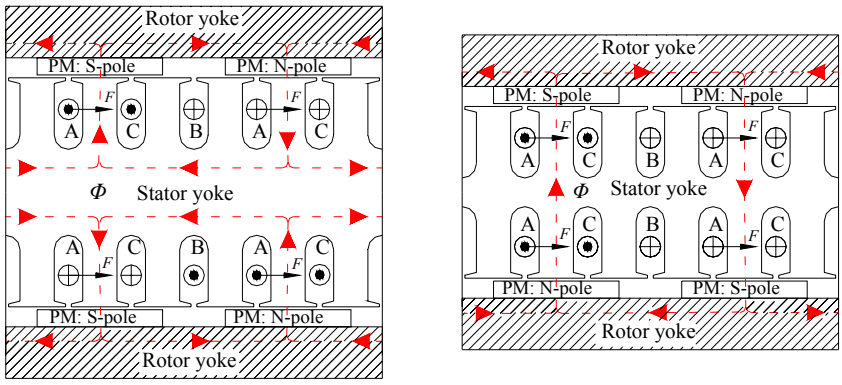

Fig. 1.4. Flux paths in 2D plane for the slotted TORUS machine. (a) North-North type magnet arrangement. (b) North-South type magnet arrangement. The tangential Lorentz forces affecting the phase A coils are illustrated for both structures.

The structures, shown in Fig. 1.4, are identical except for the thickness of the stator yoke and the winding arrangement. For the North-North (NN) structure, the phase winding is wound around the stator core giving short end windings in both the axial and radial directions of the machine. In this structure the copper losses are reduced due to the very short end windings. But, since the main flux has to flow circumferentially along the stator core, a thick stator yoke is required, which on turn increases the iron losses and the end winding lengths as well. For the North-South (NS) structure, the main flux flows axially through the stator, thus the structure does not need a stator yoke at all, in principle. This decreases the iron losses but, on the other hand, lap windings have to be used so that the machine is capable of producing torque. This

increases the length of the end winding, which again increases the copper losses. To compare the NS to the NN structure, also the external diameter of the machine with NS structure is increased (Huang et al., 2001). As a conclusion, the NN structure has lower copper losses and a smaller external diameter but higher iron losses and a grater axial length.

In a single rotor - two stators structure, Fig. 1.4 (c), the permanent magnets may be located on a surface of the rotor disk according to Fig. 1.5 (a). Alternatively, the magnets may be located inside the rotor disk according to Fig. 1.5 (b). Thereby, the main flux may flow axially through the rotor disk or flow circumferentially along the rotor disk. To build a single-stator – single-rotor structure both magnet arrangements may be used, but, in this case, the main flux flows always circumferentially along the rotor disk.

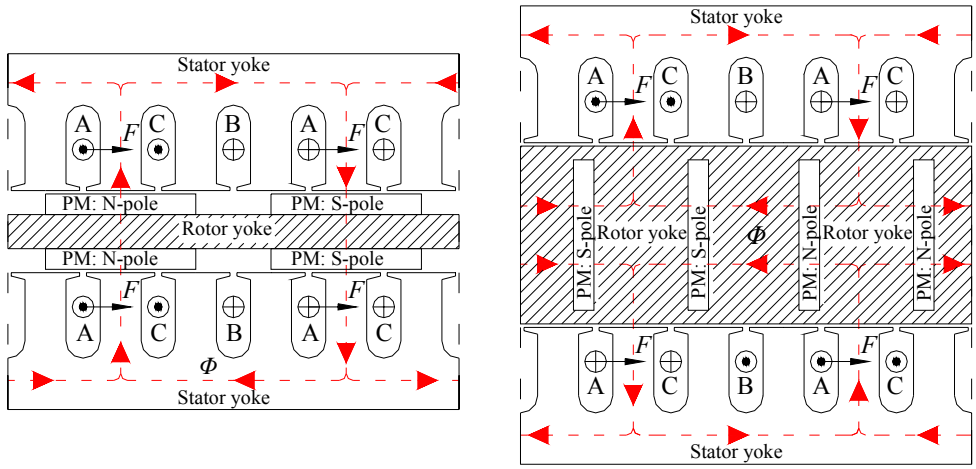

Fig. 1.5. Flux paths in 2D plane for a single-rotor – two-stators structure. (a) Flux flowing through the rotor disk. (b) Main flux flowing circumferentially in a rotor core.

The surface-mounted structure, illustrated in Fig. 1.5 (a), has a very thin rotor, especially if the magnets are installed inside a non-ferromagnetic rotor core (Gieras, 1997; Platt, 1989). An alternative solution, in which the permanent magnets are buried into the rotor disk according to Fig. 1.5 (b), has a much thicker rotor disk, which consequently reduces the power density of the machine the stator structure of the machine remaining basically the same. The leakage flux in the magnet ends is higher, as compared to the surface-mounted structure, since the magnets are surrounded by ferromagnetic material. Some difficulties may arise if the thickness and the magnetisation of the magnets are constant along the machine radius; on the inner radius the permanent magnets may be located very close to each other, depending on the machine inner diameter and pole pairs. This may result in excessive saturation in the rotor core on the inner radius. On the other hand, the flux density level on the outer radius is much smaller, causing non-constant flux density distribution in the air-gap along the machine radius. To further compare the surface-mounted structure with the buried structure: for the buried structure the armature reaction is higher since, for the surface-mounted configuration, the permanent magnets act almost as air thus forming a longer air-gap. As an advantage, the buried structure better protects the magnets against mechanical impacts, wear and corrosion.

For the buried magnet structure, Fig. 1.5 (b), a modular rotor pole construction including layers of ferromagnetic and non-ferromagnetic materials may reduce the armature reaction (Weh et al., 1984). Such a rotor structure is illustrated in Fig. 1.6. The non-ferromagnetic bridges between the ferromagnetic layers cause that the reluctance for the field lines of the armature field is strongly increased. This, as a result, considerably reduces the armature field when compared to a case in which the rotor pole includes only ferromagnetic material. For the proposed structure,

each of the stator teeth are supplied with approximately the same magnetic flux, thus there exists a virtually constant excitation field. Furthermore, there appears also a diminution of leakage fluxes in the magnet ends due to the slits arranged between the ferromagnetic bridges (Weh et al., 1984).

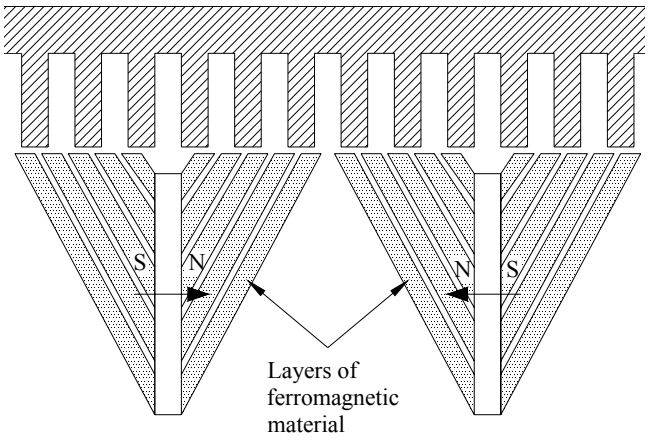

Fig. 1.6. Rotor pole structure capable of reducing the armature reaction (Weh at al., 1984).

It is also possible to use stator structures without ferromagnetic cores. Ironless stator configurations are typically used in applications with rated power lower than 1 kW and with a relatively high rotation speed since the air-gap flux density level, as a result of the long air-gap, tends to be low. In such machines the stator winding is fixed to the resin. The iron losses are minimised since there is no iron in the stator core. But, additional eddy currents appear in the conductors because these are exposed directly to the alternating flux produced by the permanent magnets. Thus, the copper losses increase. However, this effect may be reduced by using thin conductors. A similar situation appears also with a non-slotted "TORUS" type machine which has its phase winding fixed on the surface of the stator core (Söderlund et al., 1996).

Considering high-speed applications, an interesting idea is to introduce a passive rotor concept for axial-flux type machines even though the outcome is not a pure axial-flux machine anymore. In this machine structure the permanent magnets are included into the stator of the machine and the flux path is mainly in transversal plane, Fig. 1.7. The structure corresponds to that of electrically excited homopolar synchronous machines (Weh, 1980).

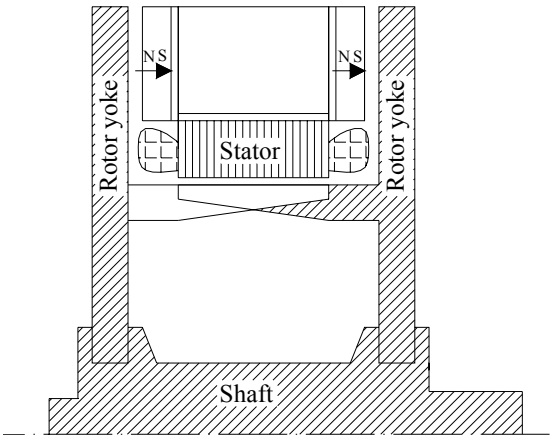

Fig. 1.7. Axial-flux type machine with passive rotors (Weh, 1980).

1.3.1. Torque production

Considering an idealized axial-flux machine structure with double air-gaps, according to Fig. 1.8, the expression for the electromagnetic torque produced by the machine may be derived (Campbell, 1974). In the analysis, it is assumed that the permanent magnets produce a square wave flux density distribution into the air-gap with maximum value B_{max}. It is also assumed that all the winding conductors carry constant current with RMS value I, and the current is appropriately timed and perpendicularly oriented with the flux density distribution in the air-gaps. The conductors are located as closely together as possible on the inner radius of the stator core r_{in}. Therefore, the linear current density A on radius r can be written as

$$A(r) = \frac{A_{in} r_{in}}{r}, \tag{1.1}$$

where

A_{in} is the linear current density on the inner radius r_{in} of the machine and is defined as

$$A_{in} = \frac{m N_{ph} I}{\pi r_{in}}, \tag{1.2}$$

where

m is the number of phases
N_{ph} is the number of coil turns in series per stator phase winding

With the given assumptions, the machine torque can be calculated from the elementary forces dF acting on the surface of the stator core. The elementary torque component dT_{em} on radius r takes the form

$$\mathrm{d}T_{em} = 2\pi r_{in} A_{in} B_{max} r \mathrm{d}r, \tag{1.3}$$

where

B_{max} is the maximum value of the air-gap flux density produced by the permanent magnet.

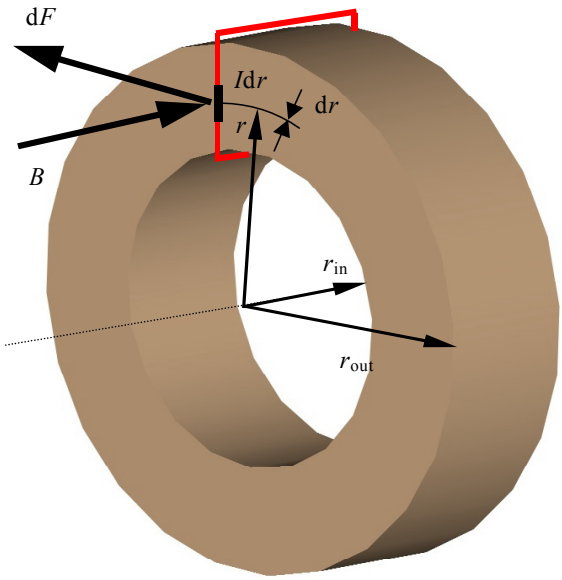

Fig. 1.8. Illustration of torque production mechanism in axial-flux machines.

Integrating (1.3) over the machine radius gives the electromagnetic torque for the ideal double-sided axial-flux machine

$$T_{\mathrm{em}} = 2\pi B_{\max} A_{\mathrm{in}} 2 \int_{r_{\mathrm{in}}}^{r_{\mathrm{out}}} r_{\mathrm{in}} r \mathrm{d}r = 2\pi B_{\max} A_{\mathrm{in}} r_{\mathrm{out}}^3 k_{\mathrm{D}} (1 - k_{\mathrm{D}}^2) , \tag{1.4}$$

where

k_{D} is the diameter ratio and is defined as

$$k_{\mathrm{D}} = \frac{r_{\mathrm{in}}}{r_{\mathrm{out}}} . \tag{1.5}$$

The electromagnetic torque produced by a real machine is somewhat reduced due to the actual distribution of the flux density in the air-gaps and in the current waveform. This is investigated in detail in Chapter 5. However, from (1.4) it is possible to derive the optimal diameter ratio for the idealized axial-flux machine, which is (Campbell, 1974)

$$k_{\mathrm{D,opt}} = \frac{1}{\sqrt{3}} \approx 0.58 .$$

Note that, as axial-flux machines are concerned, the diameter ratio is an important design parameter. The torque production capability of the machine, as a function of k_{D}, is described in Fig. 1.9. The curve is scaled for the maximum torque to be equal to value 1.

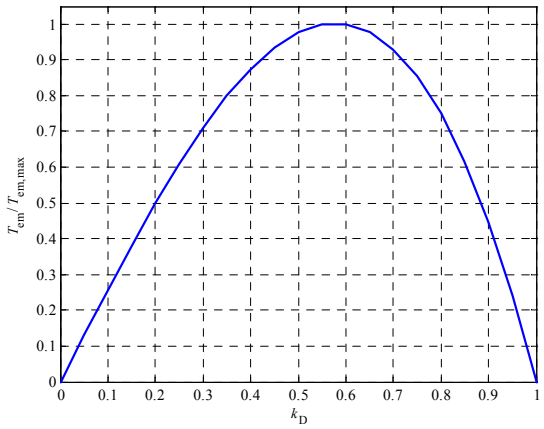

Fig. 1.9. Electromagnetic torque of an ideal axial-flux machine as a function of the machine diameter ratio.

In practice, using diameter ratios lower than 0.6 involves practical difficulties, especially in small machines with lap windings. The first problem is related to the limited space available between the stator core and the shaft. In small machines, to obtain enough free space between the shaft and the stator core for the end-windings to be properly arranged may be very difficult or even impossible. Fig. 1.10 (a) illustrates this particular problem of limited space for winding the machine with lap winding and with diameter ratio $k_{\mathrm{D}} = 0.6$. This problem can be avoided by using a "TORUS" type machine, which has its phase winding wound around the stator core. An alternative solution is to obtain the phase winding through concentrated windings. For the sake of comparison, Fig. 1.10 (b) illustrates a stator with a double-layer concentrated winding whilst a conventional integral slot winding is shown in Fig. 1.10 (a). Essentially shorter end-windings in the radial direction are obtained on both the inner radius and outer radius of the stator core.

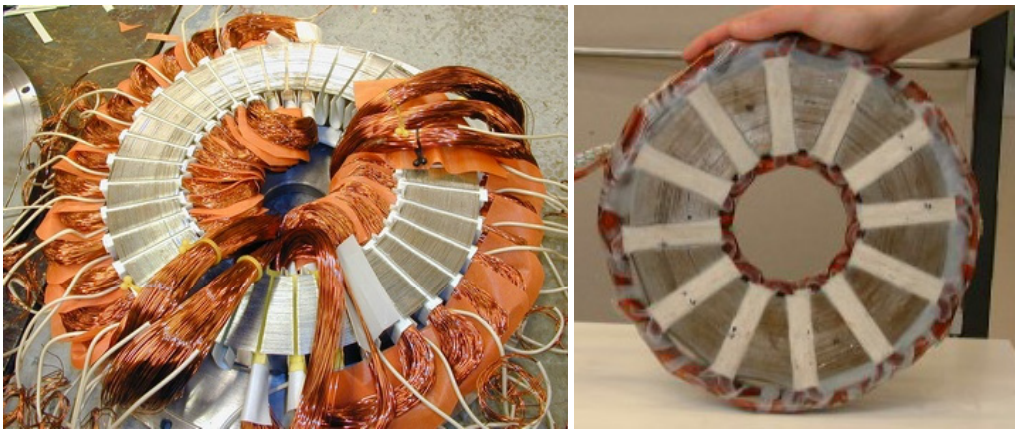

(a) (b)

Fig. 1.10. (a) Limited space on the inner radius of the axial-flux machine (Q_s = 36, p = 6, q = 1) while winding the axial-flux machine stator. A conventional two-layer lap winding is employed. (b) Concentrated stator winding enabling values for k_D lower than 0.6.

The second problem is related to the tooth width. From the viewpoint of machine design it is advantageous when the slot width is a constant. Small diameter ratios may cause that on the outer radius the tooth width is very large whereas on the inner radius it remains very narrow. A narrow tooth appears to be mechanically fragile and it may be excessively saturated on inner radius. These are both undesired properties.

Finally, it has been shown that the machine torque density reaches its maximum value when the diameter ratio is between 0.6 and 0.65 (Carrichi et al., 1998; Huang et al., 2001). Considering the previously discussed mechanical considerations in relation with the torque density characteristic of the axial-flux machine, it is correct to conclude that the practical optimum for the diameter ratio lies between 0.6 and 0.7.

1.4. Radial-flux permanent-magnet machines

Over a period of several decades radial-flux permanent-magnet machines have been used widely in fractional horsepower applications but not in large-scale industrial applications. However, the situation has changed dramatically during the latest decade. According to Waltzer (2002), the era of permanent-magnet machines for large-scale industrial use begins at the turn of the millennium with ABB, which introduced permanent-magnet machines for power ranges up to 5 MW to be applied to, for instance, ship propulsion drives and windmill generators. In the smaller power range, a permanent-magnet machine family was designed for low-speed applications (ABB, 2004). Also, e.g. Baumüller, Yaskawa, Siemens and Rotatek have been very active in the field of PMSM in the latest years.

A comprehensive review of the state-of-the-art development and design of the radial-flux PM machines is given by Heikkilä (2002). However, new development in the field of radial-flux permanent-magnet machines has since been reported. Low-speed permanent-magnet machines with concentrated windings are at the moment under great research interest (Salminen, 2004; Magnussen et al., 2003a). Furthermore, some permanent-magnet machine topologies, which may be considered to be new, were introduced (Qu et al., 2003; Magnussen et al., 2003b).

Fig. 1.11 illustrates possible radial-flux permanent-magnet machine configurations. The most commonly manufactured machine type is an external stator – internal rotor machine, which is a

traditional electric motor configuration, Fig. 1.11 (a-b). The structure with external rotor and internal stator, known also as drum motor, is an alternative configuration, Fig. 1.11 (c). This motor configuration is suitable for applications where the rotor can be integrated directly into the machine of application. Such applications are, for example, wheel motors of electrical vehicles and driving rolls of convey belts.

Recently, Qu (Qu et al., 2003) introduced a machine structure with toroidally wound internal stator and two rotors, Fig. 1.11 (d). The latter construction does not seem very practical since the mechanical structure is more complicated and the heat removal from the internal stator requires efficient air circulation inside the machine. However, the structure essentially improves the torque density of the machine and may be useful in some applications where the overall volume of the machine is limited.

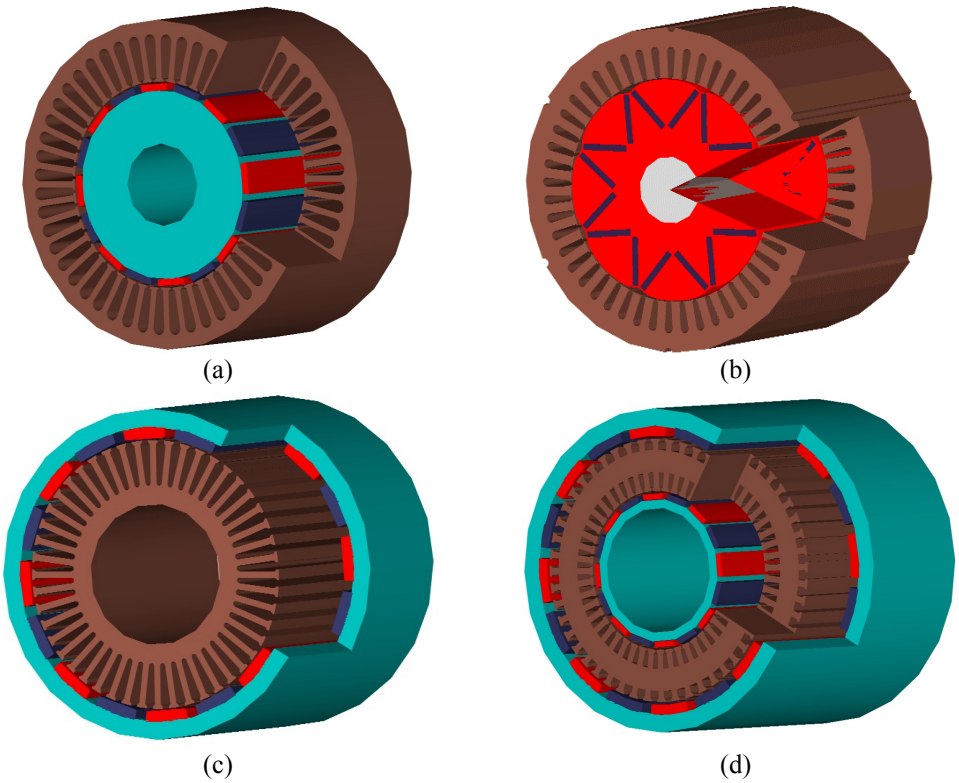

Fig. 1.11. Radial-flux PM-machine configurations. (a) and (b) are internal rotor structures with surface-mounted magnets (a) and buried magnets (b). Structure (c) is a drum motor which has only low demands for the fixing of the magnets, and structure (d) is a double rotor configuration with internal toroidally wound stator.

In contrast to axial-flux machines, which are manufactured almost exclusively with surface-mounted magnets, several variations of assembling the magnets into the rotor of a radial-flux machine are possible and reasonable. Possible rotor configurations are schematically shown in Fig. 1.12.

Surface-mounted structures are relatively simple to manufacture and assemble. If permanent magnets are glued on the surface of the rotor, the rotation speed of the machine must be limited so that centrifugal forces do not break the glue joint. It is possible to improve the mechanical

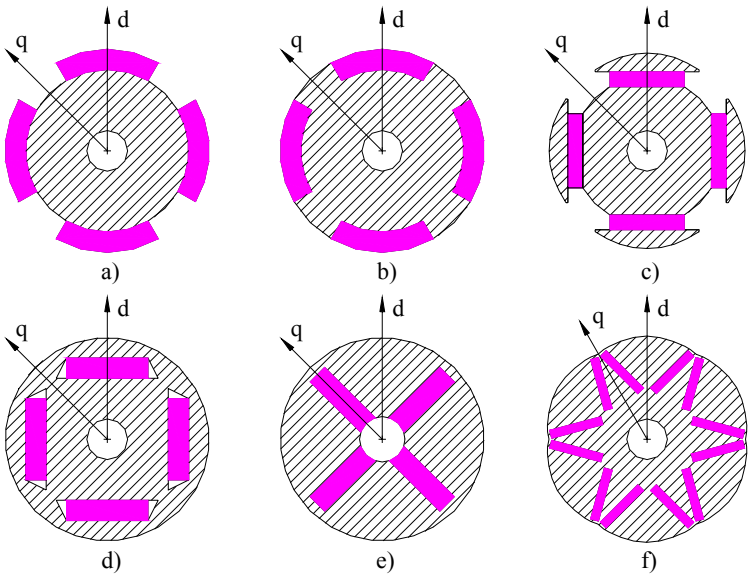

Fig. 1.12. Rotor structures and the definitions for the direct (d) and quadrature (q) axes. Surface-mounted magnets (a), inset magnets (b), surface-mounted magnets with pole shoes (c), buried magnets (d)-(e), buried magnets with shaped air-gap outline (f). Types a, b and c may easily be manufactured using either rotor lamination or a solid rotor core construction, the other types usually need a laminated rotor. If solid parts are used careful the losses should be considered. The synchronous machines are always magnetically unsymmetrical and are thus observed usually with respect to the d- and q-axes. The geometrical structure of the rotor influences strongly the L_d and L_q inductances.

rigidity of the rotor structure by adding a reinforcing belt around the rotor. The reinforcement may be a carbon fibre or fibreglass band or a stainless steel cylinder.The first mentioned are, however, thermal insulators causing additional difficulties in the rotor cooling. A reinforcement cylinder obtained by using stainless steel involves a problem in terms of eddy currents since the material is conductive. Eddy currents are formed into the cylinder due to slotting and, especially with inverter use, due to the harmonic content of the supply current.

Special arrangements may be used in order to obtain a sinusoidal air-gap flux density waveform as well as mechanical protection for the magnets, Fig. 1.12 (c).

The buried magnet configuration exists in several variants, Fig. 1.12 (d-f). Although the rotor structure is somewhat more complex to manufacture it offers several advantages over the surface-mounted structure. The required magnet shape is a rectangular parallelepiped, which is simple to manufacture. No problems occur for the magnets to be fixed, consequently higher rotation speeds may be allowed without using additional reinforcements. It is possible to achieve a nearly sinusoidal air-gap flux density waveform and low cogging torque which thus improves the torque quality. The demagnetisation risk of the permanent magnets is reduced since the magnets are surrounded by ferromagnetic iron and fixed relatively far from the air-gap. The surrounding material also protects the magnets against mechanical impacts, wear and corrosion as already discussed above for the axial-flux machines.

As a disadvantage, the structure suffers from the increased leakage flux in the ends of the magnets since magnetic short-circuits may be formed due to the surrounding iron offers. The leakage fluxes can be reduced by means of proper flux barriers or material selections but leakage fluxes are difficult to diminish to a same level as in the case of a surface-mounted structure. It is also stated that the demolition and recycling of the materials of the machine is more difficult because it is awkward to remove the magnets from the rotor core. Considering this, the surface-mounted structure is a simpler construction.

1.5. Permanent magnet materials

The unusual properties of lodestone, know also as magnetite Fe_3O_4, were known to the ancient Chinese and Greeks. The first known apparatus exploiting magnetism was a magnetic compass, invented by the Chinese around 3000 BC. An important milestone in the research field of magnetism was set in 1600 when William Gilbert published his book "De Magnete", which was the first systematic study related to the phenomenon of magnetism. The artificial permanent magnets discussed in "De Magnete" were made of sword steel and were used to lifting iron parts. According to present standards, the carbon steel used those days is an extremely poor permanent magnet material, offering a low coersivity, $H_c < 4$ kA/m, and a low energy product, $BH_{max} < 2$ kJ/m^3. This remained the quality level of artificial permanent magnets until about 1880 when the systematic study on alloy properties got started. The addition of tungsten and chromium was shown to raise H_c to some degree. An important discovery was the use of cobalt as an additional material and in 1917 K. Honda achieved the ultimate properties of steel magnets by adding to the alloy 35% of cobalt. The maximum energy product of this steel magnet was 8 kJ/m^3 and its coersivity was 20 kA/m (Atherton, 1984; Strnat, 1990).

In 1931 T. Mishima patented the first hard magnetic alloy, based on aluminium, nickel and iron. This was the start of the development of the permanent magnet family known as AlNiCo. Due to the remarkably improved magnet properties the AlNiCo magnets were now made useful for many electrical engineering applications. Supported by a better understanding of material physics, further development of the artificial permanent magnet materials has been rapid since the 1940s. In the 1950s, another permanent magnet family, known as ferrites, became commercially available. Because of their better material properties and much lower material costs the ferrites became extremely popular for DC electric motor applications used in automobiles, hand tools, etc. (Strnat, 1990).

The development of rare earth permanent magnet materials started in the 1960's with the Samarium-Cobalt alloys. The material properties of $SmCo_5$ and Sm_2Co_{17} make these permanent magnet materials very suitable to be used in electric motors and generators, but they are expensive due to the rare raw material Cobalt. The newest, important addition to permanent magnet materials was made in 1983, when the high performance Neodymium-Iron-Boron permanent magnet material was introduced. Compared to Sm-Co permanent magnets, Nd-Fe-B magnets offer compatible material properties but are essentially cheaper. A historical development of the rare earth permanent magnets is illustrated in Fig. 1.13.

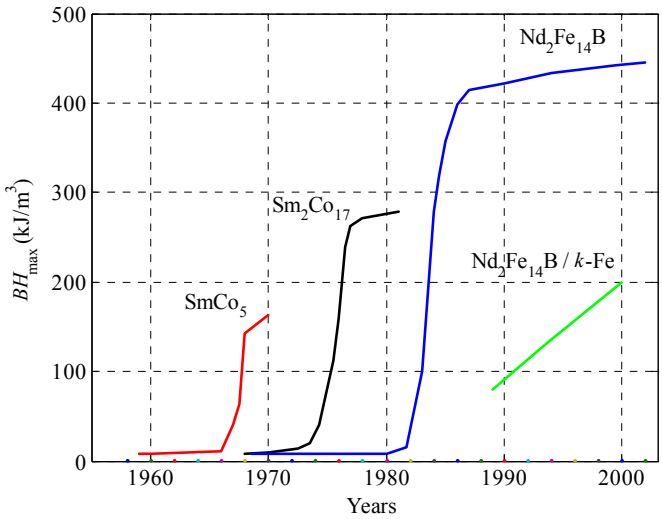

Fig. 1.13. Historical development of the rare earth magnets (Deshpande, 2003).

With the development of the high performance Nd-Fe-B permanent magnet materials, a trend towards the use of permanent-magnet machines in large-scale industrial applications got started and is recently proven by Waltzer (Waltzer, 2002). As the design of a permanent-magnet machine is concerned, it is relevant to understand some properties of the permanent magnet materials discussed in detail by Campbell (Campbell, 1994). In the next chapters the main aspects are given.

1.5.1. Magnetization and coercivity

Present-day knowledge explains that the origin of magnetism is related to the magnetic dipole moments $\boldsymbol{\mu}_m$ of the electrons. Based on the concept of the magnetic dipole moments available in a volume V, it is possible to form the sum of all magnetic dipole moments giving a quantity called magnetization $\boldsymbol{M}$**,** which is defined as (Campbell, 1994)

$$\boldsymbol{M} = \lim_{\Delta V \to 0} \frac{\sum \boldsymbol{\mu}_m}{\Delta V} = n\boldsymbol{\mu}_m \,, \tag{1.7}$$

where

$\boldsymbol{\mu}_m$ is the magnetic dipole moment.
n is the number of atoms per unit volume
ΔV is a volume

In some materials the tendency exists to align the axes of the magnetic dipoles due to their own internal field. This process is called exchange interaction. The existence of the internal field without external magnetizing field is the phenomenon called spontaneous magnetization. Spontaneous magnetization alone can cause a polarisation $\boldsymbol{J}$ within a material. Note that $\boldsymbol{J}$ is equal to the flux density $\boldsymbol{B}$ if the external field strength $\boldsymbol{H}$ is equal to zero.

$$\boldsymbol{J} = \mu_0 \boldsymbol{M} = \boldsymbol{B} - \mu_0 \boldsymbol{H} \,, \tag{1.8}$$

where

μ_0 is the permeability of the vacuum.

On rewriting (1.8) the possible influence of the external field strength $\boldsymbol{H}$ is taken into account leading to the equation

$$\boldsymbol{B} = \mu_0 (\boldsymbol{M} + \boldsymbol{H}) \,. \tag{1.9}$$

For permanent magnet materials the magnetic properties of which are based on magnetocrystalline anisotropy, such as in Nd-Fe-B or Sm-Co materials, the simplified magnetic characteristics of the material can be given according to Fig. 1.14. Point 1 in Fig. 1.14 (a) shows the situation in which all magnetic dipole moments in a material are aligned to the preferred direction, thus the magnetization $\boldsymbol{M}$ corresponds to the saturation magnetization $\boldsymbol{M}_{sat}$. The external field strength $\boldsymbol{H}$ is equal to zero in point 1. By increasing the external field strength to the direction, which opposes $\boldsymbol{M}_{sat}$, the magnetization stays as a constant $\boldsymbol{M}_{sat}$ until the direction of the magnetization suddenly reverses to the value $-\boldsymbol{M}_{sat}$ at point 2. If the applied field is reversed again, the magnetization stays at the value $-\boldsymbol{M}_{sat}$ until it suddenly flips back to the value $\boldsymbol{M}_{sat}$ at point 3 and is maintained at that level even if the external field strength is further increased. The field strength required to change the direction of the magnetization in a material at points 2 and 3 is called intrinsic coercivity H_{ci}. The intrinsic coercivity H_{ci} is the measure of permanent magnetism in a material and it is one of the most important properties of the

magnetic material. It is related to the fundamental properties of the material and can be calculated from the equation

$$H_{\mathrm{ci}} = \frac{2K}{\mu_0 M_{\mathrm{sat}}}, \tag{1.10}$$

where

K is a crystallographic constant for a magnet element

The graph given in Fig. 1.14 (a) is not usually used to define the properties of the permanent magnet material. Instead, the information is given in a form in which the magnetic flux density B in a material is plotted against H. This graph, given in Fig. 1.14 (b), is obtained from Fig. 1.14 (a) with the help of (1.9). Neglecting two singularities, $\boldsymbol{M}$ has always a value $\boldsymbol{M}_{\mathrm{sat}}$ or $-\boldsymbol{M}_{\mathrm{sat}}$, giving the value μ_0 for the slope B versus H. The value of B when the magnetizing field strength is equal to zero is called remanence flux density B_{r} (equal to polarisation) and its value may be calculated from the equation

$$B_{\mathrm{r}} = \mu_0 M_{\mathrm{sat}}. \tag{1.11}$$

The value of H, that is required to reduce the flux density to zero in a material, is called coercive force or coercivity H_{c}. This means that a smaller magnetizing force is required to remove B than is needed to reduce M to zero in a material. If the coercivity is smaller than the intrinsic coercivity H_{ci}, the portion of the B-H loop in the second quadrant is entirely linear since the knee, which occurs at $-H_{\mathrm{ci}}$, is moved into the third quadrant.

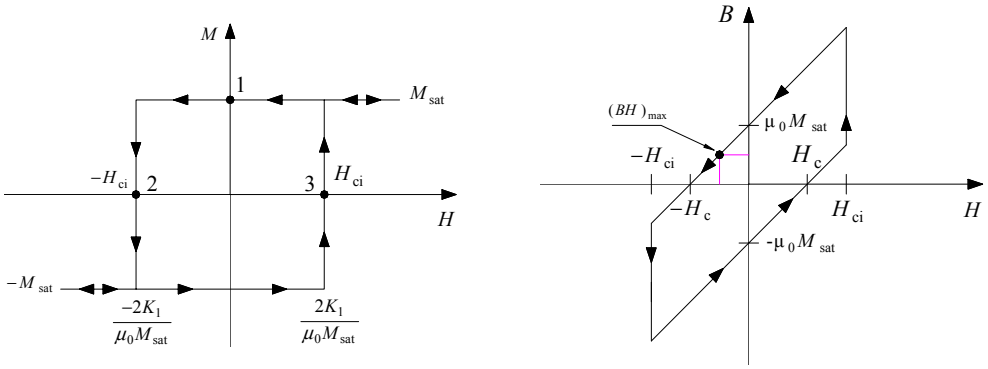

(a) (b)

Fig. 1.14. (a) Intrinsic magnetic characteristic for the elemental volume of a magnet. (b) B-H characteristics for the magnet (Campbell, 1994). The point in which the maximum energy product $(BH)_{\mathrm{max}}$ appears is given. In this operation point the permanent magnet material is full utilized.

The previous explanation for the behaviour of the permanent magnets was idealized. In practice, there is no sudden reverse in magnetization since gradual changes appear in real magnets. Thus, the knee of the B-H loop is in practice smoother as can be seen in Fig. 1.15. Furthermore, the important relation between magnetization and temperature was neglected.

1.5.2. Properties of neodymium-iron-boron permanent magnets

Since for the permanent-magnet machines discussed in this thesis permanent magnet material Nd-Fe-B is used, the material properties of this particular permanent magnet group are discussed in more detail in this chapter.

Recently, Nd-Fe-B magnet material with remanence a flux density B_r of 1.52 T and a maximum energy product of 440 kJ/m^3 was reported (Deshpande, 2003). An Nd-Fe-B magnet material of this grade has become commercially available since the year 2004 (Hitachi Metals, 2004). The values are close to the practical performance limit of sintered Nd-Fe-B magnets because the theoretical maximum energy product for $Nd_1Fe_{14}B_1$ crystal is 510 kJ/m^3. These extremely high performance grades, however, suffer from a poor thermal behaviour. The maximum operating temperature is limited to about 100 degrees Celsius. This is related to the strong temperature dependence of the neodymium magnetic moment. As the temperature increases, there appears a rapid drop in the magnetization and an even faster decline in the intrinsic coercivity to zero at about 250 °C. The temperature tolerance of Nd-Fe-B magnets can be improved by replacing neodymium atoms partially with dysprosium, which gives a higher H_{ci} and by replacing iron partially with cobalt, which improves the temperature behaviour of the compound. However, dysprosium and cobalt have an anti-ferromagnetic coupling, thus the magnetisation and the maximum energy product is reduced. The best Nd-Fe-B grades, capable of tolerating temperatures up to 200 °C, have remanence flux densities of about 1.2 T and have their maximum energy product of 300 kJ/m^3 at a 20 °C temperature.

As the intrinsic coercivity H_{ci} is also a function of the temperature, a set of *B*-*H* loops may be constructed with respect to the temperature and the external field strength. For the Nd-Fe-B permanent magnet material the curves are described in Fig. 1.15, illustrating the second quadrant behaviour. Considering the 80 °C curve, the coercivity H_c is about -820 kA/m and the intrinsic coercivity H_{ci} is about –1080 kA/m meaning that the portion of the *B*-*H* loop in the second quadrant is entirely linear. The irreversible change in the magnetisation starts to take place when the demagnetising external field reaches a value of about –1000 kA/m. The total demagnetisation takes place when the external field strength is further increased up to the value $-H_{ci}$. However, if the temperature is increased from 80 °C to 150 °C the knee is moved from the third quadrant to the second quadrant and the irreversible change in the magnetisation starts when the external demagnetising field exceeds the value of –400 kA/m.

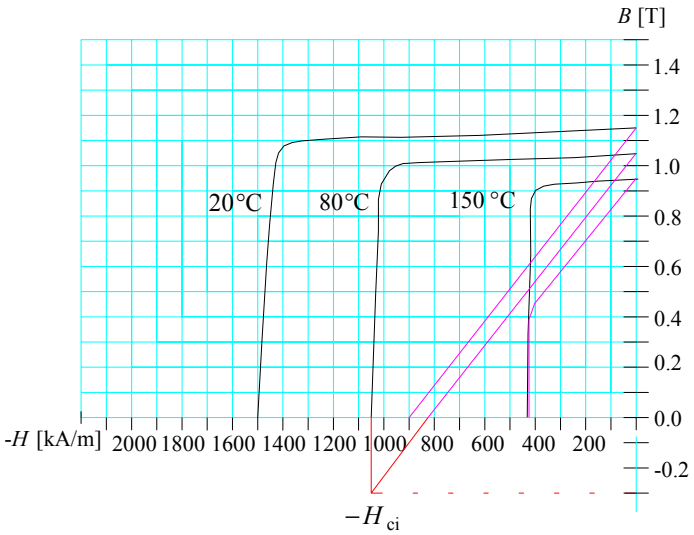

Fig. 1.15. *B*-*H* curves for Nd-Fe-B permanent magnet material.

One of the major disadvantages of Nd-Fe-B magnets is the sensitivity of the material to corrosion. This is a result of two major phenomena. Firstly, oxygen diffuses into the surface layer of the Nd-Fe-B material causing a metallurgical change in the surface layer. As a consequence, H_{ci} will decrease in this area which on turn increases the demagnetisation risk. The second major mechanism is the reaction happening between Nd-Fe-B and atmospheric

hydrogen especially when the humidity is high. Hydrogen reacts with Nd, which destroys the original grain structure of the material. This process leads ultimately to porosity of the material as a consequence of which the magnetic properties are vanished too.

As electrical machines are concerned it is highly desirable for the magnets to operate without corrosion risk over the years. There are a few means of improving the corrosion resistance of Nd-Fe-B material. Firstly, the corrosion resistance of the Nd-Fe-B compound can be improved through alloy combinations. Secondly, the Nd-Fe-B magnet can be shielded with coating. Several coating materials are possible and available, such as nickel, aluminium or epoxy. The thickness of the coating layer is typically between 10 μm and 30 μm.

From the mechanical aspects viewpoint, Nd-Fe-B materials are hard and brittle. The tensile strength is about 83 MPa and the Vickers hardness about 600. Thus, these materials may crack easily if they are exposed to mechanical impacts. For surface-mounted magnets this risk of cracking is essential during the process of installing the rotor into the stator bore. Furthermore, shaping of the magnet is difficult when specific tools for magnet shaping purposes are not available. By using bonded magnets with Nd-Fe-B alloy mixed into the polymer matrix some improvements could be achieved. The possibility to shape is thus improved and the Nd-Fe-B grains are better protected against corrosion but the magnetic properties of the material are reduced significantly. Present-day bonded Nd-Fe-B magnets can give a remanence flux density of typically 0.7 T and a maximum energy product of 90 kJ/m^3. These materials have been exploited also in some motor applications (Kiley et al., 2004).

Nd-Fe-B materials are conductors with a resistivity of about 1.5 μΩm at a 20°C temperature but with a rather poor thermal conductivity, about 9 W/mK. For the surface-mounted structures this may be problematic because there appear eddy currents in the permanent magnet material due to spatial and current harmonics. Since the heat conductivity is fairly poor, an excessive temperature rise in the magnet material is possible. This, typically, does not concern buried magnets, since the effects caused by the harmonics are mainly focused on the rotor iron near the air-gap surface. Typical values for Nd-Fe-B as well as for plastic bonded Nd-Fe-B magnets are gathered in Table 1.1.

Table 1.1. Typical properties for Nd-Fe-B magnets (Neorem Magnets, 2004; KANE Magnetics, 2004).

	B_r (T)	BH_{max} (kJ/m^3)	ρ (μΩm)	μ_r	λ (W/mK)
Nd-Fe-B	1-1.4	190-380	1.5	1.05-1.2	9
Plastic bonded Nd-Fe-B	0.5-0.7	40-90	10-30	1.15-1.2	2

1.6. Soft magnetic materials

Soft magnetic materials have a fundamental role in many electrical and electronic systems of modern society. They exhibit magnetic properties only when they are subjected to a magnetizing force such as the magnetic field created by a permanent magnet or a current passed through the coil surrounding the magnetic core. The main difference between soft magnetic materials and hard magnetic materials is the difference of coercive field strength; soft magnetic materials have characteristically a low coercive field, H_c < 1 kA/m. Some other material properties of soft magnetic materials are a low shape anisotropy, low magnetostriction, low mechanical hardness and low crystal anisotropy (Fish, 1990). For the latter grain-oriented electrical steel (Fe-Si) is an exception. Soft magnetic materials can be classified as:

- Electrical steels
  - Non-oriented
  - Grain-oriented

- Nickel-Iron alloys
- Soft ferrites
  - NiZn
  - MnZn
- Amorphous metals
- Soft magnetic composites
- Construction steels

1.6.1. Soft magnetic materials in rotating electrical machines

Electrical steel lamination is the most commonly used core material in electrical machines. Electrical steels are typically classified into grain-oriented electrical steels and non-oriented electrical steels. Typical applications for grain-oriented steels are power transformer cores whereas non-oriented steels are broadly used in different kinds of rotating electrical machines. In the latest decades there was not reported any significant improvement of the properties of electrical steel. Development has mainly been focused on the improvement of the material purity and on the coating of the materials, which causes a slight reduction of the iron losses (Fish, 1990; Deshpande, 2003).

A large variety of electrical steel grades with different material properties are commercially available (Cogent, 2004). Typical properties for electrical steels may not be given straight due to the large variety of grades available but a reasonable loss value is about 5 Watts per kilogram with 1.5 T magnetic flux density for grades used in electrical machines with a supply frequency about of 50 Hz. In high-performance or high-frequency applications electrical steels may be replaced with amorphous materials (Fukao et al., 1989; Jensen et al., 1992). With amorphous materials the losses are considerably smaller compared to electrical steels, thus they fit well for high frequency applications. The considerably low core losses are a result from the material structure and from the material thickness. The thickness of the amorphous iron ribbon is typically only 20-30 μm. From the manufacturing viewpoint, a thin lamination can be considered to be a drawback since an increased number of laminates has to be manufactured and assembled. Alternatively, in high frequency applications soft metallic magnetic materials may be replaced with soft ferrites, which are ceramic insulators causing very low eddy current losses. However, ferrites are not widely used in electrical machines since the saturation flux density level of the ferrite material is only 0.35…0.5 T. For the electrical steels the saturation flux density is typically between 2.0…2.2 T, thus being lower for the amorphous materials. The best METGLAS™ grade (Honeywell, 2004) has a saturation flux density of 1.8 T. If high flux density levels or a high saturation flux density is required, Co-Fe alloys may be used. Co-Fe alloy 2V Permendur (Fe49-Co49-2V) has the highest saturation level being 2.34 T (Magnetic metals, 2004). However, Co-Fe alloys are much more expensive compared to electrical steels; 2V Permendur costs about hundred times more than the low carbon iron (Ish-Shalom, 1995). Due to the high raw-material price the use of Co-Fe alloys as a core material must be restricted to some specific applications for which the high material cost can be allowed.

Soft magnetic composite materials (SMC-materials) form the newest group of materials to be used for rotating electrical machines. SMC-materials are basically iron powder particles coated with an electrically insulated layer as shown in Fig. 1.16. The electromagnetic and mechanical properties of the material depend on the SMC-powder type and on the mix, i.e. the added lubricant/binder and the manufacturing process (Hultman and Jack, 2003). SMC-materials have been used for quite a long time in high frequency applications but, recently, a group of SMCs has been utilised in new applications such as electrical machines with improved low-medium frequency properties. SMC-materials allow 3-dimensional shaping of the components due to the material spatially isotropic magnetic and thermal properties. In laminates the properties are uni- or bi-dimensional, for example the thermal conductivity of electrical steels varies typically

about 40 W/mK in the direction of the lamination and is only one tenth, ~ 4 W/mK, in the perpendicular direction.

At frequencies below a few hundred Hertz the losses in SMC-materials are typically higher than in laminated structures. The cross-over frequency depends on the electrical steel grade and the flux density. A rough comparison, according to the manufacturers' data sheets, shows that, in terms of power losses and if the supply frequency is below 400 Hz, most of the available laminations are better than the present-day SMC-materials. This is a generalised statement and it is therefore recommended to compare the individual lamination grades with the particular SMC-compound in order to find the exact difference between the materials since the power losses in SMC-material depend on several variables such as the compound used, lubrication, heat treatment and compact pressure.

At 50 Hz frequency the power loss in SMC-materials is typically 15 W/kg at a 1.5 T magnetic flux density whereas in M600-50A electrical steel it is about 5.3 W/kg and in M1000-100A material it is about 9 W/kg. Such a large difference in iron losses affects the overall performance of the machine, especially the temperature rise. Due to the poorer heat conductivity of the SMC-material the temperature rise is even more affected. The SMC-composite has a heat conductivity of about 17 W/mK, which is half of the typical value for non-oriented electrical steels. Fig. 1.17 illustrates the power losses at 50 Hz as a function of the magnetic flux density for some commercially available materials. In Fig. 1.18 the losses are given as a function of the frequency, respectively.

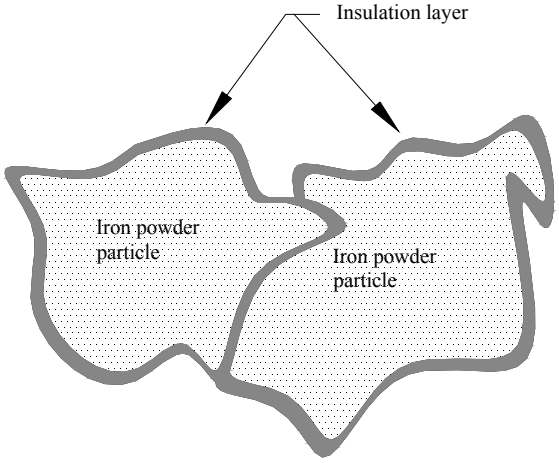

Fig. 1.16. Schematic picture of an SMC-material.

Because of their low relative permeability, $200 < \mu_r < 500$, SMC-materials are most suitable to be used for permanent-magnet machines since the reluctance of the magnetic circuit of a permanent-magnet machine is much higher than that of an induction machine. SMC-materials may also be used for the manufacturing of induction machines, but a weaker performance is to be expected since the reluctance of the stator core is considerably increased when compared to the laminate structure (Arshad et al., 1999; Hultman and Jack, 2003). The utilisation of SMC-materials for large-scale application to electrical machines is still under process, and the constructed machines are mainly prototypes but a few commercial products are already available (Hultman and Jack, 2003).

In permanent-magnet machines or solid-rotor induction machines, ferromagnetic construction steels are used as part of the magnetic circuit. In the case of surface-mounted permanent-magnet machines the permanent magnets are typically fixed to the solid iron part. The magnetic properties of construction steels grades such as S232JR (St 37-2) or S235J2G3 (St 37-3N) are

usually good enough for this type of application. There exist also special construction steels that are made for magnetic application purposes (Carpenter, 2004) and have thus improved magnetic properties. Fig. 1.19 compares the *B-H* properties of electrical steel M400-50A (Cogent, 2004), construction steel S232 JR (Flegel et al., 2000), special magnetic construction steel Chrome Core® 8 Alloy (Carpenter, 2004) and SMC-material SOMALLOY™500 (Höganäs, 2003). According to these values, SMC-material shows a significantly weaker performance compared to electrical steels. Similar results are shown for some construction steels. The special construction steel Chrome Core® 8 Alloy appears to be better than the construction steel S232JR if the magnetic flux density is below 1.4 T. Some other typical values for the soft magnetic materials are gathered in Table 1.2.

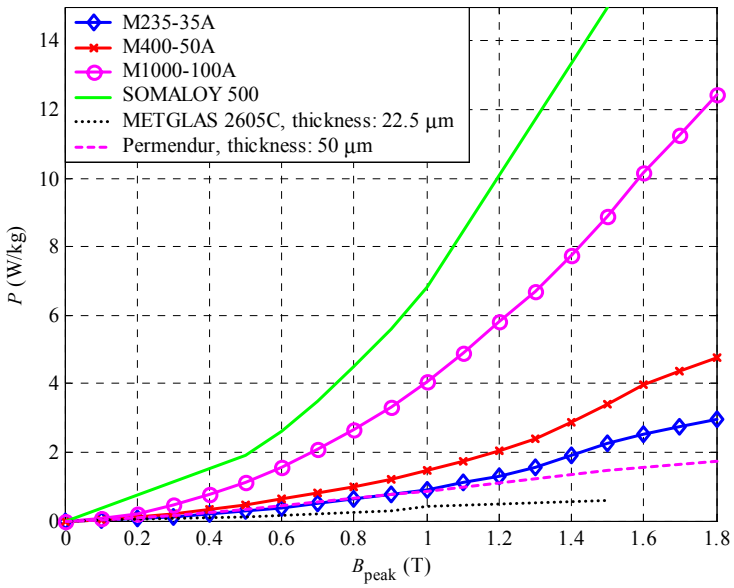

Fig. 1.17. Core loss data of some materials as a function of the magnetic flux density. 50 Hz sinusoidal excitation.

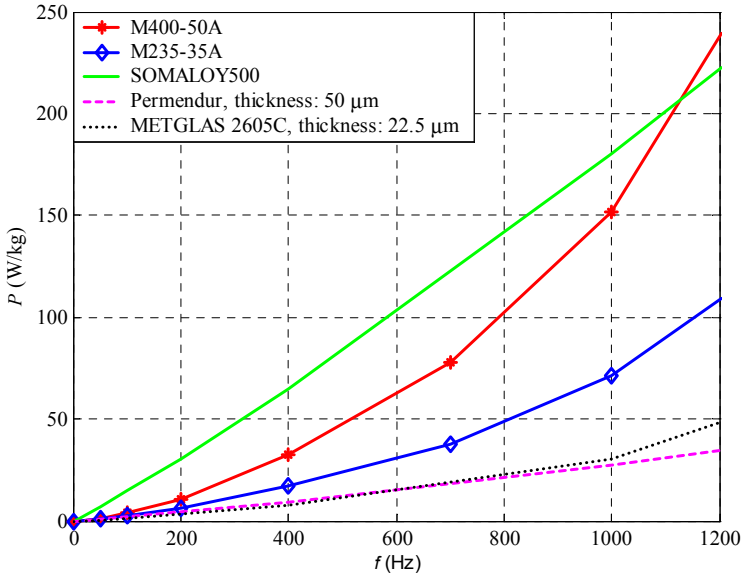

Fig. 1.18. Total losses of some materials as a function of the frequency at a 1.0 T magnetic flux density.

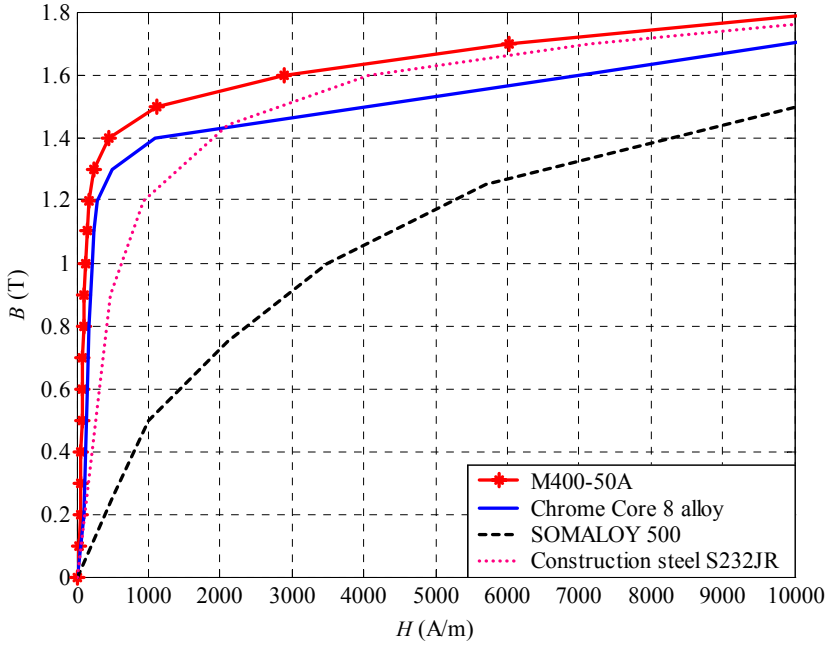

Fig. 1.19. *B-H* curves of selected soft magnetic materials.

Table 1.2. Typical properties of some soft magnetic materials. The core losses are given at 50 Hz and 1.5 T.

Material	B_{sat} [T]	ρ [μΩm]	$\mu_{r,max}$	λ [W/mK]	P [W/kg]
Non-oriented electrical steels [(1), (2)]	2.1	0.4	5000	40	5
METGLAS™ 2605C [(3)]	1.8	1.2	400000	9	0.5
Permendur (Fe49-Co49-2V) [(4)]	2.34	0.35	50000	12	1.4
SMC-composite SOMALOY™500 with 0.5 % KENOLUBE™ [(5)]	2.0	30	500	17	15
NiZn ferrites [(2), (6)]	0.35	$1 \cdot 10^{6}$	4000	$3.5\text{-}5 \cdot 10^{-3}$	-
MnZn ferrites [(2), (6)]	0.5	$0.2 \cdot 10^{6}$	6000	$3.5\text{-}5 \cdot 10^{-3}$	-
Chrome Core® 8 Alloy [(7)]	1.86	0.49	3100	-	-

(1) Cogent, 2004
(2) Fish, 1990
(3) Honeywell, 2004
(4) Magnetic metals, 2004
(5) Höganäs, 2003
(6) Ferroxcube, 2004
(7) Carpenter special steels, 2004

2. Design of axial-flux permanent-magnet machines

The first objective of the work was to develop a suitable analytical design procedure for designing surface-mounted axial-flux permanent-magnet machines. In this chapter the developed design method is described and the main facts determining the calculation of the performance of a surface-mounted axial-flux permanent-magnet machine are discussed. A review of the finite element analysis is given. Part of this work has been introduced previously. The publications by Parviainen et. al. (2003a, 2004a and 2004b) discuss the main aspects of the analytical design procedure for an axial-flux surface-mounted PM machine. In (Parviainen et. al., 2003b), the prototype machine, here used as an example for verifying the computing results, has been described.

2.1. Introduction

The modelling of axial-flux PM machines is determined by contradictory requirements related to the fastness and accuracy of the computations. From the modelling point of view, an axial-flux machine inherently has a 3D geometry. Therefore, using an analytical design method or the 2D finite element analysis (FEA), which both are usually to be performed on the average radius of the machine, does not generally yield sufficiently accurate computation results. With the 3D FEA, it is possible to take into consideration the actual 3D structure of the machine, but performing the computations is often too time-consuming, especially if the objective is to achieve a preliminary design of the machine. To solve the question of modelling axial-flux surface-mounted PM machines, in this study an analytical design method has been developed and is proposed. The basic idea of the design method is to firstly subdivide the axial-flux machine into a sufficient amount of independent computation planes, next perform the required computations on each plane, and finally compose the overall performance of the machine from the computation results obtained for each design plane. Such a design method is called quasi-3D computation (Gair et al., 1996). The corresponding analytical design tool, developed for this thesis, uses quasi-3D computation with the help of a non-linear reluctance network (Rasmussen et al., 1997) and analytical design methods introduced for example by Gieras (Gieras, 1997). It must be noted that the developed computation model does not enable the consideration of the 3D behaviour of the magnetic flux, which may have an effect on the performance of the machine. This shortcoming of the model may be considered to be irrelevant in most of the design cases due to the orientation of the laminations but, if the iron parts are designed to saturate, the effects caused by the 3D flow of the magnetic flux should be examined too.

According to the textbooks, even the newest ones dealing particularly with axial-flux machines (Gieras, 2004), the design of axial-flux PM machine is to be obtained by using the average radius of the machine as a design plane. This approach is sufficiently accurate to predict the motor performance if the magnet-width-to-pole-pitch-ratio (relative magnet width) is a constant with respect to the pole pitch, which is a function of the stator radius. If the relative magnet width varies with respect to the motor radius, the waveform of the no-load air-gap flux density may alter causing that the fundamental component of the induced back-EMF may differ from the presumed value. In designing the stator winding, this effect must be taken into account in order to obtain the required back-EMF. For low-speed permanent-magnet machines the copper losses are usually the dominating loss component and it is important to minimize the required number of coil turns in order to find a good efficiency and to avoid that the inverter has to operate in the field weakening area already at or even before the rated speed conditions.

Using the average radius as a design plane may be misleading also when considering the iron losses. This is caused by the fact that the flux density in a tooth reaches usually its maximum

value at the inner radius of the machine stator and, respectively, in the stator yoke at the outer radius. This is, however, dependent on the shape of the permanent magnet as shown in Fig. 2.1.

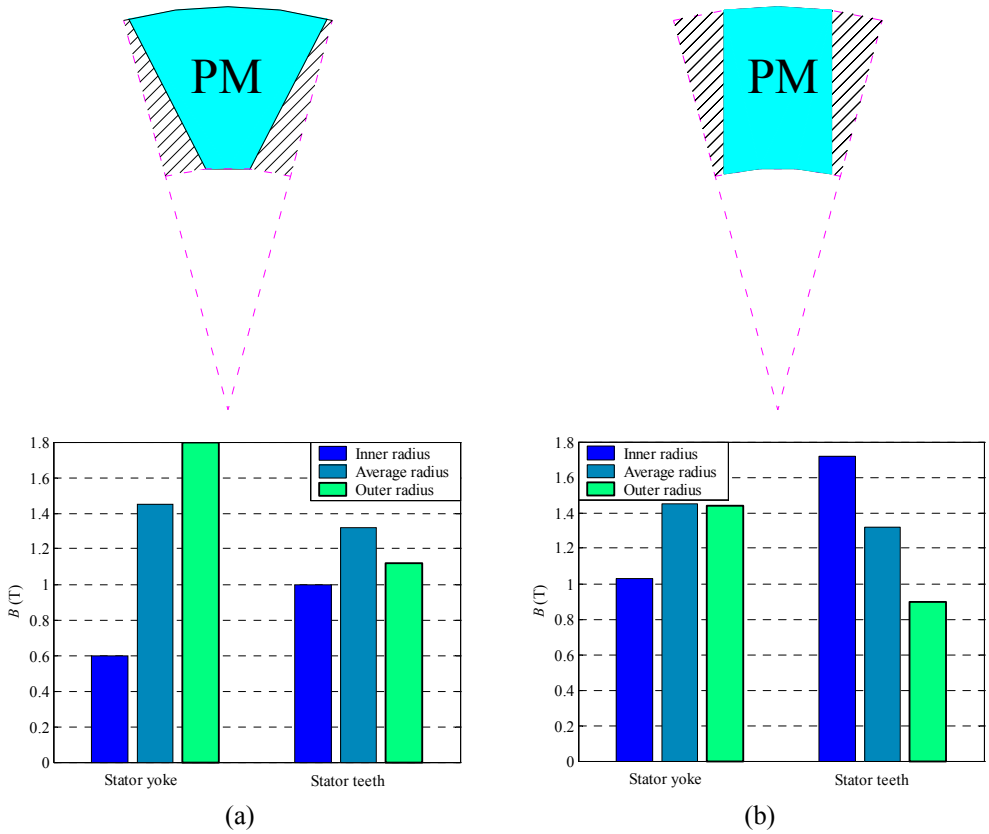

Fig. 2.1. Illustration of the relation between the permanent magnet shape and the obtained flux density levels in the stator yoke and stator teeth. (a) The relative magnet width reduces towards the inner radius of the stator. In this case, saturation may occur in the yoke at the outer radius. (b) The relative magnet width reduces towards the outer radius of the stator. In this case, saturation may occur in the stator teeth at the inner radius.

Because the iron losses are strongly non-linear as a function of the flux density it is recommended to use quasi-3D computation, which calculates the iron losses separately for each design plane. If the flux density significantly differs at the outer and inner radii of the machine, part of the flux flows also diagonally in the magnetic circuit. This causes extra eddy current losses in the laminations since the flux does not any more completely flow in the directions of the laminations. The extent of the flux behaviour on the iron losses may be of relevant interest for future research. However, this is not considered in this study.

2.2. Analytical quasi-3D modelling

Concerning the quasi-3D modelling, the axial-flux PM machine may be considered to be composed of several axial-flux machines with differential radial length. The overall performance of an axial-flux machine is obtained by summing the performances of individual machines and by neglecting the possible flux flow in the depth direction of the machine. This

approach allows the consideration of different magnet shapes and variations of the teeth width in the direction of the machine radius. The method of transforming the 3D geometry of an axial-flux machine to a corresponding 2D model, to be used in quasi-3D computation, is illustrated in Fig. 2.2. In Fig. 2.3 the main geometrical parameters for quasi-3D modelling are shown.

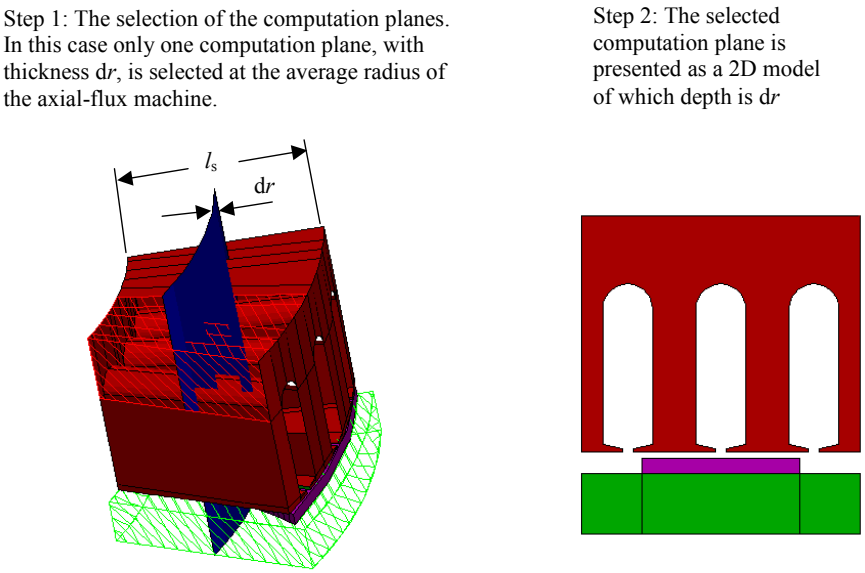

Fig. 2.2. Method of transforming the 3D geometry of an axial-flux machine to a 2D geometry, which can be used in quasi-3D computation.

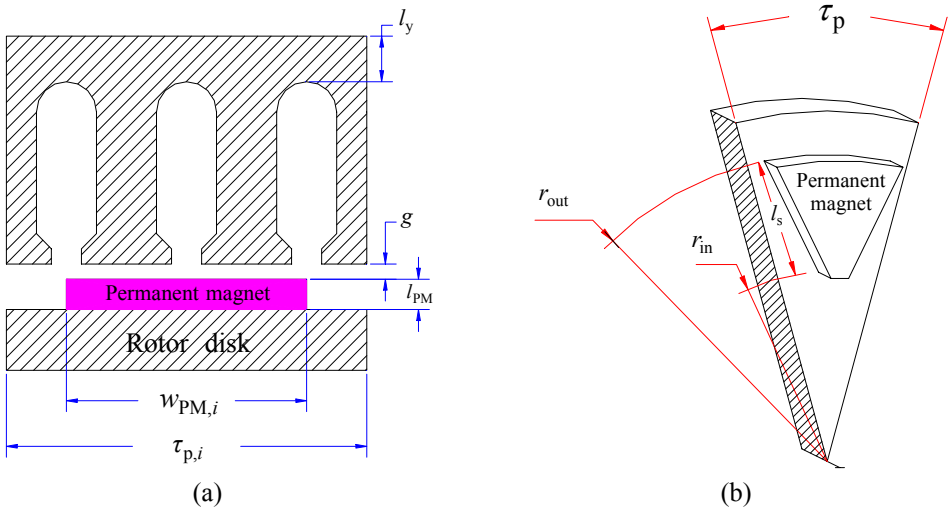

Fig. 2.3. Definitions for the magnet width w_{PM}, for the pole pitch τ_p, for the permanent thickness l_{PM}, for the stator yoke thickness l_y and for the physical length of air-gap g. In (b) r_{in} is the inner radius of the machine stator, r_{out} is the outer radius- and l_s is the length of stator stack, respectively.

For the quasi-3D computation, the average diameter D_{ave} of a particular computation plane i, starting from the outer diameter of the machine is given by the equation

$$D_{\mathrm{ave},i} = D_{\mathrm{out}} - j \cdot \frac{l_{\mathrm{s}}}{N}, \tag{2.1}$$

where

D_{out} is the external diameter of the stator
N is the number of computation planes used in a computation
l_{s} is the length of the stator stack in meters

The parameter j in (2.1) is defined as

$$j = 2i\text{-}1. \tag{2.2}$$

Please note that in (2.2) index i goes from 1 to N. The length of the stator stack l_{s} is defined as

$$l_{\mathrm{s}} = \frac{D_{\mathrm{out}} - D_{\mathrm{in}}}{2}, \tag{2.3}$$

where

D_{in} is the internal diameter of the axial-flux machine stator.

The pole pitch τ_{p} for each computation plane is given by the equation

$$\tau_{\mathrm{p},i} = \frac{\pi D_{\mathrm{ave},i}}{2p}, \tag{2.4}$$

where

p is the pole pair number.

In general, the relative magnet width α_{p} may vary along with the machine radius. It is defined as

$$\alpha_{\mathrm{p},i} = \frac{w_{\mathrm{PM},i}}{\tau_{\mathrm{p},i}}, \tag{2.5}$$

where

$w_{\mathrm{PM},i}$ is the width of the magnet at the computation plane i according to Fig. 2.3 (a).

Based on the set of equations (2.1)-(2.5) it is possible to divide the machine into a certain amount of computation planes. The number of computation planes needed for computation depends on the purpose of the computation. In the simplest case when the magnet relative width is a constant and the stator is not skewed, basically only one computation plane is required, for instance, for the computation of the induced voltage or cogging torque. But, for example for the computation of iron losses one computation plane is not necessarily sufficient, this because of the non-linear behaviour of the iron losses. Generally, the amount of computation planes required is case-dependent and must be defined according to the case concerned.

The computations of the motor parameters, such as the phase resistances, inductances and load angle, can be obtained by using classical electrical machine design methods. These computation methods are given for example by Gieras (Gieras, 1997; Gieras et al. 2004). Even though the geometry of the axial-flux machine is an inherent 3D problem, the computation of the machine parameters can be based on the use of the average radius r_{ave} as a design plane since the considered parameters vary linearly with respect to the machine radius or are totally independent of the radius.

2.2.1. Magnetic equivalent circuit

In the computation model the flux densities in different parts of the motor are found based on a non-linear reluctance network. Such networks have been proven suitable even for very accurate analysis of electrical machines (Perho, 2000; Rasmussen et al., 1997). Fig. 2.4 illustrates part of the non-linear reluctance network used for modelling the axial-flux machine structure for which the number of slots per pole and phase equals one. The whole reluctance model consists of one pole pair so that the symmetry conditions are fulfilled.

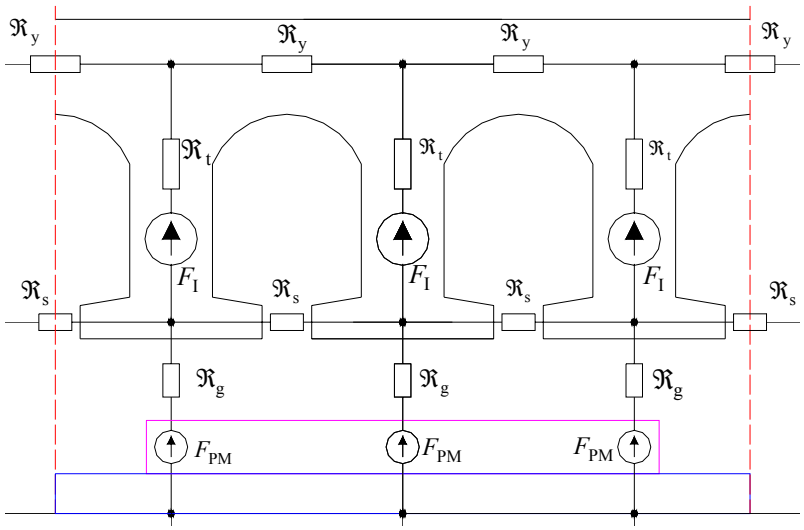

Fig. 2.4. Presentation of the reluctance network over one pole. $\Re_y$ is the reluctance for the stator yoke, $\Re_t$ is the reluctance of the tooth, $\Re_s$ is the reluctance of the slot opening and $\Re_g$ is the reluctance of the air-gap and it is a sum of reluctances of the physical air-gap, permanent magnet effects and rotor steel effects. F_{PM} is the magneto-motive-force (MMF) source due to the permanent magnet and F_I due to the stator currents.

In this study, the proposed analytical design tool has been developed with the aim of getting a preliminary design for AFPM machines. Therefore, the reluctance network remains relatively coarse and is not compatible with the FE-method in terms of accuracy. However, it is accurate enough to estimate the maximum flux density levels in the teeth, stator yoke and rotor disk. The reluctance network is solved under load and no-load situations for each computation plane. Based on the computed reluctances, the iron saturation effect is included into the effective length of the air-gap. The obtained maximum flux densities in the teeth and stator yoke are used for computation of the iron losses.

The non-linear reluctance network is solved iteratively based on the equation

$$\mathbf{\Phi} = \mathbf{\Re}^{-1}\mathbf{F}, \tag{2.6}$$

where

$\mathbf{\Phi}$ is the magnetic flux matrix
$\mathbf{\Re}$ is the reluctance matrix
$\mathbf{F}$ is the source matrix including MMF sources due to permanent magnets and stator phase currents

For the reluctance matrix, a particular reluctance $\Re_i$ is calculated as

$$\Re_{\mathrm{i}} = \frac{l_{\mathrm{i}}}{\mu_0 \mu_{\mathrm{r}} S_{\mathrm{i}}}, \tag{2.7}$$

where

l_{i} is the length of a particular part of the machine modelled with a reluctance element
μ_{r} is the relative permeability of the reluctance element material
S_{i} is the cross-sectional area of a particular part of the machine modelled with a reluctance element

The relative permeability μ_{r} of the iron parts is a function of the flux density, being the final result of (2.6). Consequently, the correct value for (2.6) has to be found iteratively. The iron reluctances are modelled by using *B-H* curves, shown in Fig. 1.19, for the stator lamination and construction steel is used for the rotor material. Please note that the *B-H* curve of the lamination material M600-50A, which is used in a prototype machine, is not given in Fig. 1.19.

The magneto-motive-force produced by each stator phase current is calculated as

$$F_{\mathrm{I,ph}} = N_{\mathrm{s}} I, \tag{2.8}$$

where

N_{s} is the number of coil turns in a slot
I is the current through one coil turn

The magneto-motive-force F_{PM}, produced by the permanent magnet, is calculated as

$$F_{\mathrm{PM}} = \frac{B_{\mathrm{r}} l_{\mathrm{PM}}}{\mu_0 \mu_{\mathrm{r,PM}}}, \tag{2.9}$$

where

l_{PM} is the thickness of the permanent magnet, defined in Fig. 2.3.

Solving (2.6) gives the values for the magnetic fluxes through each reluctance element. Based on the known value of the magnetic flux and the cross sectional area of the particular reluctance element, it is possible to calculate the corresponding flux density B_{i} in an element as

$$B_{\mathrm{i}} = \frac{\Phi_{\mathrm{i}}}{S_{\mathrm{i}}}. \tag{2.10}$$

The flux density amplitudes provided by (2.10) are used in the computation while computing the iron losses. This is discussed in detail in Chapter 2.2.7.

Since the relative permeability of the stator lamination and the rotor material is not infinite, a magnetic voltage drop is obtained on the flux path over the stator and rotor iron. This reduces the effective flux density level in the air-gap and must be taken into account in designing the machine. A possible way to include the iron saturation into the computation model is to use a correction coefficient called saturation factor k_{sat} (Gieras, 1997). In this case, the effective air-gap length g_{eff} is given as

$$g_{\mathrm{eff}} = k_{\mathrm{sat}} k_{\mathrm{C}} g = k_{\mathrm{sat}} g', \tag{2.11}$$

where

k_{sat} is the saturation coefficient
k_{C} is Carter's coefficient taking into account the stator slotting
g is the physical length of the air-gap

The saturation factor itself is defined to be the ratio of the magnetic voltage drop per pole to the air-gap magnetic voltage drop (Gieras, 1997). Fig. 1.4 (a) describes the considered magnetic flux path.

$$k_{\text{sat}} = \frac{\Theta_{\text{agap}} + \Theta_{\text{t}} + 0.5\left(\Theta_{\text{y}} + \Theta_{\text{rotor}}\right)}{\Theta_{\text{agap}}}, \tag{2.12}$$

where

Θ_{agap} is the magnetic voltage drop across the air-gap (the length of air-gap includes the thickness of permanent magnet l_{PM} and the length of air-gap g')
Θ_{t} is the magnetic voltage drop along the stator teeth
Θ_{y} is the magnetic voltage drop along the stator yoke
Θ_{rotor} is the magnetic voltage drop along the rotor core

For the computation model, the value for the saturation factor is achieved by computing the magnetic voltage drop over the stator and rotor reluctances for each computation plane separately. The saturation level, which may vary with respect to the radius, may now be taken into account in the quasi-3D modelling.

The magnetic equivalent circuit may also be used for computation of the d-axis and q-axis synchronous inductances. This computation is described in Chapter 2.2.10. For the computation of the synchronous inductances the influence of the iron parts on the effective air-gap length has to be estimated. The reluctances which are considered to produce the magnetic voltage drop on the d-axis are shown in Fig. 2.5 (a) (for one pole) and in Fig. 2.5 (b) for the quadrature axis, respectively.

For surface-mounted PM machines, equipped with Nd-Fe-B magnets, the effective air-gap length is typically almost the same on both axes. This results from the relative permeability of the permanent magnet material, which is near to unity. The permanent magnets are located on the d-axis. The flux created by the permanent magnets may saturate both the teeth and the stator yoke on the magnetic circuit of the d-axis. If the stator yoke is saturated, also the q-axis will be partly saturated since the stator yoke is a common part for both axes and the flux produced by the permanent magnet is always present. The main difference between the axes in terms of saturation is due to the stator teeth. Based on these considerations, differences typically below 10 % between the effective lengths of the air-gaps are to be expected (Heikkilä, 2002).

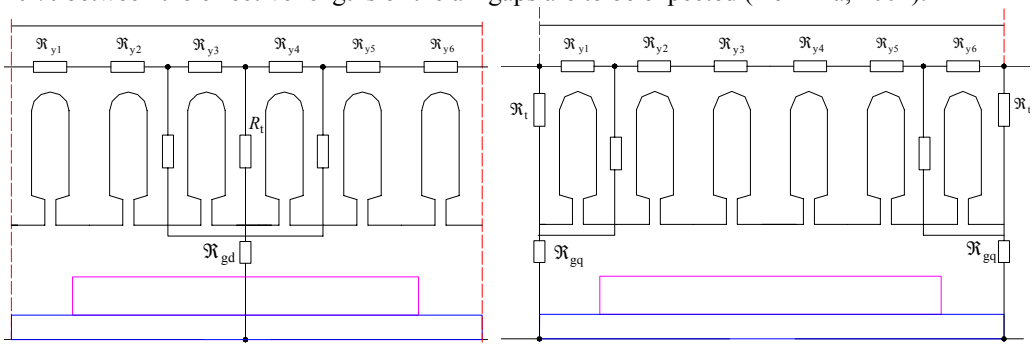

(a) (b)

Fig. 2.5. (a) Reluctance network for one pole describing the reluctances on the d-axis. (b) Reluctance network for one pole describing the reluctances on the q-axis. In this case, the number of slots per pole and per phase is equal to 2. These reluctances are used in the computations of the respective d- and q-axis inductances.

2.2.2. Computation of permanent-magnet leakage fluxes

For the design of surface-mounted permanent-magnet machines, it should be taken into consideration that the leakage fluxes of the permanent magnets cause a substantial reduction effect on the useful magnetic flux. To reduce the permanent-magnet flux Φ_{PM} resulting from the leakage fluxes it can be used a leakage coefficient, which also is introduced into the analytical computation. The effective flux Φ_{eff} is given by

$$\Phi_{eff} = k_{\sigma PM} \Phi_{PM}, \tag{2.13}$$

where

$k_{\sigma PM}$ is a leakage coefficient of permanent-magnet flux

The drawback of the method is that, if high computation accuracy is demanded, a 3D finite element analysis is needed in order to find the correct leakage coefficient $k_{\sigma PM}$ for each design. In analytical computations the leakage coefficient $k_{\sigma PM}$ may be estimated by using the method introduced by Hwang (Hwang et al., 2001) and improved by Qu (Qu et al., 2004). In the analysis, the magnet leakage factor is computed by using Qu's model and the method is improved to cover axial-flux machines with complex magnet shapes. The effective leakage coefficient for axial-flux surface-mounted permanent-magnet machines is then calculated as

$$k_{\sigma PM} = \frac{\sum_{i=1}^{N} k_{\sigma PM,i}}{N} k_{\sigma PM,add}, \tag{2.14}$$

where

$k_{\sigma PM,add}$ is an additional leakage coefficient

The additional leakage coefficient $k_{\sigma PM,add}$ includes the reduction of the effective flux caused by the additional leakage flux components which are not included in the leakage flux model. These components are leakage fluxes occurring between the magnet and the rotor on the inner and outer radii of the stator as well as leakage fluxes flowing from the magnet pole into the adjacent magnet pole through the slot openings and slots.

The permanent-magnet leakage factor $k_{\sigma PM}$ includes two leakage components: (Qu et al., 2004)

1. Permanent-magnet zigzag leakage, illustrated in Fig. 2.5 (a)
2. Permanent-magnet air-gap leakage which is composed of
    - Magnet-to-rotor leakage, illustrated in Fig. 2.5 (b)
    - Magnet-to-magnet leakage, illustrated in Fig. 2.5 (c)

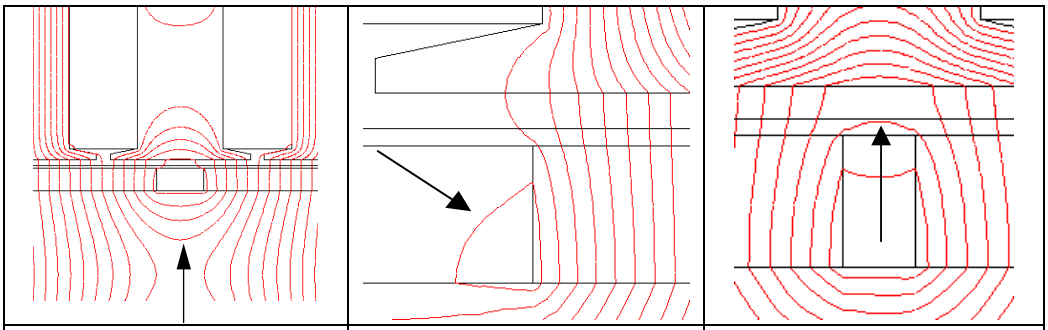

Fig. 2.6. (a) Zigzag leakage flux paths when the magnets are short-circuited via the stator iron. (b) Magnet-to-rotor leakage flux. (c) Magnet-to-magnet leakage flux.

The permanent-magnet air-gap leakage coefficient for each computation plane is calculated according to Qu (Qu et al., 2004).

$$k_{\sigma\mathrm{PM,agap},i} = \frac{1}{1+\left(\mu_{\mathrm{r,PM}}\frac{g'}{l_{\mathrm{PM}}}\frac{w_{\mathrm{PM},i}}{w_{\mathrm{PM},i}+2g'}\right)} \cdot \frac{1}{\left(\frac{2l_{\mathrm{PM}}}{\pi\mu_{\mathrm{r,PM}}w_{\mathrm{PM},i}}\ln\left(1+\frac{\pi g'}{l_{\mathrm{PM}}}\right)+\frac{4l_{\mathrm{PM}}}{\pi\mu_{\mathrm{r,PM}}w_{\mathrm{PM},i}}\ln\left(1+\frac{\pi g'}{\tau_{\mathrm{p},i}-w_{\mathrm{PM},i}}\right)\right)}, \quad (2.15)$$

where

g' is the physical length of the air-gap multiplied with the Carter coefficient k_{C}.

The zigzag leakage factor is calculated as Qu (Qu et al., 2004)

$$k_{\sigma\mathrm{PM,zz},i} = 1 - \frac{\left(\tau_{\mathrm{slot},i} - \left(\tau_{\mathrm{p},i} - w_{\mathrm{PM},i}\right)\right)^2}{2w_{\mathrm{PM},i}\tau_{\mathrm{slot},i}}, \quad (2.16)$$

where

τ_{slot} is the slot pitch.

The effective leakage factor for each computation plane is then given by

$$k_{\sigma\mathrm{PM},i} = k_{\sigma\mathrm{PM,agap},i}k_{\sigma\mathrm{PM,zz},i}. \quad (2.17)$$

The zigzag leakage represents the leakage flux flowing through the air-gap and tooth tip from the magnet to the adjacent magnet as it is illustrated in Fig. 2.6 (a). The zigzag leakage is considered to be present when the distance between two adjacent magnets is less than a slot pitch. For a surface-mounted magnet machine the zigzag leakage flux component is usually larger than the air-gap leakage flux (Qu et al., 2004) but the value of the zigzag leakage flux is also related to the value of α_{p} as can be noticed from Fig. 2.7. If the distance between two adjacent magnet poles is larger than the slot pitch the zigzag leakage is zero and thereby the air-gap leakage is the dominating leakage flux component.

For the sinusoidal magnet structure (discussed in Chapter 3), which is used hereafter as a

computation example, the considered leakage flux components are given in Table 2.1 and are drawn in Fig. 2.7 as a function of the magnet relative width α_p.

Table 2.1. Leakage flux coefficients obtained for the sinusoidal magnet shape from the 3D FEA and from the analytical approach.

$k_{\sigma PM}$ (3D FEA)	$k_{\sigma PM}$ (Analytical)	$k_{\sigma PM,zz}$	$k_{\sigma PM,agap}$
0.89	0.94	0.98	0.97

Fig. 2.7 shows that the air-gap leakage flux reaches its minimum value when the value of α_p is about 0.8 ($k_{\sigma PM}$ reaches the maximum value). For smaller values of α_p, there exists a significant magnet-to-rotor core leakage flux. The minimum of this leakage is reached at $\alpha_p = 0.68$ after which the leakage increases rapidly. The magnet-to-magnet zigzag leakage flux is insignificant for values $\alpha_p < 0.7$ after which it starts to increase rapidly. Table 2.1 shows that the leakage flux coefficient obtained from the 3D FEA is smaller than that obtained from the analytical model without the use of an additional leakage flux coefficient $k_{\sigma PM,add}$. If the value $k_{\sigma PM,add} = 0.95$ is introduced the total leakage flux corresponds to the value obtained from the 3D FEA. Note that, in this case, the additional leakage flux component seems to be equal to the main leakage components.

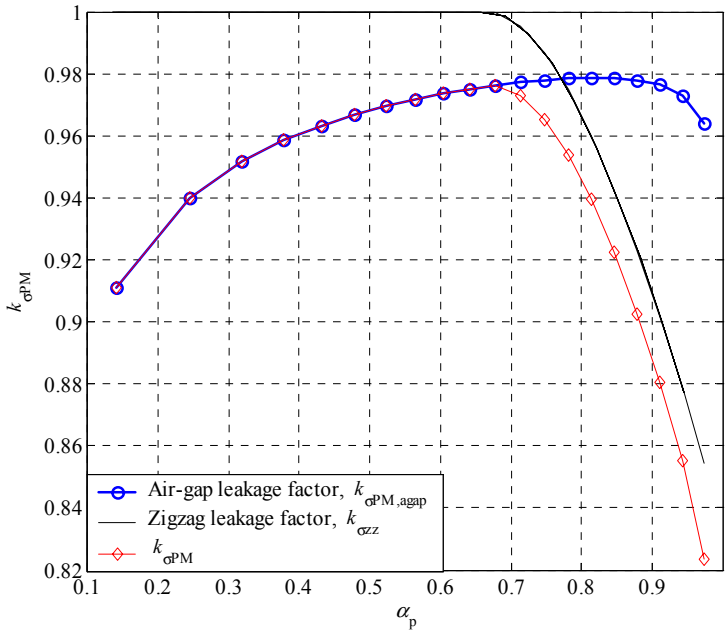

Fig. 2.7. Leakage flux coefficients as a function of permanent magnet relative width α_p.

2.2.3. Analytical model for the air-gap flux density distribution

For the dimensioning of a phase winding the fundamental component of the air-gap flux density distribution is an essential parameter. For the computation method the fundamental component of the air-gap flux density distribution is obtained based on an analytical expression for the air-gap flux density distribution, which is derived assuming an infinite relative permeability for the stator and rotor iron. For radial-flux machines, an analytical expression for the air-gap flux density distribution $B(\theta)$, produced only by the permanent magnet, is given by Zhu (Zhu et al,

1993). For axial-flux machines considered as linear machines, it is more convenient to use the Cartesian co-ordinates with $B(x)$ distribution. This expression is given in Hanselman (2003) or Chung (Chung et al., 2002). The latter approach is used hereafter for the axial-flux permanent-magnet machines

$$B_{\mathrm{PM},i}(x) = -\sum_{n=1,3,5,\ldots}^{\infty} \frac{\frac{8B_{\mathrm{r}}}{n\pi}\sin\left[\frac{\alpha_{\mathrm{p},i}n\pi}{2}\right]\mathrm{e}^{-\frac{n\pi g'}{\tau_{\mathrm{p},i}}}\cos\left(\frac{n\pi x}{\tau_{\mathrm{p},i}}\right)}{\left(\mathrm{e}^{-\frac{2n\pi g'}{\tau_{\mathrm{p},i}}}+1\right)+\frac{\mu_{\mathrm{PM}}\left(-\mathrm{e}^{-\frac{2n\pi g'}{\tau_{\mathrm{p},i}}}+1\right)\left(\mathrm{e}^{\frac{2n\pi l_{\mathrm{PM}}}{\tau_{\mathrm{p},i}}}+1\right)}{\mu_0\left(\mathrm{e}^{\frac{2n\pi l_{\mathrm{PM}}}{\tau_{\mathrm{p},i}}}-1\right)}}, \tag{2.18}$$

where μ_{PM} is the permeability of the permanent magnet.

In the model, the influence of the slot openings on the waveform of $B_{\mathrm{PM}}(x)$ is taken into consideration by introducing a relative permeance function $\widetilde{\lambda}(x)$ (Zhu et al., 1992). The relative permeance distribution is illustrated in Fig. 2.8 (a). The air-gap flux density distribution $B_{\mathrm{agap}}(x)$, which includes the effect of slot openings, is given by the equation

$$B_{\mathrm{agap},i}(x) = \widetilde{\lambda}(x)B_{\mathrm{PM},i}(x), \tag{2.19}$$

and is illustrated in Fig. 2.8 (b), respectively.

The approach used does not take into consideration the flux concentration effects near the tooth tips, which increase the amplitude of the flux density below the tooth tip in the vicinity of the slot opening. This effect is described in Fig. 2.10 (b). In deriving (2.18) an infinite permeability for the iron parts was assumed, thus the computation accuracy may be improves by replacing g' with the value g_{eff}, which, for each computation plane used, includes the magnetic voltage drop caused by the stator lamination and the rotor iron according to (2.11). On replacing in (2.18) g' by g_{eff} the physical length of the air-gap increases and thereby a reduction in the amplitude of the $B_{\mathrm{PM}}(x)$ is obtained.

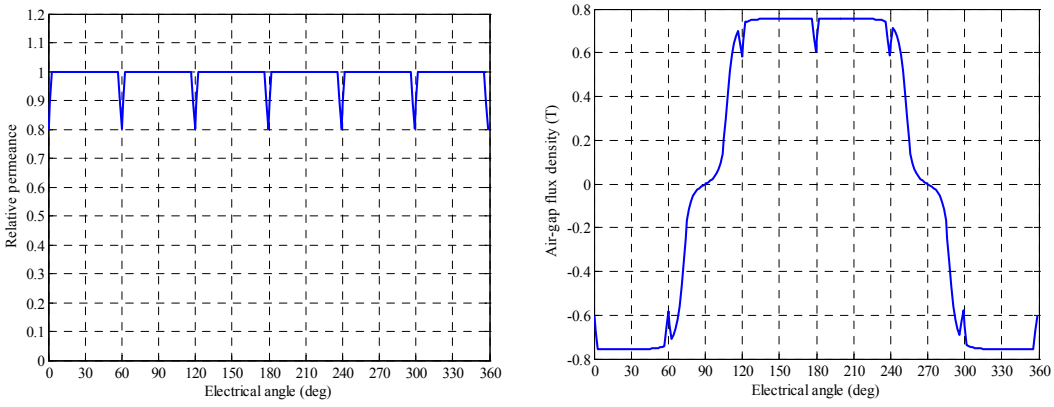

(a) (b)

Fig. 2.8. (a) Relative permeance distribution. (b) Air-gap flux density distribution including the effects of the slot openings.

The method for constructing the air-gap flux density distribution applies the Fourier series. Thereby, the model shows some sensitivity to the amount of the harmonics in (2.18). Fig. 2.9 describes the effect caused by the number of used harmonics. In the computation 30 harmonics are used. This is a sufficient amount, as the comparison, given in Fig. 2.9, shows

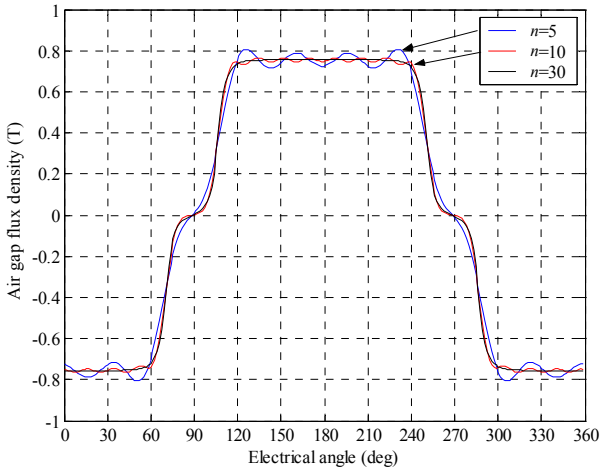

Fig. 2.9. Effect of the number of harmonics on the air-gap flux density distribution.

The amplitude of the resulting fundamental component $\hat{B}_{\text{agap1}}$ of the air-gap flux density is evaluated based on (2.19) and on the equation

$$\hat{B}_{\text{agap1}} = \frac{\sum_{i=1}^{N} \hat{B}_{\text{agap1},i}}{N}, \tag{2.20}$$

where

$\hat{B}_{\text{agap1},i}$ is the peak value of the fundamental component of the air-gap flux density on the computation plane i produced by the permanent magnet.

The values for the fundamental components $\hat{B}_{\text{agap1},i}$ of the no-load air-gap flux density are obtained by means of an FFT-algorithm, which is performed for all the computation planes used in the computation.

The analysis is expanded to cover the load situation. In this case, the air-gap flux density distribution $B_s(x)$, produced by the 3-phase currents in the stator windings, is evaluated with the Fourier series (Heller et al., 1977)

$$B_{\text{s},i}(x) = \frac{\mu_0}{g'} \sum_{n=1}^{\infty} \frac{2N_s q \xi_n}{\pi n} \left\{ i_a \cos\left(n \frac{px}{r_i} \right) + i_b \cos\left(n \frac{px}{r_i} + \frac{2\pi}{3} \right) + i_c \cos\left(n \frac{px}{r_i} - \frac{2\pi}{3} \right) \right\}, \tag{2.21}$$

where

q is a number of slots per pole and phase
p is the number of pole pairs
ξ_n is the stator winding factor
i_a, i_b and i_c are the instantaneous values of the phase currents.

In this case, the order of harmonics n is computed from the equation

$$n = 1 \pm 2mk \,, \tag{2.22}$$

where

$k = 0, 1, 2, 3, \ldots$

The stator winding factor ξ_n is defined as

$$\xi_n = \frac{2\sin\left(n\frac{w_c}{\tau_p}\frac{\pi}{2}\right)\sin\left(\frac{n}{m}\frac{\pi}{2}\right)}{\frac{Q}{mp}\sin\left(n\pi\frac{p}{Q}\right)}, \tag{2.23}$$

where

Q is the number of slots in a stator,
m is the number of phases
w_c is the coil span.

The approach creates a stepping air-gap flux density distribution for the armature reaction field. Next, it is assumed that the air-gap flux density distributions produced by the permanent magnets and the stator currents are independent. Based on this assumption, the air-gap flux density distribution including the armature reaction is achieved by adding the $B_{PM}(x)$ distribution to the $B_s(x)$ distribution

$$B_{agap,i}(x) = \left[B_{PM,i}(x) + B_{s,i}(x)\right]\tilde{\lambda}(x). \tag{2.24}$$

A comparison between the air-gap flux density values given by different modelling methods under no-load and load condition is given in Figs. 2.10- 2.12. In Fig. 2.12 the 3D presentation of the corresponding air-gap flux density distribution is given. As a conclusion, there is only a small difference between the values given by the analytical computation method, the 2D and 3D FEA.

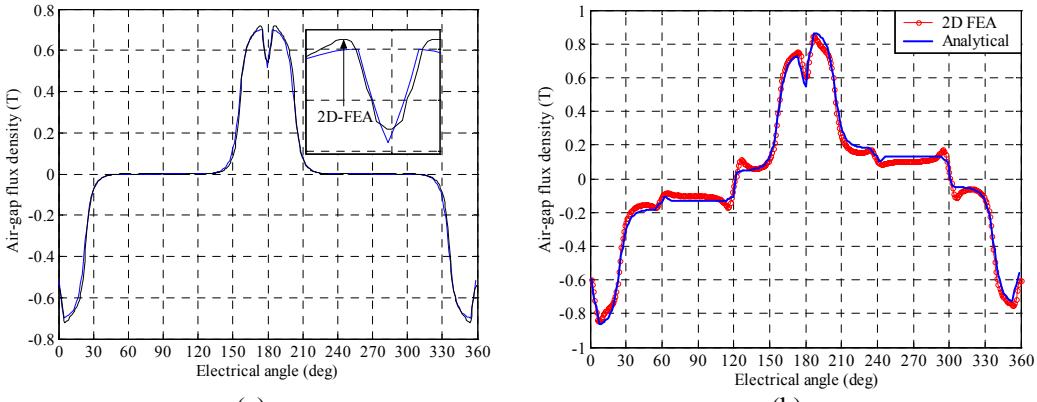

Fig. 2.10. (a) No-load air-gap flux density distribution obtained from the analytical model and the 2D FEA. (b) Air-gap flux density distribution under load condition. Here, the relative magnet width is 0.26. Such a low value may occur e.g. in cases where the magnets are tapered.

Fig. 2.11 reveals that the values given by the analytical approach are slightly lower when compared to the results obtained from the FEA under no-load condition. This difference is most likely due to the accuracy of defining the leakage fluxes on each computation plane. Furthermore, the 3D flow of the magnetic flux is not taken into account in the analytical model, neither in the 2D FEA, which may contribute to the flux density levels obtained on each computation plane. Nevertheless, for machine design purposes, the results for $\hat{B}_{\mathrm{agap1}}$, obtained from the analytical model, are sufficiently accurate.

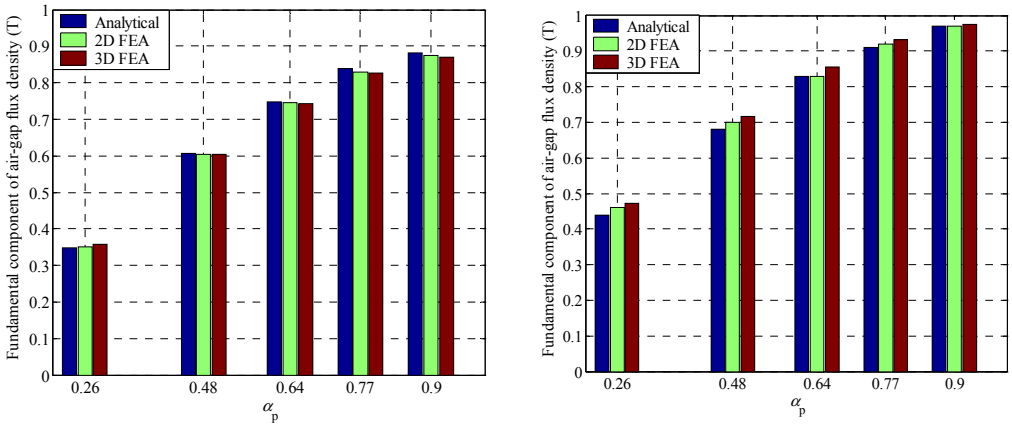

Fig. 2.11. Comparison between the flux density values given by the analytical approach, the 2D FEA and 3D FEA for five different pole shoe width – to – pole pitch ratio values. (a) No-load condition. (b) Load condition. The fundamental component of the air-gap flux density is shown.

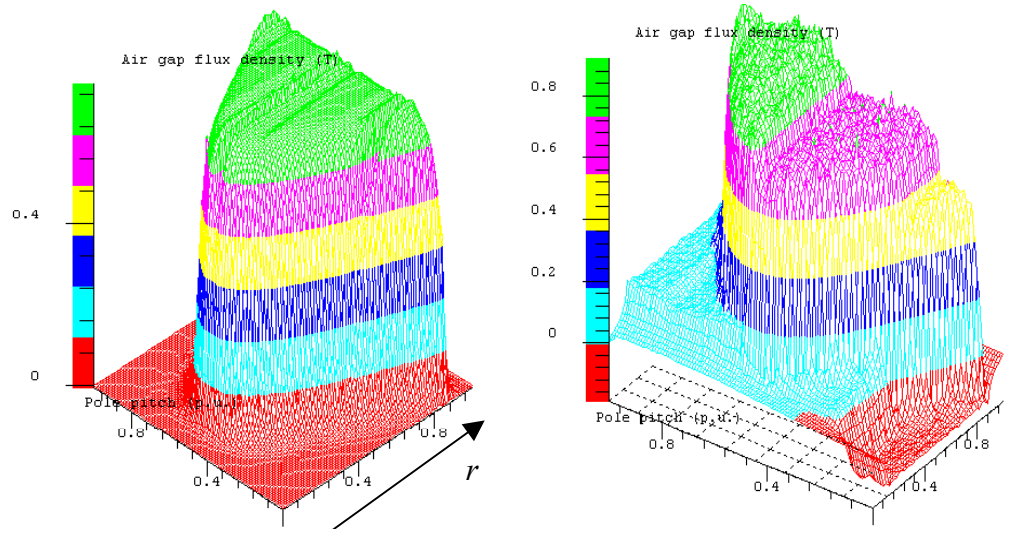

Fig. 2.12. (a) Actual no-load flux density distribution in the air-gap obtained from the 3D FEA. Direction of radius is visualized. (b) Flux density distribution under load condition. Note that the visualization plane is extended over the actual air-gap area in the direction of the machine radius.

2.2.4. Computation of no-load phase voltage

The RMS value of the fundamental component of the permanent-magnet-induced back-EMF is an important design quantity. The back-EMF value is directly proportional to the electromagnetic torque produced by the machine. Furthermore, the interaction between the no-load phase voltage and the phase current may produce some torque ripple if these quantities are non-sinusoidal. Therefore, not only the RMS value of the induced back-EMF, but also its harmonics are to be considered. Next, the computation method for the no-load phase voltage, used in the analysis, is described.

When the machine is driven as a generator, the no-load phase voltage is produced only by the flux linkage created by the permanent magnets and is evaluated based on the air-gap flux density distribution (2.19) as

$$e_{i,\mathrm{PM}}(t) = -N_{\mathrm{ph}}\xi_1 \frac{\Delta\Phi_{i,\mathrm{PM}}}{\Delta t}, \tag{2.25}$$

where N_{ph} is the number of coil turns in series per phase, ξ_1 is the winding factor for the fundamental wave, $\Phi_{\mathrm{i,PM}}$ is the air-gap flux which is obtained by integrating numerically the air-gap flux density distribution given by (2.18)

$$\Phi_{i,\mathrm{PM}} = \int_0^{\tau_{\mathrm{p},i}} \int_0^{\frac{l_{\mathrm{S}}}{N}} B_{\mathrm{agap},i}(x)\,\mathrm{d}x\,\mathrm{d}l\,. \tag{2.26}$$

The no-load phase voltage $e_{\mathrm{PM}}(t)$ for the whole machine is then computed from the equation

$$e_{\mathrm{PM}}(t) = \sum_{i=1}^{N} e_{i,\mathrm{PM}}(t)\,. \tag{2.27}$$

The comparison between the analytical approach and time transient 3D FEA is illustrated in Fig. 2.13 (a) for the machine described in Chapter 3. According to the 3D FEA, the amplitude of the obtained no-load voltage is about 11 % less compared to the voltage amplitude given by the analytical method. However, both computations give very similar waveforms for the induced back-EMF. The difference between the amplitudes may be explained through the leakage fluxes discussed earlier. On introducing the leakage coefficient $k_{\sigma\mathrm{PM}} = 0.89$ into the analytical computation of the induced back-EMF, a good agreement between the 3D FEA and the analytical approach is obtained.

In Fig. 2.13 (b) the effect of the number of used computation planes on the waveform of the back-EMF is illustrated. Typically 10 to 15 computation planes are required to achieve an accurate result. If more planes are used, the changes in the waveform are usually so small that increasing the number of the computation planes does not bring any practical improvement. However, if the computation of the cogging torque is to be included into the analysis, more computation planes are usually needed since the computation of the cogging torque tends to be more sensitive to the amount of computation planes used. In this case, as a guideline, 20 to 25 computation planes are needed.

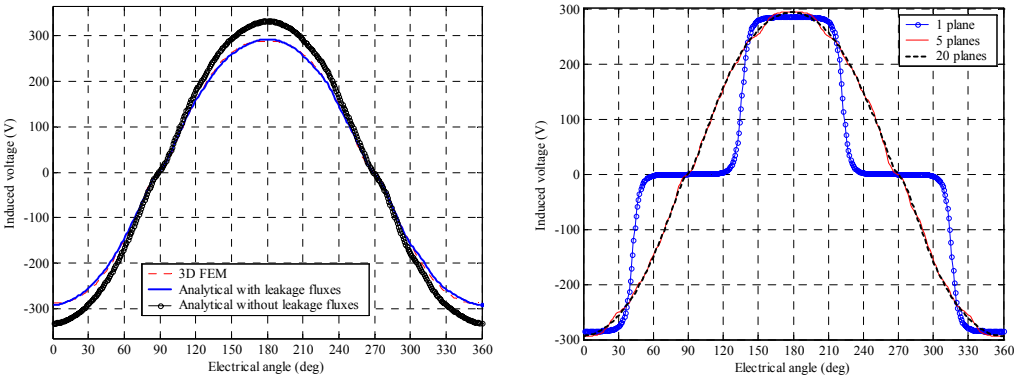

(a) (b)

Fig. 2.13. (a) Waveforms of the no-load phase voltage obtained with the analytical method by using 20 computation planes and the waveform of the no-load phase voltage obtained from the time transient 3D FEA. (b) The effect of the number of the computation planes on the waveform of the induced back-EMF. The magnet shape is sinusoidal.

In the previous sections of this chapter the focus has been placed on the computation of the waveform of the back-EMF. For the sizing of the phase winding the waveform is not that important, when compared to the amplitude of the induced back-EMF with known coil-turns (or alternatively the number of coil turns needed to achieve the required amplitude for the back-EMF). Thereby, calculating the RMS value of the induced back-EMF will be sufficient. With the known geometry and with the known fundamental component of the air-gap flux density $\hat{B}_{\text{agap1}}$, according to Eqn. (2.20), the RMS value of the induced back-EMF is

$$E_{\text{ph,PM}} = \frac{4 f \xi_1 N_{\text{ph}} \hat{B}_{\text{agap1}} \tau_{\text{p,ave}} l_{\text{s}}}{\sqrt{2}} . \tag{2.28}$$

If needed, the number of coil turns per phase, N_{ph}, can be solved based on (2.28) if the required no-load phase voltage is a known quantity, as it usually is.

2.2.5. Cogging torque

For permanent-magnet machine designing minimizing the cogging torque is one of the objects. The literature of the subject introduces several methods for minimizing and a review of the literature concerning axial-flux PM machines is given by Parviainen et al. (2002b). To give a rapid analysis of different magnet shapes, the computation of the cogging torque is included into the design tool. The cogging torque is calculated from the no-load air-gap flux density distribution with the virtual work method for each computation plane as (Barakat et al., 2001)

$$T_{\text{cog},i}(\theta) = \frac{\partial W}{\partial \theta} = \frac{1}{2\mu_0} \frac{\partial}{\partial \theta} \left(\iiint_V B_{\text{agap},i}^2 \, dV \right), \tag{2.29}$$

where

V is the volume of the air-gap
θ is the angular position of the rotor.

The cogging torque T_{cog} produced by the whole machine is obtained in a similar way as the no-

load voltage

$$T_{\mathrm{cog}}(\theta) = \sum_{i=1}^{N} T_{\mathrm{cog},i}(\theta). \tag{2.30}$$

During the computation of the cogging torque it is assumed for the each computation plane that the flux density distribution does not vary in the depth direction of computation plane. The analytical computation of the cogging torque is verified with the 3D FEA. A set of magneto-static problems was solved in order to evaluate the cogging torque produced by the machine. Fig. 2.14 shows a comparison between the analytical method and 3D FEA. In this case, the analytical model gives higher amplitude values for the cogging torque but the curvatures are similar. According to the result given here for the axial-flux PM machine and according to other analytical calculation results presented in (Barakat et al., 2001; Kurronen, 2003), it is possible to evaluate the cogging torque with reasonable accuracy by using the analytical approach. This is a result that may be considered to be advantageous for certain computation applications, since the analytical calculation is much faster to perform than the 3D FEA and is therefore useful if a rapid comparison between the different shapes is required. For detailed cogging torque investigations the FEA is nevertheless to be recommended because certain saturation effects of different stator parts may contribute to the cogging of the torque.

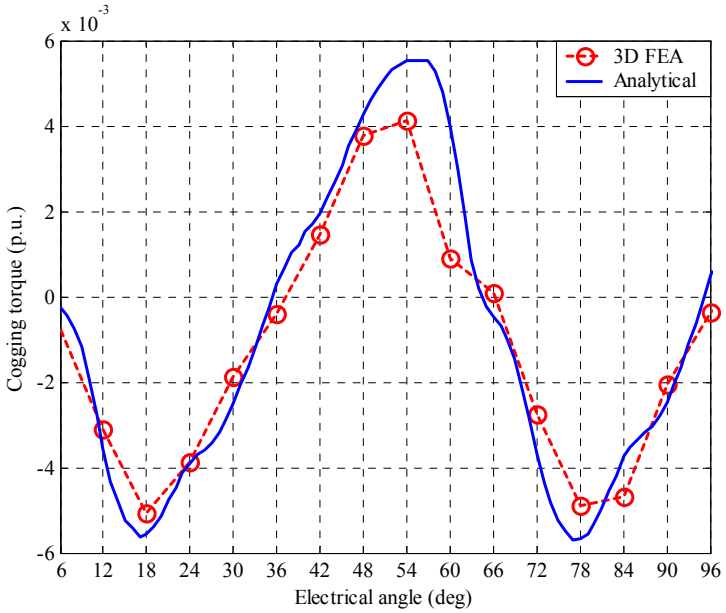

Fig. 2.14. Comparison between the 3D FEA and analytical model in the computation of a cogging torque. In the analytical model, the number of the used computation planes is 20.

2.2.6. Computation of phase resistance and copper losses

In low-speed machines, among all losses, the copper losses, known also as Joule losses, are often dominating. Thereby, accurate predicting of the motor phase resistance is needed. The resistance of a copper wire shows temperature dependency, causing that also the operation temperature of the winding has to be known. In the analysis, the phase DC-resistance is calculated based on the equation

$$R_{\mathrm{ph,DC}} = \frac{l_{\mathrm{Cu}}\left(1 + k_{\mathrm{Cu}}\left(T - 20\right)\right)}{\sigma_{\mathrm{Cu}} S_{\mathrm{Cu}} a}, \tag{2.31}$$

where

l_{Cu} is the total length of phase coil
T is the average temperature of the coil in °C degrees
k_{Cu} is the temperature coefficient of copper resistivity ($k_{\mathrm{Cu}} = 3.8 \cdot 10^{-3}$ 1/°C)
σ_{Cu} is the electric conductivity of the copper at 20 °C temperature
S_{Cu} is the cross-sectional area of copper in one coil turn
a is the number of parallel branches

The total length of the phase coil l_{Cu} is calculated based on the equation (Gieras, 1997)

$$l_{\mathrm{Cu}} = 2N_{\mathrm{ph}}\left(l_{\mathrm{s}} + \left(0.083p + 1.217\right)\tau_{\mathrm{p,ave}} + 0.02\ \mathrm{m}\right). \tag{2.32}$$

Since the value of the phase DC-resistance, $R_{\mathrm{ph,DC}}$, depends on the temperature, the operation temperature T of the phase winding must be correctly estimated. This is done iteratively by using a thermal resistance network, which will be described later in Chapter 2.4.

For the AC-current the resistance is larger than for the DC-current because of the effects caused by the alternating current, which are the skin effect and proximity effect. Furthermore, the leakage fluxes through the slots cause additional eddy currents to the conductors. Due to these phenomena, the phase resistance is further increased and may be approximated as (Hanselman, 2003)

$$R_{\mathrm{ph}} \approx R_{\mathrm{ph,DC}}\left(1 + \frac{1}{9}\left(\frac{y}{\chi}\right)^2\left(\frac{d_{\mathrm{w}}}{\chi}\right)^2\right), \tag{2.33}$$

where

y is the depth of the slot
d_{w} is the diameter of single conductor
χ is the skin depth of the conductor in free space

Eq. (2.33) is valid only if the slot shape is rectangular and if the number of conductor rows in a depth direction of slot is five or more (Hanselman, 2003). The skin depth χ in free space is defined as

$$\chi = \sqrt{\frac{2}{\omega\mu\sigma_{\mathrm{Cu}}}}, \tag{2.34}$$

where

ω is the angular frequency

Considering low-speed machines wound by using round conductors with typical wire diameters about 1.0 mm, the AC resistance of the phase winding is practically the same as the phase DC resistance. Thereby, (2.31) is usually sufficiently accurate for the computation of the phase resistance and is used in the computation model.

Based on the calculated phase current and phase resistance, the copper losses in a stator winding are calculated as

$$P_{\mathrm{Cu}} = mR_{\mathrm{ph}} I_{\mathrm{ph}}^2 , \tag{2.35}$$

where

m	is the number of phases
I_{ph}	is the RMS value of phase current

2.2.7. Computation of iron losses

The accurate computation of the iron losses is a difficult task due the complex phenomena related to the iron loss generation in a laminated medium. The material properties of the steel sheet, the nature of the flux density variation (alternating vs. rotational, sinusoidal vs. trapezoidal) and even the manufacturing process of the laminations and the stack, these all affect the iron losses. Several studies present different approaches to predict the amount of iron losses for surface-mounted permanent-magnet machines. A review is given recently by Heikkilä (2002).

A classical equation to estimate iron losses in laminations is (Vogt, 1983)

$$P_{\mathrm{Fe}} = k_{\mathrm{Fe,y}} P_{1.0} G_{\mathrm{y}} \hat{B}_{\mathrm{y}}^2 \left(\frac{f}{50} \right)^{1.5} + k_{\mathrm{Fe,t}} P_{1.0} G_{\mathrm{t}} \hat{B}_{\mathrm{t}}^2 \left(\frac{f}{50} \right)^{1.5} , \tag{2.36}$$

where

$k_{\mathrm{Fe,y}}$ and $k_{\mathrm{Fe,t}}$	are an experimental loss coefficients for the yoke and the teeth
$P_{1.0}$	is the loss value of the steel grade at 50 Hz and at the flux density of 1.0 T
G_{y} and G_{t}	are the masses of the yoke and the teeth
$\hat{B}_{\mathrm{y}}$ and $\hat{B}_{\mathrm{t}}$	are the peak flux density values in the yoke and the teeth
f	is the fundamental electric frequency

An alternative approach is to subdivide the iron loses into three parts classified as

- Hysteresis losses
- Eddy current losses
- Excess losses (known also as anomalous losses)

Based on above classification it is possible to calculate the iron losses per unit volume as (Deng, 1999)

$$P_{\mathrm{Fe}} = k_{\mathrm{hys}} \hat{B}^2 f + \pi^2 \frac{\sigma_{\mathrm{Fe}} d^2}{6} \left(\hat{B} f \right)^2 + 8.67 \cdot k_{\mathrm{ex}} \left(\hat{B} f \right)^{1.5} , \tag{2.37}$$

where

k_{hys}	is the hysteresis loss coefficient
k_{ex}	is the excess loss coefficient
d	is the thickness of the used steel sheet
σ_{Fe}	is the electric conductivity of the lamination material

The hysteresis loss coefficient k_{hys} and excess loss coefficient k_{ex} are found based on the loss curves measured at several frequencies as a function of the flux density. Usually, these curves are provided by the manufacturer of the steel grade. Note that in (2.37) it is assumed a sinusoidal variation of the flux density in iron, whilst for surface-mounted PM machines the

variation of the flux density is typically trapezoidal. The modified expression for (2.37) taking into account the non-sinusoidal variation of flux density will be

$$\frac{1}{T}\int_0^T P_{\mathrm{Fe}}\mathrm{d}t = k_{\mathrm{hys}}\hat{B}^2 f + \frac{1}{T}\int_0^T\left(\frac{\sigma_{\mathrm{Fe}}d^2}{12}\left(\frac{\mathrm{d}B}{\mathrm{d}t}(t)\right)^2 + k_{\mathrm{ex}}\left(\frac{\mathrm{d}B}{\mathrm{d}t}(t)\right)^{1.5}\right)\mathrm{d}t \tag{2.38}$$

Since (2.38) includes integration over the period T, the computation has to be performed over one full cycle and is most suitable to be used with the finite element method, especially, because the result given by (2.38) is depending on the term dB/dt. Therefore, the computation model must enable the describing of the dynamic flux behaviour in a particular part of the machine with a high accuracy.

To analytically compute the iron losses caused by the trapezoidal flux density variation the iron loss model derived by Deng (Deng, 1999) for the trapezoidal flux density waveform may be used. The model is based on the flux density distribution for different magnet widths with respect to the tooth width α_{tt}, Fig. 2.15.

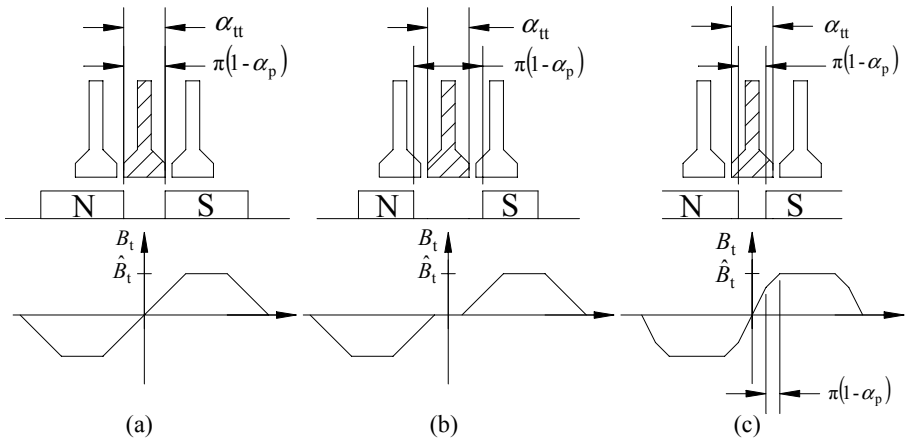

Fig. 2.15. Tooth flux density waveforms (Deng, 1999).

By using the simplified flux density waveforms, shown in Fig. 2.15, the following iron loss equations can be derived for the stator teeth (Deng, 1999)

$$P_{\mathrm{Fe,t}} = \begin{cases} \left(k_{\mathrm{hys}} f\hat{B}_{\mathrm{t}}^2 + \dfrac{2\pi d^2 f^2 \hat{B}_{\mathrm{t}}^2}{3\rho_{\mathrm{Fe}}\alpha_{\mathrm{tt}}} + k_{\mathrm{ex}}\left(\dfrac{4}{\pi\alpha_{\mathrm{tt}}}\right)^{3/4}\left(f\hat{B}_{\mathrm{t}}\right)^{3/2}\right)G_{\mathrm{t}}, & \text{if } \alpha_{\mathrm{tt}} \le \pi(1-\alpha_{\mathrm{p}}) \\ \left(k_{\mathrm{hys}} f\hat{B}_{\mathrm{t}}^2 + \dfrac{2\pi d^2 f^2 \hat{B}_{\mathrm{t}}^2}{3\rho_{\mathrm{Fe}}\alpha_{\mathrm{tt}}} k_{\mathrm{l}} + k_{\mathrm{ex}}\left(\dfrac{4}{\pi\alpha_{\mathrm{tt}}}\right)^{3/4} k_{\mathrm{l}}^{3/4}\left(f\hat{B}_{\mathrm{t}}\right)^{3/2}\right)G_{\mathrm{t}}, & \text{if } \alpha_{\mathrm{tt}} > \pi(1-\alpha_{\mathrm{p}}) \end{cases}, \tag{2.39}$$

where

ρ_{Fe} is the density of the lamination material

The coefficient k_{l} in (2.39) is defined as

$$k_{\mathrm{l}} = 2 - \frac{\pi(1-\alpha_{\mathrm{p}})}{\alpha_{\mathrm{tt}}}. \tag{2.40}$$

The maximum flux density used in (2.39) is obtained from the solution of reluctance network. Please notice also that in expressions (2.39) and (2.40), the tooth width α_{tt} must be expressed in electrical radians.

An expression for the iron losses in a stator yoke may be derived based on the flux density distribution, illustrated in Fig. 2.16.

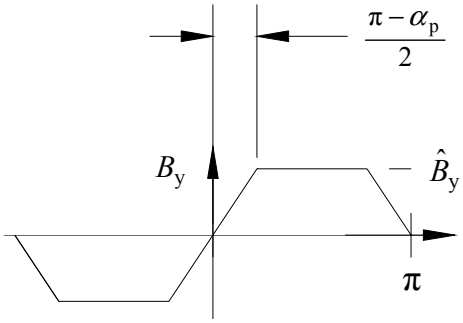

Fig. 2.16. Yoke flux density waveform (Deng, 1999).

The corresponding iron loss equation is (Deng, 1999)

$$P_{Fe,y} = \left(k_{hys} f \hat{B}_y^2 + \frac{4\pi d^2 f^2 \hat{B}_y^2}{3\rho_{Fe}\pi\alpha_p} + k_{ex} \left(\frac{8}{\pi^2 \alpha_p} \right)^{3/4} \left(f\hat{B}_y \right)^{3/2} \right) G_y , \tag{2.41}$$

In the analytical approach the axial-flux PM machine is subdivided into yoke and teeth parts and the iron losses are calculated as

$$P_{Fe} = \sum_{i=1}^{N} P_{Fe,y,i} + \sum_{i=1}^{N} P_{Fe,t,i} \ . \tag{2.42}$$

Fig. 2.17 shows the calculated iron loss distribution for the surface-mounted axial-flux PM machine based on equations (2.37) and (2.42) as a function of the machine stator radius. For the computation the stator is subdivided into twenty computation planes. Since the flux density and the iron volume increase in a stator yoke towards the outer radius, the iron losses in the stator yoke show a significant increment as the radius increases. The increment of the stator yoke flux density is due to the employed magnet shape, Fig. 3.1 (b). As a contrast, the flux density in the teeth tends to decrease as the tooth volume (on a certain computation plane) increases towards the outer periphery of the axial-flux machine stator. In this case, the iron loss in the teeth reaches almost a constant value as a function of the radius on the outer periphery of the stator. In some cases even a decreasing trend may be observed. The curvature of the total iron losses also shows that the major part of the iron losses is generated on the outer periphery of the stator.

In order to compare the losses, calculated by using Egn. (2.37) and the loss model described by Deng (Egns. (2.39) and (2.41)), the same loss computation was performed with the iron loss model including a trapezoidal flux density variation. The obtained total loss is given in Fig. 2.17. The loss model with trapezoidal flux density variation shows about 20 % higher total iron losses than the loss model employing sinusoidal flux density variation.

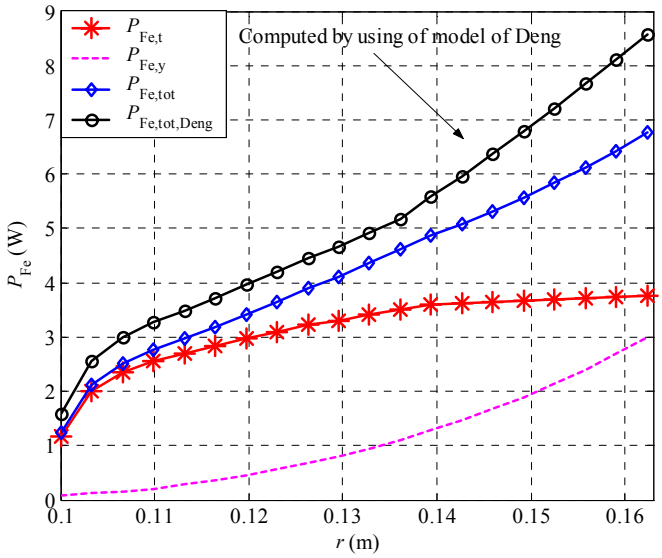

Fig. 2.17. Iron losses for the prototype machine as a function of the stator radius. The reported computation example is made for the machine of which dimensions are defined in Table 3.1.

There appear also additional iron losses called stray load losses. Stray load losses are permeance-variation-induced high-frequency losses in the ferromagnetic cores of AC machines and other anomalous electromagnetic losses. The computation of stray losses is difficult and does not guarantee a satisfactory accurate results (Gieras, 1997).

Stray load losses P_{str} are often considered to be a fraction of the output power

$$P_{str} = k_{str} P_{output} \,, \tag{2.43}$$

where

k_{str} is the coefficient for stray load losses.

The stray loss coefficient k_{str} may to vary between 0.03…0.05 for machines rated up to 10 kW, k_{str} = 0.005…0.01 for machines rated up to 100 kW and k_{str} = 0.003…0.005 for large machines (Gieras, 1997). However, the stray load loss shows a quadratic behaviour with respect to the output power of the machine. Thus, a linear interpolation between the recommended values for k_{str} makes defining of the stray load loss even more difficult. A more precise expression for the stray load losses may be derived as a function of the output power of the machine by doing some measurements (Haataja, 2003) but since the proper correlation is based on measurement, a lot of similar machines have to be constructed and tested in order to find the appropriate correlation.

Based on the previous discussion, it is to be expected that the computation of the iron losses includes uncertainties. For machines with considerably smaller iron losses than copper losses, the inaccuracy in the computation of the iron losses does not, however, cause significant errors.

2.2.8. Eddy current losses in permanent magnets and rotor iron

The main loss components in low-speed permanent-magnet machines are caused by the copper and iron losses. In addition, there appear eddy current losses in the permanent magnets due to

the harmonic content of an air-gap flux density distribution. Eddy current losses may also appear under the permanent magnets in the rotor disk. These eddy current loss components are usually neglected since the fundamental air-gap field usually rotates in synchronism with the rotor and the time harmonics in the current waveform and space harmonics in the winding distribution are generally small (Atallah et al., 2000). For machines equipped with semi-open slots the influence of the no-load eddy current losses caused by the stator slotting is not very significant (Sahin, 2001). It has to be noted that for high-speed machines this may be different and the rotor eddy current losses may become the major part of the total losses (Sahin, 2001).

Based on the previous considerations and because of the rotational speeds of the machines discussed in this thesis the computation of the rotor eddy current losses is not included in the analytical design procedure . However, if totally open slots are introduced it is recommended to calculate the eddy current losses in a rotor with the FE-analysis, even when low-speed machines are considered. Gieras (2004) presents also analytical methods to calculate the eddy current losses in the permanent magnets or in the solid-iron disk under the permanent magnets.

2.2.9. Mechanical losses

Mechanical losses may be divided into two major parts being

- Friction losses
- Bearing losses

The friction losses are caused by the friction of air with the rotating rotor. The friction losses for the axial-flux machines may be calculated by using friction factor correlations for rotating enclosed disks (Daily et al., 1960). Based on a known friction factor k_f, the friction torque may be calculated for axial-flux machines as

$$T_f = \frac{k_f \rho_{air} \pi \omega^2 \left(r_{out}^5 - r_{in}^5\right)}{2}, \tag{2.44}$$

where

ρ_{air} is the density of air

The bearing losses may be calculated by using the calculation tools provided by the bearing manufacturer or analytical equations as (Gieras, 1997)

$$P_b = 3 \frac{k_b G_r \Omega}{100\pi} \tag{2.45}$$

where

k_b is a factor with value k_b = 1 to 3
G_r is the mass of the rotor in kg
Ω is the rotational angular speed of the rotor.

The bearing loss depends on the axial and radial loads of the bearing. For the axial-flux machine including one rotor and two stators, it is possible to reduce the axial load of the bearing by centring the rotor correctly, when the net attractive force between the rotor and the stators equals zero. Otherwise, the bearing losses are increased due to the axial force component. The radial loading of the bearing is a result of the weight of the rotor structure, including the shaft.

2.2.10. Computation of the inductances

For the machine performance computations, the synchronous inductances are important parameters. The direct- and quadrature axis magnetizing inductances (L_{md}, L_{mq}) and the leakage inductance L_σ form together the synchronous inductances, which are used in the evaluation of the machine toque production capabilities. Based on the concept of the d- and q-axis, the corresponding inductances are

$$\begin{cases} L_d = L_{md} + L_\sigma \\ L_q = L_{mq} + L_\sigma \end{cases}, \tag{2.46}$$

where

L_d is the direct axis synchronous inductance
L_q is the quadrature axis synchronous inductance
L_{md} is the direct axis magnetizing inductance
L_{mq} is the quadrature axis magnetizing inductance
L_σ is the leakage inductance

The leakage inductance L_σ can be evaluated based on the leakage coefficients, which are (Gieras, 1997)

1. Slot leakage permeance coefficient λ_{slot}
2. End connection leakage permeance coefficient λ_{end}
3. Differential leakage permeance coefficient λ_{dif}
4. Tooth-tip leakage permeance coefficient λ_{tt}

The equations for the coefficients depend on the slot and winding geometry and, in literature, they are introduced for the most common slot structures. Based on the calculated leakage coefficients the leakage inductance L_σ can be calculated as

$$L_\sigma = 2\mu_0 \frac{N_{ph}^2 l_{eff}}{pq}\left(\lambda_{slot} + \frac{l_{end}}{l_{eff}}\lambda_{end} + \lambda_{dif} + \lambda_{tt}\right), \tag{2.47}$$

where

l_{end} is the average length of the end connection.
l_{eff} is the effective length of stator stack ($l_{eff} \approx l_s + 2g$)

The magnetizing inductance per stator for the direct axis is calculated as

$$L_{md} = \frac{2}{\pi} m \mu_0 \frac{\left(N_{ph}\xi_1\right)^2}{\pi p} \frac{\tau_p l_{eff}}{g_{d,eff}}, \tag{2.48}$$

and for the quadrature axis as

$$L_{mq} = \frac{2}{\pi} m \mu_0 \frac{\left(N_{ph}\xi_1\right)^2}{\pi p} \frac{\tau_p l_{eff}}{g_{q,eff}}. \tag{2.49}$$

The equivalent air-gaps, $g_{d,eff}$ and $g_{q,eff}$ include the effect of the physical air-gap, of the permanent magnets as well as of the iron parts in the stator and the rotor, i.e. the influence of saturation of iron parts is taken into account. Since the saturation level may vary as a function of the stator radius, an averaged value, taking into account the iron parts, is introduced to be placed into (2.48) and (2.49)

$$g_{\mathrm{d,eff}} = g' + \frac{l_{\mathrm{PM}}}{\mu_{\mathrm{r,PM}}} + \frac{\sum_{i=1}^{N} g_{\mathrm{d,Fe,i}}}{N}, \tag{2.50}$$

$$g_{\mathrm{q,eff}} = g' + l_{\mathrm{PM}} + \frac{\sum_{i=1}^{N} g_{\mathrm{q,Fe,i}}}{N} \tag{2.51}$$

Depending on the number of the stators and whether the stators are connected in parallel or in series, the synchronous inductances have to be calculated using the equivalent circuit approach for the particular axial-flux machine. As an example, for the axial-flux machine with double air-gap through which the stator flux has to flow, i.e. the stators are connected parallel, the effective length of the one air-gap must be multiplied by a factor of two if it is used with Eqns. (2.48) and (2.49). The corresponding circuit representation for such a machine is given in Fig. 2.18.

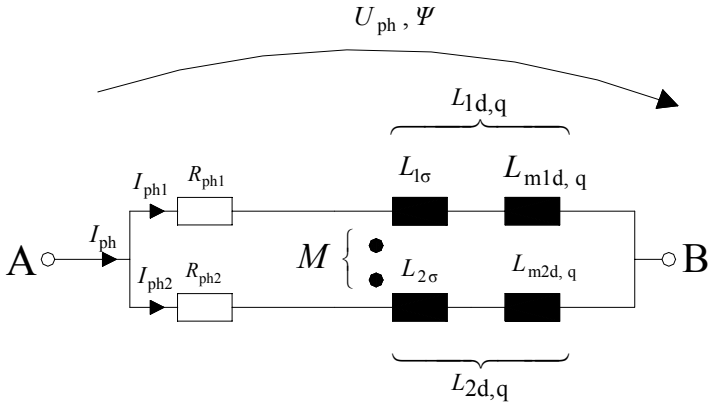

Fig. 2.18. Equivalent circuit of an axial-flux machine with two stators, connected electrically in parallel.

Since the inductances of the individual stators are connected together via a mutual inductance M, the equivalent inductances need to be determined from the terminals of the machine (between points A-B), because Eqs. (2.47)-(2.49) consider only structures with one stator and do not include the influence of mutual coupling between the independent stators if the stators are magnetically linked. For parallel-connected stators the equivalent inductances may be calculated as

$$L_{\mathrm{d,q,eqv}} = \frac{L_{1\mathrm{d,q}} L_{2\mathrm{d,q}} - M_{12\mathrm{d,q}}^2}{L_{1\mathrm{d,q}} + L_{2\mathrm{d,q}} - 2M_{12\mathrm{d,q}}}. \tag{2.52}$$

By introducing a coupling constant k, which describes the mutual coupling between the stators inductances $L_{1\mathrm{d,q}}$ and $L_{2\mathrm{d,q}}$ and by assuming that stator inductances are equal ($L_{1\mathrm{d,q}} = L_{2\mathrm{d,q}} = L_{\mathrm{d,q}}$ and $L_{1\sigma} = L_{2\sigma} = L_{\sigma}$) the mutual inductance $M_{12\mathrm{d,q}}$ may be described as

$$M_{12\mathrm{d,q}} = k\sqrt{L_{1\mathrm{d,q}} L_{2\mathrm{d,q}}} = kL_{\mathrm{d,q}}. \tag{2.53}$$

The assumption of equal inductances between the stators ($L_{1\mathrm{d,q}} = L_{2\mathrm{d,q}}$) is valid for design purposes. However, in practise, it is difficult to construct and assemble independent stators such that exactly equal magnetic parameters can be obtained. For the considered electrical machines, nevertheless, exactly equal parameters are needed.

As the stators synchronous inductances $L_{\mathrm{d,q}}$ are composed of two parts, the leakage inductance L_{σ} and magnetizing inductance $L_{\mathrm{md,q}}$, it is convenient to assume that the stators leakage

inductances are not coupled together via a mutual inductance whereas the magnetising inductances are. By rewriting (2.52) with the help of (2.53) a simplified equation to calculate the synchronous inductances is found.

$$L_{\mathrm{d,q,eqv}} = \frac{{L_{\mathrm{d,q}}}^2 - (kL_{\mathrm{d,q}})^2}{2L_{\mathrm{d,q}} - 2kL_{\mathrm{d,q}}} = \frac{{L_{\mathrm{d,q}}}^2\left(1-k^2\right)}{2L_{\mathrm{d,q}}\left(1-k\right)} = \frac{L_{\mathrm{d,q}}\left(1-k^2\right)}{2\left(1-k\right)} = \frac{L_{\mathrm{d,q}}\left(1+k\right)}{2} \tag{2.54}$$

Based on (2.54) the synchronous inductances of the parallel-connected stators are combined to one equivalent synchronous inductance. Assuming that the leakage inductances of the stators are not coupled together via a mutual inductance whereas the magnetizing inductances are fully coupled and that the absolute values of inductances between the stators are equal, allows to evaluate a numerical value for the coupling constant k with the help of Eqs. (2.47)-(2.49) as a ratio $k = L_{\mathrm{md,q}}/L_{\mathrm{d,q}}$.

2.2.11. Computation of the load angle of the machine

As the values of the supply voltage, the induced back-EMF and inductances are known, it is possible to find the load angle of the machine based on the torque equation for the synchronous machines

$$T = \frac{m}{\Omega}\left(\frac{E_{\mathrm{ph,PM}}U_{\mathrm{ph}}}{\omega L_{\mathrm{d}}}\sin(\delta) + \frac{U_{\mathrm{ph}}^2\left(L_{\mathrm{d}}-L_{\mathrm{q}}\right)}{2\omega\left(L_{\mathrm{q}}L_{\mathrm{d}}\right)}\sin(2\delta)\right), \tag{2.55a}$$

where

δ is the load angle
U_{ph} is the supply line voltage

The output torque as a function of the load angle is illustrated in Fig. 2.19.

For machines for which the stator resistive voltage drop is larger than the inductive voltage drop, it is recommended to replace Eqn. (2.55a) with a torque equation including the phase resistance. This may be the case, for example, with small machines (Gieras, 1997).

$$\begin{aligned} T = \frac{m}{\Omega}\Bigg\{ & \frac{U_{\mathrm{ph}}E_{\mathrm{ph,PM}}\left(R_{\mathrm{ph}}\cos(\delta)+\omega L_{\mathrm{d}}\sin(\delta)\right)}{\left(\omega^2 L_{\mathrm{d}}L_{\mathrm{q}}+R_{\mathrm{ph}}^2\right)^2}\Bigg\{\left[\left(\omega^2 L_{\mathrm{d}}L_{\mathrm{q}}+R_{\mathrm{ph}}^2\right)-\omega^2 L_{\mathrm{q}}\left(L_{\mathrm{d}}-L_{\mathrm{q}}\right)\right]- \\ & U_{\mathrm{ph}}E_{\mathrm{ph,PM}}R_{\mathrm{ph}}\left(\omega L_{\mathrm{q}}\cos(\delta)-R_{\mathrm{ph}}\sin(\delta)\right)\left(\omega L_{\mathrm{d}}-\omega L_{\mathrm{q}}\right)+ \\ & U_{\mathrm{ph}}^2\left(R_{\mathrm{ph}}\cos(\delta)+\omega L_{\mathrm{d}}\sin(\delta)\right)\left(\omega L_{\mathrm{q}}\cos(\delta)-R_{\mathrm{ph}}\sin(\delta)\right)\left(\omega L_{\mathrm{d}}-\omega L_{\mathrm{q}}\right)- \\ & E_{\mathrm{ph,PM}}^2R_{\mathrm{ph}}\left[\left(\omega^2 L_{\mathrm{d}}L_{\mathrm{q}}-R_{\mathrm{ph}}^2\right)-\omega^2 L_{\mathrm{q}}\left(L_{\mathrm{d}}-L_{\mathrm{q}}\right)\right]\Bigg\}\Bigg\} \end{aligned} \tag{2.55b}$$

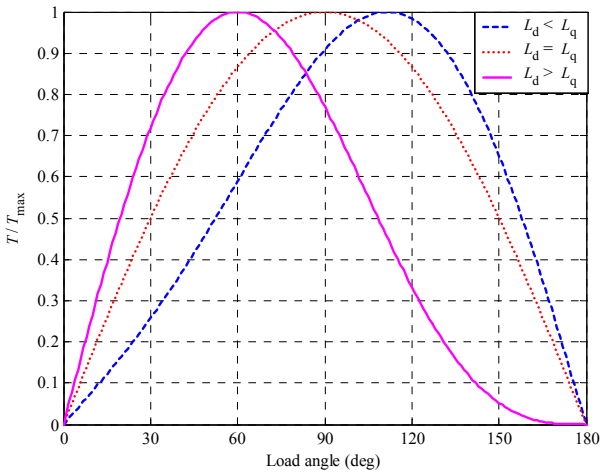

Fig. 2.19. Output torque as a function of load angle as different inductance ratios are introduced. The curves are scaled for the maximum torque to be equal to value 1.

2.2.12. Efficiency and power factor

After that the computation of the overall efficiency and the power factor of the machine is performed the electromagnetic design of the machine is completed. The machine efficiency is obtained by using the calculated input power and the calculated losses as

$$\eta = \frac{P_{\text{output}}}{P_{\text{input}}} = \frac{P_{\text{input}} - P_{\text{Cu}} - P_{\text{Fe}} - P_{\text{str}} - P_{\text{b}}}{P_{\text{input}}}. \tag{2.56}$$

The machine power factor is obtained by using a relation between the active power and the apparent power as

$$\cos\varphi = \frac{mU_{\text{ph}}\left(I_{\text{q}}\cos\delta - I_{\text{d}}\sin\delta\right)}{mU_{\text{ph}}\sqrt{I_{\text{d}}^2 + I_{\text{q}}^2}}, \tag{2.57}$$

where the corresponding direct– and quadrature axis currents are calculated as

$$I_{\text{d}} = \frac{U_{\text{ph}}\left(\omega L_{\text{q}}\cos\delta - R_{\text{ph}}\sin\delta\right) - E_{\text{ph,PM}}\omega L_{\text{q}}}{\omega^2 L_{\text{d}}L_{\text{q}} + R_{\text{ph}}^2} \tag{2.58}$$

$$I_{\text{q}} = \frac{U_{\text{ph}}\left(R_{\text{ph}}\cos\delta + \omega L_{\text{d}}\sin\delta\right) - E_{\text{ph,PM}}R_{\text{ph}}}{\omega^2 L_{\text{d}}L_{\text{q}} + R_{\text{ph}}^2}. \tag{2.59}$$

Based on the calculated motor parameters, it is possible to illustrate the machine operation point by using a phasor diagram. In Fig. 2.20 the phasor diagram is shown for an under-excited permanent-magnet motor.

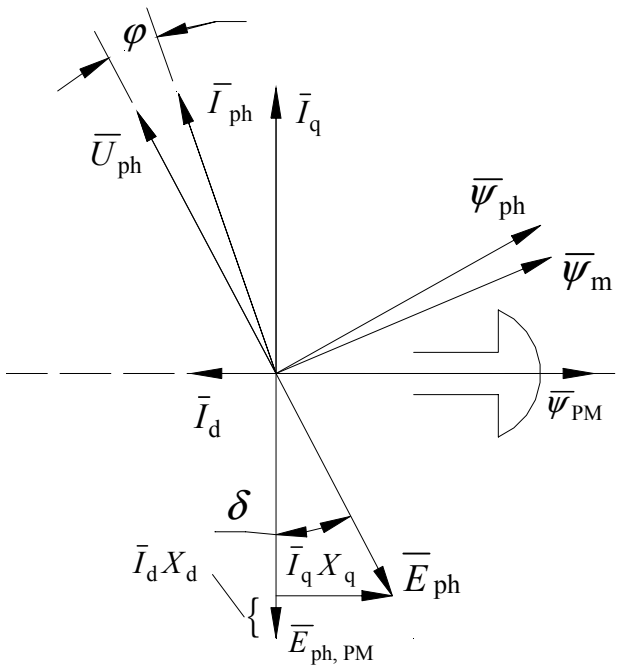

Fig. 2.20. A phasor diagram of an under-excited synchronous motor. Please observe that usually the armature reaction is demagnetising on the d-axis, $I_d < 0$.

2.3. Finite element method

For accurately solving original problems containing partial differential equations or integral equations an effective computer program based on the finite element method (FEM) is a useful tool. At present, several commercial 2D/3D finite element packages are available and may be applied also to permanent-magnet machine design. For the electromagnetic design of electrical machines the finite element analysis may be considered to be a well-established design method, even though occasionally, certain particular computation procedures are to be updated. Although in course of the study the 2D/3D finite element method has been a significant tool for modelling, in this thesis, the emphasis has not been placed on the finite element analysis itself.

The leading function of the finite element method is subdividing the described geometry into portions for which a particular covering equation is valid. Each of the described geometrical portions is further subdivided into a large amount of smaller elements, called finite elements. In each element a simple polynomial is used to approximate the solution, first or second order polynomials are usually used. When applied to electrical machines, the described problem is usually reduced to cover only one pole or one pole pair with the help of boundary and symmetry conditions in order to reduce the computation time. In addition, it is often sufficient to reduce the problem to a 2D plane and use the 2D finite element analysis (FEA). For complex machine structures, however, using the 3D FEA may be necessary.

The main considerations and covering equations for the finite element method are reported in (Silvester et al., 1983, Gieras, 1997). Even though examples are often given for radial-flux machines, a description of 2D FEA used for axial field machines is also given in (Caricchi et al., 1992). As a summary, with the 2D FEA modelling axial-flux machines is possible in a similar way as it is with the analytical computation, i.e. by using the average radius of the machine as a design plane or by using the quasi-3D computation method. A finite element program enabling the modelling of linear movement is recommended. If such tool is not

available, it is possible to perform the finite element analysis by solving a sufficient amount of magneto-static problems. This, however, requires that the FE-models needed for each rotor position and computation plane are to be build separately and thereby this approach is rather laborious (Caricchi, 1998). In this case, it may be appropriate to use directly the 3D FEA or analytical design methods, especially, if the procedure of sizing the machine is included in the analytical design. In Fig. 2.21 the flux lines and the relevant boundary / symmetry conditions of a typical 2D FE-model for a double-sided axial-flux machine are depicted.

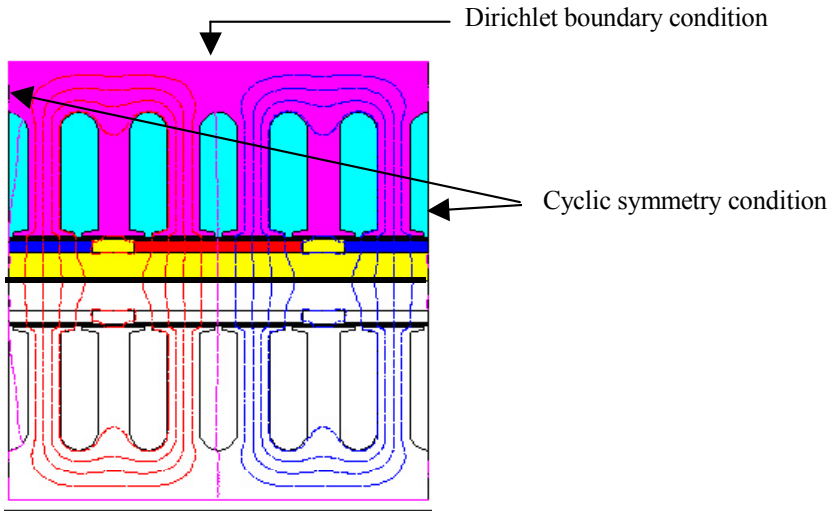

Fig. 2.21. Boundary and symmetry conditions in a 2D FEA describing the pole pair of an axial-flux PM machine. The flux lines are depicted.

Contrary to the 2D FEM, the 3D FEM takes into account the 3D effects appearing in the electromagnetic behaviour of the machine. This, evidently, makes the model most accurate if a proper mesh is used. The 3D FEA provides also additional information regarding the leakage fluxes and the end-winding inductances, which are difficult to evaluate otherwise. Since the air-gap regime of the electrical machine requires a dense mesh pattern concerning the accuracy of the computation result, the number of the generated volume elements in the 3D FEM tends to be large. This is usually acceptable for machines including several pole pairs. However, for large machines including one or two pole pairs the size of the system matrix grows unacceptably large and the computation power of present-day personal computers is not sufficient to handle such matrixes fluently.

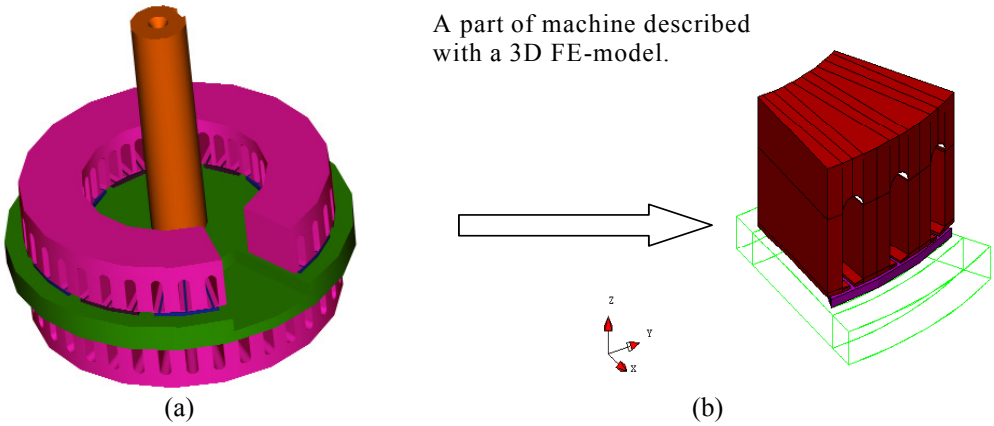

Fig. 2.22. (a) Structure of AFIPM machine. (b) A pole of machine described with a 3D FE-model. The described pole represents the smallest geometrical entity needed in 3D FEA.

Compared to the 2D FEA, the 3D FEA, consequently, often needs considerably more computation time. Furthermore, since the 3D model requires more definitions than the corresponding 2D model, accordingly more time will be needed to build a 3D FE-model. However, since the 2D-FEA must be performed separately for all computations planes, the problem of long during computation may be not concerned with the developed quasi-3D method. In table 2.2 the duration of model preparation and computation is compared. The time given here for the preparation work of the models is based on the experiences with the FE-software used (FLUX2D™/FLUX3D™) and with the analytical design tool described in this study.

Table 2.2. Computation time comparison between analytical and FE-methods.

Method	Number of elements	Preparation time / computation time
Analytical, full analysis using 20 computation planes	-	5 min / 31 s
2D-FEA, one time step for one computation plane	5524 (2^{nd} order)	30 min / 6s
3D-FEA, one time step	116709 (2^{nd} order)	4 hours / 23 min

Irrespective of the fact that the quasi-3D method has been used with the 2D FEA the preparation work in has to be done only once since it is possible to parameterise the computation model. For the 2D and 3D FEA the required computation time is given for one computation step. The number of surface elements (2D FEA) or volume elements (3D FEA) is given. From the data given in table 2.2 it may be seen that the 2D FEA tends to be more time consuming than the 3D FEA if the number of computation planes is high. For the given FE-models this is the case if there are over 200 planes, which is practically too much.

2.4. Thermal modelling

An accurate performance analysis of the electrical machine requires information regarding the thermal behaviour of the machine. For electrical machines magnetised with Nd-Fe-B permanent magnets, the remanence flux density of the permanent magnet material depends on the temperature affecting the amplitude of the induced back-EMF and, thereby, on the performance characteristics of the machine. A thermal demagnetisation risk of the permanent magnet may exist if the magnet temperature exceeds the limit allowed, which is typically between 120-210 °C for present-day Nd-Fe-B magnets. Furthermore, mechanical hazards are possible if the permanent magnets are glued on the surface of the rotor disk and the temperature of the glue joint exceeds the critical value. An accurate value for the phase resistance, which also is a temperature depending quantity, is required in order to find the correct Joule losses. Thus, estimation of the operation temperature of the phase winding and the permanent magnets is necessary.

For radial-flux machines several detailed investigations on thermal modelling have been introduced (Kylander, 1995; Saari, 1998; Negrea et al., 2001) while for axial-flux machines the matter has not been stressed (Sahin, 2001; Scowby et al., 2004; Gieras, 2004). Sahin (2001) discusses the thermal analysis of a high-speed (16 000 min^{-1}) axial-flux PM machine with one rotor – two stators configuration. This machine was designed for a flywheel application with water-cooling. Scowby et al. (2004) reports tests results for a 300 kW, 2300 min^{-1} axial-flux machine with one stator – two rotors configuration. In this study, the authors consider an internal forced air-cooling. For the purposes of improving cooling also heat pipe arrangements have been studied. Recently, a study both on water-cooling and on air-cooling of an axial-flux

machine with one rotor – two stators configuration has been reported by (Parviainen et al., 2004b).

2.4.1. Heat transfer

Generally, the heat transfer is characterized by three mechanisms classified as

- Convection
  - Natural
  - Forced
- Radiation
- Conduction

The heat transfer from the surface to ambient due to convection is defined by the equation

$$P_{\mathrm{con}} = hS\left(T_{\mathrm{sur}} - T_{\mathrm{amb}}\right), \tag{2.60}$$

where

h is the heat transfer coefficient
T_{sur} is the surface temperature
T_{amb} is the temperature of the ambient
P_{con} is the dissipated power due to the convection

The most problematic task is to find a correct heat transfer coefficient h for the studied surface. For some simple solids, such as planes or pipes, it is possible to derive correlations (Incropera et al., 1996) but for complex structures such as electrical machines the most common method to find h is based on experimental measurements. Forced convection is the most common cooling mechanism used for the electrical machines. However, as there appears a temperature gradient between the surface and ambient, also radiation contributes to the heat transfer. The heat removal through radiation is described as

$$P_{\mathrm{rad}} = \varepsilon_{\mathrm{sur}} \varsigma S\left(T_{\mathrm{sur}}^4 - T_{\mathrm{amb}}^4\right), \tag{2.61}$$

where

$\varepsilon_{\mathrm{sur}}$ is the emissivity of the surface
ς is Stefan-Boltzmanin constant, $5.6703 \cdot 10^{-8}$ W/m^{2}K^4.

The surface emissivity is a quantity, which depends on the material of the surface. For a black painted surface the emissivity is typically nearly 0.9, but for a polished steel surface it may be below 0.3 (Incropera et al., 1996). Radiation may be a significant cooling mechanism, especially for small power machines.

Considering convection, the partial differential equation known as diffusion equation describes the heat transfer

$$\nabla^2 T = \frac{\partial^2 T}{\partial x^2} + \frac{\partial^2 T}{\partial y^2} + \frac{\partial^2 T}{\partial z^2}. \tag{2.62}$$

For the thermal analysis of electrical machines applying (2.62) causes a complex boundary value problem with several unknowns related to the contacts between the different parts. Therefore, simplifying the considered problem and using a thermal equivalent circuit to describe the heat transfer problem is often appropriate. In this thesis, this will be done too.

2.4.2. Thermal resistance network

The thermal analysis of a machine is based on the thermal resistance network, illustrated in Fig. 2.23. The computation model is developed for the steady-state analysis only and the thermal capacitances are thus omitted in the thermal model. The nodal temperatures of the network are calculated as

$$\mathbf{T} = \mathbf{G}^{-1}\mathbf{P} \tag{2.63}$$

where **T** is the temperature matrix, **G** is the thermal conductivity matrix and **P** is the loss matrix. The thermal conductivity matrix is defined as

$$\mathbf{G} = \begin{bmatrix} \sum_{i=1}^{n} \frac{1}{R_{1,i}} & -\frac{1}{R_{1,2}} & \cdots & -\frac{1}{R_{1,n}} \\ -\frac{1}{R_{2,1}} & \sum_{i=1}^{n} \frac{1}{R_{2,i}} & \cdots & -\frac{1}{R_{2,n}} \\ \vdots & \vdots & \ddots & \vdots \\ -\frac{1}{R_{n,1}} & -\frac{1}{R_{n,2}} & \cdots & \sum_{i=1}^{n} \frac{1}{R_{n,i}} \end{bmatrix}, \tag{2.64}$$

where

$\sum_{n=1}^{n} \frac{1}{R_{n,i}}$ is the sum of thermal conductances $1/R_{\text{th}}$ connected to a particular node.

The loss matrix **P** is defined as

$$\mathbf{P} = \begin{bmatrix} P_1 \\ \vdots \\ P_n \end{bmatrix}. \tag{2.65}$$

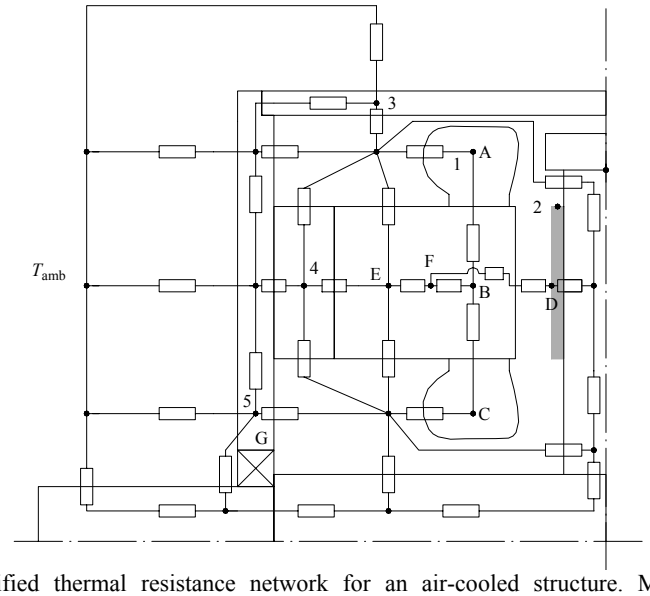

Fig. 2.23. Simplified thermal resistance network for an air-cooled structure. Most of the thermal resistances result from several parallel-series connected thermal resistances. The nodes labelled A to G represent the points indicating where the power losses are generated (Parviainen et al., 2004b).

The thermal resistances in a thermal resistance matrix may be classified into following categories

- Thermal resistances due to convection and radiation on the surfaces
- Thermal resistances due to conduction inside the solids
- Contact resistances over the joints

To define thermal resistance, the simplest form is the thermal resistance due to conduction. Its value is related to the thermal conductivity of the material, which is often a known quantity

$$R_{\text{th,cond},i} = \frac{l_i}{\lambda_i S_i}, \tag{2.66}$$

where

l_i is the length of a particular path described by a thermal resistance
λ_i is the thermal conductivity of the material

Thermal conductivities for the solids used in electrical machines can be considered to be constants with respect to the temperature, even though the thermal conductivity of the electrical steel also varies with the temperature. However, variation has a minor role in heat transfer and thus a constant value may be introduced. The thermal conductivity of air and water depends strongly on the temperature, thus the solution of (2.63) must be found iteratively. Table 2.3 gives some typical values for the thermal conductivities of solid materials used for electrical machines.

Table 2.3 Thermal conductivities of materials used in electrical machines.

Material	λ [W/mK]
Electrical steel M600-50A (in plane)	38.7
Electrical steel (perpendicular to plane)(Kylander, 1995)	3.7
Copper wire (along the wire)	395
Permanent magnet (Nd-Fe-B)	9
Slot insulation material	0.2
Rotor disk (Construction steel)	50
Frame material (Construction steel)	50
Glue used to fix PM's (Araldite AV 138)	0.34

On the surfaces, the thermal resistances due to radiation and convection are connected parallel. The heat transfer from a particular surface to the ambient may thus be described by using a thermal resistance, which takes into account both physical phenomena. The contribution of the radiation inside the machine is often less important since the temperature differences inside the frame are relatively small and the emissivity of the surfaces is low. Thereby, the heat transfer coefficient describing the convective heat transfer from the internal surfaces of the machine often includes the contribution of radiation too. With a known surface area and a known heat transfer coefficient, the corresponding thermal resistance for the particular surface is given by

$$R_{\text{th,con},i} = \frac{1}{h_i S_i}. \tag{2.67}$$

Without performing any experiments, accurately defining the thermal contact resistances remains problematic since the contact resistances between the different machine parts depend on the surface roughness, material and pressure (Incropera, et al., 1996). The values of the contact resistances may also be influenced by manufacturing tolerances. The contact resistances between the different parts may be modelled with equivalent air-gaps, even though more advanced approaches are developed. In this study, the thermal resistances for a particular joint are regarded as equivalent air-gaps and are defined as

$$R_{\mathrm{th,contact},i} = \frac{l_{\mathrm{agap},i}}{\lambda_{\mathrm{air},i} S_i}, \tag{2.68}$$

where

$l_{\mathrm{agap},i}$ is the length of the equivalent air-gap between the parts,
$\lambda_{\mathrm{air},i}$ is the thermal conductivity of air

Guidelines for evaluating the values of the individual thermal resistances for electrical machines are introduced e.g. by Kylander (Kylander, 1995). However, the given model is developed for radial-flux machines and requires some modifications in the parameter definitions if to be used for axial-flux machines. Furthermore, the individual thermal resistances depend on the employed manufacturing technique. For this reason, it may be necessary to adjust the developed thermal models based on empirical test results, as it is proposed in this study.

2.4.3. Main heat transfer path

For axial-flux machines with a one-or-two-stators-plus-one-rotor configuration, the stator can be attached to the bearing shield by using bolt joints. This construction may be achieved by welding an additional steel plate to the stator yoke, illustrated in Fig. 2.24 (a). Here, the main heat flux flows from the stator winding through the stator iron into the stator fixing plates and finally through the bearing shields into the coolant. This assumption is valid if the air circulation inside the frame is weak, i.e. there is no external air blow through the frame and the rotor peripheral speed is low. Consequently, the thermal resistances along this heat flux path, illustrated in Fig. 2.24 (b), most contribute to the operational temperature of the machine.

The first major thermal resistance, labelled resistance A in Fig. 2.24 (b), is caused by slot insulation between the copper and stator iron. The slot insulation material is a relatively good insulator for the heat transfer, as may be seen from Table 2.3. Furthermore, due to the rough surface of the slot cavities are generated between the insulation material and the slot wall. Depending on the manufacturing technique, these cavities are partly or fully filled with resin. The joint between the stator yoke and the fixing plate forms the second major thermal resistance, labelled resistance B in Fig. 2.24 (b). If the plate is welded to the stator yoke modelling the joint is inaccurate without measurements. Heath transfer through the joint is characterised by the smoothness of the stator yoke lamination and by manufacturing considerations such as the welding quality. Especially with coated laminations cavities may occur inside the joint due to vaporisation of a coating material. Such cavities in turn reduce the thermal conductivity of the joint. The third major contact resistance, labelled resistance C in Fig. 2.24 (b), appears between the fixing plate and the bearing shield and is basically a pure contact resistance characterised by the surface qualities of the fixing plate and the bearing shield as well as by the obtained pressure.

In order to achieve a good heat transfer rate from the winding to the ambient, the thermal resistances along the path described previously should be minimised. Using a proper insulation

may minimise the thermal resistance between the stator winding and the stator iron, i.e. a proper thickness for the slot insulation material should be selected the slot surface should be manufactured as smooth as possible. In order to remove the heat efficiently from the stator iron, there should be a good contact between the stator lamination and the fixing plate. This can be achieved by using large welding joints and by minimising the effective air-gap between the stator yoke and the plate.

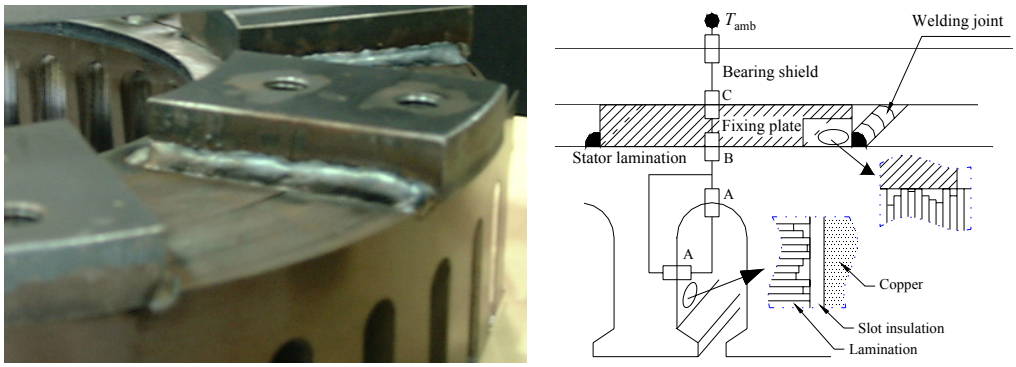

(a) (b)

Fig. 2.24. (a) Steel plates used to fix the stator to the bearing shield. (b) Schematic presentation of heat transfer path from the winding to the bearing shield.

2.4.4. Heat transfer in the air-gap

The temperature of the permanent magnets is mainly depending on the heat transfer between the stator and the rotor in the air-gap region since the permanent magnets are faced directly towards the air-gap. An air-gap heat transfer coefficient with reasonable accuracy is needed. There is an obvious lack of information regarding the thermal modelling of axial-flux machines, since appropriate semi-empirical correlations to define the heat transfer coefficient for the air-gap region of an axial-flux machine are not available.

The structure of an axial-flux machine with an interior rotor may be considered to be comparable to a heat transfer problem with enclosed rotor-stator system (Sahin, 2001). For smooth rotor and stator surfaces, the enclosed rotating disk taking into consideration the friction factor is studied by (Daily et al., 1960). In Daily's study evaluating the heat transfer coefficient is possible based on the Chilton-Colburn analogy. Empirical results and correlations for the heat transfer between a smooth rotating disk and a stationary heated disk have also been reported. However, these results are not quite valid for the application discussed here, since, for example, for the results discussed in (Yuan et al., 2003) the rotational speed is higher and the minimum air-gap used in the measurements is 5 mm, which may be too large to be used for the low-speed PM machines. In the analysis, the heat transfer coefficient for the air-gap is calculated based on the Reynolds number *Re* and the corresponding Taylor number *Ta* (Sahin, 2001)

$$Re_{\text{agap}} = \frac{vg}{\nu_{\text{air}}}, \tag{2.69}$$

where

v is the circumferential speed the rotor,

ν_{air} is the kinematic viscosity of air.

The corresponding Taylor number *Ta* is

$$Ta = Re_{\text{agap}}^2 \frac{g}{r}. \tag{2.70}$$

Based on (2.70) the corresponding Nusselt number *Nu* can be evaluated by using the relations

$$Nu = \begin{cases} 2 & \text{if} \quad Ta < 1700 \\ 0.128 Ta^{0.367} & \text{if} \quad 1700 < Ta < 1 \cdot 10^4 \\ 0.409 Ta^{0.241} & \text{if} \quad 1 \cdot 10^4 < Ta < 1 \cdot 10^7 \end{cases}. \tag{2.71}$$

Finally, the heat transfer coefficient *h* for the air-gap can be calculated as

$$h = \frac{Nu \lambda_{\text{air}}}{g}, \tag{2.72}$$

Since the surfaces of both the rotor and stator are not smooth, the heat transfer in the air-gap an axial-flux machine may be improved similarly as it has been discussed previously the radial-flux machine (Negrea et al., 2001; Saari, 1998). This is due to two mechanisms. Firstly, the effective air-gap area is increased. Secondly, the rough surfaces due to the slotting on the stator side and due to the edges of the permanent magnets on the rotor side may lead to an enhancement of the turbulence level of the flow.

2.4.5. Water cooling

For one-rotor-two-stators arrangements the main heat removal path is through the bearing shields into the ambient as it has been discussed previously. As a result for this case, arranging the external cooling directly into the vicinity of the stator yokes would be appropriate. This may be done by milling water ducts into the bearing shield or by fixing an external water duct on the shield.

In order to find the thermal resistance from the bearing shield to the coolant, the heat transfer coefficient between the surface and the coolant have to be evaluated. The analysis is started by calculating the corresponding Reynolds number Re_{D} for the structure used with the known velocity of the coolant.

$$Re_{\text{D}} = \frac{v_{\text{m}} D_{\text{h}}}{\nu}, \tag{2.73}$$

where

v_{m} is the mean velocity of the coolant fluid
D_{h} is the hydraulic diameter of the channel.

The hydraulic diameter for a rectangular duct is given by

$$D_{\text{h}} = \frac{4 S_{\text{cross}}}{l_{\text{wet}}}, \tag{2.74}$$

where

S_{cross} is the cross-sectional area of duct
l_{wet} is the wetted perimeter.

On establishing the state of the flow based on (2.73), the corresponding Nusselt number *Nu* for the fully developed laminar flow can be found from the tables given for rectangular ducts

(Incropera, et al., 1996). In the case of a turbulent flow the first approximation for the Nusselt number can be calculated from equation

$$Nu = 0.023 Re_{\mathrm{D}}^{0.8} Pr^{0.3}, \tag{2.75}$$

where
Pr is the Prandtl number.

One way of implementing a cooling channel is to fix the channel to be an external part of the bearing shield, similarly as it has been done for the prototype machine. In this case, the stator fixing bolts may be left inside the cooling channel, Fig. 2.25. Considering the heat transfer, this may be an appropriate solution since the bolt ends act as turbulators enhancing the heat transfer. Furthermore, the effective heat transfer area is increased. As a disadvantage, the turbulators increase the channel's friction factor and thereby more pumping power is required to establish the flow. Bilen (Bilen et al., 2002) studied the effects of a rectangular turbulator with different orientation angles on the heat transfer characteristics of a rectangular duct. The problem reported is, basically, similar to the problem discussed here and the results show that, unlike with a smooth duct surface, the rectangular blocks in the cooling channel may increase the Nusselt number by a factor 1.4…1.8. These results are obtained for the Reynolds numbers 7500 $< Re_{\mathrm{D}} <$ 30000. The inlet of a coolant into the channel can be arranged to act as an impinging jet, further affecting the average heat transfer coefficient of a duct. Due to these modifications, it may be stated that (2.75) underestimates the actual Nusselt number, causing that the actual heat transfer is better than the estimated one.

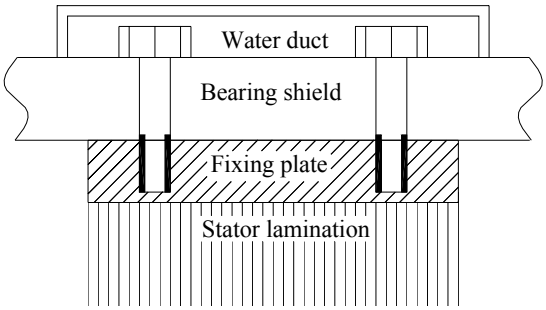

Fig. 2.25. Cross-sectional view of a water duct fixed on the bearing shield of the test machine.

2.4.6. Power losses

Power losses are injected into the particular nodes labelled A-G in Fig. 2.23. In a model the copper losses are separated into three parts

- Copper losses in outer end-windings
- Copper losses in copper bars in slots
- Copper losses in inner end-windings

The iron losses are described as losses in the stator yoke (node E) and teeth (node F). Iron losses are calculated according to (2.37). Copper losses are distributed to nodes A, B and C. Losses in node A represent copper losses in the end-winding on the outer radius of the stator. Losses in node B represent copper losses in slots and losses in node C represent copper losses in the end-winding on the inner radius of the stator. Copper losses are calculated based on Egn. (2.31). The bearing losses are considered to be generated in the node G. The stray load losses are distributed evenly into the nodes E and F.

2.4.7. Thermal model as part of analytical design procedure

The developed thermal model is implemented to be part of the analytical design procedure. Based on the temperatures obtained from the thermal model, the material properties of the permanent magnets (remanence flux density) and the phase winding (resistivity) are recalculated. The machine is redesigned using the updated parameters and new machine parameters are distributed for the thermal model. The iteration is continued in a loop as long as the desired accuracy is reached. Fig. 2.26 shows the flowchart of the used analytical design procedure including the thermal model.

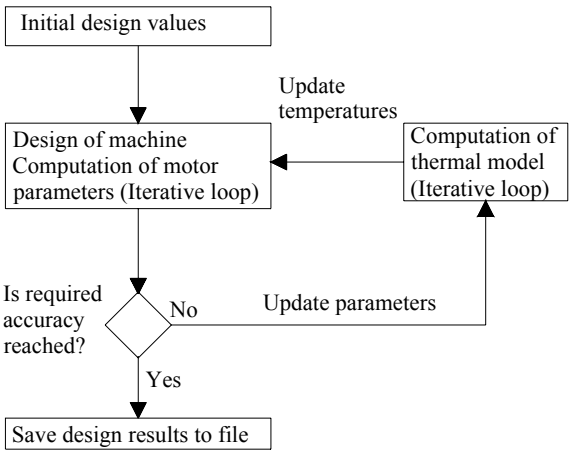

Fig. 2.26. Design procedure including thermal model.

2.5. Summary

In chapter 2 the main considerations related to the analytical modelling of axial-flux permanent-magnet machines are provided. An analytical design procedure using the quasi-3D computation method has been developed. This procedure may be used together with the thermal model described. Since in this study analytical design procedure is mainly considered for preliminary machine design purposes, some simplifications are included in the described computation model. Particularly, the discussion of the reluctance network and the thermal resistance network has been limited. Despite of the simplifications, a reasonable accuracy in the computation results can be expected.

For the thermal modelling of axial-flux machines, some uncertainties in the parameter definitions are remaining. This is because, in practise, to verify the parameters performing measurements with several machines is required. This would demand excessive work efforts and the construction of several prototype machines, which was not within the scope of this thesis. Furthermore, it seems that there are no correlations developed for the purpose of defining the heat transfer coefficient in the air-gap of an axial-flux machine. The development of appropriate correlations may be considered to be one of the most relevant needs for future research in the field of thermal modelling of the axial-flux permanent-magnet machines.

3. Prototype machine and test results

Using the theory given in previous chapters a prototype machine was designed and manufactured. The prototype constructed is not a result of any optimisation process. With the prototype machine the operational results generated by the developed analytical design tool have been verified. The prototype machine is an axial-flux permanent-magnet machine with one-rotor-two-stators configuration. The stators are operating electrically in parallel in star connection by default. This configuration may lead to unbalanced loading between the stators, thus the air-gap has to be adjusted. The nominal power of the machine is 5 kW and the nominal rotational speed is 300 min^{-1}. The magnets are Neodymium-Iron-Boron magnets, manufactured by Neorem Magnets Oy. The material properties of the magnets are given in Appendix A3. The magnets are glued on the surface of the solid-iron rotor disk, which is manufactured of construction steel S232JR. The magnet shape is sinusoidal (Parviainen et al, 2004a). The material of the stator core is a fully processed electrical steel sheet M600-50A. The machine winding type is a conventional double layer lap winding for which the number of slots per pole and phase is equal to one. The main parameters of the machine are listed in Table 3.1.

Table 3.1. Main parameters of the prototype machine.

Parameter	EXPLANATION	Value
P	Rated power	5 kW
n	Rated speed	300 min^{-1}
T	Rated torque	159 Nm
U_{ph}	Rated phase voltage	230 V
E_{PM}	Permanent-magnet induced phase voltage	211 V
I_{ph}	Rated phase current	8.4 A
l_{PM}	Thickness of PM	4.0 mm
B_{r}	PM's remanence flux density, 100 °C	1.05 T
H_{ci}	PM's intrinsic coercivity, 20 °C	2400 kA/m
G_{PM}	Mass of PM's	2.1 kg
Q	Number of stator slots	36
p	Number of pole pairs	6
g	Length of the air-gap per stator	1.5 mm
D_{out}	External diameter of the stator stack	328 mm
D_{in}	Internal diameter of the stator stack	197 mm
N_{ph}	Number of coil turns in series per phase	840

The prototype machine was designed particularly for laboratory test use (Parviainen et al., 2003b). The constructed machine allows modifying the machine structure without having to consider an excessive machinery. The rotor structure, shown in Fig. 3.1, allows changing the magnets without the rotor disk needing full reinstallation because the magnets are firstly glued

to additional iron plates, which are then bolted to the rotor core. This benefits the study of the effects of different magnet shapes. If needed, the whole rotor disk may be changed without changing the shaft because the rotor disk is fixed to the shaft via bolt joints. A non-laminated rotor disk, manufactured of magnetic iron alloy, renders possible using the machine as a single-sided machine too. This is based on the fact that a 20 mm + 5 mm thickness for the rotor iron is enough to keep the flux density level in the rotor iron below the saturation value also in single-sided operation mode. Furthermore, the mechanical structure of the prototype machine, including deep groove ball bearings, is rigid enough to handle the attractive force between the stator and the rotor disk. This force is 7.3 kN per stator according to the performed 3D FEA under load condition with nominal 1.5 mm air-gap. It must be noted that in normal operation conditions the presence of another stator mostly cancels out the net attractive force between the rotor and one stator. However, if unbalanced loading occurs between the stators due to the manufacturing tolerances, the net axial force affecting the rotor structure is not necessarily equal to zero.

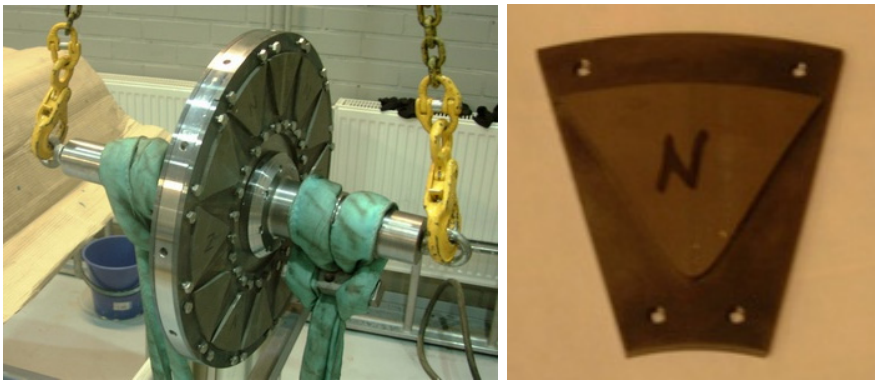

Fig. 3.1. Rotor in magnet installation sequence and one of the magnets glued onto the support plate (seen on the right below a magnet) by the magnet manufacturer.

In order to align the rotor exactly between the stators, a special bearing nut arrangement has been introduced. The bearing nuts, located at both ends of the shaft, make possible to change the rotor position inside the machine without opening the frame. This structure is suitable for purposes when the influence of the rotor misalignment on the performance of the machine is to be studied. Furthermore, considering the assembling of the machine, with the aid of the bearing nuts the stator and the rotor can be easily detached, if these parts snap together as it may happen accidentally during the machine construction.

Both stators of the prototype machine were manufactured of fully processed electrical steel sheet using a laser cutting method and are fixed to the bearing shields by bolt joints. Each of the stators includes 36 slots. Due to the manufacturing technique, the obtained stator lamination stacking-factor was poorer than expected during the designing process, being only 0.92. The stator diameter ratio was selected to be near to the theoretical optimal value. For the prototype machine it was 0.6, which, however from the winding manufacturing point of view, is shown to be slightly too small. Fitting the end-winding on the inner radius of the machine into the available space turned out to be rather time consuming. One of the machine stators is shown in Fig. 3.2 before and after winding.

In the stator winding the number of coils per pole and per phase is equal to one. Each of the phase coils includes 140 turns and the total number of phase turns is then 840. Both ends of the phase windings of the stators are available in a connection box. This, as a result, renders possible changing the machine electrical connection from star connection to delta connection and changing the connection between the stators from parallel to series, or running the machine by using one stator only. The machine is designed to operate in star connection while the stators

are connected in parallel but it is possible to run the machine in different connections by modifying the machine operating point.

During the manufacturing of the machine there was a slight error in the construction of the permanent magnets. Each magnet is composed of two independent blocks and the joint is parallel to the radius of the machine. The joint reduces the flux produced by the PM causing an unexpected flattened top for the measured no-load phase voltage and having also an effect on the cogging torque of the machine. Since the permanent magnet shape, in its basic form, produces a very low cogging, it may be observed that the rotor, while being rotated manually, will align into such position for which the magnet joint is exactly below the slot opening.

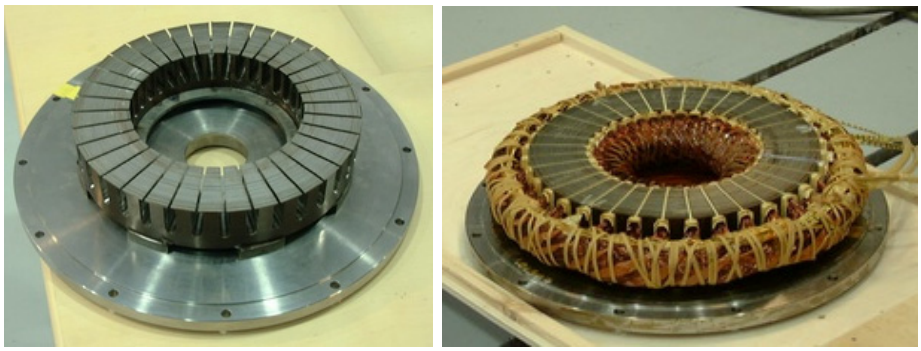

Fig. 3.2. One of the stators before and after winding.

The temperature measurements were carried out with 20 Pt-100 temperature sensors. A total amount of fourteen temperature sensors were mounted into the frame and the rest six sensors in the phase windings. Fig. 3.3 shows the locations of the temperature sensors within the frame of the machine. It must be noted that a few temperature sensors should have been inserted also in the rotor disk for the rotor to achieve an accurate temperature profile. For the construction of the prototype machine this has been omitted and therefore the rotor temperatures are measured on the surface of the rotor by using an infrared measurement device.

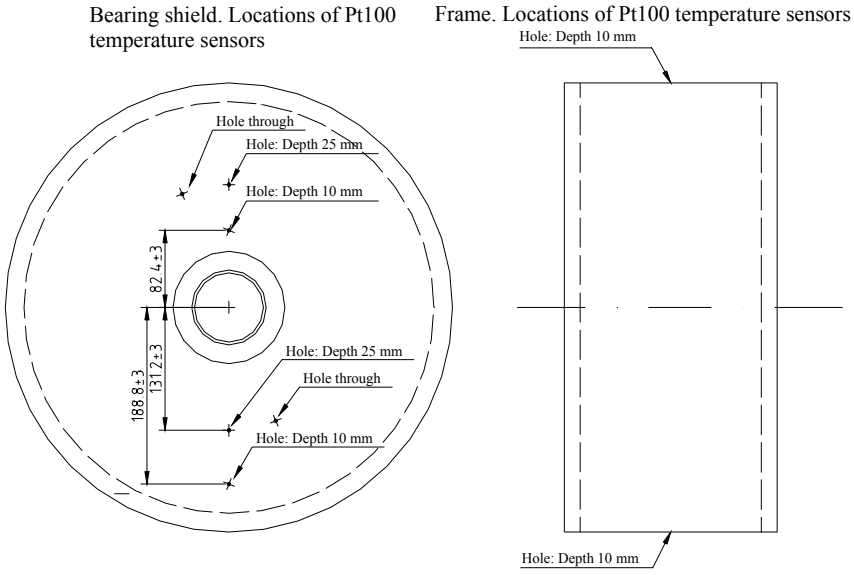

Fig. 3.3. Locations of Pt-100 temperature sensors in the machine frame.

3.1. Measurement set-up

The set-up arranged for the test is described in Fig. 3.4 and in Fig. 3.5. The machine under test has been fed by a variable speed frequency converter (ABB ACS600) and loaded by a DC machine. The shaft torque has been measured by a torque transducer (Vibro-meter, model: TORQUEMASTER TM-214). The torque transducer is connected via a reading unit (Vibro-meter, model: DCU 280) to a PC, which collects the data from a power analyser and from the temperature sensors. The electrical power has been measured by a power analyser (Yokogawa PZ4000) and the temperature has been registered in twenty points by Pt-100 temperature sensors. The temperature values are stored up in a PC by a reading unit (FlukeHydra). Immediately after stopping the machine, the surface temperatures of the shaft, rotor disk and the permanent magnets are received by an infrared temperature sensor (SENSYCON, model: SYCST6LSD). In order for the infrared measurement device to get reliable temperatures from the steel surfaces, the corresponding locations have been marked by spots of black matt paint. The value of the emissivity of the black matt paint has been fixed to the value of 0.9. The readings of the infrared measurement device have been confirmed by a contact thermometer. Table 3.2 shows the accuracies of the measurement devices.

Table 3.2. Accuracies of the employed measurement devices.

Device	Accuracy [%]
Torque transducer: Vibro-meter, model: TORQUEMASTER TM-214	0.2
Current transformer: GSA 120 A 50	0.2
Power analyser: Yokogawa PZ4000	0.1

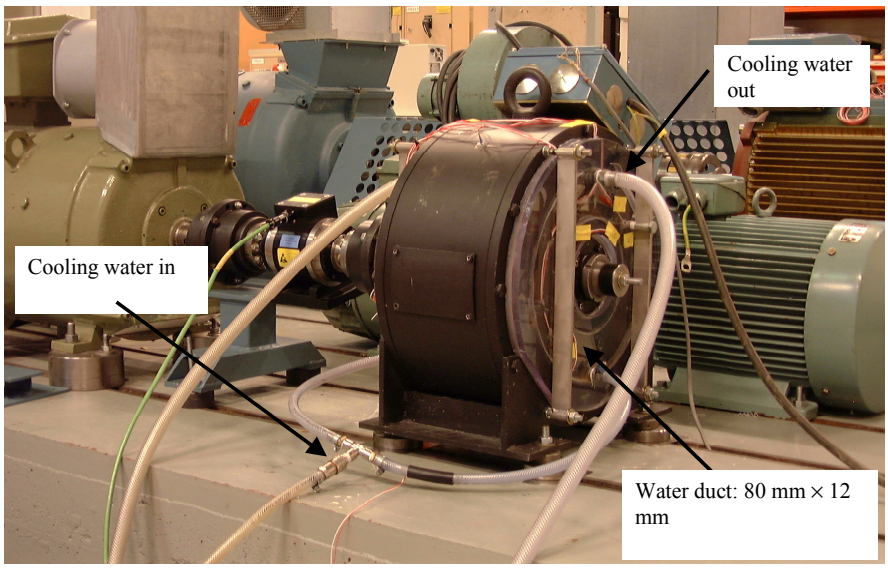

Fig. 3.4. Prototype machine in the test bench with external water ducts fixed on the bearing shields.

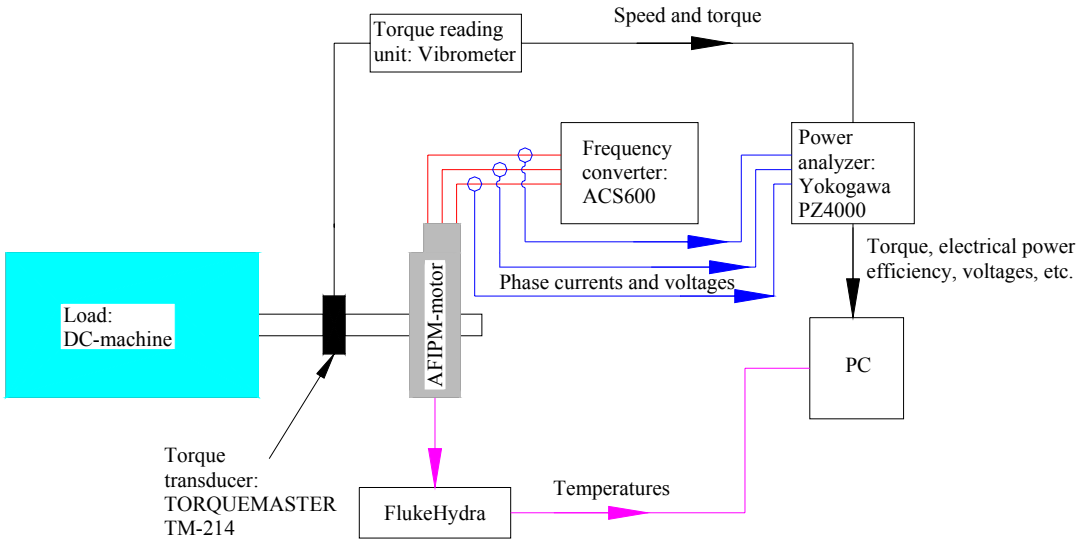

Fig. 3.5. Measurement set-up.

3.2. Motor parameters

The motor parameters are obtained from the identification run made by the frequency converter (ABB ACS600). The procedure used by the ACS600 for defining the machine parameters is described by Luukko (Luukko, 2001).

Table 3.3. Calculated and measured values for the 5 kW, 300 min^{-1} prototype machine.

Parameter	Analytical	Measured
L_d [H]	0.064	0.055 (Estimated by the inverter)
L_q [H]	0.065	0.06 (Estimated by the inverter)
R_{ph} [Ω] (DC-resistance)	3.7	3.7
Load angle	27°	25° (Estimated by the inverter)
$E_{ph,PM,rms}$ [V]	211	211

Table 3.3 shows that a good agreement is achieved between the measured and the calculated values for the no-load phase voltage, load angle and phase resistance. The no-load phase voltage is calculated analytically according to Eqns. (2.25) and (2.27), inductances are calculated according to Egns. (2.46)-(2.49) and (2.54), load angle is calculated based on Eqn. (2.55a) and finally the result obtained for the phase resistance shows that Eqn. (2.31) is suitable to be applied also for the considered axial-flux PM machines. However, the values for the inductance differ to some extent. In the direct axis inductance the difference is approximately 16 % whereas on the q-axis the difference is 8 %.

Also the d-axis synchronous inductance has been determined by using a no-load test. The motor has been connected to a 50 Hz grid and the supply voltage amplitude has been varied. As the induced no-load voltage due to permanent magnet excitation is known, it is possible to calculate the synchronous inductance from the measured line voltage and phase current and known no-load voltage. The result obtained is 0.057 H, which is in agreement with the values reported in Table 3.3.

3.3. Induced back-EMF

Adjusting of the rotor position could be done by comparing the amplitudes of the induced back-EMF for both stators. With the bearing nuts the rotor position could be fixed into such location for which the amplitudes of the fundamentals are equal for both of the stators. A comparison between the measurement and the computations results is given in Fig. 3.6 for the machine operating in steady state at rated load conditions. The comparison shows that the curvatures are in good agreement expect for the values on the top of the measured curve, which is flattened. This flattening is a consequence of the manufacturing method of the magnets mentioned above. The results obtained for the fundamental component of the induced back-EMF agree well with the calculated results, as shown in Table 3.3.

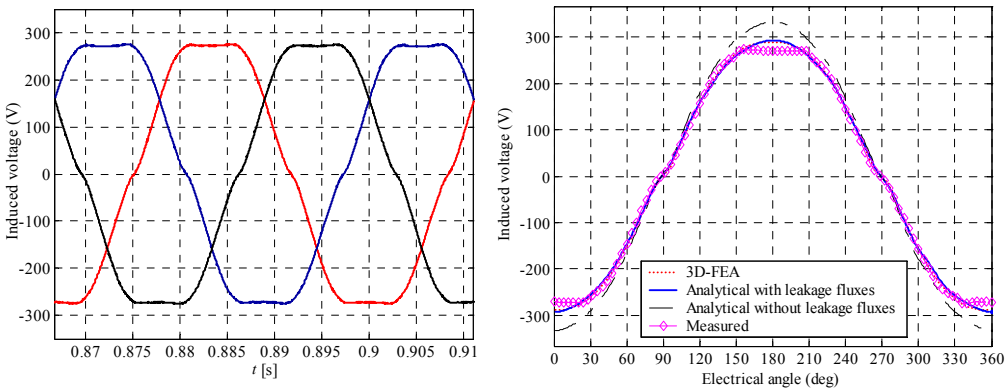

(a) (b)

Fig. 3.6. (a) Measured phase voltages for the machine having reached its operation temperature. The permanent magnets are operating at a temperature of approximately 95 °C. (b) Comparison with the calculated values.

3.4. Cogging torque

The torque has been measured by using 50 Nm torque transducer, the prototype machine being rotated at a 10 min^{-1} speed and the speed controlled DC machine being operated as a motor. The rotation speed corresponds to the electrical frequency of 1 Hz for the prototype machine. In Fig. 3.7 the measured and the calculated cogging torque are compared. It may be seen from Fig. 3.7 that the amplitude of the measured cogging torque is almost 100% larger compared to the result obtained with the 3D FEA and about 40 % larger than the result obtained with the analytical computations. The significant difference between the calculated and the measured values arises from the influence of the permanent magnet radial joint, which increases the cogging torque. For this reason, the use of magnets for which the possible joint is in parallel with the slot opening should be avoided, if a high-torque quality is required. Fig. 3.7 also shows that the major contribution to the cogging torque is by the 6^{th} harmonic. This is an obvious result since for the prototype machine the number of slots per pole and phase is equal to 1.

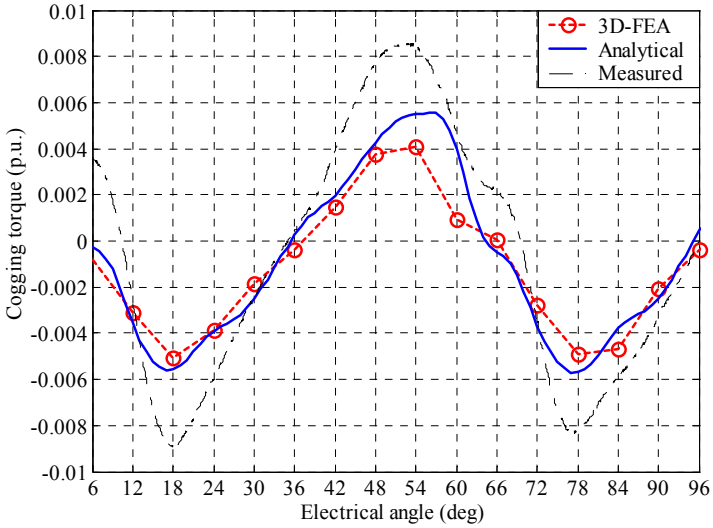

Fig. 3.7 Calculated and measured cogging torque.

3.5. Efficiency

The motor efficiency has been calculated based on the measured electrical and mechanical powers. Fig. 3.8 illustrates the behaviour of the motor efficiency as a function of time in a test run for which the cooling of the machine was arranged by natural convection and radiation. This cooling method, in particular, has been in the primary design criterion for the prototype motor. The efficiency is calculated according to Egn. (2.56) and its value is at steady state 89.6 % whereas the measured efficiency is 89.2 %. A reasonable agreement between the results is thus found. The measured efficiency is determined from the measured electrical power and from the measured mechanical power.

The other test runs were performed with the external water duct being fixed on both bearing shields. Fig. 3.9 compares the computations and the measurements as a function of load with coolant flow being 2.5 kg/min. In this comparison, the parameters of the analytical computation model are fixed to the design values of the prototype machine. The computed efficiency tends to be slightly lower than the measured efficiency if the machine load is below 6 kW, and the opposite is valid for machine loads above 6.5 kW.

Fig. 3.9 shows also that a rapid reduction in the efficiency is obtained when the output power exceeds 6 kW. This may be explained by the typical behaviour of permanent-magnet machines. As the permanent magnet temperature increases, the remanence flux density of the permanent magnet decreases. Thereby, if the original stator flux linkage is maintained, more magnetizing current in the stator is needed causing more copper losses. As the copper losses increase, the temperature starts to grow up, causing further reduction in a permanent magnet remanence and an increment in the phase winding resistance. These phenomena further increase the power losses in the stator winding. As a certain output power is exceeded, the described self-feeding phenomenon happens very rapidly and only a little percent change in the output power may cause tens of percents increment in the temperature rise if the cooling is kept the same. For the prototype machine this is the case at an output power of approximately 7 kW with the water-cooling method, Fig. 3.10. The maximum available output power is 7.4 kW if the maximum allowed stator-winding temperature is limited to the value of 150 °C, which is the design value for the slot insulation. On the other hand, the phenomena described causes that the time required to achieve a steady state is long, Fig. 3.8.

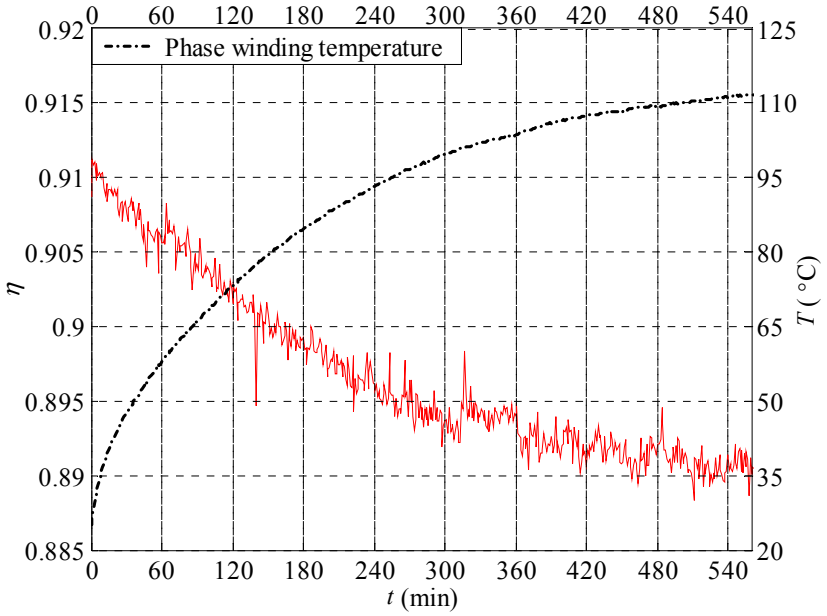

Fig. 3.8. Input - output measurement-based efficiency as a function of stator temperature, the machine cooling being arranged by radiation and natural convection. 5 kW load is applied at rated speed. The instantaneous steps in the efficiency curve are probably resulting from the voltage fluctuations in the laboratory supply grid. Such a phenomenon occurs for example with a time interval 310 min < t < 360 min.

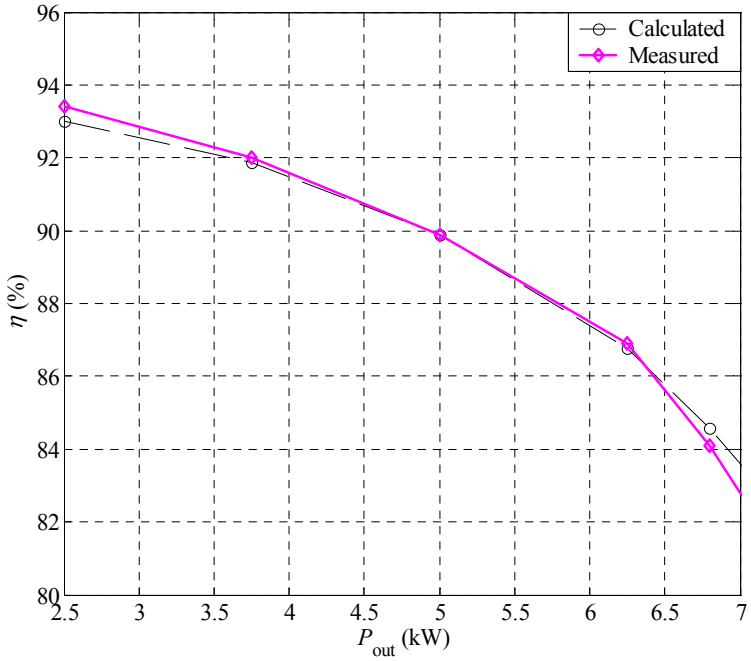

Fig. 3.9. Machine efficiency as a function of the output power. Results for the water-cooled machine with a coolant flow of 2.5 kg/min. Measured at rated speed. Rated power is 5 kW for the machine. Please note that the efficiency starts to decrease if smaller output powers than 2.5 kW are employed.

3.6. Temperature measurements

The measured and calculated temperatures in different parts of the machine are compared in Tables 3.4-3.6.

Table 3.4. Calculated and measured temperatures for the air-cooled machine version.

Point	Calculated [°C]	Measured [°C]
1 (Outer end-winding)	107	110
2 (Magnet)	95	98
3 (Frame)	72	73
4 (Fixing plate)	84	85
5 (Bearing shield)	78	80

Table 3.5. Calculated and measured temperatures for the water-cooled machine version with coolant flow of 1 kg/min, P_{out} = 5 kW.

Point	Calculated [°C]	Measured [°C]
1 (Outer end-winding)	53	52
2 (Magnet)	42	41
3 (Rotor)	42	40
4 (Frame)	28	30
5 (Fixing plate)	26	26
6 (Bearing shield)	25	25
7 (Shaft, N-end)	32	32

Table 3.6. Calculated and measured temperatures for the water-cooled machine version with coolant flow of 5 kg/min, P_{out} = 7 kW.

Point	Calculated [°C]	Measured [°C]
1 (Outer end-winding)	98	97
2 (Magnet)	70	70
3 (Rotor)	68	68
4 (Frame)	37	40
5 (Fixing plate)	34	32
6 (Bearing shield)	30	27
7 (Shaft, N-end)	45	44

The computed and measured values in Tables 3.3-3.5 are in good agreement. However, it must be noted that the values of the thermal resistances were adjusted according to the measurement results. This had to be done because of the fact that the prior estimation of the contact thermal

resistances in the machine structure was difficult for the reason that, for these machine types, no previous test results were available.

In Fig. 3.10 a comparison between the measured and calculated temperatures is given with respect to the output power of the machine. The water flow is 2.5 kg/min per cooling channel. Fig. 3.10 shows also a reasonable agreement between the measurement and computation results.

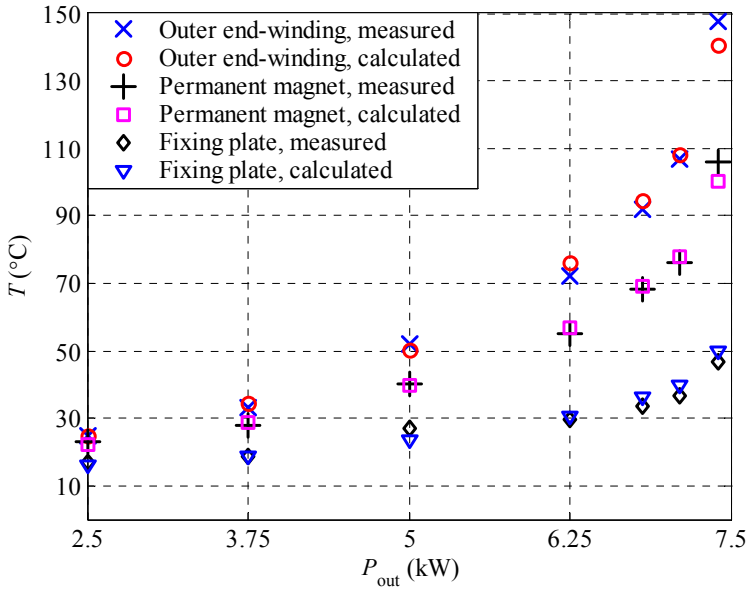

Fig. 3.10. Measured and calculated temperatures as a function of the load for the water-cooled structure with coolant flow of 2.5 kg/min.

3.7. Conclusions

A 5 kW AFIPM machine is designed and constructed. Comparison of the calculated and measured values for the prototype machine shows, generally, a good agreement. The difference in the waveform of the induced back-EMF as well as the difference in the amplitude of the cogging torque can be explained by magnet manufacturing the influence of which on the experimental results may be considered significant. Avoiding the use of permanent magnets for which the magnet joint align directly with the slot opening is recommended, if a high-performance surface-mounted permanent-magnet machine is aimed for. For the thermal modelling the thermal resistances of which were difficult to find accurately were adjusted according to the measurement result obtained at a rated 5 kW load. For the other power ranges in using the same values a good correspondence with respect to calculated efficiency and temperature rise is obtained. However, to be able to define the statistical behaviour for the parameters of the thermal model more tests should be performed, implying of the construction of more test machines. Especially solving the thermal contact resistances for the studied machine structure appears to be a problem.

Based on the results obtained in this study, it is found that the developed analytical design procedure shows a sufficient accuracy for the design of surface-mounted axial-flux permanent-machines and may then be used with reasonable exactness for the design of other, similar axial-flux permanent-magnet machines.

4. Mechanical constrains for axial and radial-flux machines

In the previous chapters a procedure for the electromagnetic design of axial-flux machines has been presented. This chapter presents special considerations of some fundamental aspects with respect to the mechanical structures of the considered permanent-magnet machine types. This study is essential for the further comparative analysis for which – in addition to the electromagnetic comparison – also the practical, mechanical constraints with respect to the machine construction are to be taken into account. The aspects to be studied are:

- Fixing of the stator to the motor frame or to the bearing shield
- Required thickness of the stator yoke
- Tooth dimensions
- Thickness of the rotor disk of an axial-flux machine
- Allowed external radius for the rotors due to centrifugal forces

There is a direct relationship between the fixing of the stator and the volume required for the electrical machine and this has to be taken into account in the calculation of the torque density of the machine. The volume of the axial-flux machine is directly proportional to the thickness of the stator yoke whereas the overall volume of the radial-flux machine shows a quadratic behaviour with respect to the stator yoke thickness. The value of stator yoke thickness is also dependent on the magnetic loading of the machine as well as on the mechanical stiffness of the stator structure. For multi-pole machines the magnetic loading may not be a limiting factor for the stator yoke measures but the minimum stator yoke dimension is determined by mechanical and some practical constraints. The tooth dimensions are determined by the mechanical constraints as well as by the allowable magnetic loading of the machine.

The rotor thickness is also directly proportional to the volume requirements by the axial-flux permanent-magnet machine. Because, as an example, a flat rotor with a large diameter may be mechanically weak and vibrate, this means that the thickness of the rotor disk of an axial-flux machine is an important quantity. Thus a method for calculating this parameter must be found. Finally, the study also considers the mechanical limits due to the centrifugal forces acting on the glue joints of the permanent magnets as well as the rotor iron. The maximum values for the rotor radius at a given rotational speed are presented.

For the purposes of not being a too complex mechanical study, the discussion here mainly focuses on the analytical approach. In practise, the accurate mechanical analysis of an electrical machine should involve the whole machine including the frame structures. Such a study would require the use of mechanical FE software for each design to be such that the mechanical behaviour of the machine could be accurately demonstrated. This would lead to an iterative design procedure since, after having found the mechanical constraints, it may be necessary to perform a new electromagnetic analysis. If then the electromagnetic design shows to be impracticable, the mechanical analysis should be renewed causing excessive computational efforts. For the purposes of comparing the analyses of several machines, comparison based on the use of two different FEA programs is not attractive. Therefore, for this study, it was chosen to rely on the analytical computation methods for mechanical design.

One has to keep in mind that this part of the study was accomplished after the construction of the prototype machine was finished. For this reason, the discussion on the mechanical constraints is provided here, after the prototype machine has first been introduced. The designed prototype offers, however, useful practical information about the manufacturing of AFIPM machines and thus some experiences gained during the process of manufacturing the prototype machine are exploited here.

4.1. Fixing of the stator

For this study, the method for fixing the stator to the frame is relevant since it is one of the basic arrangements in the process of assembling the electrical machine. The stators may be fixed to the frame by

- Gluing (RF and with some precautions in AF)
- Welding (RF)
- Shrink fitting (not usually applicable to axial-flux machines)
- Welding with bolt joints (practical method with AFPM)
- Frameless structures (RF stator stack is fixed to the bearing shield with the stud).

Shrink fitting is often used for radial-flux machines with cast-iron frames since it is reliable solution, easy to do, and allows a good thermal contact between the frame and stator yoke. Gluing may be used in some cases but a glue joint may generate some uncertainties with relation to the mechanical strength and heat transfer. Welding is often an appropriate method to be used with frames manufactured of steel plate. Such frames are usually mechanically weaker than cast iron frames. However, applying these methods to interior type radial-flux machines does not require any additional parts in order to resolve the stator fixing. Furthermore, the stator external diameter may be directly used as the external diameter of the machine, if the machine does not include a frame structure. For the frameless structure the frame pipe is obviously not used.

This does not apply for axial-flux machines. For some types of axial-flux machines, such as TORUS machines, shrink fitting of the stators to the frame or bearing shields is practically difficult or even impossible. The stator(s) of a TORUS type machine may be fixed to the frame by ribs. The stators of a single-stator-single-rotor or two-stators-single-rotor type axial-flux machine may be fixed to the bearing shields by gluing. Alternatively, extra supporting parts may be added to the stator yokes in order to obtain a good mechanical strength for the joint. Such a supporting structure is illustrated in Fig. 2.24 (a). The use of additional supporting structures increases, however, the need for more space because the length of the stator is extended. It is, of course, possible to manufacture corresponding holes in the bearing shield and mount the supporting structures into the holes. For economical reasons this may be an unattractive solution since it demands additional work. From this it follows the assumption that the axial length of the AFIRPM type machines has to include also the length of the fixing parts. These fixing parts may be manufactured simply by using rectangular steel bars or alternatively by integrating the cooling channels into the supporting structure, as demonstrated by Sahin (2001), which makes implementing of the additional parts more attractive.

4.2. Thickness of the stator yoke

The thickness required for the stator yoke depends on the magnetic loading of the machine as well as on the mechanical properties. If the number of the pole pairs is small, often the allowable magnetic loading determines the thickness of the stator yoke. However, if the number of pole pairs is high enough the stator yoke may be very thin if it is sized according to the allowed magnetic loading. The mechanical constraints may thus determine the minimum thickness of the stator yoke. The thickness of the stator yoke is dependent on the natural frequency of the stator core in combination with the height of the stator teeth and winding. Thus, a case-by-case study is needed in order to find the regime for which the excitation frequencies due to the air-gap harmonics do no match with the natural frequencies of the stator.

The task of evaluating the natural frequencies of the stator core by using analytical methods is far from straightforward since many variables are to be taken into consideration. For radial-flux

machines studies on the determination of the stator natural frequencies have been reported by Yang (Yang, 1981). For axial-flux machines, the case of a travelling wave ultrasonic motor the operation of which is based on the vibration of the stator presents interesting example. The stator of such machine type is an annular disk similar as for the axial-flux machine type. Hagedorn (Hagedorn et al., 1992; Hagedorn et al., 1993) derives a method for evaluating the natural frequencies of the stators of ultrasonic travelling wave motors with non-constant stator thickness. In this study, a constant thickness for the stator yoke is valid simplifying the evaluation of the natural frequencies and thus an approach based on vibrations of annular disks may be established (Leissa, 1969). Furthermore, the influence of mass of phase winding is added to the computation model. This is achieved by increasing the actual bulk density of the stator material with a portion corresponding to the mass of copper (Appendix A1, Eq, (A.2)). The stator teeth are treated as being an additional mass and it is assumed that the teeth do not contribute to the stiffness of the stator yoke. This assumption is valid only if the lowest mode shapes are considered, as it is the case for this study. Figs. 4.1-4.2 illustrate the lowest mode shape for a radial-flux and axial-flux machine. The analysis is carried out for two different axial-flux and radial-flux machines with the ANSYS™ FE-program.

(a) (b)

Fig. 4.1. (a) Mode shape for an axial-flux machine stator at the frequency of 497 Hz. (b) Mode shape for the radial-flux machine stator at the frequency of 355 Hz. Parameters used in both cases: D_o = 328 mm, Q = 36, y = 40 mm, l_y =19 mm. Structural damping due to the lamination is not included in the computation model.

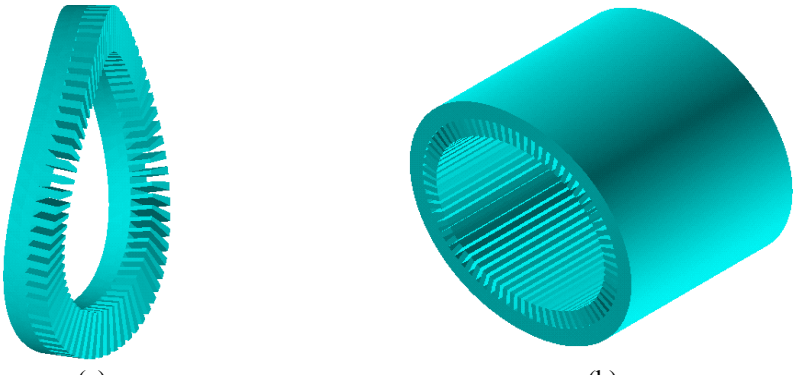

(a) (b)

Fig. 4.2. (a) Mode shape for an axial-flux machine stator at frequency of 317 Hz. (b) Mode shape for radial-flux machine stator at frequency of 283 Hz. Parameters used in both cases: D_o = 0.6 m, Q = 72, y = 40 mm, l_y =40 mm. Structural damping due to the lamination is not included in the computation model.

As can be seen from the results in Fig. 4.1 and Fig. 4.2, the natural frequencies of radial-flux machine stators tend to be slightly lower than they are for axial-flux machine stators if the contribution of the frame structures and windings are not included in the study and the other geometrical parameters (Q, D_o, l_y, y) as well as the material properties are set to be equal. If the study includes consideration of the frame a stiffer RF stator structure is to be expected leading to higher natural frequencies. Considering the axial-flux case, however, fixing of the stator to the bearing shield by bolt joints may be expected not to make the actual structure much stiffer.

Irrespective of the impreciseness of the analytical expressions used to calculate the natural frequencies of the stator (Vijayraghavan, 1999), a frequency area for the excitation to occur may be found. This is a good starting point and may be used here for comparison purposes without making the comparative study too complicated. Appendix A.1 reports the equations used to estimate the natural frequencies of the stators for both the RF and the AF machines. Table 4.1 compares the natural frequencies calculated both with the FEA and with the analytical approach. Comparison of the values shows that there is a slight difference between the results gained with the analytical approach and those obtained by the structural FEA. However, this difference is rather insignificant and the employed equations are thus reliable to be used for predicting the natural frequency of the stators under consideration (with free body assumption).

Table 4.1. Comparison of the computation results for the natural frequencies of the stators using the FEA and analytical method.

	Analytical: AF	FEA: AF	Analytical: RF	FEA: RF
f_n (Hz) (for Fig. 4.1 structures)	490	500	340	350
f_n (Hz) (for Fig. 4.2 structures)	320	320	270	280

A further, interesting consideration on the natural frequencies of axial-flux and radial-flux machine stators is related to the staking factor. The laminated structure generates some structural damping in the system. The stator stack of a radial-flux machine may be pressed very tightly after punching, thus a typical staking factor is around $k_{Fe} = 0.98$. With an axial-flux machine a lower value for the stacking factor is to be expected due to the procedure of manufacturing the stator and the structural damping of the stator of a radial-flux machine may be assumed to be weaker than that of an axial-flux machine. In this study, this aspect is not further studied.

4.3. Width of the teeth

Another mechanical constraint is due to the tooth width. For radial-flux machine the tooth width is often determined by the magnetic loading and the mechanical aspects. The tooth width is typically approximately one half of the slot pitch, thus the tooth width is equal to the slot width. The slot structures may possibly be narrower but when the slots are very deep and narrow problems may arise as for the stator winding.

For axial-flux machines the tooth width is a function of the stator radius. The number of poles and the number of slots have to be selected such that a certain thickness for the tooth remains on the inner radius of the stator. In this study, for practical reasons due to manufacturing constraints as well as due to the magnetic loading, a minimum of 5 mm is considered. For the radial-flux machines, accordingly, the minimum tooth thickness is fixed to the value 5 mm.

4.4. Thickness required for the rotor disk of an axial-flux machine

The rotor disk of an axial-flux machine is exposed to electromagnetic forces acting in the axial direction of the machine. This phenomenon especially concerns the assembly of the machine since the absence of another stator has as a consequence that the attractive force F between the stator and rotor is significant due to the flux density created by the permanent magnets

$$F \approx \frac{\alpha_{\mathrm{p}} S_{\mathrm{agap}} B_{\mathrm{agap}}^2}{2\mu_0}. \tag{4.1}$$

In Eqn. (4.1) α_{p} is the ratio of an air-gap surface that is covered by magnets of even thickness. Considering the machine assembly or repair work, the rotor disk should be rigid enough to resist the force needed to detach the rotor core from the stator if it occurs that the rotor and the stator get attached together. In such a case, a reasonable sizing constraint is defined for the rotor thickness to be such that the maximum deflection of the rotor disk is a small fraction of the air gap length.

For the analysis, it is assumed that the permanent magnets are fixed on the surface of the rotor disk and they do not support the rotor structure itself. The support of the rotor structure due to the joint between the shaft and the rotor structure as well as the forces caused by the permanent magnets is described in Figs. 4.3 and Fig. 4.4. Due to the end-winding, which is located on the inner radius of the stator, the maximum support radius r_{sup} on which the rotor disk may be fixed to the shaft structure is given by

$$r_{\mathrm{sup}} = r_{\mathrm{in}} - l_{\mathrm{end}}, \tag{4.2}$$

where

l_{end} is the length of end-winding protrusion towards the shaft on the inner radius of the stator.

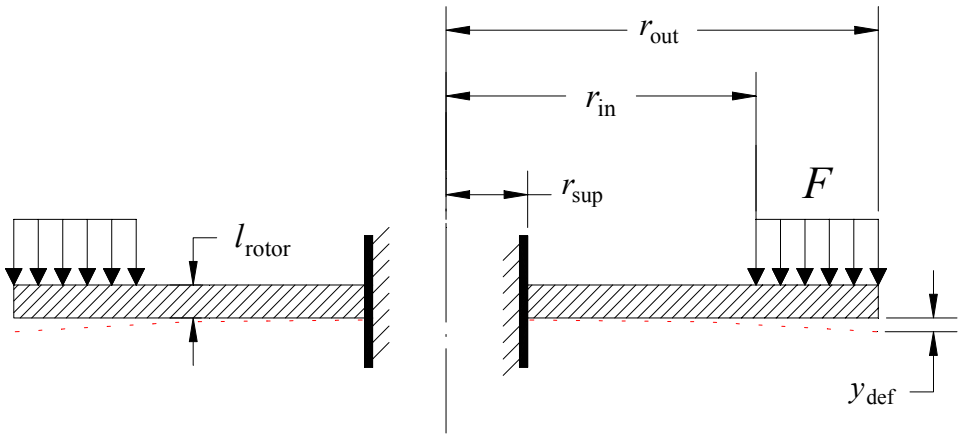

Fig. 4.3. Stiff rotor support, for example the rotor disk is a turned flange on the shaft. The rotor structure of the prototype machine is – more or less – equivalent to stiff rotor structure. In a prototype, however, the rotor disk is fixed with bolts to a turned flange that locates on shaft. This reduces the overall stiffness of the system.

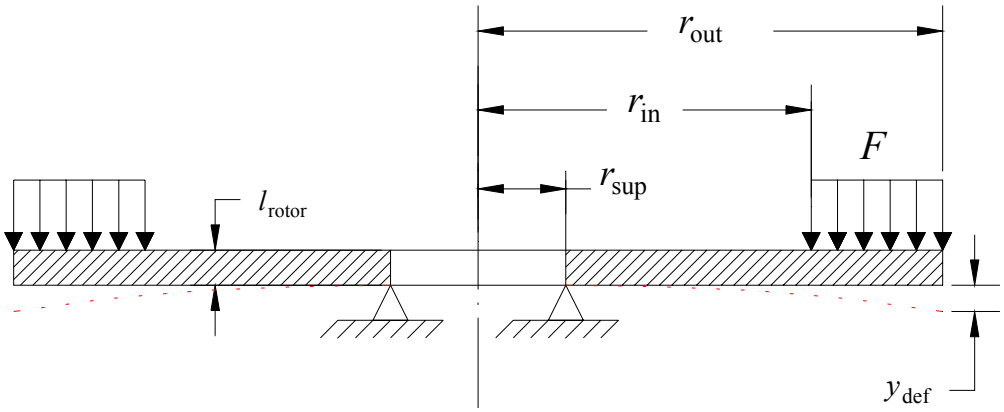

Fig. 4.4. Rotor support is a simple point support (free support) on radius r_{sup}.

Considering the support structures shown in Fig. 4.3 and 4.4, the corresponding equations to calculate the maximum deflection and the maximum stress in the rotor disk due to the static load F are given for example by Young (1989). The equations used in the computation of the maximum deflection y_{def} are reported in Appendix A.2. The calculated deflections for both support cases under similar load conditions may be plotted as a function of the thickness of the rotor disk. The result is illustrated in Fig. 4.5.

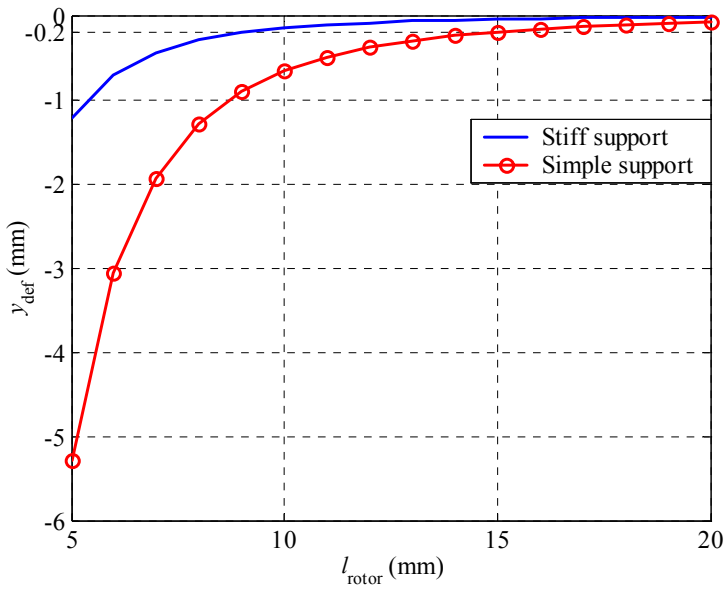

Fig. 4.5. Illustration of the difference between the stiff support and free support solution for one particular structure. l_{rotor} is the thickness of the rotor core. The free support, naturally, gives an considerably higher deflection for the thin rotor skeletons compared to stiff support. r_{out} = 0.164 m, r_{sup} = 0.058 m, r_{in} = 0.098 m, F/S = 0.178 MPa. Rotor deflection y_{def} is measured at radius r_{out}.

In the computations the deflection allowed for the rotor disk is considered to be a fraction of the air-gap length g and is fixed to the value

$$y_{\mathrm{def}} = \frac{g}{10}\,. \tag{4.3}$$

From Fig. 4.5 it may be seen that the free support, naturally, gives an considerably higher deflection on the external radius of the rotor disk. In practise, with the actual rotor fixed to the shaft a support construction is obtained for which the deflection y_{def} lies between the values of the cases discussed above. Thus, applying the worst-case scenario and assuming simple support will be a safe solution for calculating the required rotor thickness based on static load. In the case of Fig. 4.5, a rotor thickness of 16 mm or more will be satisfactory.

4.4.1. Dynamical stability

During machine operation the rotor structure is exposed to excitation due to the harmonics of the air-gap flux density waveform, and an undesired vibration may arise in the rotor structure. In order to avoid vibration the natural frequencies of the rotor, which depend on the dimensions as well as on the materials used for the rotor disk, have to diverse from the excitation frequencies. In the analysis, the rotor disk is treated as a solid horizontal circular plate with thickness l_{rotor} and external radius r_{out}. For such a structure the natural frequency may be approximated analytically as (Timoshenko et al., 1974; Yuang, 1989)

$$f_{\mathrm{n}} = \frac{k_{\mathrm{n}}}{2\pi}\left(\frac{\sqrt{\dfrac{\Gamma}{\rho_{\mathrm{Fe}}}}}{\sqrt{12\left(1-\upsilon^2\right)}}\right)\frac{l_{\mathrm{rotor}}}{r_{\mathrm{out}}^2}\,, \tag{4.4}$$

where

k_{n} is the mode coefficient and indicates relative frequency.
Γ is the modulus of elasticity (for steels typically $2.1\cdot10^{11}$ N/m^2)
υ is the Poisson's ratio (for steels typically 0.3)

In (4.4) the mass of the permanent magnets is taken into account by increasing the bulk density of the rotor iron. Furthermore, the permanent magnets are assumed not to contribute to the stiffness of the rotor plate due to the glue joint.

Assuming a free disk edge, the lowest value for k_{n} is $k_1 = 5.25$ in the case of a circular disk (Young, 1989). If the natural frequency of the rotor is now set to a value that differs from the line frequency of the motor and from the most important harmonics, the required rotor thickness may be found as

$$l_{\mathrm{rotor}} = \frac{2\pi f_{\mathrm{d}} r_{\mathrm{out}}^2}{k_{\mathrm{n}}\left(\dfrac{\sqrt{\dfrac{\Gamma}{\rho_{\mathrm{Fe}}}}}{\sqrt{12\left(1-\upsilon^2\right)}}\right)}\,. \tag{4.5}$$

where

f_{d} is the rotor's lowest vibration mode design frequency which differs from the excitation frequencies

Based on the discussion introduced in Chapters 4.4 and 4.4.1, a comparative study between the static and dynamic analysis may be presented and the rotor thickness may be selected based on a more critical scenario. Since a simple rotor model was assumed, a modal analysis was carried out with the ANSYS FE-program to analyse more practical rotor structures. Fig. 4.6 shows the rotor structures considered here. The rotor disk diameter is 0.4 m whereas the shaft length is 0.2 m and the shaft diameter of 60 mm. The plate thickness is a varying parameter in the analysis. The natural frequencies calculated for the circular plate have been found to correspond to the frequencies based on (4.4). However, if the same analysis is carried out for the plate with shaft hole, Fig. 4.6 (b), - for the shaft and for the hole surface all degrees of freedoms are constrained - the lowest natural frequency of the plate tends to be about 30 % lower. If the shaft is included in the model and if the shaft ends are fixed, the lowest natural frequency is approximately the same as for case (b). Finally, for structure (d), which is considered well corresponding to the practical rotor structure of an axial-flux machine, the lowest natural frequency is found to be about 15 % higher than it is for structure (a) since the fixing structure of (d) increases the stiffness of the system. According to the analysis, it is shown that applying Eqn. (4.4) in the computation of the rotor natural frequencies gives values that are suitable for using with actual rotor structures. Finally, it must be noted that with a thick rotor disk and a thin and long shaft, the opposite outcome is valid since the lowest natural frequencies are caused by vibration of the shaft and not by vibration of the rotor disk. In the analysis the shaft is assumed not to vibrate because it is thick enough.

For low-speed radial-flux machines the dynamical stability of the rotor may become a problem if the rotor structure is thin and long.

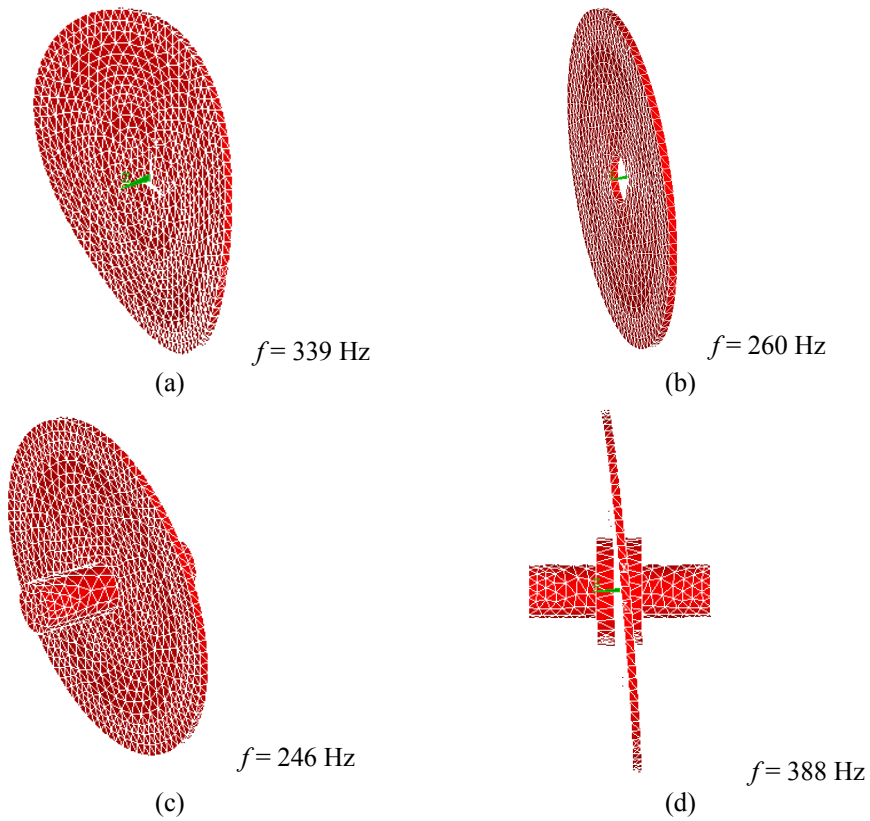

Fig. 4.6. Rotor structures analysed. (a) Circular disk. (b) Circular disk with shaft hole. (c) Disk including shaft. (d) Shaft with flange and rotor, which may be consider to correspond stiff support in Fig. 4.3. This structure may be considered to be the most practical rotor structure for interior rotor axial-flux machines.

4.5. Mechanical limits due to centrifugal forces

Centrifugal forces cause mechanical stress on the rotating parts and the forces may break the structure. The centrifugal force F_{cen} acting on a magnet block glued at average radius r_{ave} may be calculated as

$$F_{cen} = G_{PM}\omega^2 r_{ave} \ . \tag{4.6}$$

The stress due to the centrifugal forces is dependent on the mass of the permanent magnet. Consequently, the thickness of the permanent magnet affects the value of the centrifugal force. For a surface-mounted radial-flux machine, which has its permanent magnets glued on the surface of the rotor disk and for a corresponding axial-flux machine, the stress distribution affecting the glue joint is different. For the radial-flux machine with surface-mounted magnets, the tensile stress is a dominating stress component whereas for the axial-flux machine the dominating stress mechanism is a shear stress. Referring to the glue manufacturer datasheets, the shear strength of the glue joint is roughly one third of its tensile strength (Huntsman, 2004). For example, the glue ARALDITE® AV 138M with hardener HV 998, which is used for the prototype machine, a tensile strength of 43 MPa at 40 °C is guaranteed whereas for the shear strength the value given is only 15 MPa at the same temperature. For this reason, the glue joint is of more critical importance as axial-flux machines are concerned. If needed, some mechanical support to bear the centrifugal forces must be arranged.

The centrifugal forces act also on the rotor structures. Considering a solid rotor structure, the maximum stress due to centrifugal forces in the iron is given as

$$\sigma = k_{cen}\rho r^2\omega^2 , \tag{4.7}$$

The parameter k_{cen} is defined as

$$k_{cen} = \frac{3+\upsilon}{4} \tag{4.8}$$

where

υ is the Poissons ratio of the rotor material.

When it is used construction steel St-37 3N, which has a tensile strength of about 400 MPa, the maximum allowed peripheral speed is approximately 200 m/s. When half the tensile strength (200 MPa) is selected to be the allowed sizing constraint, the diagram showing the maximum allowed diameter may be plotted as a function of the rotation speed of the rotor. By assuming that the glue joint may withstand a 2.5 MPa shear stress at operation temperature 100 °C, the maximum rotor radius may also be plotted as a function of the permanent magnet thickness. Fig. 4.7 shows examples of such graphs.

From Fig. 4.7 it may be seen that the sizing of the rotor steel is a more critical factor than the glue joint if the rotational speed is low and if the permanent magnets have a practical thickness, i.e. below 20 mm. The crossover speed appears at about 900 min^{-1} if the thickness of the permanent magnet is 20 mm. The curves, in Fig. 4.7, show also that for machines operating at speeds below 600 min^{-1} the external diameter of the rotor may be several meters because of the stress that is to be withstood. Considering the power ranges used in this study, it is shown that for actual machine structures the mechanical centrifugal stress is no limiting factor for the rotor diameter.

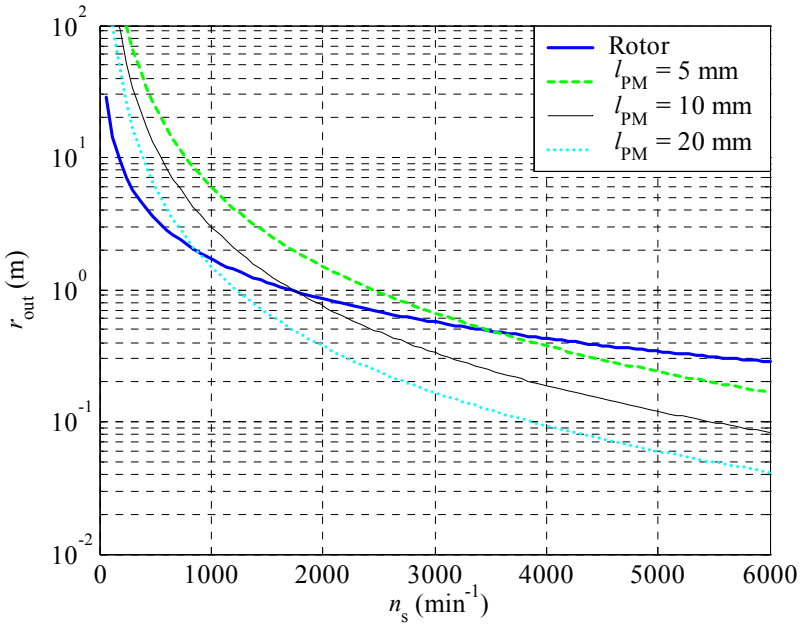

Fig. 4.7. Maximum external radius as a function of the calculated rotation speed based on the stress allowed (2.5 MPa) for the glue joint. The curves are given for magnet thickness 5 mm, 10 mm and 20 mm. At low speeds and large diameters the rotor core strength is the limiting factor and high speeds and small radii the strength of the glue joint is the limiting factor.

For high-speed applications for which the glue joint is subjected to the centrifugal forces and may break before the limit of the mechanical strength of the rotor iron is reached, additional support structures may be embedded in the rotor as shown by Sahin (2001). Here, an additional fibreglass band is used to retain the permanent magnets.

4.6. Discussion

Chapter 4 considers the fundamental aspects related to the mechanical design of the machines under study. It is shown that the axial-flux machine stators require more complex fixing structures than interior rotor radial-flux machine stators. Fixing the stator(s) of an AF machine to the bearing shields by gluing may be a too unreliable solution if for the machine long-term operation in challenging operation conditions is demanded. As welding directly to the bearing shield would be a too difficult task for manufacturing reasons, it must be taken into consideration that the space needed for the stators of an interior rotor type axial-flux machine has to include also extra volume for the supporting structures. The dimensions required by the stator yoke are defined either by the magnetic loading of the stator or the mechanical constraints due to the stator natural frequencies or the manufacturing constraints. The rotor of an axial-flux machine is subject to significant magnetic forces, especially, during the assembly of the machine. From the constructional point of view, it is recommended that the rotor disk should be able to resist these forces without excessive deflection, which has to be far less than the air-gap length. The rotor disk has to be rigid enough so that, during machine operation, it will be possible to avoid harmful vibrations resulting from the electromagnetic forces acting in the air-gap. Apparently, the centrifugal forces do not play a significant role in the dimensioning of the machines under consideration due to the low rotational speeds and due to the power range used in this study.

5. Performance comparisons

The thesis includes two main parts. The first part has given a review of the discussed permanent-magnet machines and materials, as well as design considerations related to the analytical modelling of axial-flux surface-mounted permanent-magnet machines. In addition to this, chapter 4 introduced the necessary mechanical boundary conditions. In the second part – starting here – a relevant theory needed for drawing the comparison is provided.

Along with the development of frequency converters it is now possible to select for a specific variable speed application the most suitable electrical machine from among several electrical machine types such as induction machines, permanent-magnet machines or reluctance machines. Because of the large variety of available machine types, the machine manufacturer is set the difficult task of deciding which type of electrical machine is needed for a specific variable speed application. Comparative information on the highest performance, e.g. highest efficiency, torque density or minimum mass, of the different machines should be available in order for the manufacturer to be able to do the right choice. The economical factors with relation to machine manufacturing, obviously, do have a crucial influence on decision-making.

Comparison of the performances generated by different machine topologies has been an interesting subject for study. The results of the comparing work are influenced by many possible variations. Several studies have shown that, regarding the torque density, axial-flux permanent-magnet machines perform better than radial-flux machines within speed ranges of 1000-3000 min^{-1}. Generally, comparing different electrical machine types is not a straightforward task since for each machine many variables exists and it is difficult to define which variables should be kept constants and which may vary. One frequently used method is based on the $D_{\text{agap}}^2 l$ sizing equation, which compares the machine torque on the basis of the air-gap volume. On the other hand, comparison of the machine outer diameter D_{out} may be more useful since the stator outer diameter is more directly related to the machine total volume and thus affect the size and the cost of the machine. Honsinger (1987) developed the use of a D_{out}^3 sizing equation in the analysis of induction machines. Partly based on the work of Honsinger, Huang et al. (1998) extended the sizing analysis to cover the different types of electrical machines, including axial and radial-flux permanent-magnet machines.

This study provides a performance comparison between low-speed radial-flux surface-mounted permanent-magnet machines and surface-mounted axial-flux machines. The axial-flux machine type includes one rotor and parallel-connected stators. The main focus is on 55 kW machines with rotation speeds 150 min^{-1}, 300 min^{-1} and 600 min^{-1}. Also machines with output power 11 kW, 200 kW and 500 kW and with the same rotation speeds 150 min^{-1}, 300 min^{-1} and 600 min^{-1} are studied. Sizing of the machines under study is based on equivalent electrical loading and equivalent magnetic loading in the air-gap. As a result, the machine main dimensions are calculated in an equivalent way for all considered machine types by using as constants only the most fundamental properties (rotation speed, output power, electrical loading, magnetic loading). Thus, a comparative electromagnetic sizing for the machines is obtained, which may be also used for the purposes of comparing the machine topologies.

In the literature on the subject, theoretical comparisons of different machine types have been reported without the studies giving sufficient discussion on the mechanical limitations. Comparison work may be relatively simply to perform, but if the mechanical constraints for the machine are not fulfilled the results obtained will not be reliable. The comparing analysis provided in this study includes the mechanical constraints which are considered to be practical mechanical design limitations for machines with given power-speed range. The principles for selecting the mechanical constraints may be considered to be a topic stimulating criticism. Different variants of mechanical design constraints are thus introduced and the results obtained

by using different constraints are compared to define the influence of a specific parameter on the overall results.

5.1. Literature on performance comparisons of RFPM and AFPM machines

Starting with Zhang et al. (1996) a torque density comparison between single-sided axial-flux machines and radial-flux machines has been presented. Zhang's approach may be considered to be the simplest move towards comparison of both machine topologies. His approach is based on the $D_{\text{agap}}^2 l_{\text{eff}}$ sizing equations, in which the torque output (T_{RF}, T_{AF}) and synchronous speed to the rotor volume are related through an output coefficient C as

$$\begin{cases} T_{\text{RF}} = C_{\text{RF}} D_{\text{agap}}^2 l_{\text{eff,RF}} \\ T_{\text{AF}} = C_{\text{AF}} D_{\text{ave}}^2 l_{\text{eff,AF}} \end{cases}, \tag{5.1}$$

where

C_{RF} and C_{AF} are the output coefficient for radial-flux- and axial-flux machines

The used analysis assumes non-slotted stators, i.e. air-gap windings are used. The contribution of the end-windings to the overall volume, required by the machine, is neglected. Based on the above approach an explicit expression for the torque density ratio between the machine topologies can be derived. The torque density of the motor, ρ_{T}, is defined as (Zhang, et al., 1996)

$$\rho_{\text{T}} = \frac{\text{Motor rated torque}\,[\text{Nm}]}{\text{Motor core volume}\,[\text{m}^3]} = \frac{T}{V_{\text{M}}} \ . \tag{5.2}$$

By assuming that the yoke flux density can be twice the air-gap flux density, the outer diameter D_{out} of a radial-flux machine stator can be expressed as

$$D_{\text{out}} = D_{\text{agap}} \left(1 + \frac{\pi}{4p} \right). \tag{5.3}$$

Based on (5.2) and (5.3) the torque density of a radial-flux permanent-magnet machine may be shown to be proportional to the air-gap flux density B_{agap} and the linear current density A as

$$\rho_{\text{T,RF}} \propto B_{\text{agap}} A \frac{4}{\pi} \frac{1}{\left(1 + \frac{\pi}{4p} \right)^2} . \tag{5.4}$$

In the expression (5.4) electric loading is calculated based on the RMS value for the sinusoidal phase current. The air-gap flux density B_{agap} is the maximum value for the rectangular type air-gap flux density distribution. The permanent magnet covers the pole air-gap surface and permanent-magnet leakage fluxes are ignored in the approach.

For axial-flux machines it is assumed that a same value is reached for the flux density in the stator and in the rotor yokes and the yoke flux densities are equal to twice the air-gap maximum flux density at the average radius of the axial-flux machine. Thus, the axial length l_{AF} of an axial-flux machine is dependent on the axial length of stator yoke l_{y} and can be expressed as

$$l_{\mathrm{AF}} = 2l_{\mathrm{y}} = 2 \cdot \frac{\pi D_{\mathrm{ave}}}{8p} = \frac{\pi D_{\mathrm{ave}}}{4p}. \tag{5.5}$$

The torque density of an axial-flux machine is proportional to the term

$$\rho_{\mathrm{T,AF}} = \frac{T_{\mathrm{AF}}}{V_{\mathrm{AF}}} \propto \frac{B_{\mathrm{agap}} A \frac{4p}{\pi^2} V_{\mathrm{AF}}}{V_{\mathrm{AF}}} = B_{\mathrm{agap}} A \frac{4p}{\pi^2}. \tag{5.6}$$

Based on (5.4) and (5.6) the relative torque density ratio $\rho_{\mathrm{T,rel}}$ between both machine topologies may be calculated if the linear current density A and the air-gap flux density are the same for both machines

$$\rho_{\mathrm{T,rel}} = \frac{\rho_{\mathrm{T,AF}}}{\rho_{\mathrm{T,RF}}} = \frac{\frac{4p}{\pi^2}}{\frac{4}{\pi}\frac{1}{\left(1+\frac{\pi}{4p}\right)^2}} = \frac{p\left(1+\frac{\pi}{4p}\right)^2}{\pi}. \tag{5.7}$$

The torque density ratio between the machine topologies depends only on the pole pair number as it is determined in Eqn. (5.7) and in Fig. 5.1, which shows the obtained torque density ratio plotted as a function of the pole pairs.

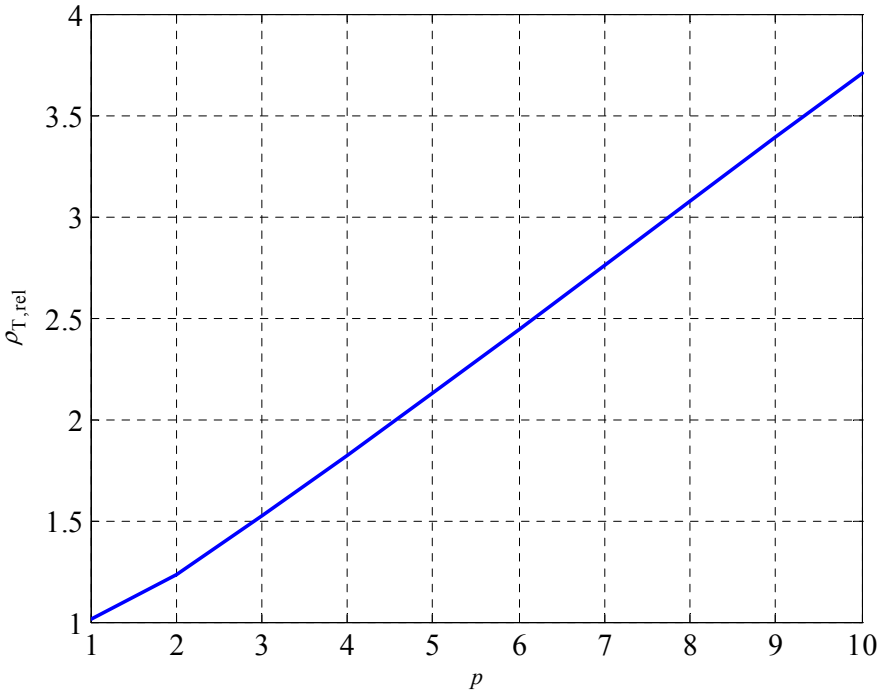

Fig. 5.1. Torque density ratio as a function of the machine pole pairs based on Zhang's approach (1996).

According to the analysis above, the torque density of an axial-flux machine would be always better than the torque density of a radial-flux machine. However, in this approach, axial-flux machines have the advantage since the volume required by the end-windings is not taken into account. For the axial-flux machine, the diameter is increased by the end-windings while for the radial-flux machine the axial length is increased by the end-windings. Thus, for the axial-flux machine the effect of the end-windings on the overall volume shows a quadratic behaviour whereas for the radial-flux machine the effect is directly proportional. For this reason, to compare both machine types a different method has to be developed. This new method should take into account the end-windings and the slots if a slotted stator structure is employed.

Other interesting comparative studies on axial-flux and radial-flux permanent-magnet machines have been introduced. Brown (Brown et al., 2002) presents a comparison similar to that by Zhang, i.e. the end-windings and the slotting are neglected in the analysis. The comparison reported by Brown includes, however, a study of the influence of the axial-flux machine diameter ratio k_D on the torque density behaviour of the measured machine types. Furthermore, the comparison is based on two different methods:

- using same permanent magnet material mass for both structures (same air-gap area)
- using same outer diameter

Brown (2002) reports the results in the shape of volume ratio. Fig. 5.2 (a) compares the axial-flux machine volume with respect to the radial-flux machine volume the amount of permanent magnet material being the same for both machines. As the results show radial-flux machines perform better than axial-flux machines if the pole pair number is small. Considering practical diameter ratios for the axial-flux machine, $0.6 < k_D < 0.7$, the crossover pole number lies around 12, i.e. the volume ratio goes below one as pole pair number goes above 12.

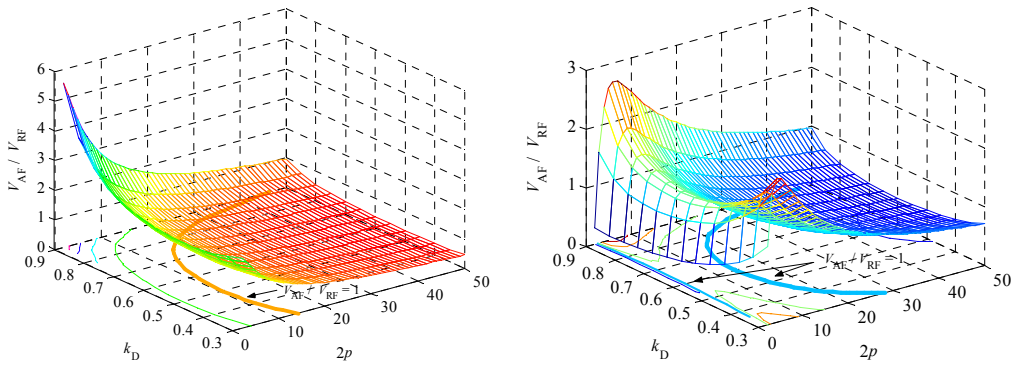

Fig. 5.2. Comparison results based on Brown's approach in the shape of volume ratio. (a) The same air-gap area, i.e. the same amount of used permanent magnet material. (b) The same outer diameter.

Fig. 5.2 (b) compares the volume of axial-flux and radial-flux machines, the outer diameter being the same for both machine types. It is interesting noting that the axial-flux machine performs better than the radial-flux machine if the number of poles is 2 or above 14, depending in this case also on the value of k_D. For two-pole machines the axial-flux structure is better since the axial length of an radial-flux machine becomes excessively long due to the very thick stator yoke, i.e. the air-gap diameter is small leading to an excessive machine length in the axial direction.

Sitapati (Sitapati et al., 2001) reports a performance comparison between surface-mounted axial-flux and radial-flux brush-less DC machines. The considered power ranges from 0.25 kW up to 10 kW and the rotational speeds are 1000 min^{-1} or 2000 min^{-1}. The results of this

comparison show that the power density of an axial-flux machines tends to be higher than the power density of a radial-flux machine. Significant volume differences (volume of active materials) between the machine topologies are reported ($V_{AF}/V_{RF} \approx 0.2$).

Cavagnino (Cavagnino et al., 2001) presents a comparison between surface-mounted axial-flux and radial-flux permanent-magnet machines. In his comparing study the conventional radial-flux machine with internal rotor, Fig. 1.11 (a), and the axial-flux machine with the one-rotor-two-stators configuration are included, Fig. 1.3 (c). The comparison is based on thermal considerations; equal losses per surface area are given for both machine types. The overall machine volume is fixed to be (0.01 m^3) and the rotational speed is 1000 min^{-1}. The results of the comparison show that the use of axial-flux machines is to be considered a very attractive solution for cases considered in the study if the number of poles is high (≥ 10) and the axial length of the machine is short, i.e. the ratio machine axial length versus the machine external diameter is below 0.3.

Huang (Huang, 2002) gives a comparison between surface-mounted radial-flux and axial-flux machines. The radial-flux machine discussed is a surface-mounted interior type permanent-magnet machine whereas, from the axial-flux machine group, a slotted and a non-slotted TORUS type machine are chosen. Axial-flux machines with one rotor – two stators, also with slotted and non-slotted stators, are studied. In this comparison, the machine output power is 150 kW and the rotational speed is 1200 min^{-1}. The results show that with the TORUS topology a better torque density and efficiency can be achieved.

Qu (Qu et al., 2003) makes a performance comparison between dual rotor radial-flux machines, illustrated in Fig. 1.11 (d), and TORUS type axial-flux machines, illustrated in Fig. 1.3 (b). The power range considered is from 2.25 kW up to 37 kW and the rotational speed is fixed to be 1800 min^{-1}. For these machines, the comparison shows that the performance data for the torque density and efficiency are equal. However, for an axial-flux machine tends the material costs tend to be higher because more magnet material is needed.

Li (1996) reports the results of a comparison between two-phase doubly salient radial-flux and axial-flux permanent-magnet machines and induction machines with nominal values 75 min^{-1} and 115 kW. He shows that a better torque density is achieved with an axial-flux permanent-magnet machine than with an induction machine.

Akatsu (Akatsu et al., 2004) presents a procedure for comparing 50 kW, 10 000 min^{-1} axial-flux and radial-flux PM machines with concentrated windings. The comparison shows that the volume required by the radial-flux machine is about 80 % higher than the volume required for the corresponding axial-flux machine.

Except for the comparison of two-phase machines presented by Li, in the comparative studies discussed above PM machines with rotational speeds over 1000 min^{-1} are considered. These are higher speeds than those considered in this study. Furthermore, the simplified comparisons by Zhang (1996) and Brown (2002), assume air-gap windings which are not practical to be used for low-speed machines due to the thickness of the required winding. Based on the above considerations, comparative analyses of low-speed axial-flux machines with one-rotor-two-stators configuration and internal type surface-mounted radial-flux machines should be regarded as insufficiently treated in the literature. That is more particularly because of the fact that any of the reported comparison works does not introduce or discuss practical limitations in relation to machine design.

5.2. Sizing equations for the surface-mounted RFPM machine

Huang (Huang et al., 1998) introduced a method for forming a general sizing procedure for the particular machine topology. This procedure is partly based on Honsinger's study (1987) on the

sizing of induction machines. Next, a procedure for sizing surface-mounted radial-flux permanent-magnet machines is suggested. The given method is, with certain improvements, based on the work of Huang.

The output power of any electrical machine (assuming hereafter permanent magnet excitation) can be expressed as

$$P_{\text{out}} = \eta m \frac{1}{T} \int_0^T e_{\text{ph,PM}}(t) i_{\text{ph}}(t) \mathrm{d}t = \eta m k_{\text{P}} \hat{e}_{\text{ph,PM}} \hat{i}_{\text{ph}}, \tag{5.8}$$

where

$e_{\text{ph,PM}}(t)$ is the phase EMF induced by the PM
$\hat{e}_{\text{ph,PM}}$ is the peak value of EMF
$i_{\text{ph}}(t)$ is the phase current
$\hat{i}_{\text{ph}}$ is the peak value of phase current

The quantity k_{P} is the electrical power waveform factor and it is defined as

$$k_{\text{P}} = \frac{1}{T} \int_0^T \frac{e_{\text{ph,PM}}(t) i_{\text{ph}}(t)}{\hat{e}_{\text{ph,PM}} \hat{i}_{\text{ph}}} \mathrm{d}t \,. \tag{5.9}$$

Since (5.9) includes the effects of the current and the back-EMF waveforms, the structure of the machine winding together with the magnet shape has an effect on the quantity of k_{P}. The phase difference between the waveforms is given by the power factor $\cos\varphi$, the influence of which is included in this case in a numerical value of k_{P}. Huang (1998) reports some typical waveforms and corresponding values for k_{P}. In this study, the current waveform is assumed to be sinusoidal but the back-EMF waveform with surface-mounted magnets is trapezoidal. However, if there are several slots per pole and phase in a stator winding, the trapezoidal waveform is converted to some extent towards a sinusoidal back-EMF. Thus, the winding structure contributes also to the value of k_{P}. In order to find the typical values for k_{P}, a parametric study has been carried out by using the 2D FEA. A range q = 1…6 is studied with the relative magnet widths (permanent magnet width to pole pitch ratio) varying from 0.4 up to 0.95. The considered range for the relative magnet width represents the typical values for α_{p} even though the values below 0.6 tend to be unsuitable for low-speed machines because a low fundamental value for the air-gap flux density would be the result. Fig. 5.3 shows typical waveforms of the induced back-EMF as a function of q when the relative magnet width is equal to 0.7. In Fig. 5.4 the corresponding values for k_{P} are illustrated assuming unity power factor, $\cos\varphi = 1$.

For the machine comparison purposes the induction law (2.28) is modified into the following form

$$\hat{e}_{\text{ph,PM}} = k_{\text{e}} N_{\text{ph}} \hat{B}_{\text{agap,PM}} \frac{\omega}{p} D_{\text{agap}} l_{\text{eff,RF}}, \tag{5.10}$$

The factor k_{e} depends on the winding factor ξ_1 for the fundamental wave, which is calculated according to Eqn. (2.23), and on the air-gap flux density distribution. Thus it takes different forms depending on the machine type if the form of Eqn. (5.10) is kept unchanged. For machines with air-gap flux density distribution being practically sinusoidal, which is the case for unsaturated induction machines and permanent-magnet machines with shaped pole shoes, the factor k_{e} takes the form

$$k_{\text{e}} = \xi_1 \,. \tag{5.11}$$

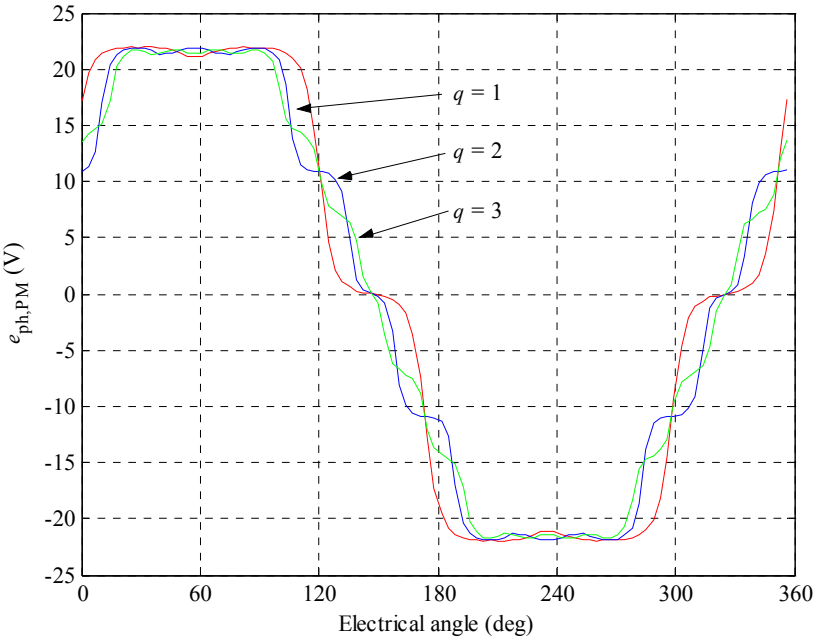

Fig. 5.3. Typical waveforms of permanent-magnet induced back-EMF as a function of q for unsaturated stator.

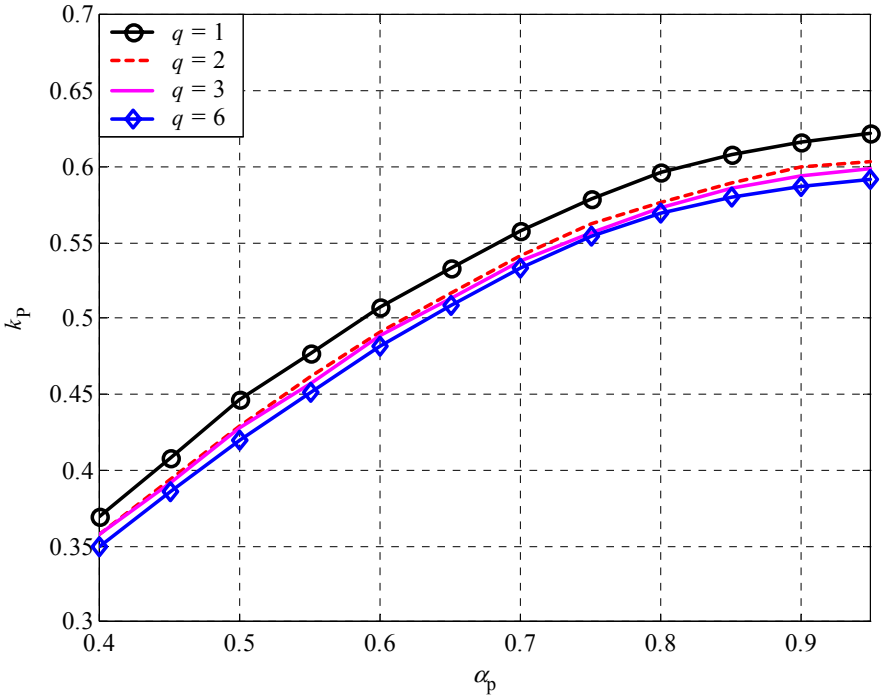

Fig. 5.4. Parameter k_P as a function of α_p and q.

Since the number of slots per pole and per phase is unknown but its value is needed in the computation of ξ_1 according to (2.23) an approach is introduced here to estimate the value of q.

In the analysis it is assumed that for the machines under study the typical value for the slot pitch τ_{slot} may vary between 10 mm < τ_{slot} < 30 mm. As the number of poles and the air-gap diameter are known, the required number of slots per pole and phase may be iteratively calculated as

$$q = \frac{\pi D_{\text{agap}}}{2mp\tau_{\text{slot}}}. \tag{5.12}$$

On rounding the value (5.12) to the nearest integer producing a slot pitch between the desired intervals, the winding structure of the machine can be estimated in a generalized sizing procedure.

The influence of the current waveform in (5.8) can be taken into account by defining the current waveform factor k_{i} as

$$k_{\text{i}} = \frac{\hat{i}}{I_{\text{rms}}}. \tag{5.13}$$

Since here synchronous machines with high-torque quality are analysed a sinusoidal current waveform is assumed and the current waveform factor k_{i} is set to be equal to the value $k_{\text{i}} = \sqrt{2}$, respectively.

The RMS value of the phase current is dependent on the linear current density A defined according to Eqn. (1.2). Generally, in the electrical loading of the stator and the rotor should be taken into account in the electrical loading, but for PM machines the rotor is usually without winding. Now the peak phase current can be expressed by using Eqns. (1.2) and (5.13) as

$$\hat{i}_{\text{ph}} = k_{\text{i}} A\pi \frac{D_{\text{agap}}}{2mN_{\text{ph}}}. \tag{5.14}$$

Combining equations (5.9) to (5.14), the following sizing equation is obtained

$$P_{\text{output,RF}} = k_{\text{e}} k_{\text{i}} k_{\text{P}} \eta \hat{B}_{\text{agap}} A \frac{\omega}{4p} D_{\text{agap}}^2 l_{\text{eff,RF}}. \tag{5.15}$$

With surface-mounted magnets the coefficient k_{e} in Eqn. (5.15) is considered to be equal to the value $k_{\text{e}} = \xi_1 \pi^2 \alpha_{\text{p}}$. On introducing the length ratio coefficient k_{l}

$$k_{\text{l}} = \frac{l_{\text{eff,RF}}}{D_{\text{agap}}}, \tag{5.16}$$

a D_{agap}^3 sizing equation is obtained

$$P_{\text{output,RF}} = k_{\text{e}} k_{\text{i}} k_{\text{P}} k_{\text{l}} \eta \hat{B}_{\text{agap}} A \frac{\omega}{4p} D_{\text{agap}}^3. \tag{5.17}$$

Using k_{l} in (5.17) causes some uncertainty since it is a parameter that has to be defined. For induction machines, k_{l} can be defined through study of catalogue values. The process of sizing an induction machine is well established causing meaning that the reasonable estimation for the parameter k_{l} may be found as a function of the pole pairs (Huang et al., 1998). Since for permanent-magnet machines this is not yet possible, a parametric study is required, i.e. in the computation the length ratio k_{l} is used as a varying parameter.

After comparison between the different machine types is done for the outer diameter of the machine stator, a diameter ratio

$$k_{\mathrm{D,RF}} = \frac{D_{\mathrm{agap}}}{D_{\mathrm{out}}}, \tag{5.18}$$

may be defined and it may be used in the sizing equation (5.17). On substituting (5.18) into (5.17) the sizing equation takes the form

$$P_{\mathrm{output}} = k_{\mathrm{e}} k_{\mathrm{i}} k_{\mathrm{p}} k_{\mathrm{l}} \eta \hat{B}_{\mathrm{agap}} A \frac{\omega}{p} k_{\mathrm{D,RF}}^3 D_{\mathrm{out}}^3 . \tag{5.19}$$

Based on the parameters defined, the radial-flux machine outer surface diameter D_{out} may be calculated as

$$D_{\mathrm{out}} = D_{\mathrm{agap}} + 2\left(y_{\mathrm{tt}} + y + l_{\mathrm{y}}\right), \tag{5.20}$$

where

y_{tt} is the depth of the tooth-tip
y is the depth of the stator slot
l_{y} is the thickness of the stator yoke

The corresponding geometrical dimensions are illustrated in Fig. 5.5.

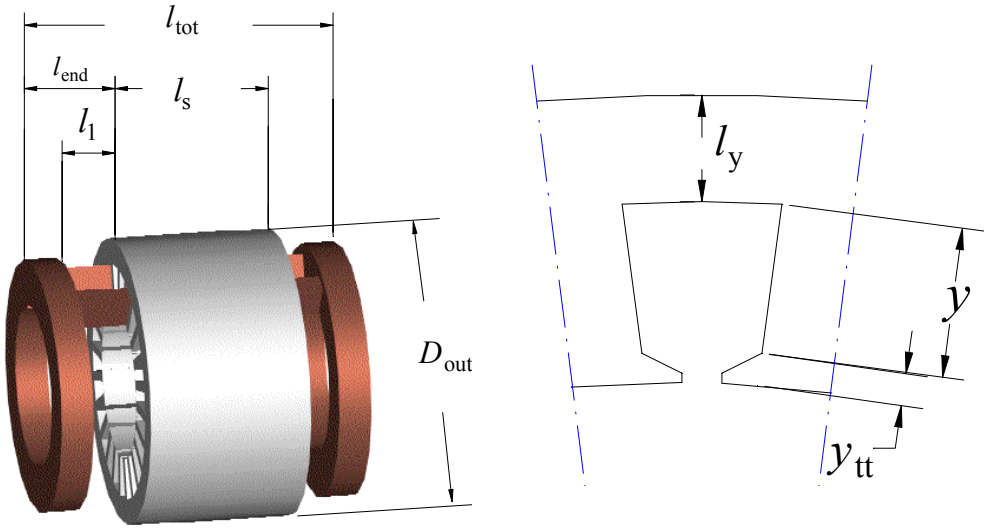

(a) (b)

Fig. 5.5. (a) Definitions for the external dimensions of a radial-flux machine. (b) Definitions for the slot dimensions.

In actual machines, the slot opening is often of the semi-open type. Thus the length of the tooth tip has to be included in the overall volume required by the machine. In this study, a constant value $y_{\mathrm{tt}} = 4$ mm is estimated to cover all practical cases.

The thickness of the stator yoke l_{y} can be calculated based on the air-gap flux and the allowed flux density B_{y} in the stator yoke as

$$l_{\mathrm{y}} = \frac{\Phi_{\mathrm{agap}}}{2 B_{\mathrm{y}} l_{\mathrm{s}}} . \tag{5.22}$$

If the mechanical structure appears to be too weak, i.e. the estimated natural frequency of the stator is below the allowable value (in the analysis $f_{\mathrm{n}} < 3f$), the thickness of the stator yoke is

calculated based on the approach described in Appendix A.1. Consequently, the flux density value in the stator yoke is shifted from the desired value B_y.

The depth of the stator slot can be calculated based on the allowed flux density value in the stator teeth, the linear current density A and the current density J as

$$y = \frac{A}{Jk_{\mathrm{Cu}}k_{\mathrm{trap}}k_{\mathrm{Bt}}}, \tag{5.23}$$

where

k_{trap} is a conversion factor that transforms the rectangular slot to an equivalent trapezoidal slot such that the slot areas are equal. $k_{\mathrm{trap}} > 1$

k_{Cu} is the slot filling factor.

k_{Bt} is a scaling coefficient between the air-gap flux density and tooth flux density, typically $k_{\mathrm{Bt}} = 1.5\ldots2$.

The coefficient k_{trap} is used in (5.23) since a constant tooth width is assumed. By using k_{trap} it is virtually possible to reduce the calculated slot height so that the actual trapezoidal shape is taken into account.

The total volume required by the radial-flux machine is obtained when the length of the end winding protrusion is evaluated. Since the phase coils are in the end-connection more or less circularly grouped and may be assembled partly over the stator yoke, the following equation is used to estimate the length of the end winding l_{end} in the axial direction of the machine.

$$l_{\mathrm{end}} = l_1 + 3\sqrt{\frac{S_{\mathrm{Cu,p}}}{\pi k_{\mathrm{Cu}}}}, \tag{5.24}$$

where

l_1 is a constant describing the distance between the stator core and end-winding, Fig. 5.5.

$S_{\mathrm{Cu,p}}$ is the cross sectional area of copper per phase and pole

The measurements made for different machines show that with Eqn. (5.24) reasonable results for the length of the end-windings are obtained, Table 5.1. The machines in Table 5.1 are self-made prototype machines.

Table 5.1. Comparison between the calculated and measured end-winding lengths.

Machine	$S_{\mathrm{Cu,p}}$ (mm^2)	l_1 (mm)	l_{end} (mm) Calculated	l_{end}(mm) Measured
AF: 5 kW / 300 min^{-1}	280	10	46	50
RF: 15 kW / 150 min^{-1}	410	30	73	75

As the total volume is known, the machine power density can be expressed as

$$\rho_{\mathrm{P,RF}} = \frac{P_{\mathrm{output}}}{V_{\mathrm{RF}}} = \frac{4P_{\mathrm{output}}}{\pi D_{\mathrm{out}}^2 l_{\mathrm{tot}}}, \tag{5.25}$$

where

l_{tot} is the radial-flux machine length in the axial direction and is given by

$$l_{\text{tot}} = l_{\text{s}} + 2l_{\text{end}}\,, \tag{5.26}$$

where the geometrical dimensions are measured according to Fig. 5.5.

The air-gap diameter, number of pole pairs p and the length ratio k_{l} being selected as variables radial-flux machine families may now be designed for which the power, magnetic loading, electrical loading and current density are equal.

In addition to Eqn. (2.35), the following modified expression for the stator copper losses may be derived

$$P_{\text{Cu}} = \frac{mV_{\text{Cu,ph}}J^2}{\sigma_{\text{Cu}}}, \tag{5.27}$$

where

$V_{\text{Cu,ph}}$ is the copper volume in m^3 per phase.

The machine efficiency is also a parameter that varies during the design. The procedure of sizing the machine is thus completed iteratively. In order a compute a large number of machines a parameterised analysis of the designs has been established. For example, according to Fig. 5.6, the losses and thereby the efficiency of the machine can be estimated as a function of the pole pair number and the length ratio.

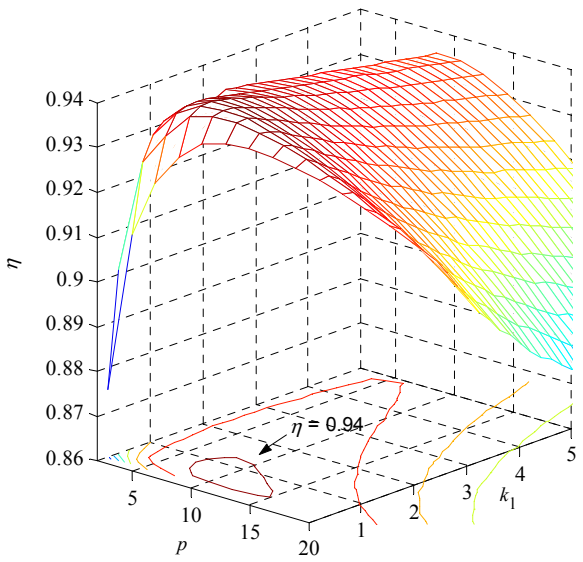

Fig. 5.6. The efficiency of a 55 kW, 600 min^{-1} radial-flux surface permanent-magnet machine as a function of the number of pole pairs and the length ratio k_{l} ($=l_{\text{s}}/D_{\text{agap}}$). Current density J = 5 A/mm^2, electrical loading A = 50 kA/m, and B_{agap} = 0.75 are employed. Note that this case does not include mechanical constraints.

Fig. 5.6 illustrates the typical performance of a low-speed radial-flux permanent magnet machine if the electrical loading and the current density are set constants throughout the

analysis (note that in this case the slot pitch or the teeth widths are not restricted). As the pole pair number and the length ratio are small, $p < 4$, $k_l < 0.5$, the machine efficiency shows a strongly decreasing tendency. In this case the machine axial length is short but the air-gap diameter is large. As a result, the length of the end winding becomes very large causing significant copper losses. As the pole-pair number and the machine length start to increase, the efficiency increases rapidly. For the reported case, the maximum efficiency point is found when the pole pair number is equal to 10 and the length ratio equals 0.8. After this point the increased number of pole pairs leads to a reduced efficiency. This is due to the iron losses, which increase with the frequency increasing with the pole pair number p. The efficiency surface shows also that the efficiency decreases as the length ratio increases. This behaviour is mainly due to the copper losses. When the machine diameter is small, for a long machine the design constraints should be fulfilled and this again will increase the needed amount of copper. This means that the overall volume of the tooth iron will also be large causing significant iron losses in the teeth and, further, a reduction in the overall efficiency.

5.3. Sizing of a surface-mounted AFIPM machine

For axial-flux machines the sizing equation is written in a different form because the average radius is used as a design plane even though the starting point is the same. Huang (Huang, 1999) introduced also corresponding sizing equations to be applied for axial-flux permanent-magnet machines. The equations are also valid for the axial-flux machines realized with the configuration one rotor – two stators (AFIPM machines).

For axial-flux surface-mounted permanent-magnet machines the peak value of the no-load phase voltage may be expressed as

$$\hat{e}_{\mathrm{ph,PM}} = k_{\mathrm{e}} N_{\mathrm{ph}} \hat{B}_{\mathrm{agap}} \frac{\omega}{p}\left(1 - k_{\mathrm{D}}^2\right) D_{\mathrm{out}}^2 , \tag{5.28}$$

Note that the expression for the no-load phase voltage slightly differs from the expression in Eqn. (5.10) for radial-flux machines since the stack length may be eliminated by using the diameter ratio k_{D}. The diameter ratio k_{D} is defined by the Eqn. (1.5). For a surface-mounted AFPM machine the coefficient k_{e} is equal to the value $k_{\mathrm{e}} = \pi\alpha_{\mathrm{p}} / 8$.

Based on the definition of the linear current density the peak value of the phase current can be expressed accordingly to the radial-flux machines. However, the air-gap diameter D_{agap} of an axial-flux machine is selected to correspond to the average diameter of the stator. The expression (5.14), modified for an axial-flux permanent-magnet machine, should be written for parallel-connected stators (N_{s} is the number of parallel-connected stators) as

$$\hat{i}_{\mathrm{ph}} = \frac{k_{\mathrm{i}} A \pi D_{\mathrm{agap,ave}}}{N_{\mathrm{s}} m N_{\mathrm{ph}}} = \frac{k_{\mathrm{i}} A \pi}{N_{\mathrm{s}} m N_{\mathrm{ph}}} \frac{D_{\mathrm{out}}\left(1 + k_{\mathrm{D}}\right)}{2} . \tag{5.29}$$

If the stators are connected in series equation (5.29) has to be multiplied by a factor of N_{s}.

The substitution of (5.28) and (5.29) into (5.8) yields to an expression

$$P_{\mathrm{output,AF}} = N_{\mathrm{s}} \eta k_{\mathrm{P}} k_{\mathrm{i}} \frac{\alpha_{\mathrm{p}} \pi^2 \xi_1}{32} \hat{B}_{\mathrm{agap}} A \frac{\omega}{p}\left(1 - k_{\mathrm{D}}^2\right)\left(1 + k_{\mathrm{D}}\right) D_{\mathrm{out}}^3 , \tag{5.30}$$

In (5.30) the relative magnet width corresponds to the area spanned by the permanent magnet, i.e. the area reaching to the area of the pole surface. If the machine stators are connected in parallel, the parameter N_{s} is the number of parallel-connected stators; in this case $N_{\mathrm{s}} = 2$. If the stators are connected in series, the parameter N_{s} is equal to one, but in the definition of the

linear current density, the number of the coil turns has to include all the phase coil turns connected in series in the machine stators. In expression (5.30) the EMF factor k_e is written out and is combined to other terms in order to define the expression.

Now the power density of the AFPM becomes

$$\rho_{AF} = \frac{P_{output,AF}}{V_{AF}} = \frac{4P_{output,AF}}{\pi D_{tot}^2 l_{tot,AF}}. \tag{5.31}$$

The external diameter of the axial-flux machine is obtained from the equation

$$D_{tot} = D_{out} + 2l_{end,AF}. \tag{5.32}$$

The radial length of the end protrusion $l_{end,AF}$ for a lap winding is evaluated based on (5.24). For the double-sided axial-flux machine, the overall axial length is then

$$l_{tot,AF} = l_{rotor} + 2\left(l_{PM} + g + y + y_{tt} + l_y + l_{sup}\right), \tag{5.33}$$

where the geometrical dimensions of axial-flux machine are according to Fig. 5.7. l_{sup} is the thickness of the fixing plate installed to a stator yoke.

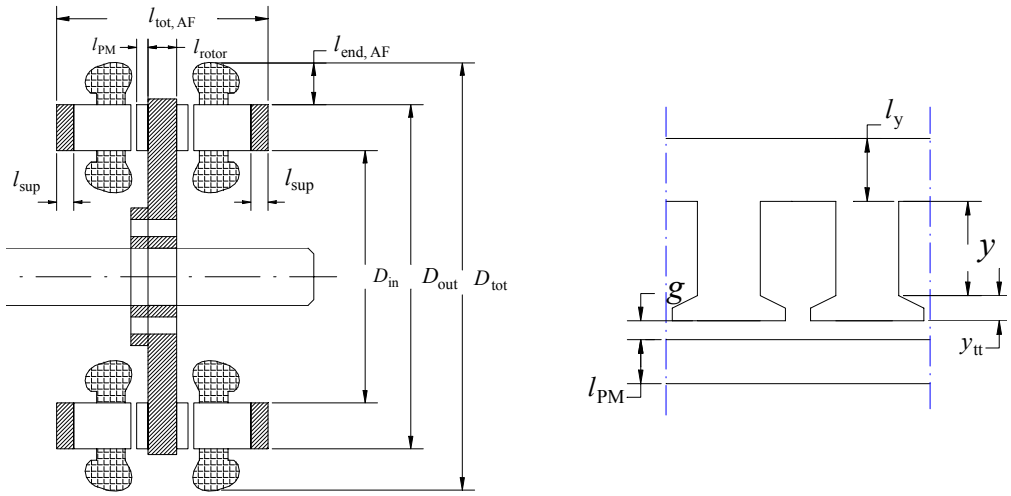

Fig. 5.7. Definitions for the geometrical dimensions of an axial-flux machine with one-rotor-two-stator configuration. (a) External dimensions. (b) Stator cross-sectional dimensions.

The thickness of the rotor core is found based on the results of either the static loadings or the dynamic loadings of the rotor as discussed in Chapter 4.4. Typically the rotor disk thickness varies between 0.05 … 0.1 D_{out}.

Differently from a radial-flux machine, the thickness of the permanent magnet l_{PM} is included directly into the expression of the axial-flux machine volume. Therefore, the thickness of the permanent magnet has to be defined. If the desired air-gap flux density B_{agap} is a given parameter and the remanence of the permanent magnet material is B_r, the required thickness for the permanent magnet may be calculated as (Huang, 1999)

$$l_{PM} = \frac{\mu_r B_{agap} g}{0.95 B_r - \dfrac{B_{agap}}{k_{\sigma PM}}}. \tag{5.34}$$

The required thickness for the stator yoke is evaluated by using equation (5.22) and by using the average radius as the design plane. Since the slot shape of an axial-flux machine is not trapezoidal but rectangular, the depth of the slot can be calculated for axial-flux machines using the linear current density A and the current density J as

$$y = \frac{A}{Jk_{\mathrm{Cu}}k_{\mathrm{Bt}}}. \tag{5.35}$$

A similar design procedure for designing axial-flux surface-mounted permanent-magnet machines may be established now as it has been done previously for radial-flux machines. The computation procedure for axial-flux machine designs follows the quasi-3D method described in Chapter 2.

5.4. Performance comparison between the surface-mounted RFPM and AFIPM

In this chapter, the results of the performance comparison between the surface-mounted axial-flux and radial-flux permanent-magnet machines are presented. A computer program using the sizing equations defined in Chapters 5.2 and 5.3 is utilized in order to find different designs for both machine types. The calculation procedure used in this study is reported in Fig. 5.6. All the reported designs are systematically checked with the help of the magneto static FEA. Validity of the designs is achieved, i.e. the magnetic flux densities are correct and the designed machines are capable of producing the required torque if the values calculated for the mechanical measures, phase coil turns and for the phase current have been used.

Some of the designs for which pole pair numbers $p = 1$ and $p = 2$ have been selected may be, in practise, unattractive since the maximum available torque of machine is basically equal to the rated torque i.e. the rated torque is obtained at the maximum load angle. Note also that especially with $p = 1$ uncertainties resulting from the effects of rotor saturation may arise in the employed analytical procedure, mainly affecting estimation of the inductances and thus estimation of the power factor and load angle. Because, in this study, the designs have been developed for comparison purposes, they were not tested with the voltage-driven time-stepping FEA, which, ultimately, could prove the functionality of the designs as generating the required torque is concerned.

In the computation procedure, the electromagnetic sizing is first obtained. Then the mechanical constraints are checked and, if the constraints are violated, the machine geometrical parameters are modified such that the mechanical constraints are fulfilled. In such a case, the magnetic constraints are overridden. It is assumed that both machines operate at the same temperature, i.e. the temperature of the phase winding and the permanent magnets is a fixed, not varying parameter. Consequently, this implies that the required cooling between the machines may be different.

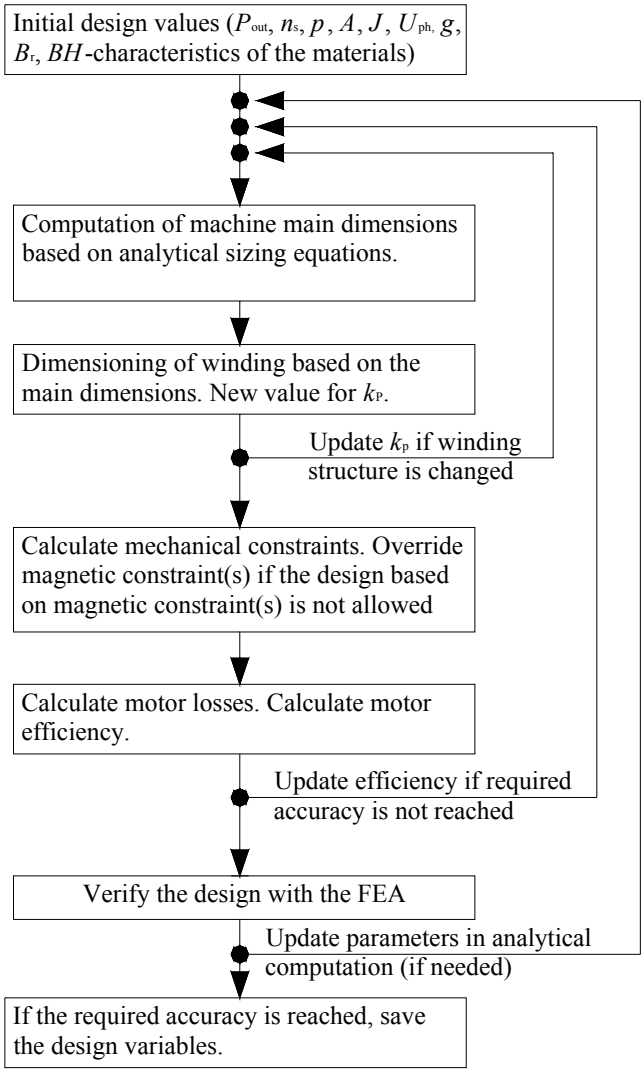

Fig. 5.8. Calculation procedure used in the comparative study.

In the computations for the machines with rotation speed 150 min^{-1} to 600 min^{-1} and with output powers of 11 kW up to 500 kW the following constraints are used:

1. In the comparison part the minimum tooth width is fixed to the value of 5 mm and the minimum allowed slot pitch to the value of 10 mm. For the axial-flux machines these constraints are employed on the inner radius of the stator instead of the average radius.
2. The thickness of the stator yoke is determined either from the magnetic loading, for the machines with low pole pair numbers, or from the mechanical constraints. However, the minimum allowed thickness for the stator yoke is fixed to the value of 15 mm if the calculated stator yoke thickness depending on the magnetic loading or natural frequencies is below this value. One design constraint is defined for the lowest natural frequency, f_n, of the stator which should be at least three times the line frequency of the machine ($f_n > 3f$). This constraint may be considered reasonable since, in this case, operation in a limited field-weakening region is also possible without violating this

constraint. However, consideration of this constraint is to some extent difficult. That is because frequency converters generate harmonics in a very large frequency area and avoiding all conditions under which there should be no match between the natural frequencies of the stator structure and the excitation frequencies may thus be almost impossible. Furthermore, the effects of fixing the stator to the frame must be considered.

3. The thickness of the rotor disk of axial-flux machines is calculated based on the maximum allowed deflection of the rotor disk or alternatively based on the dynamical stability. The maximum allowed deflection is fixed to be one tenth of the air-gap length.

4. The air gap physical length is fixed to the value g = 2.0 mm, which for the considered low-speed machines is a practical value due to the tolerances allowed for the manufacturing of stators and rotors.

5. In the computations the length ratio of radial-flux designs is varied between $0.2 \leq k_l \leq 2$. This interval covers the radial-flux machine group, which is designed for the purposes to compete with the axial-flux machines. Instead of using low-speed machines, radial-flux machines with a long stator and a small air-gap diameter ($k_l > 2$) are more appropriate for high-speed or servomotor applications.

6. The permanent magnet relative width α_p is selected to be 0.7. This value may be considered to be applicable to a large amount of specially shaped magnets. Furthermore, the value is near to the optimal value that diminishes the cogging torque if the number of slots per pole and per phase is equal to 1, which usually applies to multi-pole machines.

7. The air-gap flux density level is fixed to the value of 0.75 T. This value is calculated as an average value of the air-gap flux density above the magnet width in the air-gap including the effects of slotting; see Fig. 2.8 (b). This value produces a peak value of 0.9 T for the fundamental component of the air-gap flux density (the permanent magnet relative width α_p is 0.7). The value 0.75 T may be considered to be relatively high since it is above the point in which the selected permanent magnet material produces its maximum energy product with the selected air-gap length. (Permanent magnet material with B_r = 1.1 T is used). However, for low-speed applications higher air-gap flux density values should be used since this may considerably reduce the required amount of copper in a significant manner.

8. The current densities J = 3 A/mm2, J = 5 A/mm2 and J = 7 A/mm^2 are used with the electric loading values A = 30 kA/m, A = 50 kA/m and A = 70 kA/m. These values combine the practical values of an electrical machine if machine cooling is considered. J = 3A/mm^2 combined to an electrical loading A = 30 kA/m may be considered to demonstrate the machine being sufficient self-ventilating whereas for the opposite A = 70 kA/m with J = 7A/mm^2 a powerful external cooling arrangement may be needed, for example air flow through the machine.

The parameters compared are the machine efficiency, the power density, the weights of iron, copper and permanent magnet material as well as the design cost. The study is further subdivided into two different parts. The first part includes a comparison based on equal magnetic and electric loadings and equal current density. In the second part some of the designs are compared with respect to obtained efficiency, i.e. achievement of equal efficiency for the different machine topologies is the goal of design. Equal efficiency is obtained by using the current density as a variable while keeping the electric loading and the magnetic loading in the air-gap as constants. Furthermore, a study of the influence of the designs variables on the

designs results is provided. This work is important since in the comparison method several selected parameters such as the rotor thickness of the AF machine as well as the thickness of the fixing parts of the stators have to be utilized. The influence of these variables on the comparison results has to be demonstrated in order that generalizing of the final results could be permitted.

It must be noted that comparison is done also for pole pair numbers $p = 1$ and $p = 2$ even though the use of one or two pole pairs should be considered an unattractive choice since the line frequency remains very low. For example, a 150 min^{-1} machine with two pole pairs requires a supply frequency of 5 Hz, which is basically too small for present-day frequency converters due to thermal loading of the power switches. An oversized converter may thus be required if $p = 1$ or $p = 2$ is applied. Besides, with pole pair numbers $p = 1$or $p = 2$ difficulties may arise in the computations of some of the designs (due to inductances) as the required torque may be hard to obtain.

5.4.1. Comparison of 55 kW machines

In this chapter the study focuses on comparison of 55 kW machines with rated rotational speeds 150 min^{-1}, 300 min^{-1} or 600 min^{-1}. In the designs, the rated torques are 3500 Nm, 1750 Nm and 875 Nm, respectively. The consideration given in this study includes results obtained with designs for which the current density is set equal to 5 A/mm^2. That is because, though varying the current density, this gives computation results, which show that the behaviour obtained remains very similar. Therefore, the other designs are demonstrated only for the purposes of clearing certain additional effects. Firstly, the comparison is done with respect to efficiency. In this case, the linear current density, the air-gap flux density as well as the current density are equal for the designs. Next, the machines are compared with respect to overall volume. The same constraints are valid as for the efficiency comparison. Then, the costs of the machines are compared. Finally, the effects of the selected constraints are explained.

Efficiency-based comparison

In Figs. 5.9-5.13 the efficiency is given as a function of the pole pair number p and by using four different RF machine length ratio coefficient values. The results show that the efficiency is weakest for the axial-flux machine through the studied rotational speeds. In this case, the efficiency of the AFIPM machine is about 2 % units lower compared to the efficiency achieved by the radial-flux machines. The result agrees with the result given by Huang (2002) though in Huang's (2002) report only one pole pair number ($p = 3$) is considered. The reported behaviour is due to the copper losses since copper losses are the dominating loss component for low-speed machines with practical pole-pair numbers. If the same magnetic and electric loadings are used as a design constraint, this renders possible for the axial-flux machine to have a greater air-gap diameter (average air-gap diameter) compared to the corresponding radial-flux machine. As an exception, however, it should be mentioned radial-flux machines for which the length ratio reaches very low values. For the axial-flux machines the air-gap area may be smaller since the force producing torque is located on a greater radius. As the air-gap area of the axial-flux machine is smaller, the required number of coil turns is higher, respectively. Furthermore, the length of the end-winding portion is longer due to the greater diameter. These aspects, ultimately, result in a poorer efficiency for the measured axial-flux machine topology if the comparison is based on the same current density and the same electrical loading.

The efficiency of the radial-flux machines is also strongly affected by the length ratio coefficient k_l. If the length ratio k_l is low, i.e. below one, the air-gap diameter is large while the axial length of the stator stack is short. As a result, the air-gap area is reduced and more coil turns are needed. Furthermore, the relative portion of the end winding becomes more

significant. Due to the above effects and if the pole pair number is small the amount of copper losses is considerable and a similar efficiency behaviour is obtained as for the axial-flux machines. According to the results given for example in Fig. 5.9, and the machine efficiency being a design criterion, axial-flux machines and radial-flux machines with low length ratio k_l, obviously, are unattractive solutions.

It must be noted that the influence of the iron losses is moderate as the pole pair number increases. The efficiency shows to be basically constant if the pole pair number is above 10. This behaviour may be explained by the mechanical constraint related to the stator yoke thickness or the minimum tooth width. The use of the mechanical constraints combined to the increment in the number of pole pairs reduces the magnetic flux density level - and that of the iron losses as well - in the iron parts. The influence of the iron losses is shown most significant for the 600 min^{-1} machines. In this case, the iron losses start to reduce the efficiency as the pole pair number increases (frequency increases), which is clearly shown in Fig. 5.13.

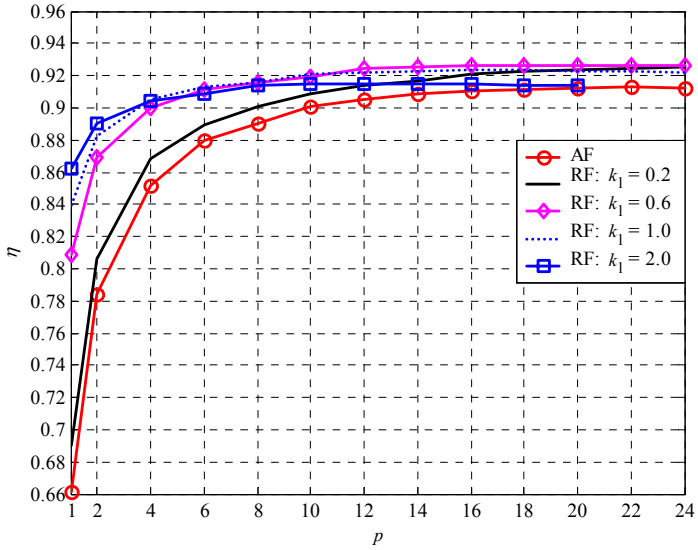

Fig. 5.9. Efficiency of 55 kW, 150 min^{-1} machines as a function of the pole pair number. The values of the electrical loading and the current density are A = 30 kA/m, J = 5 A/mm^2. The radial-flux machines have different length ratios k_l. The axial-flux machine has a diameter ratio of k_D = 0.6, defined according to Eqn. (1.5).

Note that, according to Figs. 5.10-5.12, the efficiency results for the axial-flux machine are not given for all pole pair numbers used in the radial-flux machine designs. This is due to the mechanical constraints; as the pole pair number is small and the value of the electrical loading is high, there remains not enough space to fit the end-windings into the space available on the inner radius of the axial-flux machine stator core. With high pole pair numbers the minimum slot pitch value at the inner radii is reached. As a 55 kW AF-machine with electrical loadings of 70 kA/m and rotational speed of 600 min^{-1} is considered, low as well as high pole pair numbers have been found to be unsuitable since the selected mechanical constraints could not be fulfilled. For the sake of manufacturing applicability, the consideration of such AF designs has been omitted. As a consequence, the selection pole pair number for an axial-flux machine is generally more restricted than for a radial-flux machine. This is, obviously, not valid for radial-flux machines with a high length ratio coefficient, $k_l > 2$. These machines are long in the axial direction while their air-gap diameter is small causing that only low pole pair numbers are practicable for use.

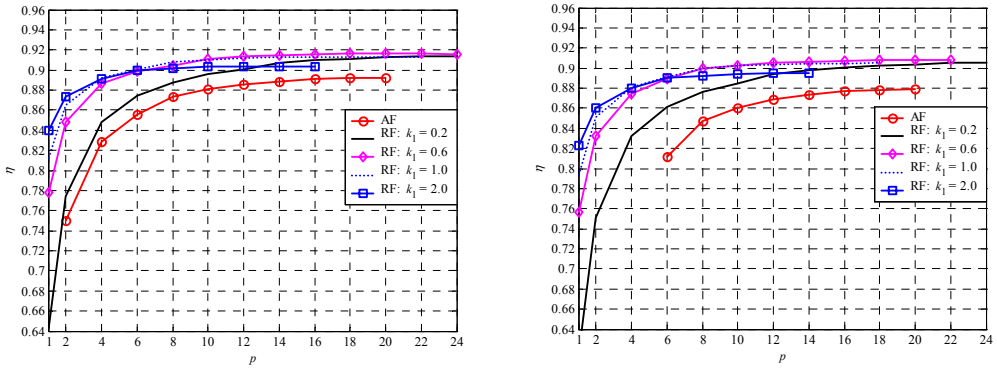

(a) (b)

Fig. 5.10. Efficiencies of 55 kW, 150 min^{-1} machines as a function of the pole pair number. The values of the electrical loading and the current density are (a) A = 50 kA/m, J = 5 A/mm^2. (b) A = 70 kA/m, J = 5 A/mm^2. The radial-flux machines have different length ratios k_l. The axial-flux machine has a diameter ratio of k_D = 0.6.

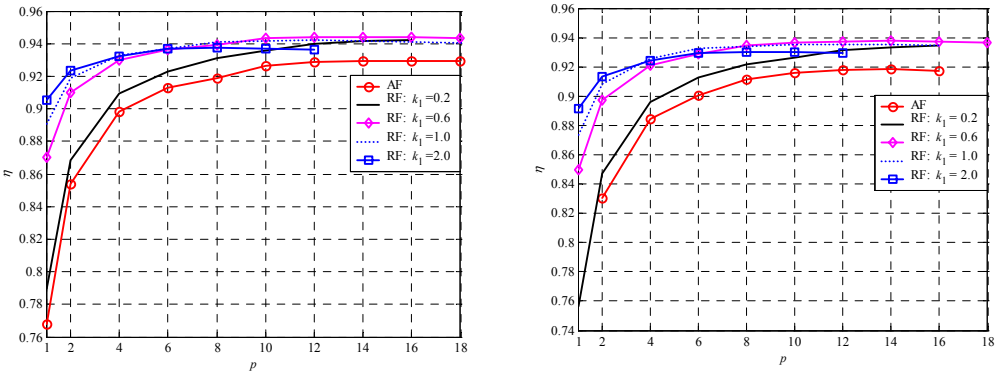

(a) (b)

Fig. 5.11. Efficiencies of 55 kW, 300 min^{-1} machines as a function of the pole pair number. The values of the electrical loading and the current density are (a) A = 30 kA/m, J = 5 A/mm^2. (b) A = 50 kA/m, J = 5 A/mm^2. The radial-flux machines have different length ratios k_l. The axial-flux machine has a diameter ratio of k_D = 0.6.

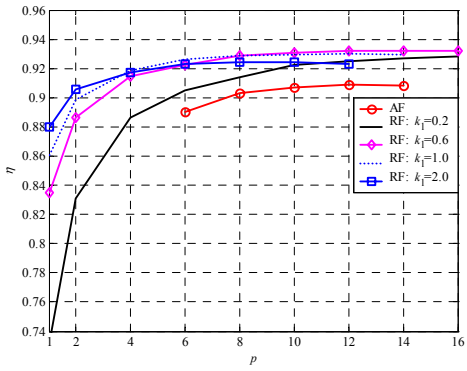

Fig. 5.12. Efficiencies of 55 kW, 300 min^{-1} machines as a function of the pole pair number. The values of electrical loading and current density are A = 70 kA/m, J = 5 A/mm^2. The radial-flux machines have different length ratios k_l. The axial-flux machine has a diameter ratio of k_D = 0.6.

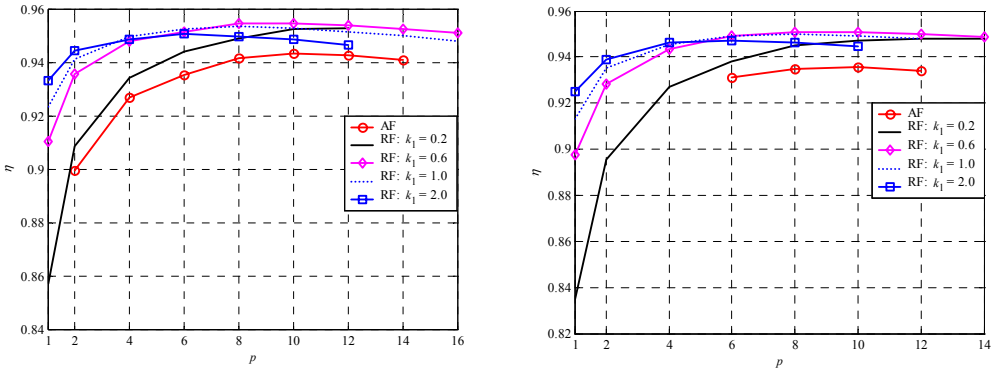

(a) (b)

Fig. 5.13. Efficiencies of 55 kW, 600 min^{-1} machines as a function of the pole pair number. The values of electrical loading and current density are (a) A = 30 kA/m, J = 5 A/mm^2. (b) A = 50 kA/m, J = 5 A/mm^2. The radial-flux machines have different length ratios k_l. The axial-flux machine has a diameter ratio of k_D = 0.6. Note that when the linear current density A increases from 30 to 50 kA/m the suitable pole pair numbers for the AFPMSM are restricted by the mechanical constraints (in the right-hand figure, there are fewer alternatives for p). With A = 70 kA/m the AFPMSM may not be produced at all because the constraints are exceeded.

To ensure the sufficient accuracy of the analytical approach in the computation of iron losses, several machines have been analysed with the time-stepping 2D FEA. Comparison between the FEA and the analytical approach, based on Eqn. (2.37), is described in Fig. 5.14 for the 300 min^{-1} machines with electrical loading A = 50 kA/m and current density J = 5 A/mm^2. According to the results, the 2D FEA shows about 5-15 % higher iron losses throughout the measured range, Fig. 5.14. The difference in the computation of the iron losses by the FEA and by the analytical method is acceptable. The electrical steel used in the calculations is M600-50A and the iron loss coefficients for this grade are according to Table 5.2.

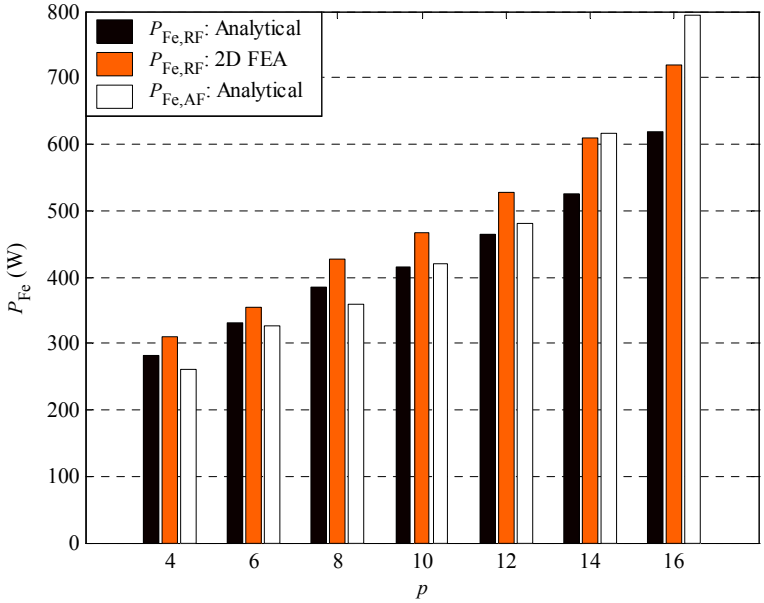

Fig. 5.14. Iron loss comparison. n_s = 300min^{-1}, A = 50 kA/m, J = 5 A/mm^2.

Table 5.2. Loss coefficients of electrical steel M600-50A used in the computation of iron losses (Haataja, 2003).

k_{hys} [Wsm^3T^{-2}]	σ [$\Omega^{-1}m^{-1}$]	k_{str} [$(W/Ts^{-1})^{1.5}m^{-3}$]
152	4 000 000	2.32

Table 5.3 summarizes the loss differences including 300 min^{-1} machines with electric loading A = 50 kA/m and copper current density 5 A/mm^2. The copper losses are subdivided into the copper losses in the end-windings and the copper losses in the slots. In order to demonstrate the influence of the efficiency, an axial-flux design with efficiency equal to that of the RF design is included in Table 5.3.

Table 5.3. Losses and consumption of materials for 55 kW, 300 min^{-1} machines with A = 50 kA/m, J = 5 A/mm^2 ($2p$ = 20). Note that the air-gap area S_{agap} of the AFIPM structures include both air-gaps.

Parameter	AF $k_D = 0.6$	AF: [2] $\eta_{AF} = \eta_{RF}$	RF: $k_l = 0.2$	RF: $k_l = 0.6$	RF: $k_l = 1.0$	RF: $k_l = 2.0$
D_{agap} [mm]	421	418	582	394	332	264
D_{out} [mm]	527	523	747	502	427	352
D_{tot} [mm]	643	645	747	502	427	352
S_{agap} [m^2]	0.279	0.275	0.213	0.292	0.326	0.438
$G_{Cu,end}$ [kg]	36.6	53.2	33.7	16.1	11.8	7.7
$G_{Cu,slot}$ [kg]	24.8	36.0	18.9	26.0	30.8	39
$G_{Cu,tot}$ [kg]	61.5	89.2	52.7	42.1	42.6	46.8
G_{Fe} [kg]	80.3	98.2	123	95.4	93.7	108
G_{PM} [kg]	8.2	8.1	6.2	9.6	11.9	16.6
I_{ph} [A]	94	92	94	93	92	93
R_{ph} [Ω]	0.15	0.11	0.14	0.11	0.11	0.12
P_{Cu} [W]	4100	2750	3510	2810	2840	3120
P_{Fe} [W]	420	490	310	380	420	480
P_{str} [W] [1]	550	550	550	550	550	550
$\cos\varphi$ [3]	0.98	0.98	0.98	0.98	0.99	0.99
η [%]	91.6	93.5	92.6	93.6	93.5	93.0

[1] Calculated as $P_{str} = 0.01 \cdot P_n$

[2] Reference case $k_l = 1.0$ for the RF machine

[3] Calculated based on (2.57). U_{ph} = 215 V, $E_{ph,PM} \approx$ 210 V.

Table 5.3 indicates an interesting result showing that in order for the AFPMSM and RFPMSM to produce equal efficiency the AF requires a considerably higher copper amount. However, the amount of needed permanent magnet material is typically smaller for the AFPMSM than for the RFPMSM.

Overall volume-based comparison

In the following, the overall volume required by the machines is compared. The dimensions used in the computation are described in Fig. 5.5 for the radial-flux machines and in Fig. 5.7 for the axial-flux machines. The overall volume is then computed by using the following equations.

$$\begin{cases} V_{\mathrm{RF,tot}} = \dfrac{\pi D_{\mathrm{out}}^2 l_{\mathrm{tot,RF}}}{4} \\ V_{\mathrm{AF,tot}} = \dfrac{\pi D_{\mathrm{tot}}^2 l_{\mathrm{tot,AF}}}{4} \end{cases}, \tag{5.36}$$

and the relative volume ratio is then computed as

$$V_{\mathrm{rel}} = \frac{V_{\mathrm{AF,tot}}}{V_{\mathrm{RF,tot}}} . \tag{5.37}$$

The results show that the axial-flux machines require a smaller volume, especially, if the length ratio of the radial-flux machine is small, $k_{\mathrm{l}} < 0.5$. A slight dependency in the relative volume with respect to the rotation speed may be observed. Based on the results obtained, the overall volume of the axial-flux machines reduces more rapidly as the current density increases, which is mainly dependent on the length of the end-windings. A similar behaviour may be observed through the measured rotational speeds. It is interesting to observe that for the 600 min^{-1} machine with length ratio $k_{\mathrm{l}} = 0.2$ the relative volume rapidly declines as the pole pair number goes above $p > 8$, which is the opposite behaviour compared to the results obtained at rotation speeds 150 min^{-1} and 300 min^{-1}. This behaviour results from the natural frequency constraint for the stator; as the stator diameter is large due to the low value of the length ratio k_{l} and because the line frequency is high due to the high pole pair number and the higher rotation speed, the stator yoke of the RF machine becomes thick so that the constraint with respect to the natural frequency is fulfilled. Furthermore, at a 600 min^{-1} rotation speed, fewer pole pair combinations are available.

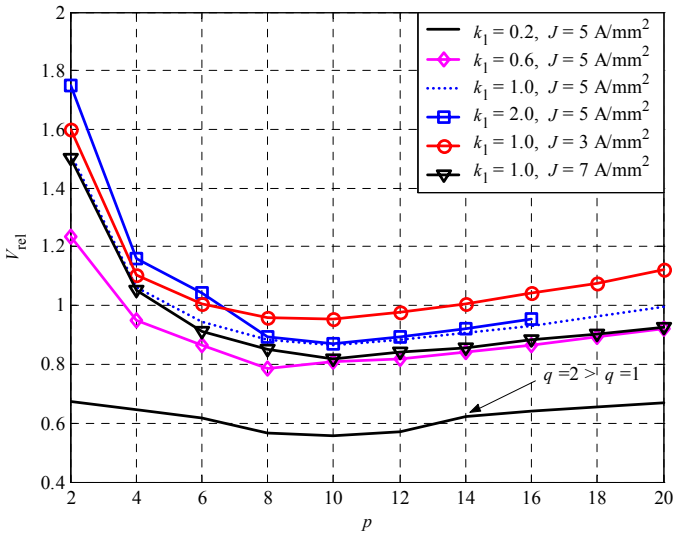

Fig. 5.15. Relative volumes $V_{\mathrm{rel}} = V_{\mathrm{AF,tot}}/V_{\mathrm{RF,tot}}$ of the 55 kW, 150 min^{-1} AF and RF machines. A = 50 kA/m. The radial-flux machines have different length ratios k_{l}. The axial-flux machine has a diameter ratio of k_{D} = 0.6. The electrical and the magnetic loadings for the machines are the same. The axial-flux machine has a lower efficiency than the radial-flux machines have, see Fig. 5.10. Note the effect of q changing to the volume ratio as the pole pair number changes from 12 to 14.

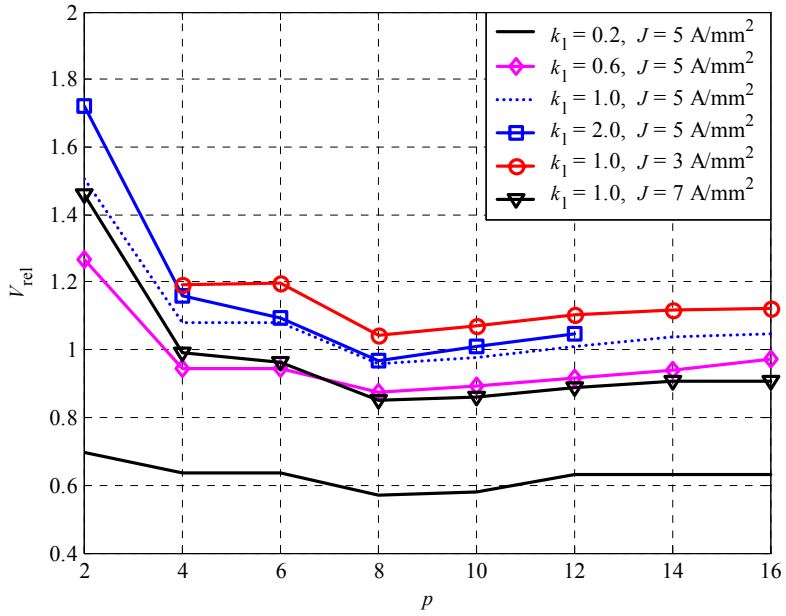

Fig. 5.16. Relative volumes $V_{rel} = V_{AF,tot}/V_{RF,tot}$ of the 55 kW, 300 min^{-1} AF and RF machines. A = 50 kA/m. The radial-flux machines have different length ratios k_l. The axial-flux machine has a diameter ratio of k_D = 0.6. The electrical and the magnetic loadings for the machines are the same. The axial-flux machine has a lower efficiency than the radial-flux machines have, see Fig. 5.11.

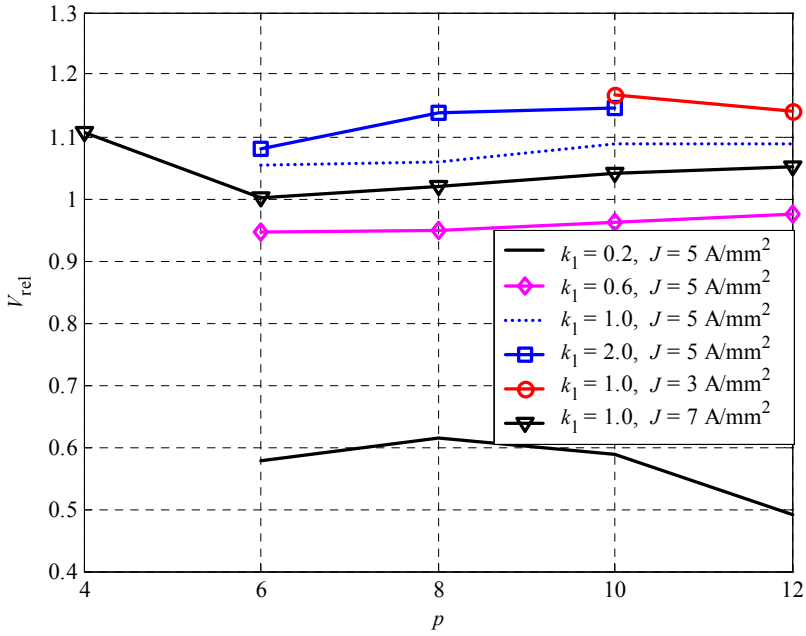

Fig. 5.17. Relative volumes $V_{rel} = V_{AF,tot}/V_{RF,tot}$ of the 55 kW, 600 min^{-1} AF and RF machines. A = 50 kA/m. The radial-flux machines have different length ratios k_l. The axial-flux machine has a diameter ratio of k_D = 0.6. The electrical and the magnetic loadings for the machines are the same. The axial-flux machine has a lower efficiency than the radial-flux machines have, see Fig. 5.13.

According to Figs. 5.15 and 5.16 if the axial-flux machine has a low pole pair number, this machine type should not be the first choice. Axial-flux machine with $1 \leq p \leq 4$ require considerably more volume. A similar behaviour is shown as for the results reported by Brown (2002) in Fig. 5.2 (a), even though the machines do not have exactly equal air-gap areas due to different approach.

With the data in Table 5.4 it may be more straightforward to compare the different geometrical measures of the designs. The total axial length of the measured axial-flux machine is 191 mm, calculated according to Eqn. (5.33). With a 34.9 mm rotor thickness l_{rotor} and a 30 mm total length of the stator support structures the influence of latter parts is, in this case, 34 % of the overall volume of the axial-flux machine, which is a significant value since for radial-flux machines similar structures are not possible. As for the stator yoke thickness of radial-flux machines, when the external diameter is large, a thick stator yoke is required due to the natural frequency constraint. As the length ratio increases, the stator yoke thickness reduces, and in the case of $k_l = 2.0$ the stator yoke thickness is determined by the allowed minimum thickness for the stator yoke.

Table 5.4. Designs of 300 min^{-1}, 55 kW machines. A = 50 kA/m, J = 5 A/mm^2 ($2p$ = 20). The electrical and the magnetic loadings for the machines are the same.

Parameter	AF	RF: $k_l = 0.2$	RF: $k_l = 0.6$	RF: $k_l = 1.0$	RF: $k_l = 2.0$
D_{agap} [mm]	421	582	394	332	264
D_{out} [mm]	527	747	502	427	352
D_{tot} [mm]	643	747	502	427	352
l_{tot} [mm]	191	242	350	442	634
l_{end} [mm]	58	63	57	55	53
l_s [mm]	105	116	236	332	528
l_{PM} [mm]	5.6	5.6	6.3	6.6	7.4
l_{rotor} [mm]	34.9	-	-	-	-
l_y [mm]	19.5	49.4	23.4	17.8	15
y [mm]	31.8	28.2	25.6	24.6	23.7
S_{agap} [m^2]	0.279	0.213	0.292	0.326	0.438
B_t [T]	1.81	1.9	1.9	1.9	1.9
B_y [T]	1.16	0.59	0.85	0.94	0.88
$B_{agap,PM}$ [T]	0.75	0.75	0.75	0.75	0.75
Q	60	120	60	60	60
q	1	2	1	1	1
V_{tot} [m^3]	0.062	0.106	0.069	0.063	0.061

The mechanical constraints used here cause also that the value for the flux density level in the stator yoke is far from the desired value 1.9 T. Basically, only pole pair numbers $p < 8$ are suitable for construction of the machine when the selected flux density constraint is used. This observation is valid for both axial and radial-flux machines. This means that the iron circuit is

not fully utilized, i.e. there is basically additional iron in the stator if only the magnetic dimensioning of the machines is considered, and this is an obvious drawback for the design.

For the permanent magnet thickness, it has been shown that thicker magnets are required as the length ratio ($k_l = l_{eff,RF} / D_{agap}$) increases. This is mainly resulting from the leakage fluxes since a relatively larger amount of permanent-magnet flux is wasted to the stray fluxes as the permanent magnet becomes narrower.

The influence of the electric loading on the overall volume is described in Fig. 5.18. The result obtained shows that the volume ratio between the machines depends to some extent on the electric loading. According to the results, with the increasing electric loading the axial-flux machine volume will be less reduced when compared to the corresponding reduction of volume for the radial-flux machines. The difference is rather insignificant, for instance a 10 % change is observed with the value of electrical loading increasing from 30 kA/m to 70 kA/m. Increasing of the rotational speed will result in a similar behaviour of the volume ratio.

This behaviour is due to required tooth height. In axial-flux machines, deeper slots are required as the value of electric loading is increased since the limiting constraint for to the minimum teeth width becomes more important as the machine air-gap diameter becomes smaller (the air-gap area reduces, thus more coil turns are required but it is impossible to employ narrower teeth). For radial-flux machines a similar behaviour is observed, but as the minimum teeth width is determined by the magnetic loading instead of the mechanical constraints, the slot depth is relatively shorter, reducing efficiently the external diameter of the machine. These aspects together enable the reduction of the stator yoke thickness. As a result, using high values for the electrical loading seems to be more beneficial for radial-flux machines than for double-sided axial-flux machines.

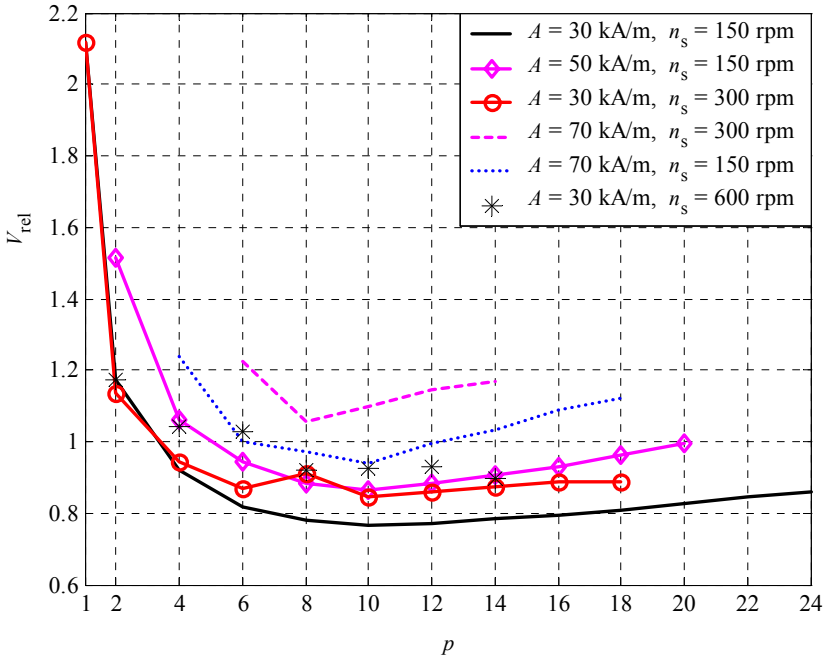

Fig. 5.18 The influence of the electric loading on the volume ratio ($V_{rel} = V_{AF,tot}/V_{RF,tot}$) of 55 kW machines as a function of the pole pair number. J = 5 A/mm^2, k_l = 1.0. The electrical and the magnetic loadings for the machines are the same. The efficiencies of the axial-flux machines are lower than the efficiencies of the radial-flux machines.

Fig. 5.19 shows the final comparison with respect to the overall volume. The relative volume is plotted as a function of the radial-flux machine length ratio k_l. In this comparison the pole pair number is fixed to the value $p = 10$. The selected pole pair number corresponds to the point in which the relative volume reaches the minimum value, Fig. 5.18.

Fig. 5.19 displays that the volume ratio strongly depends on the torque since the mechanical power is kept as constant while as the rotation speed varies (for 55 kW machines the torque-speed values were: 3500 Nm / 150 min^{-1}, 1750 Nm / 300 min^{-1} and 875 Nm / 600 min^{-1}). Axial-flux machines appear to be more suitable for use in high-torque applications. This can be explained directly by means of the sizing equations of the machines. The volume required by an axial-flux machine is proportional to the term D_o^3, Eqn. (5.30), whereas the volume of a radial-flux machine is proportional to the term $D_{agap}^2 l$, Eqn. (5.15). Thus, the external diameter of an axial-flux machine does no increase as fast as the external diameter of radial-flux machine does if the rated torque increases. On combining the behaviours described in Figs. 5.18 and 5.19 it may be stated that axial-flux machines are a more attractive choice if the value of the electric loading is small and the torque required is high. On the other hand, radial-flux machines are more appropriate for use if the value of the electrical loading is high and the rated torque is low. For the considered 55 kW machines the turn over point lies quite nicely to the rotational speed of 300 min^{-1} (rated torque $T = 1750$ Nm) and electrical loading of 50 kA/m. If lower rotational speeds or lower values of electrical loading are employed, the volume ratio V_{rel} is below one, thus in the designs the overall volume of the RF-machines is larger compared to that of the AF-machines. The previous is valid if the length ratio value of RF machines lies within the typical interval $0.8 < k_l < 2$.

The curves show also very clearly that, compared to the axial-flux machine, the overall volume required by the radial-flux machine is considerably larger if the RF-machine length ratio k_l ($k_l = l_{eff,RF} / D_{agap}$) is below 0.4.

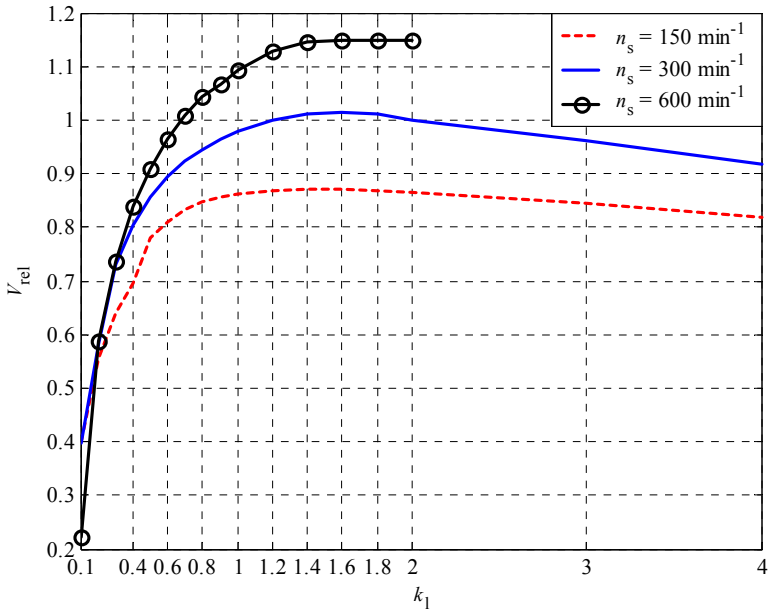

Fig. 5.19. Relative volume as a function of length ratio k_l. $A = 50$ kA/m, $J = 5$ A/mm^2, $p = 10$, $P = 55$ kW. The efficiencies of the axial-flux machines are lower than the efficiencies of the radial-flux machines. If RF and AF efficiencies are set equal the volume of the AFIPM structure increases. The volume ratio increases about 15 percent units.

Cost-based comparison

The quality of the electrical machine is dependent on the price of the raw materials needed for the manufacturing of the machine. The cost of the machines is derived based on the use of copper, permanent magnet material and electrical steel. The cost of electrical steel is calculated based on the required amount of bulk material as well as on the amount of active material used in the final product. The amount of copper and permanent magnet material needed for the machine is obtained directly from the sizing procedure and thus given as a design result. However, it is more complicated to achieve information on the consumption of electrical steel since a significant part of material turns to be scrap metal after punching, especially for the radial-flux machines. For axial-flux machines a steel strip with suitable width may be used for the manufacturing of the stator lamination and thus a smaller amount of scrap metal is formed. The material cost for each design is given by

$$\wp_{\mathrm{tot}} = \wp_{\mathrm{Cu}} G_{\mathrm{Cu}} + \wp_{\mathrm{Fe}} G_{\mathrm{Fe}} + \wp_{\mathrm{PM}} G_{\mathrm{PM}} , \tag{5.38}$$

where the mass of electrical steel G_{Fe} is either the mass of active material or the overall mass of steel required in the construction of the laminations.

The following material prices are used in the computations:

- For copper: $\wp_{\mathrm{Cu}}$ = 4.0 €/kg
- For electrical steel: $\wp_{\mathrm{Fe}}$ = 0.7 €/kg
- For permanent magnet material: $\wp_{\mathrm{PM}}$ = 30 €/kg

The above-mentioned prices correspond to the Finnish market prices dated autumn 2004. The comparison does not take into account the labour work required, but because the axial-flux machine includes two stators, it may be estimated that the wounding of two stators for an axial-flux machine will takes more working time than the corresponding work for one radial-flux machine stator.

First, the absolute values for the costs are demonstrated in Fig. 5.20 for the 300 min^{-1} machines with design values A = 50 kA/m, J = 5 $\mathrm{A/mm}^2$ and with k_{l} = 1.0 (for the radial-flux machine). Comparing the designs, the results - including only the costs of the active materials - show that:

- The cost of active iron is almost equal, Fig. 5.20 (a).
- The cost of copper is higher for an axial-flux machine, but the difference becomes smaller with the pole-pair number increases.
- The cost of the permanent magnet materials is higher for a radial-flux machine; that is because the air-gap area is larger and because slightly thicker magnets are required (this enables the use of higher flux density values in the stator iron).
- The overall cost comparison between the machines shows is interesting result; when the pole pair number is below 8, the total material cost is higher for the AF machine. With pole pair number p = 8, the cost is practically equal and with p > 8, the material cost becomes higher for the RF machine.

For comparison purposes, the iron costs are calculated based on the total amount of electrical steel required for the manufacturing of the lamination. These results are given in Fig. 5.20 (b). It may be noticed that

- In the AF designs, the cost of used electrical steel increases slightly, as well as the total cost of materials.

- In the RF designs, the cost of used electrical steel needed is considerably higher if the total consumption is considered. The price of the electrical steel is doubled if compared only to the cost of the active material.
- As the cost of electrical steel considerably increases this means that for the RF machine the total material cost of is now higher, except for $p = 2$.

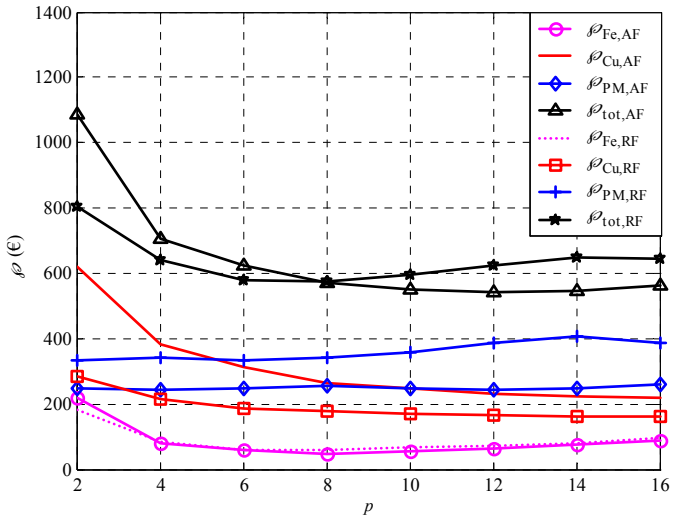

(a)

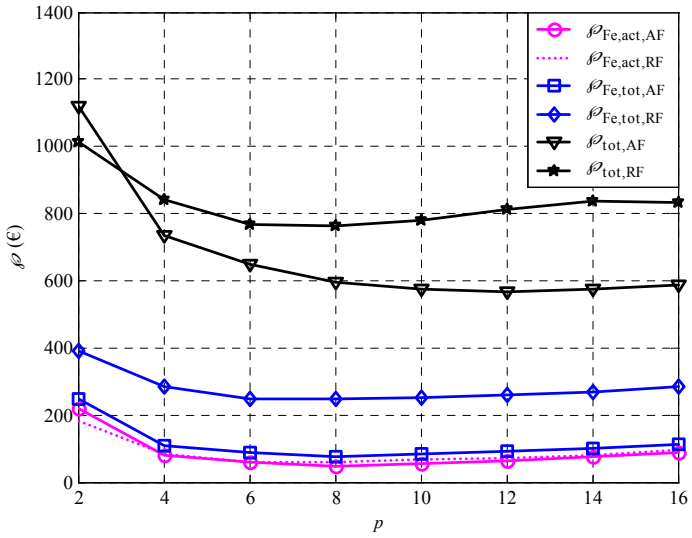

(b)

Fig. 5.20. Comparative study of the material costs for 55 kW, 300 min^{-1} machines as A = 50 kA/m, J = 5 A/mm^2 and k_l = 1.0 for the radial-flux machines. (a) Cost of active materials. (b) Cost based on the total use of raw materials. The efficiencies of the axial-flux machines are lower than the efficiencies of the radial-flux machines.

The current density strongly determines the need of copper, whereas the relation between the current density and the consumption of iron and permanent magnets remains less significant. Figs. 5.21-5.24 illustrate a cost comparison for the measured 300 min^{-1} machines with varying current densities.

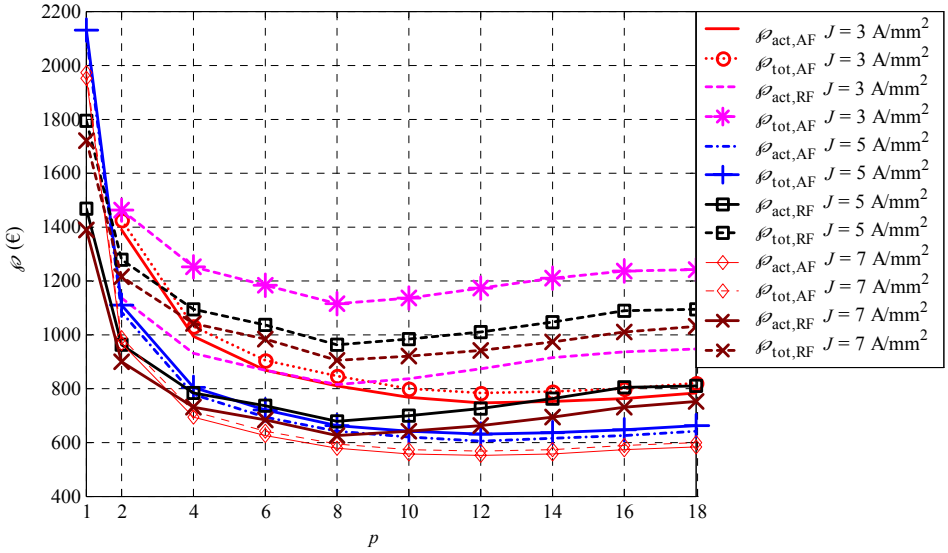

Fig. 5.21. Costs for 55 kW machines in relation to use of active materials and total consumption of materials. n_s = 300 min^{-1}, A = 30 kA/m, k_l = 1.0 for the radial-flux machine. The efficiencies of the axial-flux machines are lower than the efficiencies of the radial-flux machines.

As can be seen from the figures, the curves for the costs in relation to the varying electrical loading and current density show very similar shapes. It is obvious that the cost curves show a decreasing tendency with increasing electrical loading or increasing current density. For the cases reported here, the general tendency is that for axial-flux machines with pole pair number below $p < 10$ there will be more active material costs. On the other hand, if the total electrical steel consumption is taken into account the axial-flux machines generally produce better in terms of cost effectiveness. According to the previous considerations on machine efficiency it is obvious that for axial-flux machines more copper is required if equal efficiency is defined as a design constraint. For this reason, a comparison of the machine costs, the machine efficiency being fixed, is introduced later. In a further comparison, the magnetic loading in the stator teeth of the machines is kept equal. This, consequently, must affect the need of permanent magnet material.

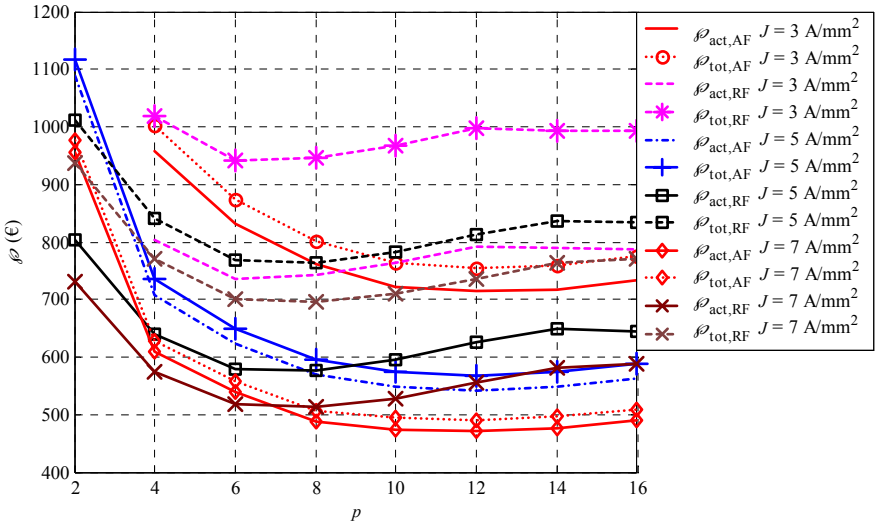

Fig. 5.22. Costs for 55 kW machines in relation to use of active materials and total consumption of materials. n_s = 300 min^{-1}, A = 50 kA/m, k_l = 1.0 for the radial-flux machine. The efficiencies of the axial-flux machines are lower than the efficiencies of the radial-flux machines.

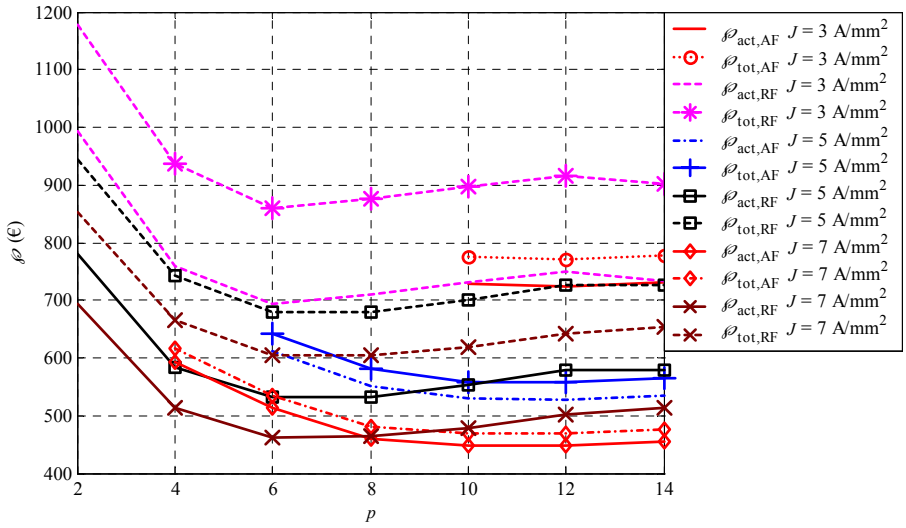

Fig. 5.23. Costs for 55 kW machines in relation to use of active materials and total consumption of materials. n_s = 300 min^{-1}, A = 70 kA/m, k_l = 1.0 for the radial-flux machine. The efficiencies of the axial-flux machines are lower than the efficiencies of the radial-flux machines.

For the comparison described in the previous study, only one length ratio k_l = 1.0 for the radial-flux machines has been used. Fig. 5.24 compares the results obtained with the measured machines using different k_l values and using the values A = 50 kA/m, J = 5 A/mm^2. Fig. 5.24 shows that, in terms of overall costs, radial-flux machines are a more competitive choice than axial-flux machines if the length ratio is kept much below one. This result is influenced mainly by the cost for permanent magnet material as the need for permanent magnet material is in direct relation to the air-gap area.

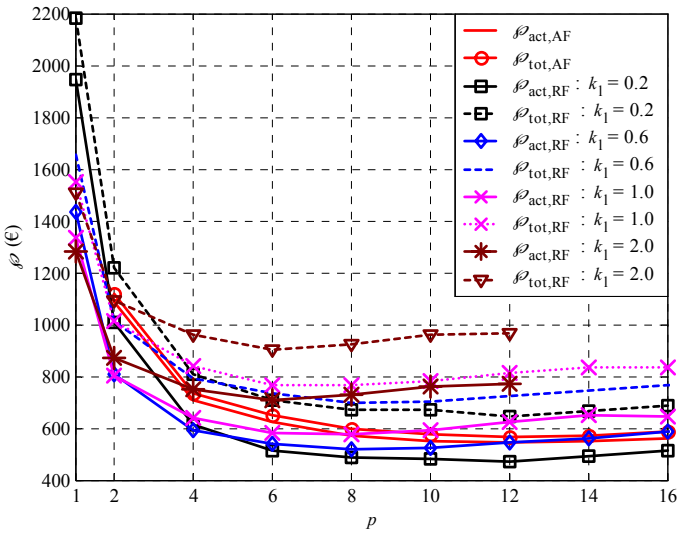

Fig. 5.24. Costs for 55 kW machines in relation to use of active materials and total consumption of materials. A = 50 kA/m, J = 5 A/mm^2, n_s = 300 min^{-1}. The efficiencies of the axial-flux machines are lower than the efficiencies of the radial-flux machines.

Finally, the material costs are compared in relation to the rotation speed. In the radial-flux designs here, it is used for the length ratio k_l = 0.6. According to the results, the material costs appear to be very similar regardless of the rotation speed. For the axial-flux machine, the material cost remains lower if the cost is calculated based on the total amount of electrical steel used. When taking into account only active materials, design comparison shows that the material costs for a radial-flux machine remain lower especially at pole pair number values p < 6. As the pole pair number increases, the costs can be kept almost equal (p > 12).

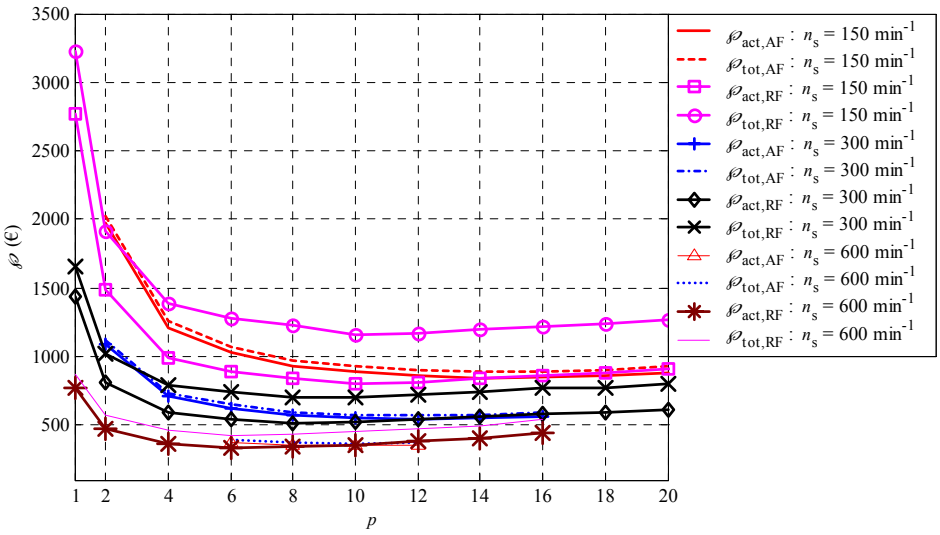

Fig. 5.25. Cost for 55 kW machines as a function of the pole pair number, rotational speed as a parameter. Designs: A = 50 kA/m, J = 5 A/mm^2, k_l = 0.6 for radial-flux machines. The efficiencies of the axial-flux machines are lower than the efficiencies of the radial-flux machines.

Summary of the costs:

In this chapter the costs between the radial-flux and the axial-flux PM machines have been compared. In the designs, equal values for the electrical and magnetic loading have been used for both machine types. Also the mechanical constraints introduced in this study have been used for both machine topologies. As a conclusion:

- The consumption of copper consumption is higher for axial-flux machines than for radial-flux machines.
- The consumption of permanent magnet material is lower for axial-flux machines if in the comparison the length ratio of the radial-flux machines is above 0.5.
- Total consumption of electrical steel is considerably higher for radial-flux machines.
- Due to the previous facts, the costs calculated from the overall cost of electrical steel are generally higher for the radial-flux machines.
- Axial-flux machines with low pole pair numbers ($p < 4$) are more expensive.
- However, in all the comparisons presented here, the efficiency produced by the axial-flux machines remains slightly lower than the efficiency produced by the radial-flux machines, especially when the number for the pole pairs is low.
- Based on the previous considerations, it may be stated that axial-flux machines (AFIPM structure) may not compete with radial-flux machines if the pole pair number is low. This result is influenced by several factors, being efficiency, manufacturing as well as costs. The pole pair number being above 6, the axial-flux machine becomes a more attractive alternative, and more particularly, because with the AFIPM structure a smaller overall volume can be obtained. The results show also that if an axially short radial-flux machine is required, it is advantageous to apply the design of an axial-flux machine since a significant reduction in overall volume can thus be obtained.

Influence of the rotor thickness and fixing structures on the overall volume of an axial-flux machine

In order to demonstrate the influence of the fixing structures and rotor thickness of an axial-flux machine on its overall volume, comparison is performed using 150 min^{-1}, 300 min^{-1} and 600 min^{-1} machines with an electric loading of 50 kA/m and a current density of 5 A/mm^2 as computation examples.

- The curves labelled “initial” describe the initial condition. The curves labelled “Fixing parts not included” are obtained by first reducing the length of the fixing structures (2×15 mm) from the overall length of the AF machine and then calculating the new volume for AFIPM.
- For the curves labelled “Fixing parts not included, l_{rotor} = 20 mm” a constant rotor thickness equal to 20 mm is assumed. Here also, the fixing structures of the stators are neglected.
- For the curves labelled “Fixing parts not included, rotor disk not included” the permanent magnets are assumed to be mounted into holes of the rotor skeleton and the rotor skeleton thickness l_{rotor} is assumed to be equal to the overall thickness of the permanent magnets ($l_{rotor} = 2l_{PM}$).

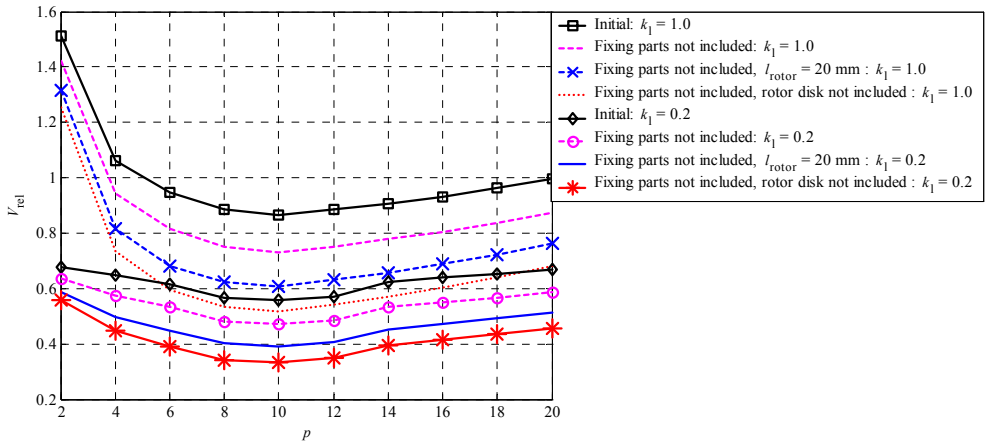

Fig. 5.26. Volume comparison (V_{AF}/V_{RF}), ignoring the mechanical structures of the AFIPM, 150 min^{-1}, 55 kW machine.

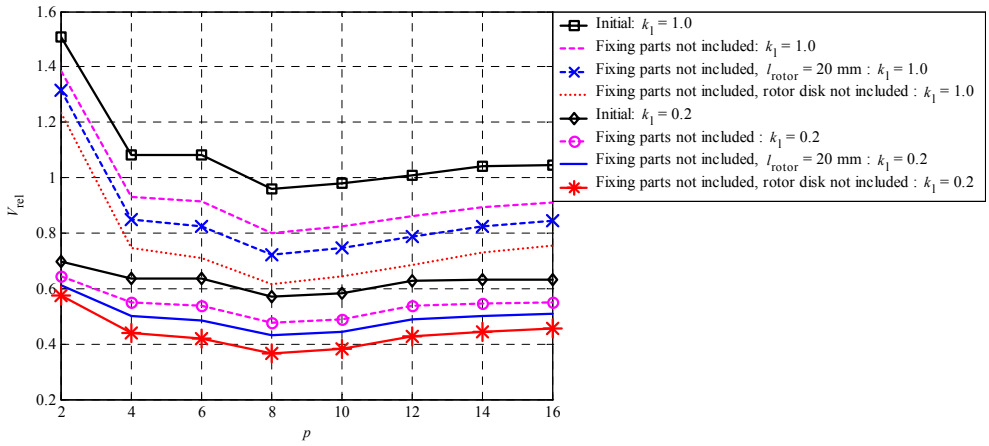

Fig. 5.27. Volume comparison (V_{AF}/V_{RF}), ignoring the mechanical structures of the AFIPM, 300 min^{-1}, 55 kW machines.

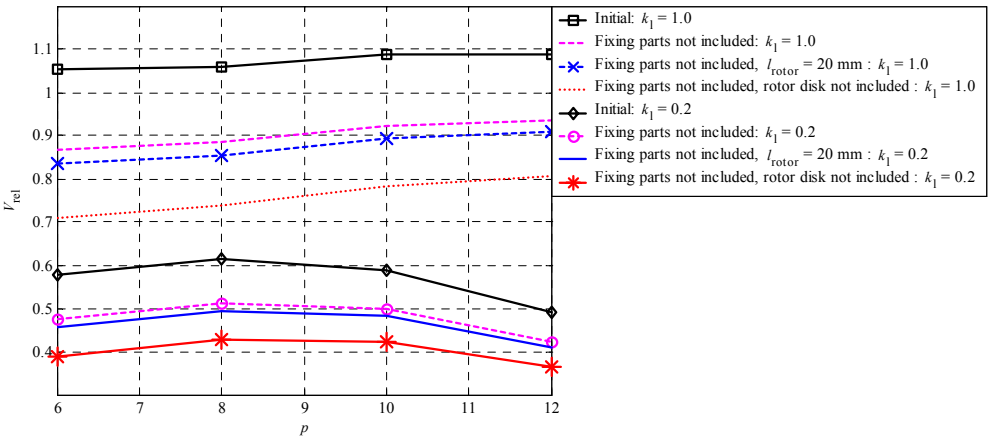

Fig. 5.28. Volume comparison (V_{AF}/V_{RF}), ignoring the mechanical structures of the AFIPM, 600 min^{-1}, 55 kW machines.

According to the results in Figs. 5.26-5.28 the additional mechanical parts have a strong influence on the overall volume required by the AFIPM. If the AFIPM structure can be manufactured without having to use additional fixing parts in the stator yoke (for example by gluing or by friction welding the stator stacks to the bearing shields), this renders possible to significantly reduce the overall volume of the AFIPM. If, further for the same structure, manufacturing of the rotor structures is possible by mounting the magnets into the rotor skeleton, a considerable volume reduction can be obtained. By removing the supporting structures and the rotor disk from the overall volume of the AFIPM, it is possible to obtain volume ratios of about 0.7 if radial-flux machines with length ratio $k_l = 1.0$ are considered. For radial-flux machines with $k_l = 0.2$ the volume ratio is about 0.4.

Conclusion

If the structure of the AFIPM is such that the rotor thickness is equal to the thickness of the permanent magnets and the stators are fixed to the bearing shields not including any additional iron parts, then the AFIPM machine will generate better volume ratios (torque density) than the radial-flux machine. As an exception to this, machines with pole pair numbers $p < 4$ are to be mentioned.

Influence of the efficiency in the volume- and cost-based comparison

It is shown that the axial-flux machines, generally, produce a weaker efficiency. Because there is a direct relation between the efficiency and cooling capacity of the machine, now, the same efficiency is used in the comparative analysis of axial-flux and radial-flux machines. The axial-flux machines are redesigned in order for the machines to achieve an equal efficiency. Since the iron losses are moderate compared to the copper losses, an equal efficiency can be obtained by reducing the value of the current density. For the reference machines, radial-flux machines are used with design values $A = 50$ kA/m, $J = 5$ A/mm^2 and rotation speeds 150 min^{-1} and 300 min^{-1}. Since the efficiency is fixed to be equal, also the tangential stress in the air-gaps between the machines will now be exactly the same.

According to the results in Figs 5.29-5.31, if the same efficiency is set to be a design constraint, the volume ratio changes about 20 %, being now slightly over one. This means that overall volume of radial-flux machines is now smaller. The computation results shows that for the measured axial-flux machines the current density J has to be 1.5-2.5 A/mm^2 smaller than the current density of the radial-flux machines if the same efficiency is required by using equal values for the magnetic loading and electrical loading.

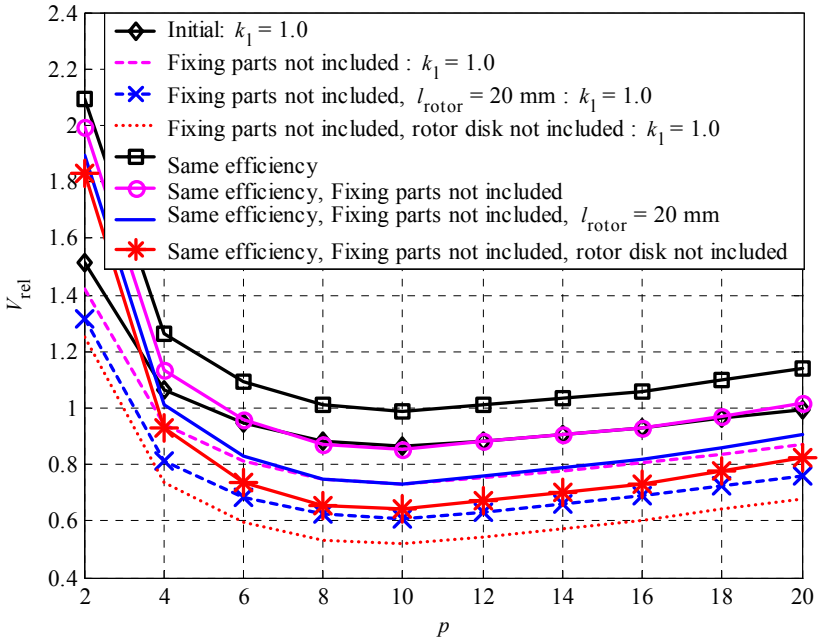

Fig. 5.29. Influence of the efficiency on the volume ratio, for 55 kW machines with A = 50 kA/m, n_s = 150 min^{-1}.

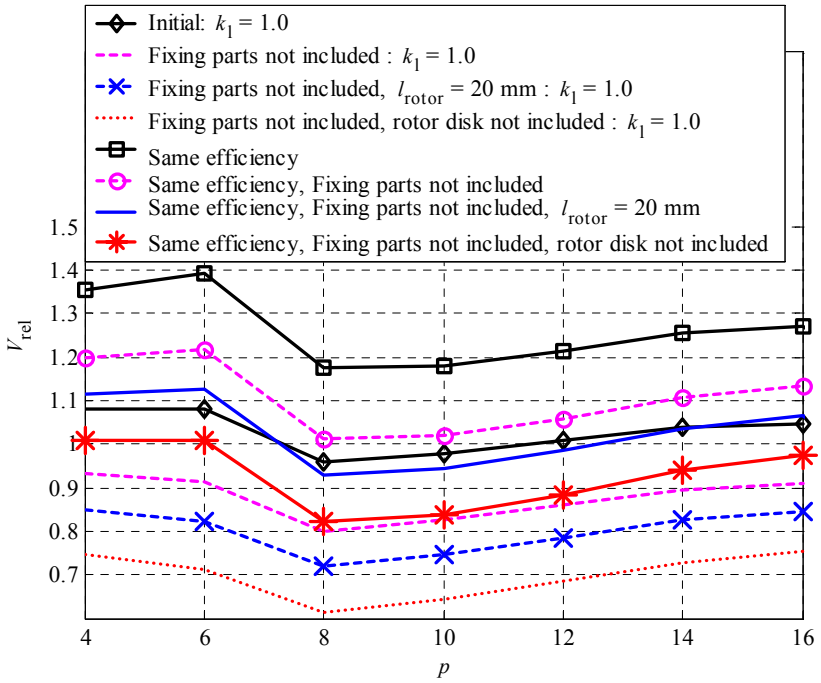

Fig. 5.30. Influence of the efficiency to the volume ratio for 55kW machines, A = 50 kA/m, n_s = 300 min^{-1}.

Because for the AFPMSM in order to achieve efficiency equal to that of the RFPMSM a larger amount of copper is needed. For the axial-flux machine the cost of copper will thus increase. Furthermore, because deeper slots are needed due to the increased copper need, also more iron will be needed. Consequently, the material costs for an axial-flux machine with enhanced efficiency have increased. The influence of these aspects is demonstrated in Figs 5.31-5.32.

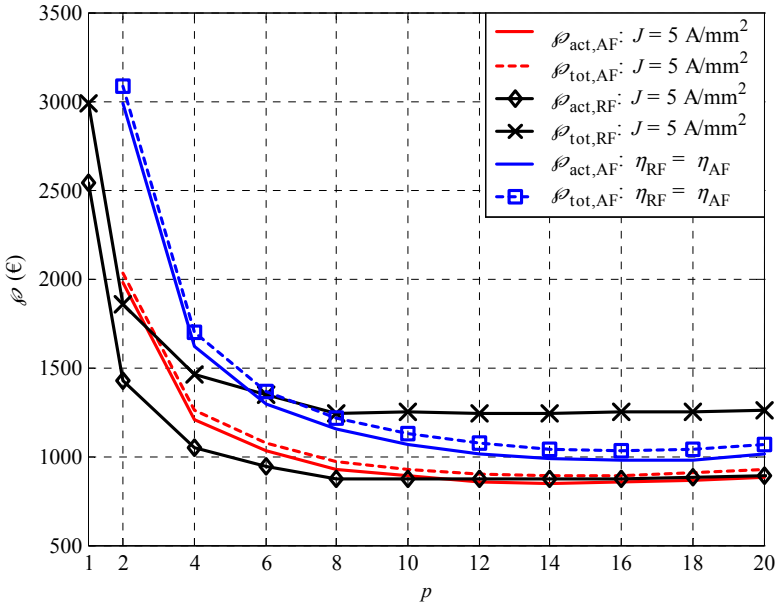

Fig. 5.31. Comparison of the material costs for 55 kW machines, the efficiency being set equal. n_s = 150 min^{-1}, A = 50 kA/m, k_l = 1.0 for the radial-flux machines.

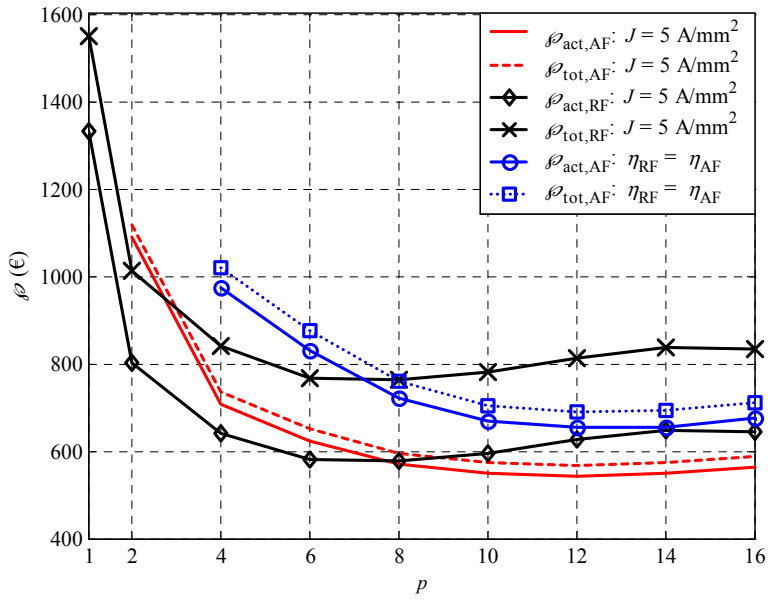

Fig. 5.32. Comparison of the material costs for 55 kW machines, the efficiency being set equal. n_s = 300 min^{-1}, A = 50 kA/m, k_l = 1.0 for radial-flux machines.

Influence of the stator yoke thickness on the volume ratio

Considering the vibrations and the noise of an electrical machine, the frame structures of the machine are of primary importance. Consequently, selection of the method for calculating the required thickness for the stator yoke may be a subject for discussion. Since no measurement-based information on the mechanical behaviour of axial-flux machine stators is available, the natural frequencies of the stators for both machine types have been calculated using a free body assumption. Therefore, to compare the machine topologies the constraints for the natural frequency may be neglected and only the constraint for the yoke thickness l_y may be taken into consideration by using its allowed minimum values. With low pole pair numbers, again the magnetic loading is used as a design constraint. The values for the stator yoke thickness are, l_y = 15 mm and l_y = 30 mm. The results are illustrated in Figs 5.33-5.34 for the 150 min^{-1} machines and again a 50 kA/m electric loading and current density J = 5A/mm^2 are used. The reference designs are the initial designs for which the stator yoke thickness has been determined based on the natural frequency constraint. According to the results, defining the constant thickness to be the stator yoke thickness does not significantly change the relative volume ratio. As expected, the radial-flux machines with large diameters are unfavourably affected by the natural frequency constraint. For example, in Fig. 5.33 a clear bifurcation in the relative volume curves may be observed for k_l = 0.2 as the pole pair number is above eight. If a constant stator yoke thickness is introduced for pole pair numbers p > 8, the volume of the AFIPM machine becomes relatively large. In this case, the axial-flux machine has a smaller diameter compared to the RF machine. Considering the natural frequency constraint, it is obvious that for the RF machine a thicker stator yoke will be required. On removing the constraint, the stator yoke thickness can be reduced and reduction of the overall volume of the RF machine is achieved. For k_l = 0.6 the curves are basically identical and for the higher values of k_l the curves represent an opposite relation than for k_l = 0.2, but the difference with respect to the initial situation remains small. Fig. 5.34 describes a similar behaviour, the constant yoke thickness l_y = 30 mm here being defined as design constraint. As a result, the influence of the natural frequency constraint on the overall volume required by the machine is obvious but not very significant, since a basically similar behaviour of the volume ratio is obtained even though a constant stator yoke thickness is introduced.

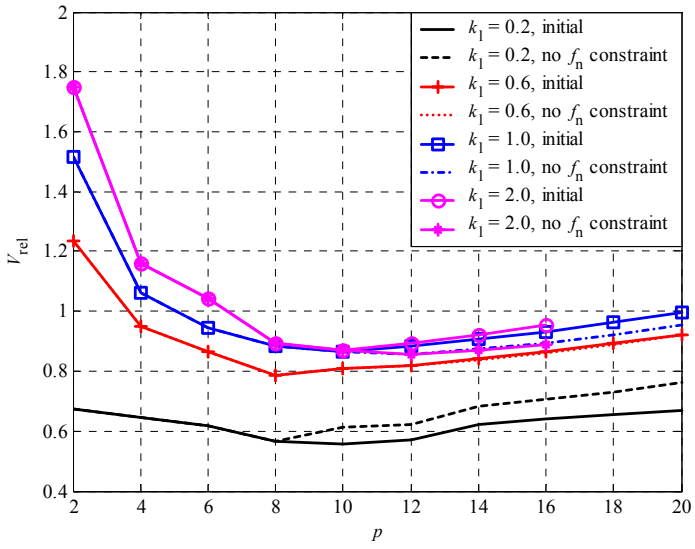

Fig. 5.33. Relative volume ratio comparison for 55 kW machines based on the natural frequency constraint or constant stator yoke thickness. The constant yoke thickness l_y = 15 mm is used if the magnetic loading is below the guide value. n_s = 150 min^{-1}, A = 50 kA/m and J = 5A/mm^2.

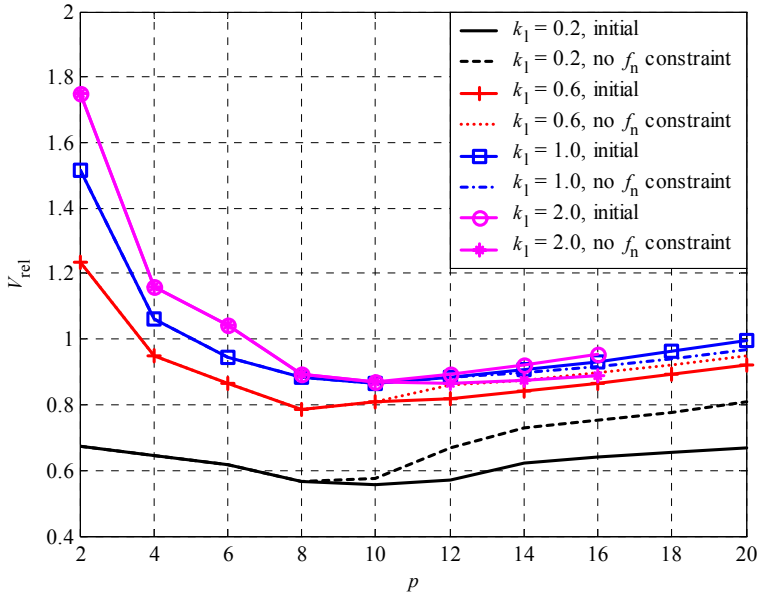

Fig. 5.34. Relative volume ratio comparison for 55 kW machines based on the natural frequency constraint or the constant stator yoke thickness. The constant yoke thickness l_y = 30 mm is used if the magnetic loading is below the guide value. n_s = 150 min^{-1}, A = 50 kA/m and J = 5A/mm^2.

Influence of teeth width on the volume- and cost-based comparison

Considering the axial-flux machines, it is shown that after a certain pole pair number the desired flux density value for the teeth on the average radius of the stator cannot be reached since there is a limiting mechanical constraint for the teeth width on the inner radius. With the radial-flux machines, however, the desired flux density value is achieved. This study compares the designs when the values for the flux density in the teeth are fixed to be equal by reducing the teeth flux density of the radial-flux machines to a level equalling that of the axial-flux machines. According to the results shown in Fig. 5.35, the relative volume for the measured 300 min^{-1} machines is almost constant, starting in this case at pole pair number p = 8, if the same magnetic flux density value is used. The initial curve shows an increasing tendency for the relative volume when p > 8. Obviously, the axial-flux machines, as regards relative volume, are adversely affected by the constraint for the minimum teeth. Even though the results in Fig. 5.35 consider only one machine type, it is obvious that for the other machine types a similar behaviour will be obtained. Correspondingly to the initial curve in Fig. 5.35, the curves for the relative volume, discussed in the previous chapters, indicate a similar slope. Presuming equal magnetic loading for the stator teeth, a turning flat of the relative volume curves is to be expected also in the other machine designs.

The further comparison shows the tendency of material costs when the magnetic loading in the teeth defined to be equal. The need for electrical steel can be expected to increase. On the other hand, because of the lower flux density in the stator teeth less permanent magnet material is required to achieve the desired flux density level in the air-gap. The results in Fig. 5.36 show a slight reduction of the cost of permanent magnet material when p > 8. Since, in this case, of the need for electrical steel correspondingly increases, the total cost, as a result, approximates the cost of the initially measured machine as the pole pair number reaches the value p = 16.

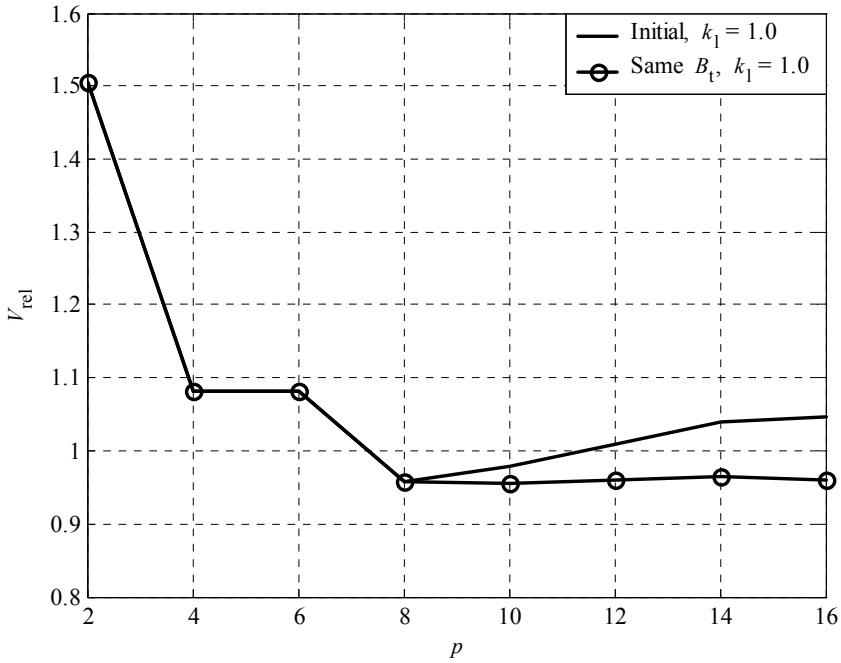

Fig. 5.35. Influence of the teeth magnetic flux density on the relative volume.

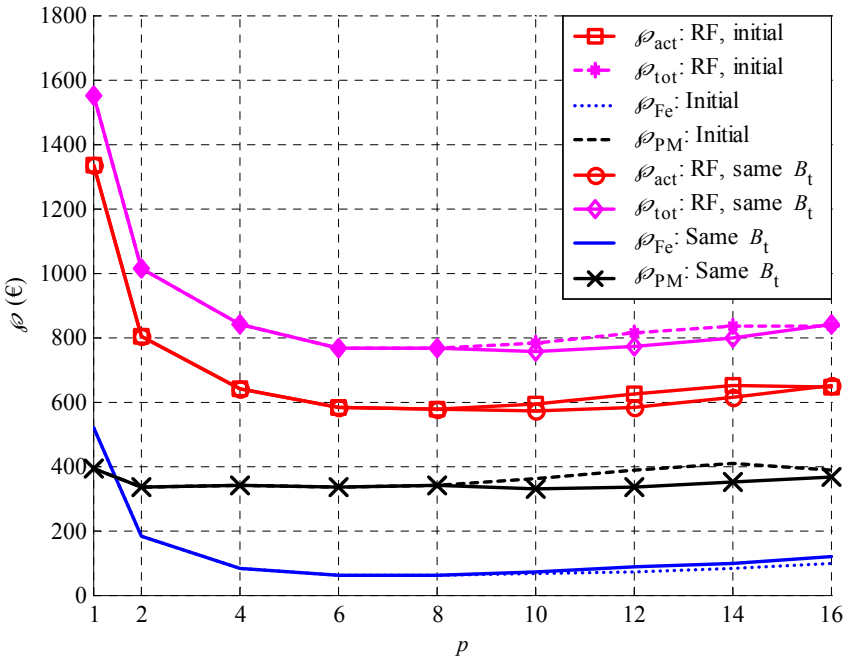

Fig. 5.36. Influence of the teeth flux density value on the material costs of 55 kW, 300 min^{-1} RF machines.

5.4.2. Summary

In the previous chapters, a detailed discussion on the performance comparison between low-speed surface-mounted AFIPM machines and surface-mounted RF machines was introduced. The comparative analyses have been based on equivalence of the electric and magnetic loadings of the machines. As a summary, the following statements may be done

- The design efficiency of an axial-flux machine is generally weaker if for the machines to be compared the current density, electrical loading and air-gap flux density are set equal.
- An equal efficiency can be obtained by reducing the current density of the AFIPM structure to about 1-2 A/mm^2 compared to the corresponding RF structure.
- Considering radial-flux machines with length ratio $k_l \approx 1$, then the overall volumes of the measured machines appear to be basically equal. As regards volume, the axial-flux machines perform better than the radial-flux machines, if the length ratio of the RF designs is below 0.5.
- If the same efficiency is obtained, the volume ratio increases by 15 to 20 %.
- Due to the excessive length of the end connections low-speed axial-flux machines with pole pair numbers $p = 1$ and $p = 2$ have extremely poor performance. Also because of the winding manufacturing, this machine type may be an impractical alternative.
- As the axial-flux machine is geometrically limited, the selection of pole pairs is restricted. While for the RF machine all pole pair numbers may be used, for the axial-flux machine certain pole pair numbers can not be used.
- The overall length of the rotor core and the stator supporting structures significantly affects the volume required by the AFIPM. For the measured 55 kW machines the net influence of these structures on the overall volume of the AFIPM is between 30 to 50 percent.
- Comparison of the raw material costs indicates, in general, following tendencies
  - The PM material cost is lower for an AF machines since the air-gap area of the AF machine is typically smaller.
  - The copper cost is higher for the AFIPM since the air-gap area of the AFIPM is smaller (more coil turns are required).
  - The active electrical steel cost is almost equal for both machine types but for the RF machine the cost of the total amount of electrical steel needed is significantly higher (up to 400 %).
- The active material costs of AF machines are generally smaller if the pole pair number is above 10.
- Considering the total raw material costs, the AFIPM is generally the cheaper alternative, except for pole pair numbers p =1 and $p = 2$.

5.4.3. Comparison between 11 kW, 200 kW and 500 kW machines

In the final part of the comparative study, different output powers are considered. Here, the pole pair number is limited. The pole pair number $p = 6$ is used for the 11 kW machines and the pole pair number 10 is used for the 200 kW and 500 kW machines. The results are described in table format and in graphical format as a function of the length ratio k_l for the selected pole pairs. Figs. 5.37-5.39 show the relative volume ratio as a function of k_l. The relative volume ratio is above one for 11 kW, except for the low k_l values. Thus, when the selected constraints are used, it seems that the construction of a 11 kW machine should not be that of an axial-flux machine if the typical length ratios may be employed for a radial-flux machine. Note that, because of the mechanical constraints, the value $A = 30$ kA/m is used for the designing of the 11 kW machines with rotational speed 600 min^{-1} whereas the value $A = 50$ kA/m is used for the calculating of the other machines. It should also be mentioned that for the calculated 11 kW machines the selected natural frequency constraints for the stator yoke do not have any contribution due to the small diameter of the machine. For the 11 kW machines the stator yoke thickness is calculated based on the magnetic loading or, alternatively, based on the minimum yoke thickness 15 mm.

As concerns the volume ratio, an opposite behaviour is obtained as described in Fig. 5.38 and in Fig. 5.39. The volume ratio is below one meaning that axial-flux machines require a smaller volume. The gradual steps in the curves are due to the change of number of slots per pole and phase q; especially, the change from value $q = 2$ to $q = 1$ causes a clearly perceptible step. The curves show also a contradictory behaviour compared to the curves in Fig. 5.37. In Fig. 5.37 a clear maximum point in the relative volume curves may be observed in the vicinity of $k_l = 1.5$, which is not the case for the 200 kW and 500 kW machines due to the selected natural frequency constraint. As the external diameter gets reduced (the length ratio k_l increases), a slightly thinner stator yoke is required and thus in the interval $2 < k_l < 4$ the relative volume curves show a behaviour opposite to that of the 11 kW machines.

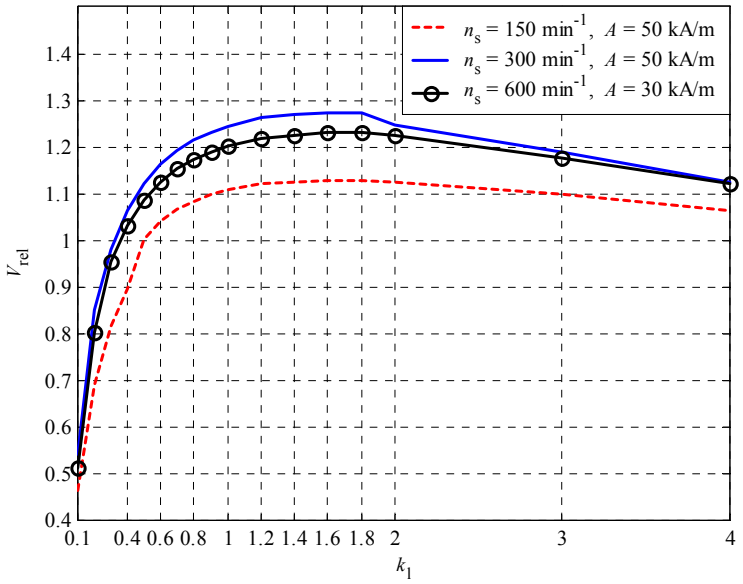

Fig. 5.37. Relative volume ratio of 11 kW machines, $p = 6$, $k_D = 0.6$ for AFIPM.

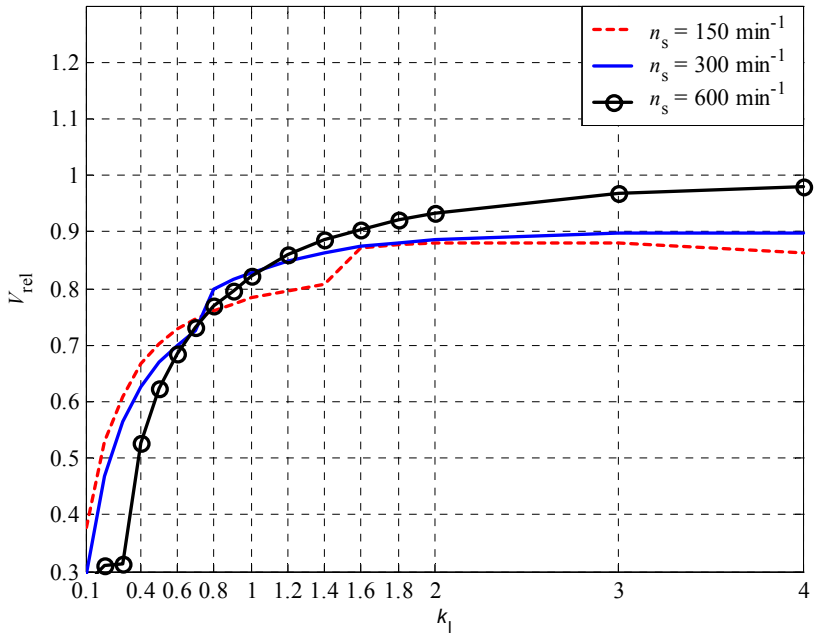

Fig. 5.38. Relative volume ratio of 200 kW machines, $p = 10$, $k_D = 0.6$ for AFIPM.

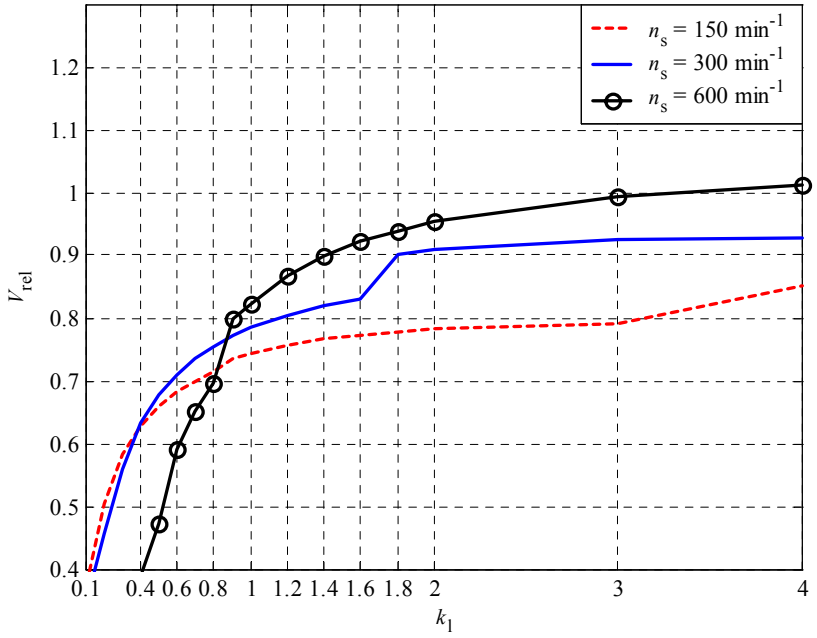

Fig. 5.39. Relative volume ratio of 500 kW machines, $p = 10$, $k_D = 0.6$ for AFIPM.

To conclude the comparative study 11 kW, 200 kW and 500 kW machines are compared using different values for the electrical loading and equal efficiencies. The results are listed in table 5.5, table 5.6 and table 5.7 for the 11 kW, 200 kW and 500 kW machines, respectively.

Table 5.5. Comparison of 11 kW, 300 min^{-1} machines with $p = 6$.

Parameter	AF: A = 30 kA/m	RF: A = 30 kA/m	AF: A = 50 kA/m	RF: A = 50 kA/m	AF: A = 70 kA/m	RF: A = 70 kA/m
D_{agap} [mm]	293	233	249	197	223	177
D_{out} [mm]	366	303	311	284	279	278
D_{tot} [mm]	486	303	442	283.5	419	278
l_{tot} [mm]	164	335	205	307	255	293
l_{end} [mm]	60	51	65.5	55	70.3	58
l_s [mm]	73	233	62	197	56	177
l_{PM} [mm]	5.6	6.5	5.5	7.1	5.5	7.5
l_{rotor} [mm]	21.5	--	16.8	--	14.4	--
l_y [mm]	15	15	15	15	15	15
y [mm]	30	15.0	52	23	79	30
S_{agap} [m^2]	0.086	0.170	0.097	0.122	0.078	0.098
V_{tot} [m^3]	0.031	0.024	0.031	0.019	0.035	0.018
$G_{Cu,end}$ [kg]	24.4	4.9	29.8	6.0	35	6.9
$G_{Cu,slot}$ [kg]	11.8	9.1	14.06	10.8	16.2	12.3
$G_{Cu,tot}$ [kg]	36.3	14	43.9	16.8	51.2	19.2
G_{Fe} [kg]	32	37	32	32	35	30
G_{PM} [kg]	4.0	5.7	2.8	4.4	2.3	3.7
$\wp_{tot}$ [€]	301	315	297	266	314	245
$\wp_{act}$ [€]	288	252	283	222	297	209
J [A/mm^2]	3.1	5.0	3.1	5.0	3.0	5.0
I_{ph} [A]	19	19	19	19	20	20
R_{ph} [Ω]	0.84	0.86	1.01	1.03	1.02	1.09
B_t [T]	1.88	1.9	1.84	1.9	1.89	1.9
B_y [T]	1.68	1.18	1.56	1.08	1.42	1.04
$B_{agap,PM}$ [T]	0.75	0.75	0.75	0.75	0.75	0.75
Q	36	36	36	36	36	36
q	1	1	1	1	1	1
P_{Cu} [W]	900	930	1100	1120	1230	1280
P_{Fe} [W]	115	92	110	79	120	74
P_{str} [W][1)]	110	110	110	110	110	110
$\cos\varphi$ [3)]	0.99	0.99	0.98	0.99	0.95	0.97
η [%]	90.7	90.7	89.3	89.3	88.3	88.3

[1)] Includes both air-gaps in the case of AFIPM machine
[2)] Calculated as $0.01 \cdot P$
[3)] Calculated based on (2.57). $E_{ph,PM} \approx 210$ V, $U_{ph} = 215$ V.

The values, given in Table 5.5, were obtained using equal electrical loadings for the measured machines and using the current density as a variable for the axial-flux machine designs in order to find the same efficiency between the designs. The results show clearly that the axial-flux machine with one rotor and two stators does not offer significant advantages over the conventional radial-flux machine that is designed using the length ratio $k_l = 1$ and using the selected design constraints. The axial-flux machine has a larger overall volume. However, if the rotor core axial length and the fixing structures are removed from the overall volume of axial-flux machine, there is no significant difference between the required overall volumes. As the electrical loading increases, the overall volume of the radial-flux machine shows a decreasing tendency whereas the tendency of the axial-flux machine volume is increasing. This is a result from the slot depth requirement. Even tough the external diameter of the axial-flux machine gets reduced, while the electrical loading increases, the axial length increases due to the deeper slots causing an increase of the overall volume.

The material costs of the AFIPM structure are smaller if A = 30 kA/m whereas the costs are higher if A = 50 kA/m and A = 70 kA/m. The behaviour of the material costs is mainly depending on the amount of copper required.

In order to obtain equivalent efficiencies for the corresponding AF and RF machines, in the axial-flux designs the values for the current density J must be, in this case, 2 A/mm^2 lower than for the radial-flux designs. Due to the larger air-gap diameter the flux density values for the stator yoke are higher for the axial-flux machine. On the other hand, the flux density levels in the stator teeth are slightly lower. The radial-flux machine has about 20 % lower iron losses. The copper losses are about 90 % of the total losses of the machine. According to the results in Fig. 5.37 and Table 5.5, it may be stated that for the 11 kW machine group the radial-flux machines are not outperformed by the AFIPM structure. In the comparison, the AFIPM structure gets a better torque density when the length ratio of the radial-flux machine is kept very low, $k_l < 0.3$. If in the RF design typical length ratio values are used, the torque density of the AFIPM structure remains smaller. Thus the axial-flux machine is beneficial to be used in such cases where the machine length is limited. Small torque AF machines seem not to be very attractive. The volume ratio depends also on whether the axial thickness of the rotor skeleton and the fixing structures of the AFIPM machine stators are taken into account. The relative volumes of the designs given in Table 5.5 are shown in Fig. 5.40.

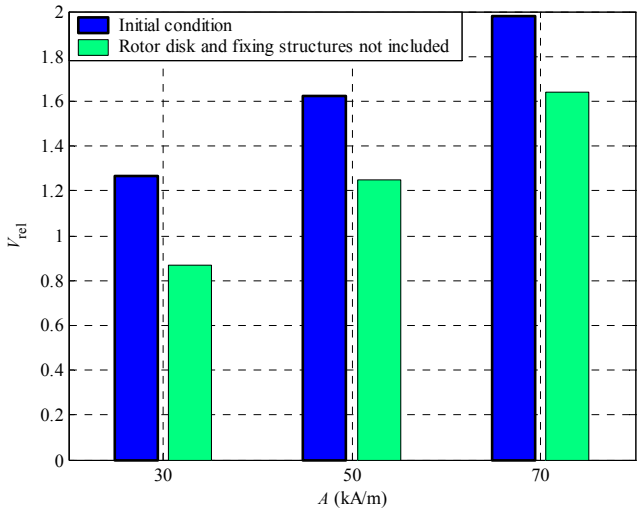

Fig. 5.40. Relative volume results of the 11kW, 300 min^{-1} designs. Comparison between initial condition and condition as the stators fixing structures as well as rotor core are not included into volume of the AFIPM machine.

Table 5.6. Comparison of 200 kW, 300 min^{-1} machines with $p = 10$.

Parameter	AF: A = 30 kA/m	RF: A = 30 kA/m	AF: A = 50 kA/m	RF: A = 50 kA/m	AF: A = 70 kA/m	RF: A = 70 kA/m
D_{agap} [mm]	774	615	661	516	594	469
D_{out} [mm]	968	744	827	650	743	622
D_{tot} [mm]	1100	744	975	650	900	622
l_{tot} [mm]	280	728	313	638	355	599
l_{end} [mm]	65	56	74	61	79	65
l_s [mm]	194	615	165	516	149	469
l_{PM} [mm]	5.1	5.6	5.1	5.9	5.2	6.0
l_{rotor} [mm]	74	--	62	--	54	--
l_y [mm]	48	43	43	38	41	35
y [mm]	28	17	56	27	84	37
S_{agap} [m^2] [1)]	0.94	1.19	0.69	0.84	0.55	0.69
V_{tot} [m^3]	0.27	0.32	0.23	0.21	0.23	0.18
$G_{Cu,end}$ [kg]	101	23	136	27	151	31
$G_{Cu,slot}$ [kg]	73	64	95	75	107	86
$G_{Cu,tot}$ [kg]	172	87	230	102	257	117
G_{Fe} [kg]	470	539	401	367	387	340
G_{PM} [kg]	25.5	35.0	18.6	25.8	15.3	21.6
$\mathcal{C}_{tot}$ [€]	1880	2820	1860	2100	1870	1870
$\mathcal{C}_{act}$ [€]	1780	1770	1760	1440	1760	1350
J [A/mm^2]	3.5	5.0	3.2	5.0	3.3	5.0
I_{ph} [A]	325	324	337	341	343	359
R_{ph} [Ω]	0.018	0.018	0.018	0.02	0.02	0.02
B_t [T]	1.79	1.9	1.75	1.9	1.76	1.9
B_y [T]	0.76	0.68	0.75	0.74	0.84	0.74
$B_{agap,PM}$ [T]	0.75	0.75	0.75	0.75	0.75	0.75
Q	120	120	120	60	120	60
q	2	2	2	1	2	1
P_{Cu} [W]	5600	5750	6300	6900	7280	7830
P_{Fe} [W]	1450	1330	1580	1170	1800	1210
P_{str} [W] [2)]	1000	1000	1000	1000	1000	1000
$\cos\varphi$ [3)]	0.99	0.99	0.96	0.95	0.95	0.91
η [%]	96.1	96.1	95.7	95.7	95.2	95.2

[1)] Includes both air-gaps in the case of AFIPM machine
[2)] Calculated as $0.005 \cdot P$
[3)] Calculated based on (2.57). $E_{ph,PM} \approx 210$ V, $U_{ph} = 215$ V.

Table 5.7. Losses and consumption of materials for 500 kW, 300 min^{-1} machines with p = 10, J = 5 A/mm^2.

Parameter	AF: A = 30 kA/m	RF: A = 30 kA/m	AF: A = 50 kA/m	RF: A = 50 kA/m	AF: A = 70 kA/m	RF: A = 70 kA/m
D_{agap} [mm]	1053	836	895	711	810	642
D_{out} [mm]	1316	1045	1120	915	1010	860
D_{tot} [mm]	1460	1045	1280	915	1180	860
l_{tot} [mm]	378	957	375	844	392	784
l_{end} [mm]	71	61	80	67	85	71
l_s [mm]	263	836	223	711	202	642
l_{PM} [mm]	5.1	5.4	5.1	5.4	5.1	5.4
l_{rotor} [mm]	110	--	91	--	80	--
l_y [mm]	81	82	68	67	62	62
y [mm]	27	18	49	30	68	42
S_{agap} [m^2] [1)]	1.74	2.2	1.26	1.6	1.03	1.29
V_{tot} [m^3]	0.63	0.82	0.48	0.56	0.43	0.45
$G_{Cu,end}$ [kg]	184	40	230	49	255	58
$G_{Cu,slot}$ [kg]	134	117	167	140	183	166
$G_{Cu,tot}$ [kg]	318	157	397	189	438	224
G_{Fe} [kg]	1280	1770	910	1180	781	1000
G_{PM} [kg]	47	62	34	45	28	37
$\mathcal{C}_{tot}$ [€]	3730	6320	3420	4600	3320	3980
$\mathcal{C}_{act}$ [€]	3600	3740	3250	2940	3140	2700
J [A/mm^2]	3.45	5.0	3.35	5.0	3.5	5.0
I_{ph} [A]	819	817	837	840	871	864
R_{ph} [mΩ]	5.0	5.2	5.7	6.0	6.3	6.7
B_t [T]	1.9	1.9	1.9	1.9	1.9	1.9
B_y [T]	0.63	0.5	0.68	0.54	0.73	0.55
$B_{agap,PM}$ [T]	0.75	0.75	0.75	0.75	0.75	0.75
Q	120	120	120	120	120	120
q	2	2	2	2	2	2
P_{Cu} [kW]	10.1	10.5	11.9	12.6	14.4	15.0
P_{Fe} [kW]	2.9	2.7	2.9	2.6	3.1	2.6
P_{str} [kW] [2)]	1.5	1.5	1.5	1.5	1.5	1.5
$\cos\varphi$ [3)]	0.98	0.98	0.96	0.95	0.92	0.93
η [%]	97.2	97.2	96.8	96.8	96.3	96.3

[1)] Includes both air-gaps in the case of AFIPM machine
[2)] Calculated as 0.003·P
[3)] Calculated based on (2.57). $E_{ph,PM} \approx 210$ V, $U_{ph} = 215$ V.

According to the results in Tables 5.5-5.7 the machines with output power 200 kW and 500 kW show a similar behavior. Here, the axial-flux machine has a smaller overall volume if the value for the electric loading is 30 kA/m. If the electric loading is increased up to 70 kA/m, then, in the 200 kW machine group, the radial-flux structure seems to have a slightly smaller overall volume whereas, in the 500 kW machine group, the volumes of both machine types are practically the same.

The total material consumption of axial-flux machines is significantly cheaper. In terms of active material costs, the axial-flux machine is generally cheaper, but, with the linear current density A being increased, the difference in active material costs for both machine types gets smaller. Note that there is a significant difference in copper consumption. Axial-flux machines require twice the amount of copper needed for radial-flux machines.

Considering the designs discussed in Tables 5.6 and 5.7, it must be noted that for the axial-flux designs the current density has to be about 2 A/mm^2 lower so that an equal efficiency could be obtained. Low current density combined with use of an 70 kA/m electric loading and mechanical constraints, these are factors that cause for the slot depth of an axial-flux machine to become significantly bigger, e.g. in the case of a 200 kW machine with A = 70 kA/m, the required slot depth is 84 mm whereas it is only 37 mm in the case of a RF machine.

According to the results given in Tables 5.6 and 5.7, it may be concluded that, if reduction of electromagnetic sizing is required, the best performance is achieved by the AFIPM structure. Furthermore, the results show that the AFIPM structure is generally cheaper to manufacture, as regarding the total consumption of material. For the AFIPM machine the consumption of electrical steel and permanent magnet material remains lower while there is a higher consumption of copper.

5.4.4. Comparison summary

Axial-flux and radial-flux permanent-magnet machines with rotor surface-mounted magnets were compared. The comparison was first based on equivalence of the electrical and magnetic loadings for the machines. Mechanical constraints, which were considered to be practical mechanical design limitations, were introduced. The designs were systematically calculated using the 2D FEA in order to eliminate uncertainties in the electromagnetic design of machines. According to the results obtained in this study, the axial-flux machine topology performs better in applications for which the radial-flux machine should be designed such that the value of the length ratio is below 0.4…0.6. The axial-flux machine is a more attractive alternative to be used in applications that require high torque values and low electrical loading values (same output power regardless of the torque required).

If for the corresponding machines the same current density is applied, then the axial-flux machines generate poorer efficiencies. The reason for this is that for the end-windings of an AFIPM structure the relative amount of copper is considerably larger. According to this consideration, the radial-flux machine may thus be the more suitable alternative.

6. Conclusions and recommendations

In this study, the first goal has been the development of an analytical design method for preliminary design of surface-mounted low-speed axial-flux permanent-magnet machines with one-rotor-two-stators configuration. Due to the computation power and time requirements of the 3D FEA a special design tool was needed. The design tool demonstrated here employs a quasi-3D computation method. The developed computation procedure is described. A thermal model, developed for the thermal design of axial-flux machines, is suggested and included in the design tool.

To verify the operation of the design tool as well as to get manufacturing expertise a prototype machine was constructed. Manufacturing of the prototype machine has been successful. Despite a slight factory error in the permanent magnets causing some distortion to the predicted back-EMF waveform and thus also affecting the measured cogging torque, the measurement results, generally, agree well with the calculation results. Comparing the other calculated parameters with the measurement values, there is a good agreement between the results. The design tool may thus be considered to be suitable for predicting the performance prediction of axial-flux permanent-magnet machines.

Future research should include further studies on the theory of thermal modelling of axial-flux machines and more thermal modelling measurement data are needed. In this study, measurements were performed to test the developed analytical thermal model but the measurement results presented here are gained with one only prototype machine and, consequently, do not show any statistical behaviour of thermal constant resistances. To find suitable correlations describing heat transfer in axial-flux machines – according to radial-flux machines - more machines with different power ratings need thus to be constructed and analysed.

The further goal of this study has been to present a comparative analysis of the performance of surface-mounted axial-flux and surface-mounted radial-flux permanent-magnet machines. This part of the research work has been encouraged by the ABB companies. The study has specialised in powers ranging from 10 kW up to 500 kW with speed ranging from 150 min^{-1} to 600 min^{-1}, thus covering a large variety of low-speed industrial applications. Here, the main focus is on 55 kW machines, which in agreement with the industrial partner was set to be the reference output power.

A discussion on the mechanical constraints of the different machine topologies is introduced. A systematic method for including the mechanical constraints in the procedure of sizing the machines has been developed and the results obtained from the mechanical studies are used in the machine designs.

In the performance comparison a large number of different machine designs is considered the calculations of which are based on the analytical sizing procedure introduced in this study as well as on the computations with the 2D FEA. The comparison is performed for corresponding machines with equal electric and magnetic loading. According to the comparison results, the efficiency of axial-flux machines, generally, remains weaker if the same magnetic loading and electrical loading are used. Furthermore, the numbers available for the pole pairs are generally more limited for the AFIPM structure since the AFIPM machine has more restricting geometrical constraints. With a small pole pair number, arranging the end-windings to the space available is difficult. On the other hand, the selection of available pole pair numbers is limited due to the minimum teeth width constraint on the inner radius of the AFIPM machine stator, i.e. high pole pair numbers may not be used.

Considering the volume comparison, the results show that the difference in overall volume between the AFIPM and RF structure is small if typical values for the main dimensions of the radial-flux machine are employed, i.e. stack length divided by air-gap diameter is in the vicinity of one. If the length ratio is below 0.5, the overall volume of the RF machine is considerably higher than the volume of the AFIPM structure.

On neglecting the fixing structures and employing a rotor thickness equal to the permanent-magnet thickness, the overall volume of the AFIPM designs can be reduced by about 30 %. The overall volume of axial-flux machines is thus significantly characterized by the mechanical aspects with relation to the rotor structure and the fixing of the stator to the bearing shields.

The material costs of the different machine types are more or less equal. The results may vary depending on the way of comparing. If active parts only are considered, the material costs of the AFIPM structure are generally smaller if the pole pair number $p \geq 8$. The amount of permanent magnet material needed for an axial-flux machine remains smaller, but, on the other hand, the copper consumption is typically higher. The total consumption of electrical steel is less for the AFIPM structure.

As a conclusion, the AFIPM structure is shown to be an attractive solution if an axially short radial-flux machine is considered to be implemented into specific geometrically limited applications. The turn-around point for the radial-flux machine length ratio is approximately 0.5. For axial-flux machines, however, an even lower current density is required in order to achieve the corresponding efficiency.

In the comparing considerations only AFIPM machine structures with conventional lap windings have been included. In future research a corresponding comparative analysis could focus on single-sided axial-flux machines and radial-flux machines for the purpose of proving the better suitability of the single-sided axial-flux machine configuration for integrated applications. A further relevant comparison could specialise in axial-flux and radial-flux machines equipped with concentrated windings. Concentrated windings reduce the amount of copper in the end windings and thus the construction of low-speed axial-flux machines by employing the double-layer concentrated winding scheme may prove to be very advantageous.

REFERENCES

ABB, 2004. Product Catalogue: Drive^{IT} Permanent Magnet Motors.

Akatsu, K., Wakui, S., 2004. A Comparison between Axial and Radial-flux PM Motor by Optimum Design Method from the Required Output NT Characteristics. In *Proceedings of International Conference on Electrical Machines ICEM'04*, Cracow, Poland, 5-8 September 2004, on CD-ROM.

Arshad, W. M., Maliti, K. C., Sadarangani, C., 1999. On the Use of Soft Magnetic Composite (SMC) Iron Powder Materials in Induction Machines. In *Proceedings of International Conference on Electrical Engineering and Technology, ICEET'99*, Dar es Salaam, Tanzania, 6-7 September 1999, pp. 132-138.

Atallah, K., Howe, D., Mellor, P. H., Stone, D. A., 2000. Rotor Loss in Permanent-Magnet Brushless AC Machines. *IEEE Transactions on Industry Applications*, Vol. 36, No. 6, pp. 1612-1618.

Atherton, W. A., 1984. *From Compass to Computer; A History of Electrical and Electronics Engineering,* London: The Macmillan Press Ltd, p. 337.

Aydin, M., Huang, S., Lipo, T.A., 2001. Design and 3D Electromagnetic Field Analysis of Non-slotted and Slotted TORUS Type Axial-flux Surface-mounted Permanent Magnet Disc Machines. In *Proceedings of IEEE Electric Machines and Drives Conference, IEMDC'01*, pp. 645-651.

Barakat, G., El-meslouhi, T., Dakyo, B., 2001. Analysis of the Cogging Torque Behavior of a Two-Phase Axial-flux Permanent Magnet Synchronous Machine. *IEEE Transactions on Magnetics*. Vol. 37, No. 4, pp. 2803-2805.

Bilen, K., Yapici, S., 2002. Heat Transfer from a Surface Fitted with Rectangular Blocks at Different Orientation Angle. *Heat and Mass Transfer*. Vol. 38, pp. 649-655.

Braid, J., van Zyl, A., Landy, C., 2003. Unbalanced Load Sharing in a Prototype Multistage Axial-Flux Permanent Magnet Synchronous Machine. In *Proceedings of IEEE Electric Machines and Drives Conference, IEMDC'03*, Madison, United States, 1-4 June 2003, Vol. 3, pp. 1935-1940.

Brown, N., Haydock, L., Bumby, J., 2002. An Idealised Geometric Approach to Electromagnetically Comparing Axial and Radial-flux Permanent Magnet machines, in *Proceedings of International Conference on Electrical Machines*, *ICEM'02*, on CD-ROM.

Campbell, P., 1974. Principles of a Permanent-Magnet Axial-Field D.C. Machine. *Proceedings of the IEE*, Vol. 121, No. 12, pp. 1489-1494.

Campbell, P., 1994. *Permanent Magnet Materials and their Applications*. Cambridge: University Press, p. 207.

Caricchi, F., Crescimbini, A., Santini, E., Santucci, C., 1998. FEM Evaluation of Performance of Axial-flux Slotted Permanent Magnet Machines. In *Proceedings of Thirty-Third IAS Annual Meeting*, pp. 12-17.

Caricchi, F., Crescimbini, F., Di Napoli, A., Santini, E., 1992. Optimum CAD-CAE Design of Axial-flux Permanent Magnet Motors. In *Proceedings of International Conference on Electrical Machines, ICEM'92*, pp. 637-641.

Carpenter, 2004. Product Catalogue: Carpenter Special Steels.

Carrichi, F., Crescimbini, F., Honorati, O., 1998. Low-Cost Compact Permanent Magnet Machine for Adjustable-Speed Pump Application. *IEEE Transactions on Industry Applications*, Vol. 34, No. 1, pp. 109-116.

Carrichi, F., Crescimbini, F., Santini, E., 1995. Basic Principle and Design Criteria of Axial-Flux PM Machines Having Counterrotating Rotors. *IEEE Transactions on Industry Applications*, Vol. 31, No. 5, pp. 1062-1068.

Cavagnino, A., Lazzari, M., Profumo, F., Tenconi, A., 2001. A Comparison Between the Axial-flux and the Radial-flux Structures for PM Synchronous Motors. In *Proceedings of IEEE Industry Applications Conference, 36th IAS Annual Meeting,* pp. 1611-1618.

Chan, C.C., 1987. Axial-Field Electrical Machines – Design and Applications. *IEEE Transactions on Energy Conversion*, Vol. EC-2, No. 2, pp. 294-300.

Chung, M-J., Gweon, D-G., 2002. Modeling of the Armature Slotting Effect in the Magnetic Field Distribution of a Linear Permanent Magnet Motor. *Electrical Engineering - Archiv für Elektrotechnik*. Vol. 84, pp. 101-108.

Cogent, 2004. Product Catalogue: Non-Oriented Fully Processed Electrical Steels.

Daily, J.W., Nece, R.E., 1960. Chamber dimension effects on induced flow and frictional resistance of enclosed rotating disks. *Journal of Basic Engineering*. Vol. 82, pp. 217-232.

Deng, F., 1999. An Improved Iron Loss Estimation for Permanent Magnet Brushless Machines. *IEEE Transactions on Energy Conversion*. Vol. 14, No. 4, pp. 1391-1395.

Deshpande, U.S., 2003. Recent Advances in Materials for Use in Permanent Magnet Machines-a Review. In *Proceedings of IEEE Electric Machines and Drives Conference, IEMDC'03*, Madison, United States, 1-4 June 2003, Vol. 1, pp. 509-515.

El-Hasan, T.S., Luk, P.C.K., Bhinder, F.S., Ebaid, M.S., 2000. Modular Design of High-Speed Permanent-Magnet Axial-Flux Generators. *IEEE Transactions on Magnetics*, Vol. 36, No. 5, pp. 3358-3561.

Ferroxcube, 2004. Datasheets of Ferrites. http://www.ferroxcube.com/prod/assets/powapp.htm. [cited 19 November 2004]. Available from Ferroxcube International Holding B.V.

Fish, G.E., 1990. Soft Magnetic Materials. In *Proceedings of the IEEE*, Vol. 78, No. 6, pp. 947-972.

Flegel, W., Losasso, M., Rohner, F., 2000. LHCb Magnet: Technical Design Report. http://doc.cern.ch//archive/electronic/other/generic/public/cer-2173340.pdf. [cited 19 November 2004]. Available from CERN.

Fukao, T., Chiba, A., Matsui, M., 1989. Test Results on a Super-High-Speed Amorphous-Iron Reluctance Motor. *IEEE Transactions on Industry Applications.* Vol. 25, No. 1, pp. 119-125.

Gair, S., Canova, A., Eastham, J. F., Betzer, T., 1995. A New 2D FEM Analysis of a Disc Machine with Offset Rotor. In *Proceedings of the International Conference on Power Electronics, Drives and Energy Systems for Industrial Growth*. Vol. I, pp. 617-621.

Gieras, J. F., Wang, R-J., Kamper, M. J., 2004. *Axial-flux Permanent Magnet Machines.* Dordrecht: Kluwer Academic Publishers, p. 340.

Gieras, J.F., Wing, M., 1997. *Permanent Magnet Motor Technology – Design and Applications*. New York: Marcel Dekker Inc, p. 444.

Haataja, J., 2003. A Comparative Performance Study of Four-Pole Induction Motors and Synchronous Reluctance Motors in Variable Speed Drives. Dissertation. Lappeenranta University of Technology, Finland, p. 135.

Hagedorn, P., Wallaschek, J., 1992. Travelling Wave Ultrasonic Motors, Part I: Working Principle and Mathematical Modelling of the Stator. *Journal of Sound and Vibration*, Vol. 155, No. 1, pp. 31-46.

Hagedorn, P., Wallaschek, J., 1993. Travelling Wave Ultrasonic Motors, Part II: A Numerical Method for the Flexural Vibrations of the Stator. *Journal of Sound and Vibration*, Vol. 168, No. 1, pp. 115-122.

Hakala, H., 2000. Integration of Motor and Hoisting Machine Changes the Elevator Business, In *Proceedings of International Conference on Electrical Machines, ICEM2000*, Helsinki, Finland, Vol. 3, pp. 1242-1245.

Hanselman, D. C., 2003. Brushless Permanent Magnet Motor Design. New York: Elsevier Scientific Publishing Company, p. 330.

Heikkilä, T., 2002. Permanent Magnet Synchronous Motor for Industrial Inverter Applications – Analysis and Design. Dissertation. Lappeenranta University of Technology, Finland, p. 109.

Heller, B., Hamata, V., 1977. *Harmonic field effects in induction machines*. Amsterdam: Elsevier Scientific Publishing Company, p. 330.

Hitachi Metals, 2004. Product Catalogue: HILOP™. Available at: http://www.hitachi-metals.co.jp/e/prod/prod03/pdf/hg-a17_e.pdf. [cited 10 December 2004]. Available from Hitachi Metals Ltd, Tokyo, Japan.

Höganäs, 2003. Product Catalogue: SOMALLOY™500.

Honeywell, 2004. Product Catalogue: METGLAS™.

Honsinger, V. B., 1987. Sizing Equations for Electrical Machinery. *IEEE Transactions on Energy Conversion*. Vol. EC-2, No. 1, pp. 116-121.

Huang, S., Aydin, M., Lipo, T.A., 2001. TORUS Concept Machines: Pre-Prototyping Design Assessment for Two Major Topologies. In *Proceedings of IEEE Industry Applications Conference, Thirty-Sixth IAS Annual Meeting*. Vol. 3, p. 1619-1625.

Huang, S., Aydin, M., Lipo, T.A., 2002. A Direct Approach to Electrical Machine Performance Evaluation: Torque Density Assessment and Sizing Optimization. In *Proceedings of International Conference on Electrical Machines, ICEM'02*, on CD-ROM.

Huang, S., Luo, J., Leonardi, F., Lipo, T.A., 1998. A General Approach to Sizing and Power Density Equations for Comparison of Electrical Machines. *IEEE Transactions on Industry Applications*. Vol. 34, No. 1, pp. 92-97.

Huang, S., Luo, J., Leonardi, F., Lipo, T.A., 1999. A Comparison of Power Density for Axial-flux Machines Based on General Purpose Sizing Equations. *IEEE Transactions on Energy Conversion*. Vol. 14, No. 2, pp. 185-192.

Hultman, L.O., Jack, A.G., 2003. Soft Magnetic Composites-Materials and Applications. In *Proceedings of IEEE Electric Machines and Drives Conference, IEMDC'03*, Madison, United States, 1-4 June 2003, Vol. 1, pp. 516- 522.

Huntsman, 2004. User guide for Adhesives. http://www.huntsman.com/structural-adhesives/Media/usersGuide_Uk.pdf. [cited 22 November 2004]. Available from Huntsman Advanced Materials, Everberg, Belgium.

Hwang, C-C., Cho, Y.H., 2001. Effects of Leakage Flux on Magnetic Fields of Interior Permanent Magnet Synchronous Motors. *IEEE Transactions on Magnetics*. Vol. 37, No. 4, pp. 3021-3024.

Incropera, F.P., DeWitt, D.P., 1996. *Fundamentals of Heat and Mass Transfer*. New York: John Wiley&Sons, p. 886.

Ish-Salom, J., 1995. Composite Magnetic Structure for Planar Motors. *IEEE Transactions on Magnetics*. Vol. 31, No. 6, pp. 4077-4079.

Jensen, C. C., Profumo, F., Lipo, T. A., 1992. A low-Loss Permanent-Magnet Brushless dc Motor Utilizing Tape Wound Amorphous Iron. *IEEE Transactions on Industry Applications*. Vol. 28, No. 3, pp. 646-651.

KANE Magnetics International, 2004. Engineering data sheets. http://www.kanemagnetics.de/products/pdf/magnets/magnet_mechandphys.pdf, [cited 19 November 2004]. Available from Kane Magnetics GmbH, Essen, Germany.

Kiley, J., Tolikas, M., 2004. Design of a 28 HP, 47 000 rpm Permanent Magnet Motor for Rooftop Air Conditioning, http://www.satcon.com/pdf/47000rpm.pdf, [cited 16 August 2004], Available from SatCon Technology Corporation, Boston, USA.

Kurronen, P., 2003. Torque Vibration Model of Axial-Flux Surface-Mounted Permanent Magnet Synchronous Machine. Dissertation. Lappeenranta University of Technology, Finland, p. 123.

Kylander, G., 1995. Thermal Modeling of Small Cage induction Motors. Dissertation. Chalmers University of Technology, Sweden, p. 113.

Leissa, A. W., 1969. *Vibration of Plates* -- *NASA SP-160*. Washington, DC. U.S. Government Printing Office, p. 343.

Li, Y., 1996. Design and Control of New Class of Doubly Salient Permanent Magnet Machines. Dissertation. University of Wisconsin-Madison, United States, p. 164.

Luukko, J., 2001. Direct Torque Control of Permanent Magnet Synchronous Machines – Analysis and Implementation. Dissertation. Lappeenranta University of Technology, Finland, p. 172.

Magnetic Metals, 2004. Product Catalogue: Ni-Fe alloys.

Magnussen, F., Sadarangani, C., 2003a. Winding Factors and Joule Losses of Permanent Magnet Machines with Concentrated Windings. In *Proceedings of IEEE Electric Machines and Drives Conference, IEMDC'03*, Vol. 1, pp. 333-339.

Magnussen, F., Thelin, P., Sadarangani, C., 2003b. Design of Compact Permanent Magnet Machines for a Novel HEV Propulsion System. In *Proceedings of the 20th International Electric Vehicle Symposium (EVS) and Exposition,* on CD-ROM.

Negrea, M., Rosu, M., 2001. Thermal Analysis of a Large Permanent Magnet Syncronous Motor for different Permanent Magnet Rotor Configurations. In *Proceedings of IEEE Electric Machines and Drives Conference, IEMDC'01*, Cambridge, United States, 17-20 June 2001, pp. 777-781.

Neorem magnets, 2004. Neorem magnets data sheets. http://www.neorem.fi/n/index.html. [cited 19 November 2004]. Available from Neorem Magnets Oy, Ulvila, Finland.

Parviainen, A., Niemelä, M., Pyrhönen, J., 2002b. Reduction of Torque Pulsations in Axial-flux Interior PM Synchronous Machines, In *Proceedings of Nordic Workshop on Power and Industrial Electronics*, Stockholm, Sweden, 12-14 August 2002, on CD-ROM.

Parviainen, A., Niemelä, M., Pyrhönen, J., 2003a. Analytical, 2D FEM and 3D FEM modelling of PM axial-flux machines, In *Proceedings of 10th European Conference on Power Electronics and Applications*, EPE'03, Toulouse, France, 1-4 September 2003, on CD-ROM.

Parviainen, A., Niemelä, M., Pyrhönen, J., 2003b. A Novel Axial-flux Permanent Magnet Machine to Laboratory Use, In *Proceedings of 11th International Symposium on*

Electromagnetic Fields in Electrical Engineering, Maribor, Slovenia, 18-20 September 2003, pp. 277-280.

Parviainen, A., Niemelä, M., Pyrhönen, J., 2004a. Modeling Axial-flux Permanent-Magnet Machines. *IEEE Transaction on Industry Applications*. Vol. 40, No. 5, pp. 1333-1340.

Parviainen, A., Niemelä, M., Pyrhönen, J., 2004b. Modeling Axial-flux PM Machines: Thermal Analysis. In *Proceedings of International Conference on Electrical Machines ICEM'04*, Cracow, Poland, 5-8 September 2004, on CD-ROM.

Parviainen, A., Pyrhönen, J., Niemelä, M., 2002a. Axial-flux Permanent Magnet Synchronous Motor With Sinusoidally Shaped Magnets. *Studies in Applied Electromagnetics and Mechanics*, Vol. 22, pp. 271-276. Amsterdam, The Netherlands: IOS Press.

Perho, J., 2002. Reluctance Network for Analysing Induction Machines. Dissertation. Helsinki University of Technology, Finland, p. 147.

Platt, D., 1989. Permanent Magnet Synchronous Motor with Axial-flux Geometry. *IEEE Transactions on Magnetics*, Vol. 25, No. 4, pp. 3076-3079.

Profumo, F., Tenconi, A., Zhang, Z., Cavagnino, A., 1998. Novel Axial-flux Interior PM Synchronous Motor Realized with Powdered Soft Magnetic Materials. Industry Applications Conference, 1998. In *Proceedings of IEEE Industry Applications Conference, Thirty- Third IAS Annual Meeting*. Vol. 1, p.152-158.

Profumo, F., Zhang, Z., Tenconi, A., 1997. Axial-flux Machines Drives: A New Viable Solution for Electric Cars. *IEEE Transactions on Industrial Electronics*, Vol. 44, No. 1, pp. 39-45.

Qu, R., Aydin, M., Lipo, T.A., 2003. Performance Comparison of Dual-Rotor Radial-Flux and Axial-Flux Permanent-Magnet BLDC Machines. In *Proceedings of IEEE Electric Machines and Drives Conference, IEMDC'03*, Madison, United States, 1-4 June 2003, Vol. 3, pp. 1948-1954.

Qu, R., Lipo, T.A., 2004. Analysis and Modeling of Air-Gap and Zigzag Leakage Fluxes in a Surface-Mounted Permanent Magnet Machine. *IEEE Transactions on Industry Applications.* Vol. 40, No. 1, pp. 121-127.

Rasmussen, C.B., Ritchie, E., 1997. A magnetic Equivalent Circuit Approach for Predicting PM Motor Performance. In *Proceedings of IEEE Industry Applications Conference, IAS Annual Meeting*. pp. 10-17.

Saari, J., 1998. Thermal Analysis of high-Speed Induction Machines. Dissertation. Helsinki University of Technology, Finland, p. 73.

Sahin, F., 2001. Design and Development of a High-Speed Axial-Flux Permanent-Magnet Machine, Dissertation. Eindhoven University of Technology, The Netherlands, p. 228.

Salminen, P., 2004. Fractional Slot Permanent Magnet Synchronous Motors For Low Speed Applications. Dissertation. Lappeenranta University of Technology, Finland, p. 150.

Scowby, S.T., Dobson, R.T., Kamper M.J., 2004. Thermal Modeling of an Axial-flux Permanent Magnet Machine. *Applied Thermal Engineering*. Vol. 24, pp. 193-207.

Silvester, P.P., Ferrari, R.L., 1983. *Finite Elements for Electrical Engineers*. Cambridge: Cambridge University Press. p. 209.

Sitapati, K., Krishnan, R., 2001. Performance Comparisons of Radial and Axial Field Permanent-Magnet, Brushless Machines. *IEEE Transactions on Industry Applications*. Vol. 37, No. 5, pp. 1219-1226.

Söderlund, L., Eriksson, J-T., Salonen, J., Vihriälä, H., Perälä, R., 1996. A Permanent-Magnet Generator for Wind Power Applications. *IEEE Transactions on Magnetics*, Vol. 32, No. 4, pp. 2389-2392.

Spooner, E., Chalmers, B.J., 1988. Toroidally-wound, slotless, axial-flux permanent magnet, Brushless-DC motor. In *Proceedings of International Conference on Electrical Machines, ICEM'88*, Pisa, Italy, 1988. pp. 81-86.

Strnat, K.J., 1990. Modern Permanent Magnets for Applications in Electro-Technology. *Proceedings of The IEEE*, Vol. 78, No. 6, pp. 923-946.

Timoshenko, S., Young, D.H., Weaver, W., 1974. *Vibration Problems in Engineering*. New York: John Wiley & Sons Inc, p. 521.

Vijayraghavan, P., Krishnan, R., 1999. Noise in Electric Machines: A Review. *IEEE Transactions on Industry Applications*. Vol. 35, No. 5, pp. 1007-1013.

Vogt, K., 1983. *Elektrische Maschinen*. Berlin: VEB Verlag Technik, p. 500. In German.

Walzer, I., 2002. Technological Trends in Large Permanent Magnet Motor Applications. In *Proceedings of International Conference on Electrical Machines, ICEM'02*, Brygge, Belgium. On CD-ROM.

Weh, H., 1980. High Power Synchronous Machines with Permanent Magnet Excitation. *Proceedings of International Conference on Electrical Machines, ICEM'80*, Athens, Greece, pp. 295-303.

Weh, H., Mosebach, H., May, H., 1984. Design Concepts and Force Generation in Inverter-Fed Synchronous Machines with Permanent Magnet Excitation. *IEEE Transactions on Magnetics*. Vol. 20, No. 5, pp. 1756-1761.

Yang, S. J., 1981. *Low-Noise Electrical Motors*, Oxford: Clarendon Press, p. 101.

Young, W. C., 1989. *Roark's formulas for stress and strain,* Singapore: McGraw-Hill Book Co., p. 763.

Yuan, Z.X., Saniei, N., Yan, X.T., 2003. Turbulent Heat Transfer on the Stationary Disk in a Rotor-Stator System. *International Journal of Heat and Mass Transfer*, Vol. 46, 2003, pp. 2207-2218.

Zhang, Z., Profumo, F., Tenconi, A., 1996. Axial-flux Versus Radial-flux PM Machines. *Electromotion*, Vol. 3, No. 3, pp. 23-29.

Zhu, Z. Q., Howe, D., 1992. Analytical Prediction of the Cogging Torque in Radial-Field Permanent Magnet Brushless Motors. *IEEE Transaction on Magnetics,* Vol. 28, pp. 1371-1374.

Zhu, Z.Q., Howe, D., Bolte, E., Ackermann, B., 1993. Instantaneous Magnetic Field Distribution in Brushless Permanent Magnet DC Motors, Part I: Open-Circuit Field. *IEEE Transaction on Magnetics*. Vol. 29, pp. 124-135.

A.1 Equations to calculate stator natural frequencies

Appendix A.1 describes a method for calculating the stator natural frequencies according to Yang (1981). The considered stator structure is illustrated in Fig. A.1.

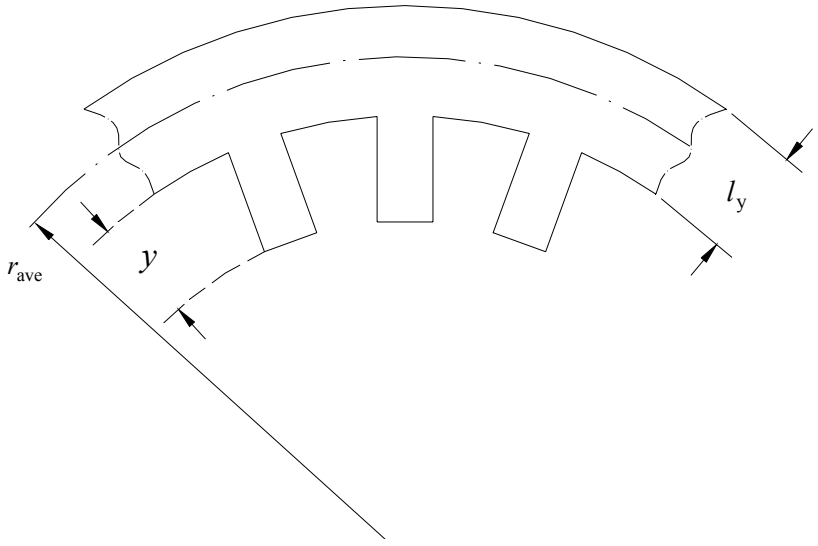

Fig. A.1. Part of the stator structure.

The natural frequencies may be divided into different modes. The natural frequency of the pulsating vibration mode may be defined as

$$f_{m0} = \frac{1}{2\pi r_{ave}} \sqrt{\frac{\Gamma}{\rho_{Fe} k_G}}, \tag{A.1}$$

where

Γ is the modulus of the elasticity of the stator core material
r_{ave} is the mean radius of the stator core according to Fig. A.1.
k_G is the mass addition factor for the displacement

The mass addition factor for the displacement is defined as

$$k_G = 1 + \frac{G_t + G_w + G_{ins}}{G_y}, \tag{A.2}$$

where

G_t is the total weight of the teeth
G_w is the copper weight in the winding
G_{ins} is the weight of the insulation
G_y is the weight of the stator yoke iron

The natural frequency for the unity circumferential vibration mode may be calculated as

$$f_{\mathrm{m1}} = f_{\mathrm{m0}} \sqrt{\frac{2}{1+\frac{l_{\mathrm{y}}^2}{3D_{\mathrm{ave,s}}^2}\left(\frac{\left(1+\frac{12\mathrm{Q}k_{\mathrm{y}}}{\pi D_{\mathrm{ave,s}} l_{\mathrm{RF}} l_{\mathrm{y}}^3}\right)}{k_{\mathrm{G}}}\right)}}, \tag{A.3}$$

where

l_{RF} is the axial length of the radial-flux machine stator stack
Q is the number of slots
$D_{\mathrm{ave,s}}$ is the average diameter of the stator yoke, i.e. $D_{\mathrm{ave,s}} = 2r_{\mathrm{ave}}$

The coefficient k_{y} is defined as

$$k_{\mathrm{y}} = S_{\mathrm{t}} \frac{G_{\mathrm{t}} + G_{\mathrm{w}} + G_{\mathrm{ins}}}{G_{\mathrm{t}}} \left(y^3 \left(\frac{1}{3} + \frac{l_{\mathrm{y}}}{2y} + \left(\frac{l_{\mathrm{y}}}{2y} \right)^2 \right) \right), \tag{A.4}$$

where

S_{t} is the tooth cross sectional area

For the rest circumferential vibration modes m_{m} the natural frequencies may be found as

$$f_{\mathrm{m}\geq 2} \frac{f_{\mathrm{m0}} l_{\mathrm{y}} \left(m_{\mathrm{m}}^2 - 1\right) k_{\varphi}}{D_{\mathrm{ave,s}} \sqrt{3} \sqrt{m_{\mathrm{m}}^2 + 1}}, \tag{A.5}$$

where

m_{m} is the mode number of vibration

The coefficient k_{φ} in (A.5) is defined as

$$k_{\varphi} = \left(1 + \frac{\left(\frac{l_{\mathrm{y}}^2}{3D_{\mathrm{ave,s}}^2}\right)\left(m_{\mathrm{m}}^2 - 1\right)\left(m_{\mathrm{m}}^2 \left(4 + \frac{\left(1+\frac{12Qk_{\mathrm{y}}}{\pi D_{\mathrm{ave,s}} l_{\mathrm{RF}} l_{\mathrm{y}}^3}\right)}{k_{\mathrm{G}}} \right) + 3 \right)}{m_{\mathrm{m}}^2 + 1} \right)^{-0.5} \tag{A.6}$$

In the analysis only the vibration mode (2,0) is of interest. Thus, the teeth and windings do not notably contribute to the stiffness of the stator. With vibration mode (2,0) the influence on the rotary inertia of the stator core is also insignificant and thus when $m_{\mathrm{m}} = 2$ the result obtained

from Eqn. (A.5), with a practical accuracy, corresponds with the result calculated for the smooth ring. As a result the reported approach is equivalent with respect to (?) the computation model of an axial-flux machine stator the natural frequency of which is calculated next.

The natural frequency of an axial-flux machine stator is calculated using the vibration model of an annular disk. It is assumed that the contribution of the teeth to both the stiffness and the rotary inertia of the disk is insignificant, which is a valid assumption for the considered vibration mode. For the AF structures the vibration mode (0,2) is considered. For free annular plates the natural frequency may be calculated as

$$f_{\mathrm{n}} = \frac{k_{\mathrm{n}}}{2\pi}\left(\frac{\sqrt{\dfrac{\Gamma}{k_{\mathrm{G}}\rho_{\mathrm{Fe}}}}}{\sqrt{12\left(1-\upsilon^2\right)}}\right)\frac{l_{\mathrm{y,AF}}}{r_{\mathrm{s,out}}^2}, \tag{A.7}$$

where

$l_{\mathrm{y,AF}}$ is the axial thickness of the stator yoke of an axial-flux machine

In this case the mode coefficient k_{n} depends on both the mode number and diameter ratio k_{D} of an axial-flux machine stator. In table A1 the k_{n} values are given as a function of k_{D}. The values are calculated according to Leissa (1969).

Table A1. k_{n} values for some k_{D} values (Leissa, 1969).

k_{D}	0.4	0.5	0.6	0.7	0.8
k_{n}	4.567	4.203	3.865	3.519	3.2

A.2 Equations to calculate deflection of rotor disk of AFIPM machine

In Appendix A.2 a method for calculating the deflection of the circular disk is described according to Yuang (1989). The rotor structure considered in this thesis is shown in Fig. A.2.

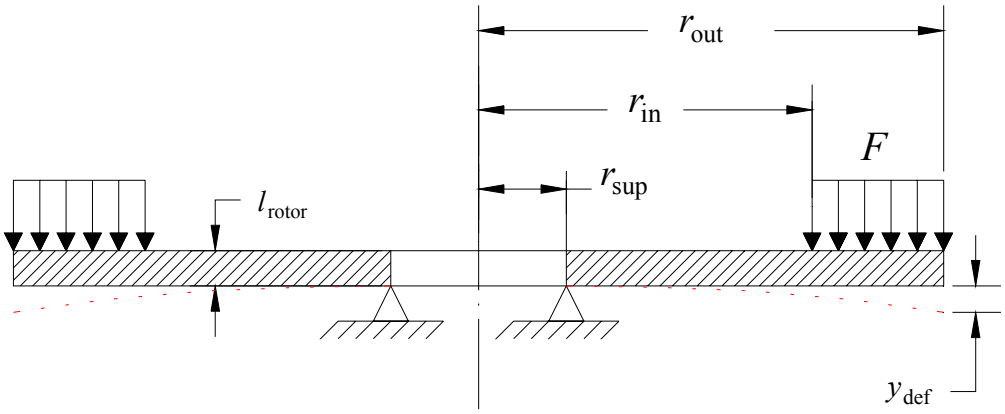

Fig. A.2. Rotor support structure a.

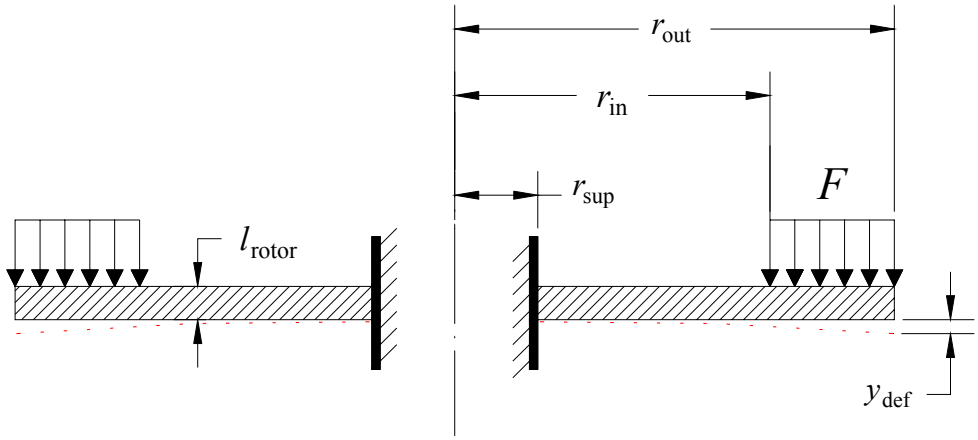

Fig. A.3. Rotor support structure b.

For the structure depicted in Fig. A.2 the maximum deflection due to the uniformly distributed load F (force per unit area) may be calculated as

$$y_{\mathrm{def}} = k_1 r_{\mathrm{out}} k_2 + k_3 \frac{r_{\mathrm{out}}^3}{k_4} k_5 - \frac{F r_{\mathrm{out}}^4}{k_4} k_6 , \tag{A.7}$$

and for the rotor structure b depicted in Fig. A.3 the maximum deflection due to the uniformly distributed load F (force per unit area) may be calculated as

$$y_{\mathrm{def}} = k_{10} \frac{r_{\mathrm{out}}^2 k_{11}}{k_4} + k_1 \frac{r_{\mathrm{out}}^3}{k_4} k_5 - \frac{F r_{\mathrm{out}}^4}{k_4} k_6 . \tag{A.8}$$

The coefficients k in (A.7) and (A.8) are described as follows (to find the definitions for the geometrical measures it is referred to Fig. A.2 and Fig. A.3).

$$k_1 = \frac{-Fr_{\text{out}}^3}{k_4 k_7}\left[\frac{k_8}{2r_{\text{out}}r_{\text{sup}}}\left(r_{\text{out}}^2 - r_{\text{in}}^2\right) - k_9\right]. \tag{A.9}$$

$$k_2 = \frac{1+\upsilon}{2}\frac{r_{\text{sup}}}{r_{\text{out}}}\ln\frac{r_{\text{out}}}{r_{\text{sup}}} + \frac{1-\upsilon}{4}\left(\frac{r_{\text{out}}}{r_{\text{sup}}} - \frac{r_{\text{sup}}}{r_{\text{out}}}\right), \tag{A.10}$$

where

υ is the Poisson's ratio

$$k_3 = \frac{F}{2r_{\text{sup}}}\left(r_{\text{out}}^2 - r_{\text{in}}^2\right). \tag{A.11}$$

$$k_4 = \frac{\Gamma l_{\text{rotor}}^3}{12\left(1-\upsilon^2\right)}, \tag{A.12}$$

where

Γ is the modulus of elasticity

$$k_5 = \frac{r_{\text{sup}}}{4r_{\text{out}}}\left[\left(\left(\frac{r_{\text{sup}}}{r_{\text{out}}}\right)^2 + 1\right)\ln\frac{r_{\text{out}}}{r_{\text{sup}}} + \left(\frac{r_{\text{sup}}}{r_{\text{out}}}\right)^2 - 1\right] \tag{A.13}$$

$$k_6 = \frac{1}{64}\left(1 + 4\left(\frac{r_{\text{in}}}{r_{\text{out}}}\right)^2 - 5\left(\frac{r_{\text{in}}}{r_{\text{out}}}\right)^4 - 4\left(\frac{r_{\text{in}}}{r_{\text{out}}}\right)^2\left(2 + \left(\frac{r_{\text{in}}}{r_{\text{out}}}\right)^2\right)\ln\frac{r_{\text{out}}}{r_{\text{in}}}\right) \tag{A.14}$$

$$k_7 = \frac{1}{2}\left(1-\upsilon^2\right)\left(\frac{r_{\text{out}}}{r_{\text{sup}}} - \frac{r_{\text{sup}}}{r_{\text{out}}}\right) \tag{A.15}$$

$$k_8 = \frac{r_{\text{sup}}}{r_{\text{out}}}\left[\frac{1+\upsilon}{2}\ln\frac{r_{\text{out}}}{r_{\text{sup}}} + \frac{1-\upsilon}{4}\left(1 - \left(\frac{r_{\text{sup}}}{r_{\text{out}}}\right)^2\right)\right] \tag{A.16}$$

$$k_9 = \frac{1}{4}\left(1 - \frac{1-\upsilon}{4}\left(1 - \left(\frac{r_{\text{in}}}{r_{\text{out}}}\right)^4\right) - \left(\frac{r_{\text{in}}}{r_{\text{out}}}\right)^2\left(1 + (1+\upsilon)\ln\frac{r_{\text{out}}}{r_{\text{in}}}\right)\right) \tag{A.17}$$

$$k_{10} = \frac{-Fr_{\text{out}}^2}{k_{12}}\left(\frac{k_8}{2r_{\text{out}}r_{\text{sup}}}\left(r_{\text{out}}^2 - r_{\text{in}}^2\right) - k_9\right). \tag{A.18}$$

$$k_{11} = \frac{1}{4}\left(1 - \left(\frac{r_{\text{sup}}}{r_{\text{out}}}\right)^2\left(1 + 2\ln\frac{r_{\text{out}}}{r_{\text{sup}}}\right)\right) \tag{A.19}$$

$$k_{12} = \frac{1}{2}\left(1 + \upsilon + (1-\upsilon)\left(\frac{r_{\text{sup}}}{r_{\text{out}}}\right)^2\right) \tag{A.20}$$

A.3 Properties of permanent magnet material used in prototype machine

The prototype machine, described in Chapter 3, was equipped with the permanent magnet material Neorem 495a, manufactured by Neorem Magnets Oy. The material characteristics of Neorem 495a are reported in Fig. A3.1.

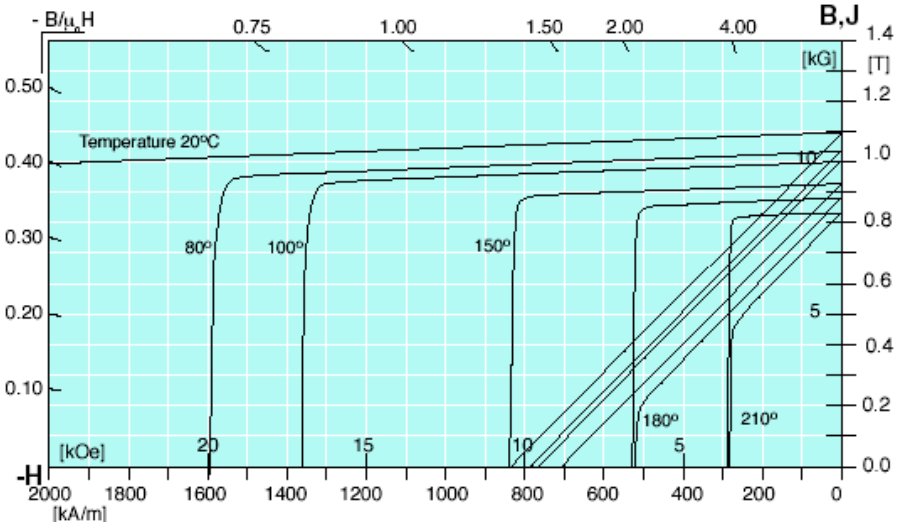

Fig. A3.1. Material characteristics of Neorem 495a. (Neorem, 2004).

The nominal values (at 20 °C) for the material Neorem 495a are reported in Table A3.1.

Table A3.1. Nominal values of Neorem 495a at a 20 °C temperature.

Property	Explanation	Value
B_r [T]	Remanence flux density	1.10
H_c [kA/m]	Coersivity	830
H_{ci} [kA/m]	Intrinsic coersivity	2400
$(BH)_{max}$ [kJ/m^3]	Maximum energy product	230

ACTA UNIVERSITATIS LAPPEENRANTAENSIS

172. KOISTINEN, PETRI. Development and use of organizational memory in close and long-term cooperation between organizations. 2003. 170 s. Diss.

173. HALLIKAS, JUKKA. Managing risk in supplier networks: case studies in inter-firm collaboration. 2003. U.s. Diss.

174. LINDH, TUOMO. On the condition monitoring of induction machines. 2003. 146 s. Diss.

175. NIKKANEN, MARKKU. Railcarrier in intermodal freight transportation network. 2003. 217 s. Diss.

176. HUISKONEN, JANNE. Supply chain integration: studies on linking customer responsiveness and operational efficiency in logistics policy planning. 2004. 151 s. Diss.

177. KUISMA, MIKKO. Minimizing conducted RF-emissions in switch mode power supplies using spread-spectrum techniques. 2004. 190 s. Diss.

178. SOPANEN, JUSSI. Studies of rotor dynamics using a multibody simulation approach. 2004. 91 s. Diss.

179. On the edge of fuzziness. Studies in honor of Jorma K. Mattila on his sixtieth birthday. Editors Vesa A. Niskanen and Jari Kortelainen. 2004. 132 s.

180. VÄISÄNEN, PASI. Characterisation of clean and fouled polymeric membrane materials. 2004. U.s. Diss.

181. IKÄVALKO, MINNA. Pas de deux of art and business: a study of commitment in art sponsorship relationships. 2004. 277 s. Diss.

182. ENQVIST, YUKO. Comprehensive study of crystal growth from solution. 2004. U.s . Diss.

183. JÄPPINEN, PEKKA. ME – mobile electronic personality. 2004. U.s. Diss.

184. HALME, TAPANI. Novel techniques and applications in generalised beam theory. 2004. 101 s. Diss.

185. LOISA, ANTTI. Studies on integrating kinematic design method with mechanical systems simulation techniques. 2004. 143 s., liitt. Diss.

186. 2nd Workshop on Applications of Wireless Communications. 2004. 74 s.

187. LI, XIAONING. Conflict-based method for conceptual process synthesis. 2004. U.s. Diss.

188. LAURILA, LASSE. Analysis of torque and speed ripple producing non-idealities of frequency converters in electric drives. 2004. 124 s. Diss.

189. NIKULA, UOLEVI. Introducing basic systematic requirements engineering practices in small organizations with an easy to adopt method. 2004. 207 s., liitt. Diss.

190. TANNINEN, JUKKA. Importance of charge in nanofiltration. 2004. U.s. Diss.

191. VIHTONEN, TIINA. Tuote- vai liiketoimintaosaamista? Pienten ja keskisuurten leipomoalan yritysten strategiset valinnat, liikkeenjohdon käytännöt ja menestyminen. 2004. 238 s. Diss.

192. TURUNEN-SAARESTI, TEEMU. Computational and experimental analysis of flow field in the diffusers of centrifugal compressors. 2004. 103 s. Diss.

193. SOLEYMANI, AZITA. Advanced topics in deformation and flow of dense gas-particle mixtures. 2004. U.s. Diss.

194. SALLINEN, PETRI. Modeling dynamic behavior in tilting pad gas journal bearings. 2004. 157 s. Diss.

195. HEILMANN, PIA. Careers of managers, comparison between ICT and paper business sectors. 2004. 262 s. Diss.

196. AHMED, MOHAMMAD. Sliding mode control for switched mode power supplies. 2004. U.s. Diss.

197. HUPPUNEN, JUSSI. High-speed solid-rotor induction machine – electromagnetic calculation and design. 2004. 168 s. Diss.

198. SALMINEN, PIA. Fractional slot permanent magnet synchronous motors for low speed applications. 2004. 150 s. Diss.

199. VARIS, JARI. Partner selection in knowledge intensive firms. 2004. U.s. Diss.

200. PÖYHÖNEN, AINO. Modeling and measuring organizational renewal capability. 2004. U.s. Diss.

201. RATAMÄKI, KATJA. Product platform development from the product lines´ perspective: case of switching platform. 2004. 218 s. Diss.

202. VIRTANEN, PERTTU. Database rights in safe European home: the path to more rigorous protection of information. 2005. 425 s. Diss.

203. Säädöksiä, systematiikkaa vai ihmisoikeuksia? Oikeustieteen päivät 19. – 21.8.2003. Toim. Marjut Heikkilä. 2004. 350 s.

204. PANTSAR, HENRIKKI. Models for diode laser transformation hardening of steels. 2005. 134 s., liitt. Diss.

205. LOHJALA, JUHA. Haja-asutusalueiden sähkönjakelujärjestelmien kehittäminen – erityisesti 1000 V jakelujännitteen käyttömahdollisuudet. 2005. 201 s., liitt. Diss.

206. TARKIAINEN, ANTTI. Power quality improving with virtual flux-based voltage source line converter. 2005. U.s. Diss.